

University of Windsor

Scholarship at UWindor

Electronic Theses and Dissertations

Theses, Dissertations, and Major Papers

10-15-2019

Semi-Analytical Approach Towards Design and Optimization of Induction Machines for Electric Vehicles

Aida Mollaeian
University of Windsor

Follow this and additional works at: <https://scholar.uwindsor.ca/etd>

Recommended Citation

Mollaeian, Aida, "Semi-Analytical Approach Towards Design and Optimization of Induction Machines for Electric Vehicles" (2019). *Electronic Theses and Dissertations*. 8146.
<https://scholar.uwindsor.ca/etd/8146>

This online database contains the full-text of PhD dissertations and Masters' theses of University of Windsor students from 1954 forward. These documents are made available for personal study and research purposes only, in accordance with the Canadian Copyright Act and the Creative Commons license—CC BY-NC-ND (Attribution, Non-Commercial, No Derivative Works). Under this license, works must always be attributed to the copyright holder (original author), cannot be used for any commercial purposes, and may not be altered. Any other use would require the permission of the copyright holder. Students may inquire about withdrawing their dissertation and/or thesis from this database. For additional inquiries, please contact the repository administrator via email (scholarship@uwindsor.ca) or by telephone at 519-253-3000ext. 3208.

SEMI-ANALYTICAL APPROACH TOWARDS DESIGN AND OPTIMIZATION OF INDUCTION MACHINES FOR ELECTRIC VEHICLES

By

Aida Mollaeian

A Dissertation

Submitted to the Faculty of Graduate Studies
through the Department of Electrical and Computer Engineering
in Partial Fulfillment of the Requirements for
the Degree of Doctor of Philosophy
at the University of Windsor

Windsor, Ontario, Canada

© 2019 Aida Mollaeian

**SEMI-ANALYTICAL APPROACH TOWARDS DESIGN AND OPTIMIZATION
OF INDUCTION MACHINES FOR ELECTRIC VEHICLES**

By

Aida Mollaeian

APPROVED BY:

M. Youssef, External Examiner
University of Ontario Institute of Technology

A. Edrisy
Department of Mechanical, Automotive & Materials Engineering

M. Azzouz
Department of Electrical & Computer Engineering

K. Tepe
Department of Electrical & Computer Engineering

J. Tjong, Co-Advisor
Department of Electrical & Computer Engineering

N. C. Kar, Advisor
Department of Electrical & Computer Engineering

11st October 2019

DECLARATION OF CO-AUTHORSHIP/PREVIOUS PUBLICATIONS

I hereby declare that this dissertation incorporates material that is the result of joint research, as follows: This dissertation includes the outcome of publications which also have co-authors who are/were graduate students or post-doctoral fellows supervised by Dr. Narayan Kar. In all cases, only primary contributions of the author towards these publications are included in this dissertation. The contribution of co-authors was primarily through the provision of assistance in experimentation and analysis. For Chapter 2, I am one of the co-authors, only sections with my contribution are included. I am aware of the University of Windsor Senate Policy on Authorship and I certify that I have properly acknowledged the contribution of other researchers on my dissertation and have obtained written permission from each of the co-author(s) to include the above material(s) in my dissertation. I certify that, with the above qualification, this dissertation, and the research to which it refers, is the product of my own work. This dissertation includes selected sections and extended work of research conducted in twelve original papers that have been published/submitted for publication in peer reviewed IEEE Transactions and IEEE International Conferences, as follows:

| Dissertation Chapter | Publication title/full citation | Publication status |
|----------------------|---|--------------------|
| 4 | A. Mollaeian , E. Ghosh, H. Dhulipati, J. Tjong and N. C. Kar, "3-D Sub-Domain Analytical Model to Calculate Magnetic Flux Density in Induction Machines with Semi-closed Slots Under No-Load Condition," <i>IEEE Transactions on Magnetics</i> , vol. 53, no. 6, pp. 1-5, June 2017. | Published |
| 2 and 3 | A. Mollaeian , S. M. Sangdehi, A. Balamurali, G. Feng, J. Tjong, and N. C. Kar, "Reduction of space harmonics in induction machines incorporating rotor bar optimization through a coupled IPSO and 3-D FEA algorithm," 2016 XXII International Conference on Electrical Machines (ICEM) | Published |

| | | |
|---|--|-----------|
| 5 | Aida Mollaeian , Eshaan Ghosh, Seog Kim, Jimi Tjong, and Narayan C. Kar. "Parametric and Sensitivity based Design Optimization to Extend Constant Power Speed Ratio of Induction Machine for EV Application," to be submitted to <i>IET Electric Power Application</i> , 2018 | Submitted |
| 5 | Aida Mollaeian , Mehdi Mehdi, Eshaan Ghosh, Afsaneh Edrisy, Seog Kim, Jimi Tjong, and Narayan C. Kar, "Investigation of Electromagnetic Torque Capability Reduction of Electric Machine Due to Magnetic Property Deterioration of Laminations," presented at the <i>International Conference on Magnetism</i> , San Francisco, USA, 2018 | Accepted |
| 4 | A. Mollaeian , M. Mousavi, A. Balamurali, J. Tjong, and N. C. Kar, "Optimal Design of Skewed Rotor Induction Machine for Space Harmonic Reduction Considering z-Axis Magnetic Flux Density Variation," presented at the <i>IEEE InterMag Conference</i> , San Diego, USA, 2016. | Accepted |
| 3 | E. Ghosh, A. Mollaeian , S. Kim, J. Tjong, and N. C. Kar, "DNN-Based Predictive Magnetic Flux Reference for Harmonic Compensation Control in Magnetically Unbalanced Induction Motor," <i>IEEE Transactions on Magnetics</i> , vol. 53, no. 11, pp. 1-7, Nov. 2017. | Published |
| 6 | Aida Mollaeian , Mehdi Mehdi, Eshaan Ghosh, Afsaneh Edrisy, Seog Kim, Jimi Tjong, and Narayan C. Kar, "Investigation of Electromagnetic Torque Capability Reduction of Electric Machine Due to Magnetic Property Deterioration of Laminations," to be submitted to <i>IEEE Transactions on Magnetics</i> ," | Submitted |
| 6 | A. Mollaeian , E. Ghosh, S. Kim, J. Tjong, and N.C. Kar, "Excessive Spatial Harmonic Prediction of Induction Machine Considering Manufacturing Tolerances through Sub-domain Method," Extended Abstract Submitted to the <i>IEEE Transactions on Energy Conversion</i> , Special section on Robust Design and Analysis of Electric Machines and Drives, 2019. | Submitted |

I certify that I have obtained a written permission from the copyright owners to include the above published materials in my dissertation. I certify that the above material describes work completed during my registration as graduate student at the University of Windsor.

I declare that, to the best of my knowledge, my dissertation does not infringe upon anyone's copyright nor violate any proprietary rights and that any ideas, techniques, quotations, or any other material from the work of other people included in my dissertation, published or otherwise, are fully acknowledged in accordance with the standard referencing practices. Furthermore, to the extent that I have included copyrighted material that surpasses the bounds of fair dealing within the meaning of the Canada Copyright Act, and have included copies of such copyright clearances to the appendix of this dissertation. I declare that this is a true copy of my dissertation, including any final revisions, as approved by my dissertation committee and the Graduate Studies office, and that this dissertation has not been submitted for a higher degree to any other University or Institution.

ABSTRACT

Electric machine design is a comprehensive task depending on the several factors, such as material resource limitations and economic factors. Therefore, an induction machine is a promising candidate because of the absence of magnetic material in the rotor. However, the conventional design approach can neither reflect the advances of the induction machine(IM) design nor exploit the trade-offs between design factors and the multi-physics nature of the electrical machine. Therefore, proposing fast and accurate novel methods to design, develop and analyze IMs using electromagnetic field oriented approaches is competitive to the old-fashion numerical methods. To achieve improved IM design from a baseline design to an optimal design, this dissertation: (1) Investigates the challenges of the high speed IM design specified for the electric vehicle application at the rated operating condition considering electromagnetic boundaries for the reasonable saturation level within a compact volume; (2) Proposes a new design approach of IM using modified equivalent circuit parameters to reduce spatial harmonics because of slotting effect and skewing effect; and also presents the importance of the 3-D analysis over 2-D analysis while developing the IM; (3) Proposes a novel electromagnetic field oriented mathematical model considering the slotting effect and axial flux variation because of skewing rotor bars to evaluate the IM performance with a lower and precise computational effort; (4) developed baseline IM is optimized with genetic algorithm incorporated in proposed subdomain model to improve the torque-speed profile. In order to further simplify the optimization procedure, a parametric and sensitivity based design approach is implemented to reduce the design variables.

To evaluate the proposed optimal IM with extended constant power region and high torque density within a compact volume using novel 3-D subdomain model, the machine has been prototyped and tested from low to high speed under no-load and loaded condition. Electrical circuit parameter variation is demonstrated and compared to the one simulated in the FEA environment. This innovation can be applied to a family of electric machines with various topologies.

This dissertation is dedicated to my lovely husband, parents, my little one (Adrian), sister and brothers . I love you all, each and everyone. Read it when you get some time, but don't ask me questions!

ACKNOWLEDGMENTS

I would like to express my deepest gratitude to my advisors, Narayan C. Kar and Dr. Jimi Tjong for their relentless guidance, caring, patience, and providing me with an excellent atmosphere for conducting research. To whatever I am today from the first day at University of Windsor, Dr. Narayan C. Kar has the greatest influence on me during this period. I would like to thank him for giving me this opportunity and platform to mold myself into a researcher and engineer. His constant motivation, pushing boundaries of hard work, charisma and exuding positivity all the time is infectious. A special thanks to Dr. Jimi Tjong for providing extensive help and guidance during prototyping of my motor. A special thanks to Dr. Afsaneh Edrisy, Dr. Maher A. Azzouz Abdelkhalek, Dr. Kemal Tepe for being my committee members and to Dr. Mohamed Youssef for serving as my external examiner for this doctoral degree.

I would like to thank Dr. Eshaan Ghosh for being a wonderful colleague apart from his friendship. Together we have been able to test our novel concepts and establish them. I would like to sincerely thank Dr. Seog Kim for his technical help and arrangements for my experiments. I would like to thank Dr. Aiswarya Balamurali and Dr. Mahdi Mousavi Sangdehi for their technical help. I would like to extend my thanks to Dr. Shruthi Mukundan and Dr. Himavarsha Dhulipati for their technical assistance whenever I had doubt as a doctoral candidate. Also, I would like to extend my thanks all the members of CHARGE Labs. I have learnt a lot from them which I have incorporated in both my professional and personal life. A special appreciation and thanks to my lovely husband, Dr. Hossein Ghaednia, for being the support in my life that I received more than I could have asked for and for his deep faith, patience and care for me.

TABLE OF CONTENT

| | |
|---|-------------|
| Declaration of Co-Authorship/Previous Publications | iii |
| Abstract..... | vi |
| Acknowledgments | viii |
| List of Tables | xiv |
| List of Figures..... | xvi |
| Nomenclature | xxii |
| CHAPTER 1 | 1 |
| INTRODUCTION..... | 1 |
| 1.1. Overview and Motivations..... | 1 |
| 1.2. Literature Reviews | 2 |
| 1.2.1. <i>Electric Vehicle Outlook in Market</i> | <i>4</i> |
| 1.2.2. <i>Comparison of Various Electric Machine Topologies Towards EV</i> <i>Development</i> | <i>7</i> |
| 1.3. Desired Design Targets for a High Speed Traction Motor | 9 |
| 1.4. Review of Existing Computer Aided Design Tools for Magnetic Field Analysis..... | 11 |
| 1.5. Research Objectives..... | 13 |
| 1.6. Research Contribution And Dissertation Layout..... | 14 |
| 1.7. References..... | 16 |
| CHAPTER 2 | 17 |
| DESIGN TARGETS AND TOPOLOGY SELECTION OF HIGH SPEED IM FOR ELECTRIC VEHICLE WITHIN A FIXED OUTER DIAMETER..... | 17 |
| 2.1. Introduction..... | 17 |
| 2.2. Calculating Design Targets of the Scaled down High Speed IM for Electric Vehicle Application | 18 |
| 2.3. Fixing Main Structural Sizing of Scaled Down High Speed Induction Motor for the Scaled down Design Targets | 20 |
| 2.3.1. <i>Winding Selection</i> | <i>24</i> |
| 2.3.2. <i>Selection of Stator-Rotor Slot Combination and Rotor Bar Dimensioning....</i> | <i>24</i> |

| | | |
|---|---|----|
| 2.4. | Verification of Analytical Design Structural Sizing Through Electromagnetic Design | 29 |
| 2.4.1. | <i>Comparative Analysis of Output Characteristics for Skewed and Non-Skewed Rotor Through 2D FEA.</i> | 30 |
| 2.5. | Conclusions..... | 34 |
| 2.6. | References..... | 35 |
| CHAPTER 3 | | 37 |
| COMPARISON OF 2-D AND 3-D FINITE ELEMENT ANALYSIS BASED INDUCTION MACHINE DESIGN AND VALIDATION WITH MODIFIED EQUIVALENT CIRCUIT APPROACH. | | 37 |
| 3.1. | Introduction..... | 37 |
| 3.2. | Comparative Analysis of Initial Design in 2-D FEA and 3-D FEA | 38 |
| 3.2.1 | <i>Characteristics of Initial Design of IM</i> | 38 |
| 3.2.2 | <i>Validation of 3-D FEA with Experimental Results</i> | 40 |
| 3.2.3 | <i>Performance Analysis of Initial Design in 2-D and 3-D FEA</i> | 42 |
| 3.3. | Improvement in IM Design Process Considering Space Harmonics..... | 44 |
| 3.4. | Modified Equivalent Circuit Parameters Considering Axial Field Variation and Slot Harmonics..... | 44 |
| 3.5. | Optimal Design of IM Using Modified Equivalent Circuit Parameters for Spatial Harmonic Reduction | 49 |
| 3.5.1 | <i>Torque Considering Axial Field Variation and Slot Harmonics</i> | 49 |
| 3.5.2 | <i>Improved Particle Swarm Optimization towards Design Improvement</i> | 50 |
| 3.6. | Optimal Design of IM Using Modified Equivalent Circuit Parameters for Spatial Harmonic Reduction | 53 |
| 3.7. | Conclusion | 55 |
| 3.8. | References..... | 56 |
| CHAPTER 4 | | 59 |
| 3-D SUB-DOMAIN ANALYTICAL MODEL TO CALCULATE MAGNETIC FLUX DENSITY IN INDUCTION MACHINES WITH SEMI-CLOSED SLOTS UNDER NO-LOAD CONDITION | | 59 |
| 4.1. | Introduction..... | 59 |
| 4.2. | 3-D Analytical Field Solution of IM..... | 59 |

| | | |
|---|--|-----------|
| 4.3. | General 3-D Solution of Laplace's Equation..... | 61 |
| 4.4. | General 3-D Solution of Helmholtz's Equation..... | 62 |
| 4.5. | General 3-D Solution of Poisson's Equation..... | 63 |
| 4.6. | Boundary and Interface Conditions | 64 |
| 4.7. | Validation of 3-D Sub-Domain Mathematical Model and 3-D Finite Element Analysis..... | 66 |
| 4.8. | Conclusion | 71 |
| 4.9. | References..... | 71 |
| CHAPTER 5..... | | 73 |
| SEMI-ANALYTICAL BASED MULTI-OBJECTIVE OPTIMIZATION OF ROTOR CONFIGURATION OF HIGH SPEED IM | | 73 |
| 5.1. | Introduction..... | 73 |
| 5.2. | Dimensioning of Inverter-fed Induction Motor Considering Magnetic Flux Level Boundaries | 75 |
| 5.3. | Novel Mathematical Model of Inductance Ratio Incorporating Frequency and Core Saturation | 80 |
| 5.1.1. | <i>Inductance Ratio Expressing in Terms of Supply Frequency Variation and Core Saturation in Rotor Flux Oriented Control</i> | <i>80</i> |
| 5.1.2. | <i>Inductance Ratio Expressing in Terms Of Supply Frequency and Core Saturation Using Structural Design Variables</i> | <i>84</i> |
| 5.4. | Structural Variable Reduction through Proposed Sensitivity Approach Coupled with FE Analysis | 86 |
| 5.4.1. | <i>Sensitivity Analysis Formulation</i> | <i>86</i> |
| 5.4.2. | <i>Proposed Sensitivity Analysis Approach towards Investigation of Structural Parameter on the Operation of IM</i> | <i>87</i> |
| 5.5. | Genetic Algorithm Based Structural Optimization Through FE and subdomain Analysis to Minimize Inductance Ratio to Enhance Capability of The IM.... | 91 |
| 5.5.1. | <i>Formulation of the Objective function to Optimize the Rotor Bar Geometry through Proposed Sub-Domain and FEA.....</i> | <i>91</i> |
| 5.5.2. | <i>FEA Based Investigation and Comparison of the Baseline and Improved Designs Targets</i> | <i>93</i> |

| | | |
|--|--|-----|
| 5.6. | Conclusion | 96 |
| 5.7. | References..... | 97 |
| CHAPTER 6..... | 100 | |
| EXPERIMENTAL VALIDATION OF THE PROPOSED OPTIMIZED HIGH SPEED INDUCTION MACHINE..... | 100 | |
| 6.1. | Introduction..... | 100 |
| 6.2. | Prototyping High Speed Induction Motor..... | 100 |
| 6.2.1. | <i>Stator and Rotor Cores</i> | 101 |
| 6.2.2. | <i>Housing.....</i> | 104 |
| 6.3. | Investigation of Electromagnetic Torque Capability Reduction of Electric Machine Due to Magnetic Property Deterioration of Laminations | 106 |
| 6.3.1. | <i>Methodology: Derivation of Analytical Expression for Permeability Drop.</i> | 107 |
| 6.3.2. | <i>Effective Relative Permeability.....</i> | 107 |
| 6.3.3. | <i>Experiment Based Investigation of Core Loss Variation Due to Manufacturing</i> | 109 |
| 6.3.4. | <i>Implementation of the Material Curve in Fem</i> | 110 |
| 6.4. | Investigation of Cut Edge Degradation Effect on Torque Capability of IM | 111 |
| 6.5. | Determination of Equivalent Parameter for a Wide-Speed Range through Experimental Investigation | 116 |
| 6.5.1. | <i>Determination of Electrical Circuit Parameters at Rated Condition</i> | 116 |
| 6.5.2. | <i>Determination Of the Electrical Circuit Parameters Variation Over Wide Speed Range.....</i> | 120 |
| 6.6. | Load Test | 126 |
| 6.7. | Conclusion | 128 |
| 6.8. | References..... | 129 |
| CHAPTER 7 | 131 | |
| CONCLUSION AND SUGGESTED FUTURE WORK..... | 131 | |
| 7.1. | Conclusion | 131 |
| 7.2. | Future Work..... | 131 |
| Appendix A: List of Publications | 133 | |
| Appendix B: List of Industrial Projects and Scholarships..... | 136 | |

| | |
|---|------------|
| Appendix C: Permission for Using IEEE Publications | 137 |
| Vita Auctoris..... | 142 |

LIST OF TABLES

| | |
|--|-----|
| TABLE 1. 1. Price, Acceleration, Driving Range, Power Rating and Electric Motor Configuration of Commercially Available Electrified Vehicles [18]-[19]..... | 5 |
| TABLE 1. 2. PMSM and IM comparison from marketing and performance characteristic aspects [34] | 8 |
| TABLE 1. 3. Satisfactory Powertrain Targets in 2022. | 10 |
| TABLE 1. 4. Comparison of Computational Performance of Electromagnetic Field Solutions [36-41]. | 12 |
| TABLE 2. 1. Details of Laboratory Electric Vehicle IPM Motor Drive and Transmission | 19 |
| TABLE 2. 2. Details of Scaled Down Design Targets for High Speed Induction Motor... | 19 |
| TABLE 2. 3. Inverter Specification Used for IM Development..... | 21 |
| TABLE 2. 4. Permitted flux densities of the magnetic circuit for various standard electrical machines | 28 |
| TABLE 3. 1. Rated and Geometrical Parameters of Initial IM for FEA Modeling | 39 |
| TABLE 3. 2. Calculated and Measured IM Circuit Parameters..... | 39 |
| TABLE 3. 3. IPSO PARAMETERS, BASE AND OPTIMAL VARIABLES | 52 |
| TABLE 4. 1. DESIGN DATA FOR FEA MODELING | 67 |
| TABLE 5. 1. POWER RATING AND GEOMETRICAL PARAMETERS OF THE BASELINE IM | 77 |
| TABLE 5. 2. MAIN DIMENSION AND POWER RATING OF THE BASELINE IM USED IN PARAMETRIC APPROACH BASED OPTIMIZATION | 78 |
| TABLE 5. 3. RATED AND PEAK PARAMETERS OF OPTIMAL IM..... | 96 |
| TABLE 6. 1. PROPERTIES OF THE STATOR AND ROTOR CORES..... | 101 |
| TABLE 6. 2. COMPARISON OF MBNM BEFORE AND AFTER CUTTING M230-35A..... | 110 |

| | |
|---|-----|
| TABLE 6. 3. Improved IM Parameters Validation at Rated Condition..... | 120 |
| TABLE 6. 4. Experimental validation of Magnetizing Flux Weakening beyond the Rated Speed..... | 122 |

LIST OF FIGURES

| | |
|---|----|
| Figure 1. 1. Annual global light duty vehicle sales forecast [2]. | 2 |
| Figure 1. 2. Ideal torque-power/speed characteristics of traction motor [5]. | 3 |
| Figure 1. 3. Ford Focus EV propulsion system [8]. | 4 |
| Figure 1. 4. The break down cost of PMSM [10]. | 5 |
| Figure 1. 5. 2-D cross section of mainly used electric machines in current commercial EVs, (a) squirrel cage IM, (b) interior PMSM. | 7 |
| Figure 1. 6. Comparison of power-speed characteristics: (a) IPM power versus speed curves (limited voltage), for rated and overload current amplitudes. Effect of rotor saliency on the power overload curve. (b) IM power versus speed curves, for rated and overload current amplitudes and limited voltage [34]. | 9 |
| Figure 2. 1. Vehicle rear-wheel drive powertrain diagram. | 20 |
| Figure 2. 2. Laboratory components for IM development (a) The existing industrial stator in CHARGE Labs facility used for high speed IM development, (b) Fan-cooled inverter used for high speed IM drive. | 21 |
| Figure 2. 3. The design algorithm of variable frequency IM employing Analytical Closed Form Equations. | 22 |
| Figure 2. 4. Comparison of the selected designs obtained from automated parametric based optimization approach, (a) 36-24, (b) 36-26, (c) 36-30, (d) 36-40, (e) 36-42. | 25 |
| Figure 2. 5. Comparison of steady state output and magnetic characteristics for different stator-rotor slot-pole combinations. (a)Efficiency. (b)Rated speed. (c)Power factor. (d)Rated torque (e)Torque ripple. (f)Maximum torque (g)Inductance ratio (h)Maximum torque (i)Stator yoke flux density (j) Rotor bar current (k) Stator yoke flux density at rated and peak operated conditions. | 28 |
| Figure 2. 6. A CAD drawing of developed high speed IM in FEA. | 29 |
| Figure 2. 7. Schematic of voltage fed external circuit excitation used in FE analysis. | 30 |
| Figure 2. 8. The line to line peak current of developed high speed IM in 2D FEA at the rated operating condition with a sinusoidal supply voltage. a) non-skewed rotor bars, b) skewed rotor bars. | 31 |

| | |
|---|----|
| Figure 2. 9. Torque-Speed profile of developed high speed IM in 2D FEA. a) non-skewed rotor bars, b) skewed rotor bars. | 33 |
| Figure 2. 10. Cross section of developed high speed IM and magnetic flux density distribution at steady state condition and rated operating condition. a) non-skewed rotor bars, b) skewed rotor bars. | 34 |
| Figure 3. 1. Parameter determination of the 7.5 hp, 4-pole induction machine. a) Schematic of 2-D FEA model and existing rotor. b) Experimental setup. | 40 |
| Figure 3. 2. Search coil in the stator slot opening. (a) End winding of the search coil. (b) Overview of a complete turn of the search coil around one stator slot. | 41 |
| Figure 3. 3. Measured induced voltage from search coil at the no-load condition with a slip of 0.0061. Fig. 4. Comparison of the measured and calculated magnetic flux in the air-gap at the no-load condition with the slip of 0.0061. | 41 |
| Figure 3. 4. Magnetic flux density distribution in the air-gap over one pole pair of 2-D and 3-D finite element model for variable speed under no-load condition. (a) Radial, (b) Circumferential, (c) Total flux. | 43 |
| Figure 3. 5. Performance characteristics comparison of 2-D and 3-D finite element model for variable speed. (a) Current for phase A, (b) Developed torque for a variable speed range of 0-1,780 rpm. | 44 |
| Figure 3. 6. The design process of spatial harmonic reduction of IM. | 45 |
| Figure 3. 7. Simplified equivalent circuit of IM considering stator and rotor slot harmonics. | 49 |
| Figure 3. 8. IPSO algorithm to optimize the machine model. | 51 |
| Figure 3. 9. Comparison parameters for initial and improved design with respect to related skew angle: (a) Geometrical parameters (b) Electrical and performance characteristics. | 53 |
| Figure 3. 10. Space distribution of magnetic flux density in the air-gap for the no-load operating condition for a single layer winding. (a) Radial, (b) Circumferential, and (c) Axial in 3-D FEA. | 54 |
| Figure 3. 11. Normalized harmonic components of total magnetic flux density in the air-gap for the no-load operating condition. | 55 |

| | |
|--|----|
| Figure 3. 12. Performance characteristics comparison of initial and improved designs of IM. (a) Self and magnetizing reactances under the no-load condition with a slip of 0.0061. (b) Electromagnetic torque production for 1,200 rpm. | 56 |
| Figure 4. 1. Sketch of i^{th} stator semi-closed slot for a single layer concentric winding and i^{th} rotor cage bar with domain indexing bar for stator slot, stator slot opening, rotor slot and rotor slot opening and air-gap subdomains. | 60 |
| Figure 4. 2. 3-D FEA and analytical prediction of magnetic flux density with a slip of 0.001 in the middle of the air-gap. (a) Radial. (b) Circumferential. (c) Axial components. | 69 |
| Figure 4. 3. 3-D FEA and analytical prediction of magnetic flux density with a slip of 0.001 in the rotor and stator slots. (a) Radial. (b) Circumferential. (c) axial components in the first stator slot. (d) Radial. (e) Circumferential. (f) Axial components in the first rotor slot. | 70 |
| Figure 4. 4. Comparison of torque-speed characteristics with a slip of 0.05. | 70 |
| Figure 5. 1. Flowchart of the computationally efficient design procedure. | 76 |
| Figure 5. 2. The stator of developed high-speed IM used for parametric based optimization. (a) prototyped stator core with manufactured laminations. (b) single lamination of the stator (c) schematic of the single slot. | 78 |
| Figure 5. 3. Comparison of steady state output and magnetic characteristics at different stator-rotor slot-pole combinations. (a) Maximum torque. (b) Maximum power. (c) Efficiency. (d) Rotor yoke flux density. (e) Stator yoke flux density. (f) Torque ripple at the rated operating condition for corresponding full pitch double layer winding layout for each stator slot-rotor slot-pole combination | 79 |
| Figure 5. 4. Impact of IM parameters on the torque-speed profile considering saturation effect for a wide speed range, a) Torque-speed profile, b) air-gap flux density, c) rotor leakage inductance, d) magnetizing inductance variation for the various operating condition for the same voltage and frequency variations. | 83 |
| Figure 5. 5. Inductance ratio for different slot combination for a wide speed range considering saturation and supply frequency effect. | 84 |
| Figure 5. 6. Description of the investigated induction machine structural design variables for sensitivity analysis based optimization. | 86 |

| | |
|--|-----|
| Figure 5. 7. Comparison of rotor bar geometrical parameter tolerances on output characteristics. a) Sensitivity analysis of rotor bar opening height and width. b) Sensitivity study of rotor bar height and width on inductance ratio, maximum torque, and efficiency..... | 91 |
| Figure 5. 8. Comparison of convergence rate using proposed sub-domain model and FEA to obtain the minimum inductance ratio to maximize the speed range..... | 93 |
| Figure 5. 9. Objective function evaluation for inductance ratio by optimizing rotor slot geometrical parameters using the main structural variables affecting the objective function a. | 94 |
| Figure 5. 10. Unsaturated magnetic field distribution of the optimal IM at 2,940 rpm and rated torque at rotor and stator slot edge..... | 94 |
| Figure 5. 11. Objective function convergence to maximize efficiency and peak torque by optimizing rotor slot geometrical parameters using the main structural variables affecting the objective function b..... | 95 |
| Figure 5. 12. Comparison of Inductance ratio of optimal IM and baseline design..... | 95 |
| Figure 5. 13. Comparison of Maximum torque at the rated condition of optimal IM and baseline design..... | 95 |
| Figure 5. 14. Efficiency map of optimal IM. | 96 |
| Figure 6. 1. The exploded view of the developed high speed induction machine. | 100 |
| Figure 6. 2. Electrical steel used in prototyping high speed IM, (a) Material sheets with C5 coating, (b) The B-H characteristics of M230-35A under various frequencies..... | 102 |
| Figure 6. 3. Steps of forming stator and rotor cores, (a) Fixture used to cut the stator and rotor laminations, (b) Cutting process of laminations, (c) Stator lamination, (d) Rotor lamination, (e) Stator fixture, (f) Rotor fixture. | 102 |
| Figure 6. 4. High speed induction machine assembled cores, (a) 36 slot stator core, (b) 42 slot rotor core. | 103 |
| Figure 6. 5. Steps of winding the stator, (a) insertion of insulation paper, (b). coil forming, (c) insertion of coils in slots, (d) connecting the coil groups. | 103 |
| Figure 6. 6. Steps of rotor assembly, (a) Manufactured rotor end ring with aluminum alloy 6061, (b). wire cut rotor bar, (c) assembled and welded rotor..... | 104 |

| | |
|--|-----|
| Figure 6. 7. Housing components of the developed high speed IM, (a) Main body of the housing and cooling channel sealing, (b) end cap, (c) front cap, (d) shaft. | 105 |
| Figure 6. 8. Steady temperature rises of the high speed IM. (a) The 3D meshed model of cooling channels, (b) The 3D meshed model of the housing (c) Thermal distribution of the flowing liquid in cooling channels(d) thermal distribution of the developed IM at the housing. | 105 |
| Figure 6. 9. The average MBN (V_{rms}) for the different spots at different magnetization directions before and after cutting compared with the texture factor arising from magnetocrystalline anisotropy. | 110 |
| Figure 6. 10. Degradation profile [5] permeability drops for M230-35A. | 111 |
| Figure 6. 11. The mechanical effect of cutting procedure on stator lamination stress in the x-axis, b) stress in the y-axis, c) mices and d) maximum strain. | 112 |
| Figure 6. 12. A sample comparison of IM characterization for non-degraded and degraded steel: a) self- inductance, b) mutual inductance, c) the rated electromagnetic torque at 2915.74 rpm. | 115 |
| Figure 6. 13. A sample comparison of IM characterization for non-degraded and degraded steel: a) Core loss, b) Efficiency at 2915.74 rpm. | 116 |
| Figure 6. 14. measurement of DC current for various DC voltage excitation. | 117 |
| Figure 6. 15. Experimental set up with locked rotor fixture to determine leakage inductance and rotor resistance(a) Drive unite set up to apply the voltage for locked rotor test, (b) Current measurement during the locked rotor test, (c) blocked rotor with the built fixture. | 118 |
| Figure 6. 16. Experimentally measured applied voltage and current waveforms at the no-load test and rated operating condition. | 118 |
| Figure 6. 17. Experimentally measured applied voltage and current waveforms at locked rotor test and rated operating condition, a) Applied PWM voltage signals, b) Fundamental voltage and current three-phase waveforms at 2915.74 rpm. | 119 |
| Figure 6. 18. Experimentally measured applied voltage and current waveforms at the no-load test from low to high speed operating conditions, a) Applied PWM voltage signals, b) Fundamental voltage and current three-phase waveforms at 1,500 rpm. | 122 |

| | |
|--|-----|
| Figure 6. 19. Experimentally measured applied voltage and current waveforms at locked rotor test, a) Applied PWM voltage signals, b) Fundamental voltage and current three-phase waveforms at 1,500 rpm. | 123 |
| Figure 6. 20. Experimentally measured applied voltage and current waveforms at locked rotor test from low to high speed operating conditions applied voltage and current waveforms at locked rotor test, (a) at 4,000rpm, (b) at 5,000rpm, (c) at 6,000rpm (d) at 7,000 rpm. | 124 |
| Figure 6. 21. Comparison of measured rotor resistances through experiment and finite element analysis with the similar operating condition for different supply frequencies. | 124 |
| Figure 6. 22. Experimentally measured applied voltage and current waveforms at locked rotor test from low to high speed operating conditions applied voltage and current..... | 125 |
| Figure 6. 23. Experimentally measured applied voltage and current waveforms at locked rotor test from low to high speed operating conditions applied voltage and current..... | 125 |
| Figure 6. 24. Experimentally measured applied voltage and current waveforms at locked rotor test from low to high speed operating conditions applied voltage and current..... | 126 |
| Figure 6. 25. Experimentally measured applied voltage and current waveforms at locked rotor test from low to high speed operating conditions applied voltage and current..... | 126 |
| Figure 6. 26. Conducted load test for the prototyped high speed IM, (a) Load test experimental set up with cooling inlet and outlet connections. (b) Torque demand ramp at 1,000 rpm. | 127 |
| Figure 6. 27. Conducted load test for the prototyped high speed IM, (a) Load test experimental set up with cooling inlet and outlet connections. (b) Torque demand ramp at 1,000 rpm. | 128 |

NOMENCLATURE

| Abbreviation | Explanation |
|-----------------|--------------------------------------|
| EV | Electric vehicles |
| ICE | Internal combustion engines |
| EM | Electric machine |
| PMSMs | Permanent magnet synchronous motors |
| IM | Induction motor |
| VC | Vector control |
| DTC | Direct torque control |
| R&D | Research and development |
| FEM | Finite element method |
| MEC | Magnetic equivalent circuit |
| WFM | Winding function method |
| SD | Subdomain |
| IPSO | Improved particle swarm optimization |
| FEM | Finite element Analysis |
| i_x | Engaged drive ratio |
| i_0 | Final drive gear ratio |
| T_w | Wheel torque |
| T_e | Engine torque |
| F_w | Wheel force |
| r_w | Wheel radius |
| D | Outer diameter |
| L | Effective length |
| V_r | Rotor volume |
| σ_{Ftan} | Tangential stress |

| | |
|--------------|-----------------------------------|
| K_w | Winding distribution factor |
| A | Local current density |
| B_{δ} | Local flux density |
| L_{ag} | Air-gap length |
| D_{or} | Outer rotor diameter |
| v | The peripheral speed of the rotor |
| ω | Rated frequency |
| τ_p | Pole pitch |
| α_i | Saturation factor |
| B_{ag} | Air-gap flux density |
| m | Number of phases |
| a | Number of parallel paths |
| Q_s | Number of stator slots |
| Q_r | Number of rotor slots |
| I_s | Stator phase current |
| I_r | Rotor phase current |
| P | Output power |
| p | Number of pole pairs |
| $\cos\theta$ | Power factor |
| V_{ph} | Stator phase voltage |
| Z_{Qs} | Number of conductors per slot |
| η | Efficiency |
| 2-D | Two-dimensional |
| 3-D | Three-dimensional |
| ECP | Equivalent circuit parameters |
| R_s | Stator phase resistance |
| R_r | Rotor phase resistance |

| | |
|-----------------|---|
| X_{ls} | Stator leakage reactance |
| X_{lr} | Rotor leakage reactance |
| X_m | Magnetizing reactance |
| R_{rv} | Rotor slot harmonic resistances |
| $L_{s\sigma v}$ | Stator harmonic leakage inductances |
| $L_{r\sigma v}$ | Rotor harmonic leakage inductances |
| L_{mv} | Air-gap harmonic leakage inductances |
| t_r | Thickness of the end-ring in the axial direction |
| v | Harmonic orders |
| l' | Effective core length |
| δ_{eff} | Air-gap length |
| s | Fundamental slip |
| s_v | Harmonic slip |
| V_{ind} | rms value of the induced voltage |
| rms | Root mean square |
| c_1 | Cognitive parameters |
| c_2 | Social parameters |
| w_i | Inertia weight |
| A | Magnetic vector potential |
| A_p | Radial magnetic vector potential component |
| A_θ | Circumferential magnetic vector potential component |
| A_z | Axial magnetic vector potential component |
| PDEs | Partial differential equations |
| B_\perp | Normal component of flux density |
| H_\parallel | Parallel component of the flux intensity |
| N_s | Number of conductors per phase |
| S_s | Net area of wounded stator slot |

| | |
|-----------------|---|
| W_1 | Winding layout matrix |
| I_m | Peak current in stator windings |
| ω_{rm} | Rotor speed |
| μ_0 | Permeability of the air gap |
| μ_r | Permeability of the rotor bars |
| σ | Conductivity of rotor bars |
| J_1 | First order of Bessel functions of first kinds |
| Y_1 | First order of Bessel functions of second kinds |
| F_2 | Generalized hypergeometric G -functions |
| $G_{2,4}^{2,1}$ | Generalized Meijer G -functions |
| B | Magnetic flux density |
| n | Normal unit vector |
| Γ | Integration path |
| r | Displacement vector from the rotor to the segment |

CHAPTER 1

INTRODUCTION

1.1. Overview and Motivations

The increasing demand electric vehicles (EV) requires technological improvements of individual powertrain components, including electric motors, power electronics, and energy storage. Based on 2018 sales analysis presented in Figure 1.1, it is estimated that EV sales will increase from 1.1 million worldwide to 30 million in 2030 as EVs become cheaper compared to internal combustion engine (ICE) vehicles. North America accounts for more than 11% of global sales [1] and [2]. EV powertrain is characterized by an electric motor to convert electrical energy to mechanical energy maintaining the required high energy density. Although currently, available traction motors maintain high efficiency, high torque, lower maintenance, and cost compared to the conventional ICE cars. However, they are not as cost competitive as conventional vehicles to gain large-scale market penetration [3]. For this to become a reality, further research is ongoing to develop new cost-efficient technologies and machine topologies. Therefore, advances in electrical machines with higher performance characteristics with a lower cost could significantly reduce the cost of industrial and residential energy systems to meet the potential market demand.

This Chapter first provides a summary of currently available EVs to assist in setting the required and justified design targets to improve electric motors for EV technology through scientific research and development (R&D) activities conducted in this dissertation. Section 1.2 explains the desired fundamental characteristics of traction motors for EV application. Such a background study helps understand the challenges and benefits of various design of electric machine topologies in order to improve some of their features such as weight, cost, efficiency and speed range using mathematical modeling, design, analysis methods, and testing. Section 1.3 is a review and the state-of-the-art technology in the research areas of computer-aided design tools to design electric machines-such tools

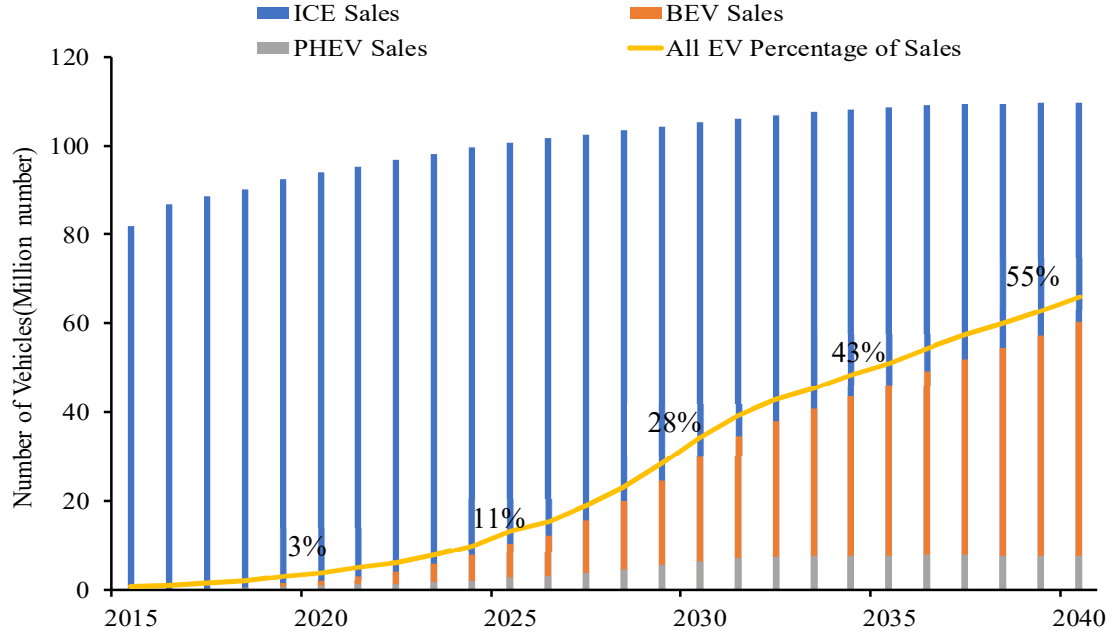


Figure. 1.1. Annual global light duty vehicle sales forecast [2].

are a major area of focus of this dissertation. Section 1.3 discusses available mathematical techniques to design and develop electric machines. Therefore, the challenges in existing traction motors are justified at design stage and research contributions that this dissertation has made, in order to solve the challenges towards the advancement of the EV drivetrain system discussed in Sections 1.4 and 1.5.

1.2. Literature Reviews

The propulsion system is the heart of an EV, and the electric motor is the core of the system, which converts electrical energy from a battery into mechanical energy enabling a vehicle to move as it is presented in Figure 1.2. Along with advanced power electronics and control systems, different motor types emerged to satisfy the needs of the automotive sector [4]. Electric machine (EM) design is a challenging task that involves multi-domain physical phenomena, many design variables, objectives, and constraints. To design an EM with satisfactory output characteristics, electromagnetic, thermal and mechanical aspects of the design need to be managed carefully. For this purpose, understanding different EV topology and EM structure of existing traction motors, the basic characteristics of EM

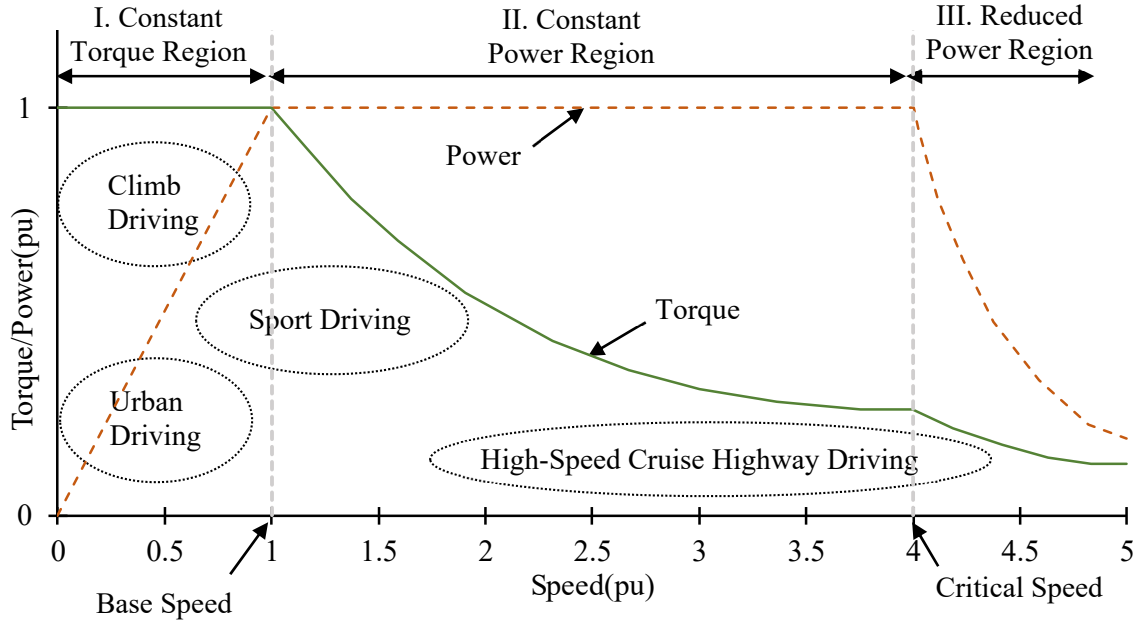


Figure. 1.2. Ideal torque-power/speed characteristics of traction motor [5].

which are required for traction applications are listed below [6]. The ideal torque-speed profile of a traction motor is shown in Figure 1.2.

- 1) High torque density and power density.
- 2) High torque at starting, low speeds, hill climbing, and high power at high speed.
- 3) Wide speed range, with a constant power operating a range of around 3–4 times the base speed is a good compromise between the peak torque requirement of the machine and the volt-ampere rating of the inverter.
- 4) High efficiency over a wide speed and torque ranges, including low torque operation.
- 5) High overload capability, typically twice the rated torque for short durations.
- 6) High reliability and robustness appropriate to the vehicle environment.
- 7) Low cost

Permanent magnet synchronous motors (PMSMs) with embedded rare-earth magnets are the most favorable EMs adopted in EVs. However, one significant exception is Tesla that employs a copper rotor induction motor (IM) instead of PMSM [7]. Figure 1.3 represents the EV propulsion system of an available vehicle in the market [8]. IM is a strong replacement of PMSM because it is simple, robust with a mature manufacturing



Figure 1.3. Ford Focus EV propulsion system [8].

technology and control method. Absence of rare-earth magnets in the IM makes it cheaper than PMSM, which increases its popularity in the future market as consumer demand increases [9]. The breakdown cost of PMSM is presented in Figure 1.4 which shows the importance of eliminating permanent magnets in the rotor. However, because the magnetizing part of stator current establishes the magnetic field of IM, the power factor is not as high as PM, leading to lower power density. Further, the constant power region of IM is not as wide as PMSM [11-13]. The overall efficiency of IM is usually lower than PMSM, except in the high-speed region, because there is no need of large stator current to respond to the PM magnetic field [13-15].

1.2.1. Electric Vehicle Outlook in Market

The idea of electrifying vehicles has existed for decades, and EM designs have changed based on the availability of technologies and design tools to make EVs popular in the market as a replacement to the existing ICE vehicles. But up to now, there is no EV achieving all the characteristics mentioned above in terms of the overall manufacturing and operating cost and driving range. Table 1.1 presents details on the cost, mileage, and driving range of the commercially available EVs. The global EV market is dominated by major players such as Tesla (US), Nissan Motor Corporation (Japan), BYD (China), BMW (Germany), and Volkswagen (Germany) [16]. A missing option is the reduction of the overall cost of the EV through technical improvements of EMs through an accurate

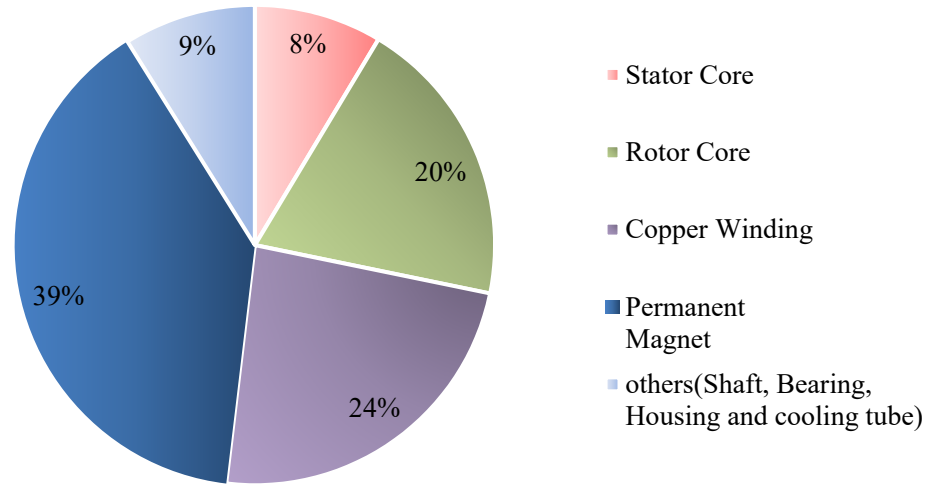


Figure. 1.4. The break down cost of a prototyped IPMSM in CHARGE Labs.

analytical tool at the design stage. Cost reduction is expected to continue because of advancements in computer-aided design tools to develop compact and optimal EMs in terms of overall performance characteristics in a component and system level. The major limitations of the design tools are the accuracy of the field calculations to simulate the performance characteristics of the developed designs over the wide speed range at the design stage.

PMSM and IM are two strong candidates used widely in EV propulsion systems. PMSM is an appropriate candidate due to its high torque, power density and high efficiency because of the usage of NdFeB permanent magnet (PM). Also, a wide constant power region can be reached for PMSMs. However, the high price of NdFeB PM in recent years, which peaked in 2011, strongly influences the popularity of PMSMs [17]. The breakdown cost of PMSM presented in Figure 1.4 illustrates the cost savings of using magnet free EMs in EV powertrain. Since the future market targets a cheaper EV, developing a new low-cost and highly efficient motor designs, alternative magnetic materials with reduced rare earth content, and improved motor manufacturing methods are essential. Long-term emphasis on non-rare earth motor architectures will reduce motor costs and mitigate rare earth market uncertainties. Hence, both industry and research have a interest in improving IM performance as it emerges to be a strong and reliable candidate.

TABLE 1. 1.
PRICE, ACCELERATION, DRIVING RANGE, POWER RATING AND ELECTRIC MOTOR
CONFIGURATION OF COMMERCIALY AVAILABLE ELECTRIFIED VEHICLES [18]-[19]

| Car Model | Price (CAD) | Range (km) | 0-60 mph | Motor Type | Power (kW) | Torque (Nm) |
|---------------------------|------------------------|-----------------------|---------------------|-----------------------|-----------------------|------------------------|
| Ford Focus Electric | \$31,498 | 185 | 10.1 | PMSM | 107 | 249 |
| Kia Soul Electric | \$35,395 | 150 | 11.8 | PMSM | 81 | 157 |
| Hyundai IONIQ Electric | \$35,649 | 177 | 8.1 | PMSM | 88 | 295 |
| Nissan Leaf | \$35,998 | 172 | 10.2 | PMSM | 80 | 157 |
| Volkswagen e-Golf | \$36,355 | 134 | 10.4 | PMSM | 100 | 290 |
| Tesla Model 3 (Base) | \$40,000 | 350 | 4.6 | PMSM | 228 | 563 |
| Chevrolet Bolt | \$42,895 | 383 | 6.5 | PMSM | 150 | 160 |
| BMW i3 | \$48,750 | 183 | 7.1 | PMSM | 127 | 249 |
| Tesla Model S (75D) | \$95,350 | 210 | 2.5 | IM | 193 | 249 |
| Tesla Model X (75D) | \$108,100 | 381 | 2.9 | IM | 193 | 249 |
| Tesla Model S (P100D) | \$174,700 | 507 | 2.28 | Dual IM | 193+375 | 249+649 |
| Tesla Model X (P100D) | \$188,300 | 465 | 2.4 | Dual IM | 193+376 | 249+650 |
| Fiat 500e | \$41,345 | 135 | 8.7 | PMSM | 83 | 200 |
| Mercedes B250e | \$51,876 | 140 | 7.9 | PMSM | 87 | 187 |

1.2.2. Comparison of Various Electric Machine Topologies Towards EV Development

Since IM and PMSM are the most favored EMs to satisfy EV requirements and emerges into the automotive industry, a comparative analysis of the performance characteristics of both gives a better idea of what needs to be done for further improvement. Table 1.2 is the summary of the advantages and disadvantages of both machines from marketing and output characteristic aspects [20-26]. Figure 1.5 demonstrates the typical IM and PMSM configurations. Based on the existence of PM in the rotor of PMSM and available field excitation in the rotor, reluctance torque is as an additional torque component and enhances the capability of PMSM. The torque-speed characteristic of an IM is mainly characterized by starting torque, pull-out torque, rated speed, and maximum speed. The dynamic performance enhancement of IM can be achieved either by the implementation of vector control (VC) or direct torque control (DTC) techniques [27-29]. High speed operation with an extended constant power range of up to 4–5 times of the base speed can be reached by flux weakening which is one of the desirable requirements for EV operation [30-32]. Although the maximum torque capability of IM limits the high speed operation and constant power range, the extended speed ranges up to 3–4 times the base speed, as well as higher efficiency of PM motors, can be achieved by applying suitable control algorithms of power converters above the base speed [33]. Important design considerations for PM motors associated with fixed excitation for electric propulsion system includes torque

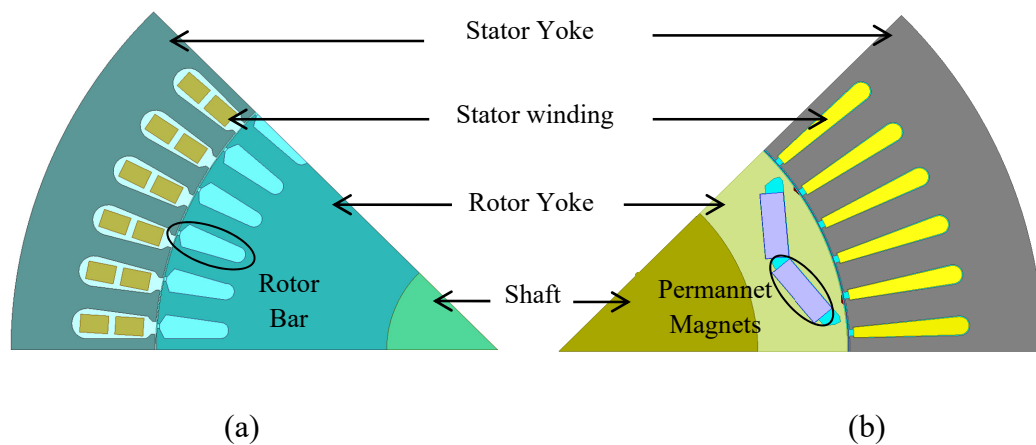
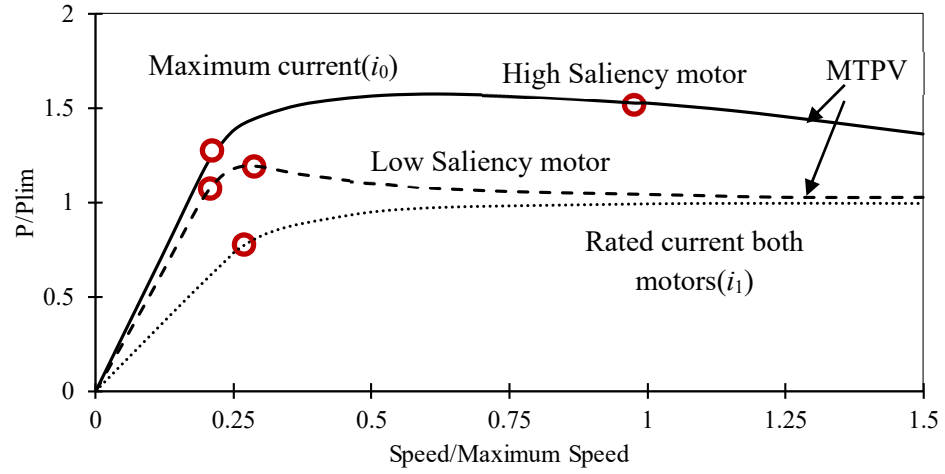


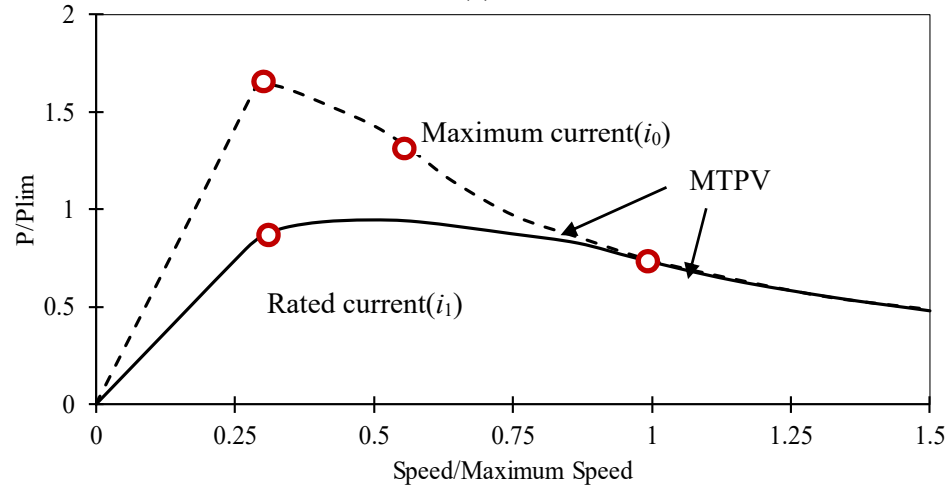
Figure. 1.5. 2-D cross section of mainly used electric machines in current commercial EVs. (a) squirrel cage IM. (b) interior PMSM.

TABLE 1. 2.
PMSM AND IM COMPARISON FROM MARKETING AND PERFORMANCE CHARACTERISTIC
ASPECTS [34]

| | | |
|--------------|------|--|
| Advantage | PMSM | <ol style="list-style-type: none"> 1) High torque and power densities hence compact volume 2) High efficiency 3) High power factor 4) Good heat dissipation because of no rotor loss 5) Various configurations and adjustable performance 6) Quick acceleration due to a lower electromechanical time constant of the rotor |
| | IM | <ol style="list-style-type: none"> 1) Robust structure 2) Relatively low cost 3) Well established manufacturing techniques 4) Reliable 5) Comparatively good efficiency at high speed 6) Good overload or peak torque capability 7) Good dynamic performance using VC and DTC control |
| Disadvantage | PMSM | <ol style="list-style-type: none"> 1) High cost and uncertainty due to rare earth PM 2) Relatively difficult on flux weakening especially when the electric loading is limited 3) Relatively lower efficiency at high speed due to additional current component required for flux weakening 4) The risk of irreversible demagnetization of PM due to high temperature, high demagnetizing armature field or vibration 5) High back EMF at high speed under in case of fault |
| | IM | <ol style="list-style-type: none"> 1) Design of IM is more complicated to satisfy the HEV/EV demand due to poor field weakening in high speed 2) Lower efficiency than a PM machine due to the inherent rotor loss. 3) Size of an induction machine is generally bigger than a PM machine with the same power and speed rating although it depends on the requirement of peak torque. 4) Low power factor and low inverter-usage factor. 5) The heat on the rotor is more difficult to be dissipated. 6) The control schemes are a little difficult due to the variable equivalent parameters. |



(a)



(b)

Figure. 1.6. Comparison of power-speed characteristics. (a) IPM power versus speed curves (limited voltage), for rated and overload current amplitudes. Effect of rotor saliency on the power overload curve. (b) IM power versus speed curves, for rated and overload current amplitudes and limited voltage [34].

density, flux weakening capability, overload capability, stator iron losses, rotor eddy current losses, and demagnetization withstanding capability. In conventional PMSMs, a compromise has to be made between low-speed torque capability and high-speed power capability. Comparison of power-speed characteristics of both machines in Figure 1.6 gives a better understanding of why IM performance needs to be enhanced to achieve the required output characteristics for future EV development for a minimal cost EV.

1.3. Desired Design Targets for a High Speed Traction Motor

Adoption of EM targets requires R&D advancement in several areas including powertrain components such as permanent magnet materials, non-rare earth magnets, conductors, laminations, and power electronics such as advanced capacitors, thermal and electrical packaging and wide bandgap semiconductors. R&D aims to achieve cost and performance targets in the above technology areas and presented in table 1.3 [35]. Improving EM performance characteristics within an appointed target is compulsory in order to adopt EV in the world market. The EM design breaks down into electromagnetic, thermal, and mechanical aspects assisting in determining and accelerating future technology advancement. Since the aforementioned design tools are strongly coupled and should follow an acceptable operating profile, EM designs attempt to: satisfy a certain duty cycle and torque-speed profile, thermal requirements, efficiency, and some constraints such as cost, weight, and volume. Each analysis to analyze the corresponding specification and aspects of EM to meet the overall output characteristics of EV.

Since developing the EM is a multidisciplinary task, summarizing each methodology towards optimal EM development helps to improve the required analysis tools: 1) Electrical analysis typically specifies the supply voltage, frequency, and the number of phases, and even the phase connection and number of poles. Also, the slot numbers, winding layouts, turns per phase, and wire sizes are determined by the designer in this step. 2) Magnetic design calculates the air gap diameter and machine stack length, or active length, based on output power, speed, pole number, and cooling type. The slot sizing, core height, and external stator diameter are also determined depending on various criteria. 3) Insulation design, which specifies the material choice of the insulation and its thickness in various parts of the machine are designed based on supply voltage, thermal management, and the environment in which the machine operates. 4) Thermal design defines the heat

TABLE 1. 3.
SATISFACTORY POWERTRAIN TARGETS IN 2022.

| 2022 Electric Drive system Targets | |
|------------------------------------|------------------------|
| \$8/kW | 4 times cost reduction |
| 1.4 kW/kg | 35% size reduction |
| 4.0 kW/L | 40% weight reduction |
| 94% system efficiency | 40% loss reduction |

extraction caused by losses from the machine which is imperative to keep the windings, core, and frame temperatures within safe limits. Depending on the application or power level, various types of cooling are used. Calculating the loss and temperature distribution in the cooling system represents the thermal design. 5) Mechanical design refers to critical rotating speed, noise, and vibration modes, mechanical stress in the shaft and frame, and its deformation displacement, bearing design, inertia calculation, and forces on the winding end coils during the most severe current transients. In the machine design problem, all the above design features are strongly coupled. As an example, the allowable operating envelope for electrical machines depends largely on the ability of the machine to reject heat generated because of internal loss. The internally generated heat limits the maximum allowable current and flux density, which has a significant impact on the electric and magnetic designs of the machine. The electric and magnetic design determines the amount of copper loss and core loss, which both are a major source of heat. However, the thermal considerations and mechanical considerations are often dealt with separately in present practice, despite the strong design relationship.

1.4. Review of Existing Computer Aided Design Tools for Magnetic Field Analysis

Modeling is one of the most important aspects of electrical machine design. Without an accurate model, it is impossible to predict performance. There are different tools and methodologies to design EMs. However, accuracy and optimization of the EMs require special attention. Since the design is a multi-domain physical phenomenon with a large number of design variables, establishing the most practical analysis tool is crucial for the design and optimization of IM under various criteria. Several numerical and analytical methods have been employed to solve the magnetic field problem of different EM topologies. Finite element method (FEM) analysis, is approved to analyze the magnetic field distribution and calculate the related electromechanical parameters. This method is highly accurate and incorporates the influence of nonlinear factors. However, it remains relatively slow and time consuming in case of a multi-dimensional investigation. The accuracy of the magnetic equivalent circuit (MEC) based analysis is generally better than analytical models, but its computational liability is lower than FEM because the number of

unknowns in a MEC model is an order of magnitude lower than the one in a FEM model. The magnetic equivalent circuit (MEC) is used to analyze the electromagnetic field inside the motor because the MEC can account for the nonlinearity, armature reaction, and end effect, among other parameters. Nevertheless, this method calculates the magnetic field only at several discrete points of the structure, and it lacks adequate precision. The usage of the analytical and semi-analytical model based on the subdomain method is gradually increasing in the design of various EMs because this method can provide more accurate predictions of the magnetic field distribution to predict the exact performance of EM within a lower computational time.

A comprehensive list of computer-aided design tools and the corresponding qualitative ratings of them are presented in Table 1.4 ('+' represents an advantage, and '-' for a disadvantage). The most important criteria of an analysis tool are mathematical model accuracy and computational effort, which generally oppose each other. Higher accuracy usually involves a heavier and time-consuming computational effort. Analytical design models are fast during simulation, but if the machine parameters are outside the considered modeling region, the results can be inaccurate. FEA can achieve accurate field solutions but is computationally expensive, especially if a 3-D analysis is needed.

TABLE 1. 4.
COMPARISON OF COMPUTATIONAL PERFORMANCE OF ELECTROMAGNETIC FIELD
SOLUTIONS [36-41].

| | MCM | 3-D FEA-EC | WF | SD |
|-----------------------------|---------|------------|---------|---------|
| Calculation time | + | --- | + | ++ |
| Overall accuracy | - | + | - | + |
| Field component calculation | No | Yes | No | Yes |
| Robustness to geometry | + | ++ | - | + |
| Skewing | No | Yes | No | Yes |
| Saturation | - | + | - | + |
| Faults | No | Yes | No | Yes |
| Topologies | PMSM-IM | PMSM-IM | PMSM-IM | PMSM-IM |

Numerical methods, such as FEA, are an efficient option in machine design field due to its accuracy. However, 3-D FEA analysis is a time- consuming and inefficient approach in the design optimization process [41] and [42] especially if detailed output characteristics need to be investigated at the end-windings and along the axial length of the EM in case of skewing effect. Hence, the need for an exact 3-D analytical solution is crucial to reduce research, time, and cost to obtain an optimal solution of the design for any industrial application. The most favorite methods by designers are the determination of Maxwell's equations using the analytical technique and winding function method (WFM) to calculate inductances. They are fast and precise and can be considered in optimization [43], [44]. However, in WFM, the determination of instantaneous rotor-position-dependent inductances is challenging [45]. In [46], 2-D analytical solutions were derived and proposed for non-skewed simple structures, solid and slotted rotor, which mostly deals with eddy current calculation for rotor bars solving Maxwell's equations. The shortcoming is in the accuracy of electromagnetic performance analysis is compromised over the simplicity of developed differential equations, and axial asymmetrical effects are neglected. Therefore, proposing novel analytical methods such as subdomain (SD) method is critical in finding a 3-D general solution for magnetic flux density distribution considering the axial variation of the magnetic field, unlike previous methods. Calculating magnetic field behavior is required in different domains such as stator, and rotor slots, which are the most dominant places of loss and saturation level to help designers to optimize the EM structure.

1.5. Research Objectives

Optimal design of the induction machine is an important and crucial task for traction application, which requires a multi-disciplinary investigation for satisfactory continuous and peak output characteristics. Thus, the objective of the dissertation is to optimize the IM design by reducing spatial harmonic and maximizing the peak performance characteristics of the motor in an effort to reduce the overall cost, weight and extend the range of the EM. The objective was divided into the following sub-objectives.

1) Understanding the principle of designing a high-speed IM for EV application considering higher frequency effects on the maximum torque and special harmonic components.

2) Investigating of the 2D and 3D finite element analyses and their discrepancies in the determination of the IM parameters and performance characterization.

3) Proposing a semi-analytical approach to design and develop a high-speed IM considering higher order of harmonics.

4) Validating the proposed semi-analytical model with the FEA as an exemplary IM to investigate the magnetic field distribution in different geometrical domains.

5) Proposing a novel design approach to reduce the number of structural variables to optimize maximum performance characteristics of IM within a limited volume through the proposed semi-analytical model.

6) Analyzing the developed high-speed IM through experimental investigation to study the electrical circuit parameters from low to high speeds.

1.6. Research Contribution And Dissertation Layout

This dissertation proposes a novel and advanced field analysis and design approach to maximize the peak characteristics of IM. The major sections are:

1) A closed-loop structural design algorithm is developed in Chapter 2 to design the high-speed IM for traction application based on equivalent circuit parameter determination, including low and high harmonic components. Also, the detailed effect of structural variation on the inverter fed IM behavior is investigated.

2) In Chapter 3, a modified equivalent circuit is proposed considering higher order of special harmonic due to slotting effect and the rotor bar geometry is optimized to achieve the lower special harmonics within a constant volume keeping the continuous average torque constant.

3) The coupled analytical and FEA design algorithm is proposed in conjunction with improved particle swarm optimization (IPSO) in Chapter 3 considering the axial magnetic flux density variation because of skewing effect and therefore inducing spatial harmonics

in the air-gap flux distribution which causes the output torque oscillation and reduces average torque production.

4) The novel mathematical solution is proposed through an exact solution of Maxwell's equations divided to a) Poisson, b) Laplace and Helmholtz equations calculating the magnetic flux distribution in stator slots, rotor bars and air-gap of a typical IM considering axial flux variation due to skewing rotor bars. A detailed mathematical derivation is described in Chapter 4, and it has been validated using 3D-FEA.

5) The impact of stator-rotor slots and pole combinations is investigated in Chapter 5 through a proposed parametric based optimization process to discover the optimal combination with minimal torque ripple, higher pull-out torque and constant efficiency to meet the specified targets for the traction application. In addition, a sensitivity-based optimization proposed to reduce the stator slot and rotor bar geometrical variables for further enhancement of overload capability of the high-speed IM is one a drawback of IM.

6) A genetic algorithm based rotor bar geometry optimization is implemented through proposed two objective functions and presented in Chapter 5 maximizing the peak capability of the developed baseline IM. It was validated through performance and parameter characterization over the entire speed range.

7) In Chapter 6, the proposed optimal design of IM is prototyped and validated for various operating condition and different speeds with the one developed in FEA. Also, the thermal distribution of prototyped high-speed IM is investigated with and without cooling.

8) A summary of the dissertation is provided in Chapter 7F. The limitations of the proposed methods are also discussed, and possible solutions are outlined for further IM optimization.

1.7. References

- [1] Electric vehicles sales update Q3 2018, Canada. Available online at: <https://www.fleetcarma.com/electric-vehicles-sales-update-q3-2018-canada>.
- [2] Electric vehicle outlook of 2018. Available online at: <https://about.bnef.com/electric-vehicle-outlook/#toc-download>.
- [3] Battery electric vehicles vs. internal combustion engine vehicles. Available online at: http://www.adlittle.de/sites/default/files/viewpoints/ADL_BEVs_vs_ICEVs_FINAL_November_292016.pdf.
- [4] Z. Q. Zhu and D. Howe, "Electrical Machines and Drives for Electric, Hybrid, and Fuel Cell Vehicles," in *Proceedings of the IEEE*, vol. 95, no. 4, pp. 746-765, April 2007.
- [5] M. Yilmaz, "Limitations/capabilities of electric machine technologies and modeling approaches for electric motor design and analysis in plug-in electric vehicle applications," *Renewable and Sustainable Energy Reviews*, vol. 52, PP 80-99.
- [6] B. Bilgin and A. Emadi, "Electric Motors in Electrified Transportation: A step toward achieving a sustainable and highly efficient transportation system," in *IEEE Power Electronics Magazine*, vol. 1, no. 2, pp. 10-17, 2014.
- [7] Y. Guan, Z. Q. Zhu, I. A. A. Afinowi, J. C. Mipo, and P. Farah, "Comparison between induction machine and interior permanent magnet machine for electric vehicle application," 2014 17th International Conference on Electrical Machines and Systems (ICEMS), Hangzhou, 2014.
- [8] Ford Launching Focus EV Amid Volt Controversy. Available online at: <https://www.wardsauto.com/technology/ford-launching-focus-ev-amid-volt-controversy>
- [9] T. Jahns, "Getting Rare-Earth Magnets Out of EV Traction Machines: A review of the many approaches being pursued to minimize or eliminate rare-earth magnets from future EV drivetrains," in *IEEE Electrification Magazine*, vol. 5, no. 1, pp. 6-18, 2017.
- [10] The break down cost of PMSM. Available online at: https://www.energy.gov/sites/prod/files/2014/03/f13/ape051_miller_2013_o.pdf.
- [11] Z. Yang, F. Shang, I. P. Brown and M. Krishnamurthy, "Comparative Study of Interior Permanent Magnet, Induction, and Switched Reluctance Motor Drives for EV and HEV Applications," in *IEEE Transactions on Transportation Electrification*, vol. 1, no. 3, pp. 245-254. 2015.
- [12] I. Boldea, L. N. Tutelea, L. Parsa and D. Dorrell, "Automotive Electric Propulsion Systems with Reduced or No Permanent Magnets: An Overview," in *IEEE Transactions on Industrial Electronics*, vol. 61, no. 10, pp. 5696-5711, 2014.
- [13] A. J. Humphrey, "Constant horsepower operation of induction motors," *IEEE Trans. Ind. and General Application*, pp. 552-557, 1969.
- [14] N. Uzhegov, J. Barta, J. Kurfürst, C. Ondrusek and J. Pyrhönen, "Comparison of High-Speed Electrical Motors for a Turbo Circulator Application," in *IEEE Transactions on Industry Applications*, vol. 53, no. 5, pp. 4308-4317, 2017.
- [15] M. Zeraoulia, M. E. H. Benbouzid, and D. Diallo, "Electric Motor Drive Selection Issues for HEV Propulsion Systems: A Comparative Study," in *IEEE Transactions on Vehicular Technology*, vol. 55, no. 6, pp. 1756-1764, 2006.

- [16] Electric Vehicle Market - Global Forecast to 2025: Market is Dominated by Tesla, Nissan, BYD, BMW, and Volkswagen. Available online at: <https://www.prnewswire.com/news-releases/electric-vehicle-market---global-forecast-to-2025-market-is-dominated-by-tesla-nissan-byd-bmw-and-volkswagen-300671659.html>.
- [17] Roskill: Neodymium Prices Surge as Permanent Magnet Demand Looks set to Take off. Available online at: <https://www.prnewswire.com/news-releases/roskill-neodymium-prices-surge-as-permanent-magnet-demand-looks-set-to-take-off-669905463.html>.
- [18] Electric Car Price Guide, Available online at: <http://www.greencarreports.com/news/1080871-electric-car-price-guide-every-2015-2016-plug-in-car-with-specs-updated/page-1>. Accessed on March 26, 2016.
- [19] Compare EVs Available online at: <https://insideevs.com/compare-plug-ins/>
- [20] J. Goss, M. Popescu, and D. Staton, "A comparison of an interior permanent magnet and copper rotor induction motor in a hybrid electric vehicle application," 2013 *International Electric Machines & Drives Conference*, Chicago, IL, 2013.
- [21] Y. Cheng R. Trigui C. Espanet A. Bouscayrol and S. Cui "Specifications and Design of a PM Electric Variable Transmission for Toyota Prius II " *IEEE Transactions on Vehicular Technology*, vol. 60 no. 9 pp. 4106-4114 Nov. 2011.
- [22] A. Boglietti et al., "Electrical Machine Topologies: Hottest Topics in the Electrical Machine Research Community," in *IEEE Industrial Electronics Magazine*, vol. 8, no. 2, pp. 18-30, 2014.
- [23] D. Gerada, D. Borg-Bartolo, A. Mebarki, C. Micallef, N. L. Brown and C. Gerada, "Electrical machines for high speed applications with a wide constant-power region requirement," 2011 *International Conference on Electrical Machines and Systems*, pp. 1-6, Beijing, 2011.
- [24] A. Walker, M. Galea, C. Gerada, A. Mebarki, and D. Gerada, "A topology selection consideration of electrical machines for traction applications: towards the FreedomCar 2020 targets," 2015 *Tenth International Conference on Ecological Vehicles and Renewable Energies (EVER)*, pp. 1-10, Monte Carlo, 2015.
- [25] D. Gerada, H. Zhang, Z. Xu, G. L. Calzo and C. Gerada, "Electrical machine type selection for high speed supercharger automotive applications," 2016 *19th International Conference on Electrical Machines and Systems (ICEMS)*, pp. 1-6, Chiba, 2016.
- [26] D. Gerada, A. Mebarki, N. L. Brown, C. Gerada, A. Cavagnino, and A. Boglietti, "High-Speed Electrical Machines: Technologies, Trends, and Developments," in *IEEE Transactions on Industrial Electronics*, vol. 61, no. 6, pp. 2946-2959, June 2014.
- [27] M. S. Huang and C. M. Liaw, "Improved field-weakening control for IFO induction motor," in *IEEE Transactions on Aerospace and Electronic Systems*, vol. 39, no. 2, pp. 647-659, April 2003.
- [28] F. Briz, A. Diez, M. W. Degner, and R. D. Lorenz, "Current and flux regulation in field-weakening operation [of induction motors]," in *IEEE Transactions on Industry Applications*, vol. 37, no. 1, pp. 42-50, Jan.-Feb. 2001.
- [29] H. Ge, Y. Miao, B. Bilgin, B. Nahid-Mobarakeh, and A. Emadi, "Speed Range Extended Maximum Torque Per Ampere Control for PM Drives Considering Inverter and Motor Nonlinearities," in *IEEE Transactions on Power Electronics*, vol. 32, no. 9, pp. 7151-7159, Sept. 2017.

- [30] Z. Mynar, L. Vesely and P. Vaclavek, "PMSM Model Predictive Control with Field-Weakening Implementation," in *IEEE Transactions on Industrial Electronics*, vol. 63, no. 8, pp. 5156-5166, Aug. 2016
- [31] R. Nalepa and T. Orłowska-Kowalska, "Optimum Trajectory Control of the Current Vector of a Nonsalient-Pole PMSM in the Field-Weakening Region," in *IEEE Transactions on Industrial Electronics*, vol. 59, no. 7, pp. 2867-2876, July 2012.
- [32] P. Lin and Y. Lai, "Novel Voltage Trajectory Control for Field-Weakening Operation of Induction Motor Drives," in *IEEE Transactions on Industry Applications*, vol. 47, no. 1, pp. 122-127, Jan.-Feb. 2011.
- [33] S. Chaithongsuk, B. Nahid-Mobarakeh, J. Caron, N. Takorabet and F. Meibody-Tabar, "Optimal Design of Permanent Magnet Motors to Improve Field-Weakening Performances in Variable Speed Drives," in *IEEE Transactions on Industrial Electronics*, vol. 59, no. 6, pp. 2484-2494, June 2012.
- [34] G. Pellegrino A. Vagati B. Boazzo P. Guglielmi "Comparison of induction and PM synchronous motor drives for EV application including design examples" *IEEE Trans. Ind. Appl.* vol. 48 no. 6 pp. 2322-2332. 2012.
- [35] EV Everywhere Grand Challenge Blueprint. Available online at: <https://www.mdpi.com/2032-6653/6/4/1008>.
- [36] M. Amrhein and P. T. Krein, "Induction Machine Modeling Approach Based on 3-D Magnetic Equivalent Circuit Framework," in *IEEE Transactions on Energy Conversion*, vol. 25, no. 2, pp. 339-347, June 2010.
- [37] M. Hsieh, I. Lin, and D. Dorrell, "Magnetic Circuit Modeling of Brushless Doubly-Fed Machines With Induction and Reluctance Rotors," in *IEEE Transactions on Magnetics*, vol. 49, no. 5, pp. 2359-2362, May 2013.
- [38] D. Wang, X. Wu, J. Chen, Y. Guo and S. Cheng, "A Distributed Magnetic Circuit Approach to Analysis of Multiphase Induction Machines with Nonsinusoidal Supply," in *IEEE Transactions on Energy Conversion*, vol. 30, no. 2, pp. 522-532, June 2015.
- [39] T. Lubin, S. Mezani and A. Rezzoug, "Analytic Calculation of Eddy Currents in the Slots of Electrical Machines: Application to Cage Rotor Induction Motors," in *IEEE Transactions on Magnetics*, vol. 47, no. 11, pp. 4650-4659, Nov. 2011.
- [40] K. Yamazaki, "Induction motor analysis considering both harmonics and end effects using combination of 2D and 3D finite element method," in *IEEE Transactions on Energy Conversion*, vol. 14, no. 3, pp. 698-703, 1999.
- [41] J. Yun and S. B. Lee, "Simplified Approach for Predicting the Starting Performance of Induction Machines Based on Rotor Design Modification," in *IEEE Transactions on Magnetics*, vol. 53, no. 6, pp. 1-4, 2017.
- [42] K. N. Gyftakis and J. C. Kappatou, "A new technique for the skewing consideration in the 2-D FEM un-skewed induction motor time-dependant electromagnetic characteristics," 2016 19th *International Conference on Electrical Machines and Systems (ICEMS)*, pp. 1-6, 2016.
- [43] J. Faiz and M. Ojaghi, "Unified winding function approach for dynamic simulation of different kinds of eccentricity faults in cage induction machines," in *IET Electric Power Applications*, vol. 3, no. 5, pp. 461-470, 2009.

- [44] P. Naderi and A. Shiri, "Rotor/Stator Inter-Turn Short Circuit Fault Detection for Saturable Wound-Rotor Induction Machine by Modified Magnetic Equivalent Circuit Approach," in *IEEE Transactions on Magnetics*, vol. 53, no. 7, pp. 1-13, 2017.
- [45] W. Bischof, B. Chatterjee, M. Boesing, M. Hennen and R. Kennel, "Modeling inverter-fed three-phase squirrel-cage induction machines including spatial and temporal harmonics," *2017 IEEE International Electric Machines and Drives Conference (IEMDC)*, pp. 1-8, 2017.
- [46] E. Devillers, J. Le Besnerais, T. Lubin, M. Hecquet and J. Lecointe, "An Improved 2-D Subdomain Model of Squirrel-Cage Induction Machine Including Winding and Slotting Harmonics at Steady State," in *IEEE Transactions on Magnetics*, vol. 54, no. 2, pp. 1-12, Art no. 8100612 2018.

CHAPTER 2

DESIGN TARGETS AND TOPOLOGY SELECTION OF HIGH SPEED IM FOR ELECTRIC VEHICLE WITHIN A FIXED OUTER DIAMETER

2.1. Introduction

The advanced technology of power electronics has been made possible to achieve higher rotational speed in EMs by increasing the input frequency from 60 Hz up to 1000 Hz, which is a complementary element for traction application demanding high efficiency and power density within a wide speed range. The mechanical robustness and simple structure of IM make it the best candidate for high speed applications. In the design and analysis of high speed IMs, mechanical, thermal, and electromagnetic problems occur due to the high rotational velocities, which conflict each other when high performance machine is required. Therefore, there are so many design factors involved in the high speed IM development, which makes the design procedure complex if satisfactory of overall performance is needed for the application.

To some extent, the design must be a compromise between a large number of conflicting requirements which can be selected based on the importance of one parameter to another depending on the application requirement. Therefore, finding a unique solution for IM design is a difficult task even for the same application, and hence designs will vary because of the diverse preference and trade-offs chosen by different designers for the same application. To a great extent, the design is an iterative process in order to obtain the desired solution. Therefore, in this chapter, an automated design package for design and optimization is reviewed for variable sine-wave has driven high speed IM. This design package is developed as a common practice and as a starting point for improving the rated performance of the IM using analytical design equation for variable speed motor. The principle of this design approach includes two main segments, one for a common laboratory stator to limit the outer diameter of the motor, second for an existing inverter in the CHARGE Labs to keep the electrical input to the IM constant. Subsequently, an improved baseline traction motor by the well-established automated design is developed,

and the weakness of the common optimization techniques in overlooking the performance requirements throughout the entire range of operation are outlined.

2.2. Calculating Design Targets of the Scaled down High Speed IM for Electric Vehicle Application

As a primary objective towards developing a high speed IM for EVs, preliminary torque, speed, and structural constraints need to be well defined to initiate the design procedure for a typical electric vehicle. Consequently, the desired performance characteristics in quantitative terms through specific technical criteria can be achieved with fine tuning of the initial parameters using closed loop analytical design process. Therefore, target categories were specified, such as torque density, power density, volume, speed range, etc. In this section, numerical targets for the characteristics mentioned above are calculated using laboratory traction machine used in commercially available Ford focus 2014 in the market [1]. The selection of the target categories varies depending on placing emphasis on any design objective. In this study, obtaining a high torque, high efficiency, low harmonic losses within a compact volume (constant outer diameter and stack length) is the desired objective within an enhanced speed rang. The continuous and peak rating of Ford Focus 2014 is represented in Table 2.1 as the final target to begin the IM development. Since the tire size (R16) and the vehicle speed (120 mph) are kept similar to the Ford Focus 2014, the electrical ratings of the scaled-down prototype are estimated exactly based on the power ratings of Ford Focus motor presented in Table 2.1. For further verification of the required continuous and peak torque and rated speed of the scaled down motor, vehicle dynamic model is also elaborated to calculate the required parameters to set the scaled down design targets in Table 2.2 using (2.1)-(2.2) with tire size of 215/55R16 and engine power and torque for the similar size ICE vehicle [2] and [3].

$$T_w = \frac{i_x \cdot i_0 \cdot T_e}{2} \quad (2.1)$$

$$F_w = \frac{i_x \cdot i_0 \cdot T_e}{2 \cdot r_w} \quad (2.2)$$

where i_x , i_0 , T_w , T_e , F_w and r_w are the engaged drive ratio, final drive gear ratio, wheel torque, engine torque, wheel force, and wheel radius. Figure 2.1 is representing the schematic of the ICE vehicle power train [3]. Internal combustion engine (ICE) vehicle powertrain includes engine, clutch, vehicle gearbox, and differential gear box. In order to provide a reasonable high speed compared with the existing traction motor, the target ratings have been modified to 11 kW, 35 Nm, and 3,000 rpm.

TABLE 2. 1.
DETAILS OF LABORATORY ELECTRIC VEHICLE IPM MOTOR DRIVE AND TRANSMISSION

| | | |
|--------------------------------|---------------------|--------------|
| Traction Motor Specifications | Peak Power | 100 kW |
| | Peak Torque | 282 Nm |
| | Continuous Power | 45 kW |
| | Continuous Torque | 150 Nm |
| | Base Speed | 3,000 rpm |
| | Maximum Speed | 10,000 rpm |
| | Transmission Ratio | 7.8 |
| Integrated Inverter with Motor | Input voltage range | 260V to 400V |
| | Peak power | 120 kW |
| | Peak current | 400 Arms |

TABLE 2. 2.
DETAILS OF SCALED DOWN DESIGN TARGETS FOR HIGH SPEED INDUCTION MOTOR

| | |
|--------------------|-------------|
| Peak Power | >25 kW |
| Peak Torque | >70 Nm |
| Continuous Power | 11 kW |
| Continuous Torque | Up to 35 Nm |
| Base Speed | 3,000 rpm |
| Maximum Speed | 10,000 rpm |
| Transmission Ratio | 7.8 |

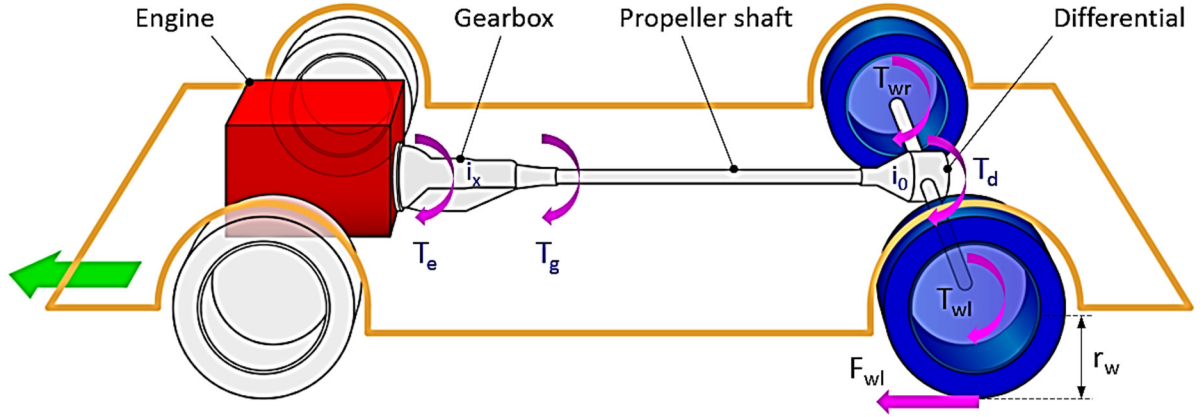


Figure. 2.1. Vehicle rear-wheel drive powertrain diagram.

2.3. Fixing Main Structural Sizing of Scaled Down High Speed Induction Motor for the Scaled down Design Targets

There are four main issues need to be addressed when designing a high-speed induction motor, if an overall good performance in the entire torque-speed envelope has to be obtained. First, the induced losses by high frequencies in the rotor and additionally stator must be limited to achieve high efficiency at different operating conditions. Second, the rotor must provide mechanically and dynamically stable behavior throughout a wide speed operation range, to allow safe operation of the motor over the entire driving range. Third, the motor must be efficiently cooled to achieve a high power density, which is much more challenging compared to the conventional IM design, as the volume needs to be constant and compact to reduce the active weight of propulsion system. Lastly, the rotor must withstand the high centrifugal forces corresponding to peripheral speed.

An available stator in CHARGE Labs facility is chosen, to initiate the high speed IM development which was previously used for general industrial application and presented in Figure 2.2a. In this manner, the volume of the motor kept as a constant value for precise investigation of the other design factors and their effect on the IM performance characteristics. The chosen outer diameter can handle the target output torque based on the D^2L rule where D is the outer diameter, and L is the effective length of the machine. Since the machine is adjusted in a defined volume, therefore the other geometrical parameters can be calculated using iterative closed-loop analytical procedure.

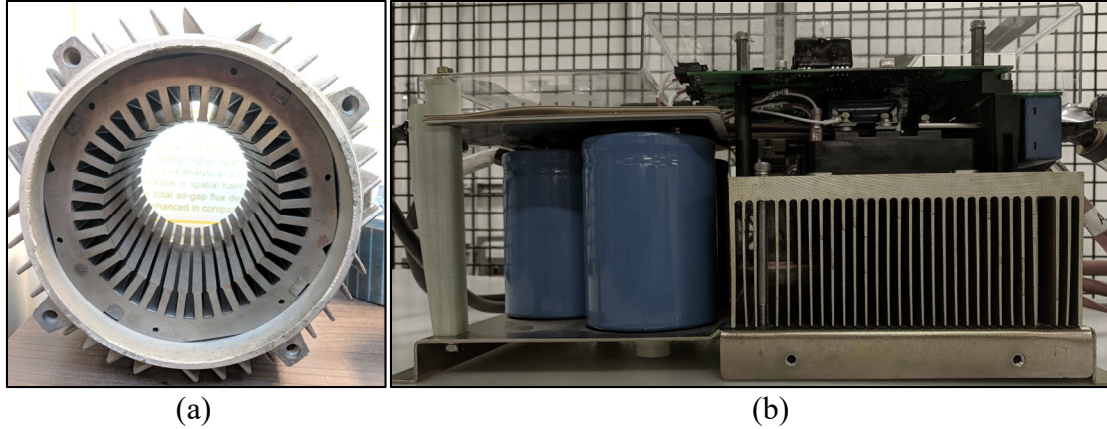


Figure. 2.2. Laboratory components for IM development: (a) The existing industrial stator in CHARGE Labs facility used for high speed IM development. (b) Fan-cooled inverter used for high speed IM drive.

After fixing torque and speed rating of IM mentioned in Table 2.1 as well as motor volume, other electrical and mechanical targets such as DC bus voltage, maximum allowable current, and torque ripple were fixed based on the existing drives and transmissions available in the CHARGE Labs. Figure 2.2b presents the existing inverter, and Table 2.3 shows its voltage and current limitation used for IM development. The summary of the automated design algorithm is presented in Figure 2.3. The outer diameter and the stack length of the existing stator are presented in the Figure. 2.2, the baseline IM geometrical dimensions are calculated employing analytical design expressions (2.3)-(2.8).

TABLE 2. 3.
INVERTER SPECIFICATION USED FOR IM DEVELOPMENT.

| Characteristics | Powerex PP200T120-ND | Characteristics | Powerex PP200T120-ND |
|---------------------------|-------------------------|---|-------------------------|
| Continuous Output Current | 200 A | Operating Temperature | -20 to 60°C |
| Peak Output Current | 400 A | Input DC Voltage | 900 V _{DC} |
| Continuous Output Voltage | 600 V | Capacitance | 2300 μ F |
| Peak Output Voltage | 1200 V | Nominal Ripple Current Rating per Capacitor | 11.6 A _{rms} |

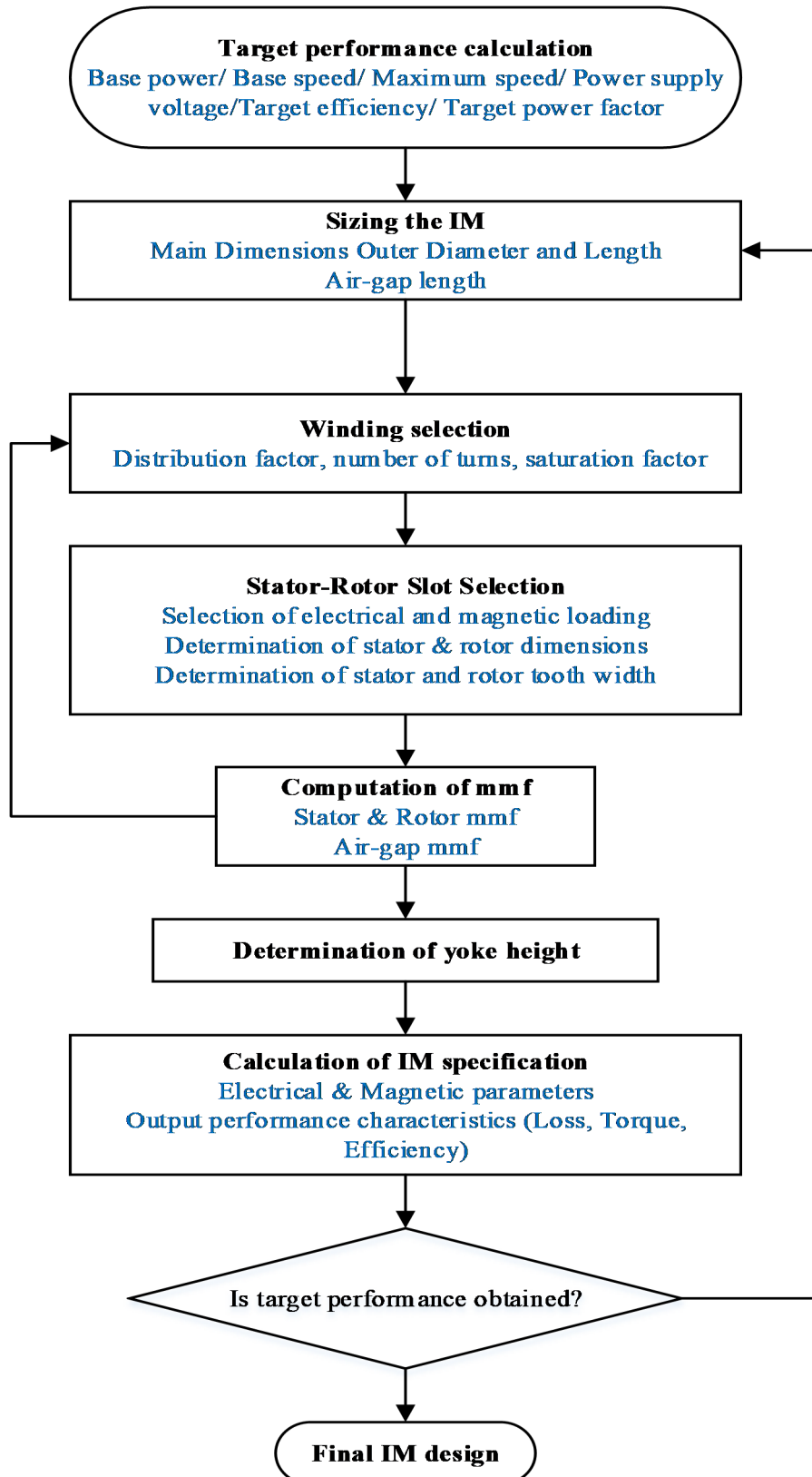


Figure. 2.3. The design algorithm of variable frequency IM employing Analytical Closed Form Equations.

The rotor volume is calculated with the suitable tangential stress (σ_{Ftan}) in the air-gap to produce the desired torque (T) [4].

$$\text{For totally enclosed IM: } \begin{cases} V_r = \frac{T}{2\sigma_{Ftan}} & 12,000Pa < \sigma_{Ftan} < 33,000Pa \\ \sigma_{Ftan} = \frac{A\hat{B}_\delta \cos \zeta}{\sqrt{2}} & \cos \zeta = 0.8 \end{cases} \quad (2.3)$$

where the V_r is the rotor volume. However, for a direct liquid cooled IM tangential stress boundaries is much higher. The derived local current and flux density for the specified rotor volume is used to calculate the machine constant using (2.4) and consequently the output power rating with (2.5) for the constrained volume.

$$C_{mec} = \frac{\pi^2}{2} K_{ws} \hat{A} \hat{B}_\delta \quad (2.4)$$

$$P_{mec} = C_{mec} D^2 L n_{syn} \quad (2.5)$$

where K_w , A , and B_δ are the winding distribution factor, local current, and flux densities. Since base speed is chosen as 3,000 rpm, special attention is required while calculating the air-gap length to eliminate non-uniform magnetic pull [4]-[6].

$$L_{ag} = 0.001 + D_{or} / 0.07 + v / 400 \quad (2.6)$$

where L_{ag} is the air-gap length, D_{or} is outer rotor diameter, and v is the peripheral speed of the rotor. Winding distribution factor is calculated for an integral winding. The number of turns per-phase is obtained with (2.7) using optimal phase voltage. The slot fill factor is limited to 70% to calculate the number of conductors per slot and achieve higher power density [4]-[6].

$$Z_s = V_{ph} / \omega k_w l \tau_p \alpha_i B_{ag} \quad (2.7)$$

where ω , k_w , τ_p , α_i and B_{ag} are rated frequency, winding factor, pole pitch, saturation factor, and air-gap flux density.

2.3.1. Winding Selection

The previously number of turns is used to calculate the suitable integer number conductors per slot. The number of conductors is calculated with (2.8)

$$Z_{Q_s} = \frac{2am}{Q_s} Z_s \quad (2.8)$$

where m is the number of phases, and a is the number of parallel paths, and Q_s is the number of stator slots.

2.3.2. Selection of Stator-Rotor Slot Combination and Rotor Bar Dimensioning

Selection of the optimal number of the stator and rotor slot combination is a crucial requirement to reduce parasitic torque, excessive losses, and radial electromagnetic forces. For this purpose, first, the acceptable slot combinations are determined from the literature review and second a parametric based optimization approach is followed combined with FEA to search the optimal number of poles and stator-rotor slot combinations within the constant volume. To find out the adequate combination (2.9) is used [7] and [8].

$$Q_s - Q_r \neq 0, \pm p, \pm 2p, \pm 3p, \pm 5p, \pm 1, \pm 2, \pm (p \pm 1), \pm (p \pm 2) \quad (2.9)$$

A comprehensive parametric analysis based optimization procedure is implemented in conjunction with FEA to find the optimal number of stator-rotor slot combination within acceptable magnetic flux density to obtain overall high peak torque, power, and efficiency with minimal torque ripple. The comparative analysis is provided for sample five different case study in Figures 2.4 and 2.5. For each individual design, the automated design package is used to calculate the rotor bar dimension and shaft correspondingly using (2.10)- (2.12). The dimension of the rotor bar is calculated for various slot type using a system of linear and non-linear equations.

$$I_s = \frac{P}{m\eta V_{ph} \cos \theta} \quad (2.10)$$

$$I_r = \frac{Z_{Q_s} Q_s}{a Q_r} I_s \cos \theta \quad (2.11)$$

$$I_{ring} = \frac{I_r}{2 \sin(\pi p / Q_r)} \quad (2.12)$$

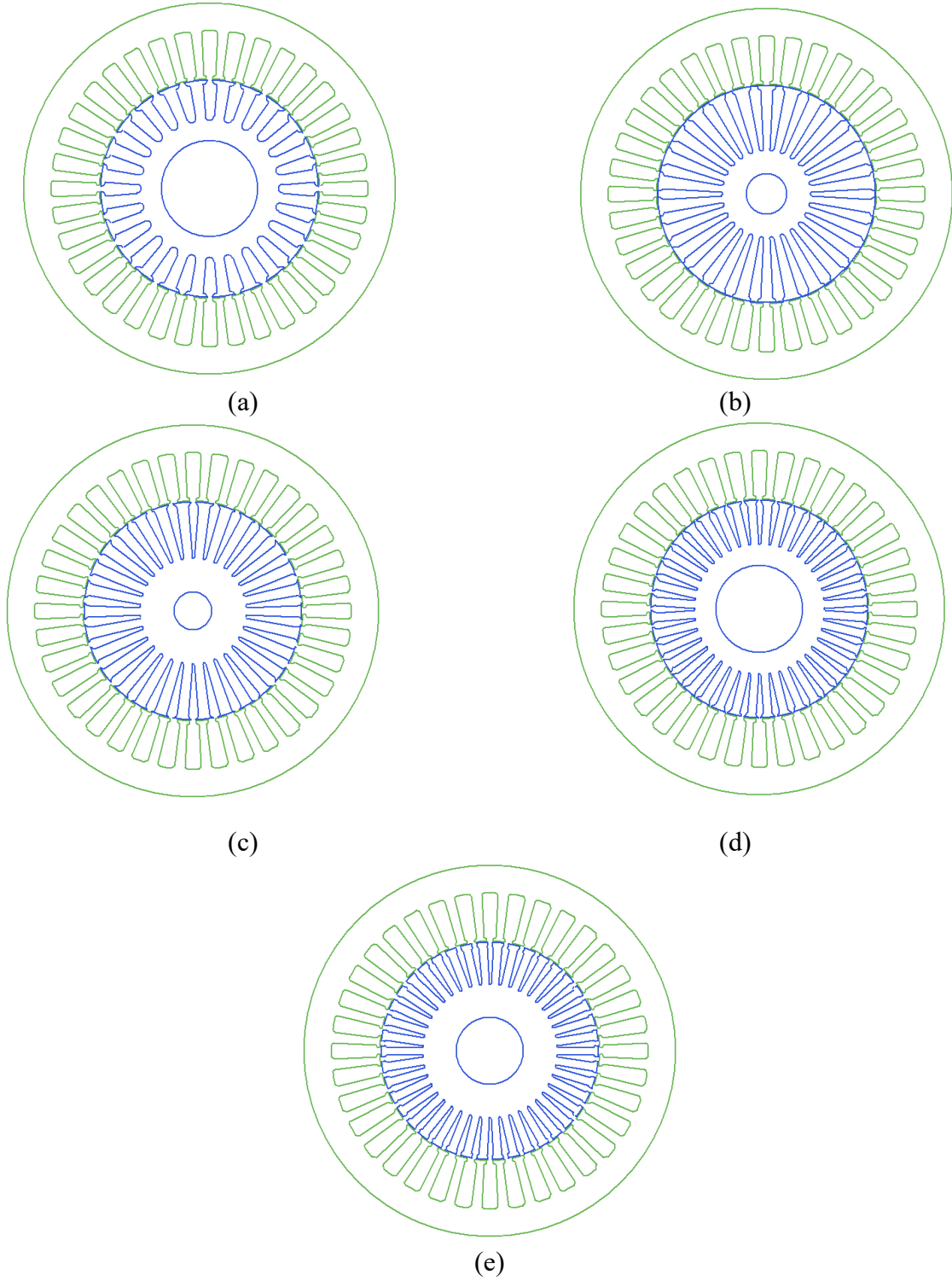
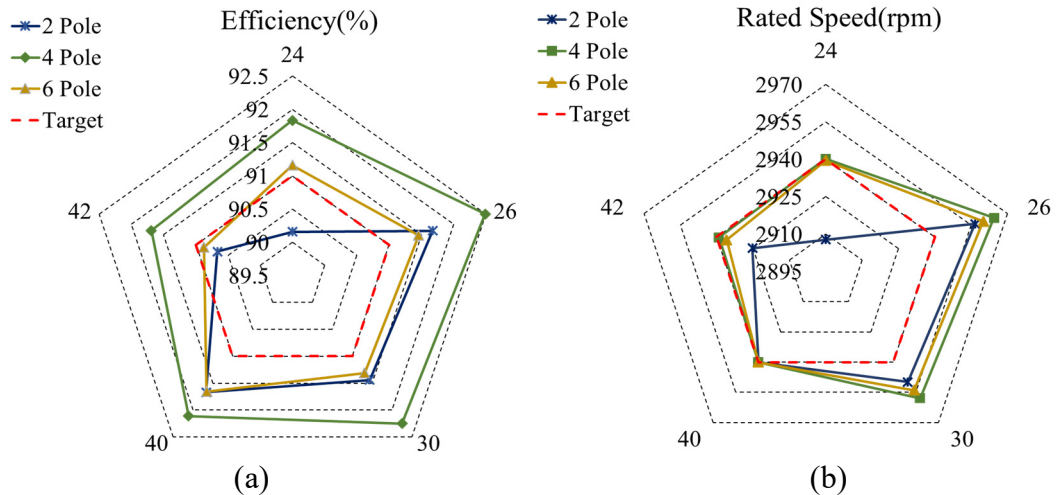
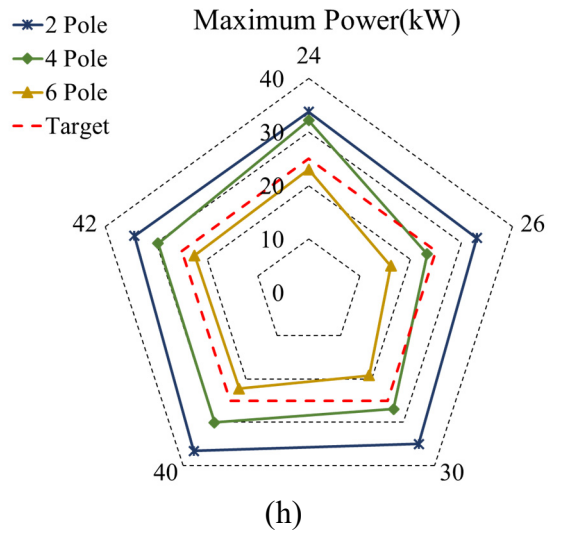
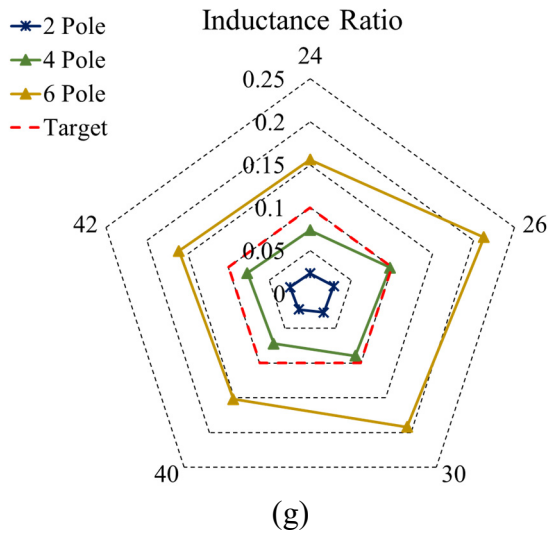
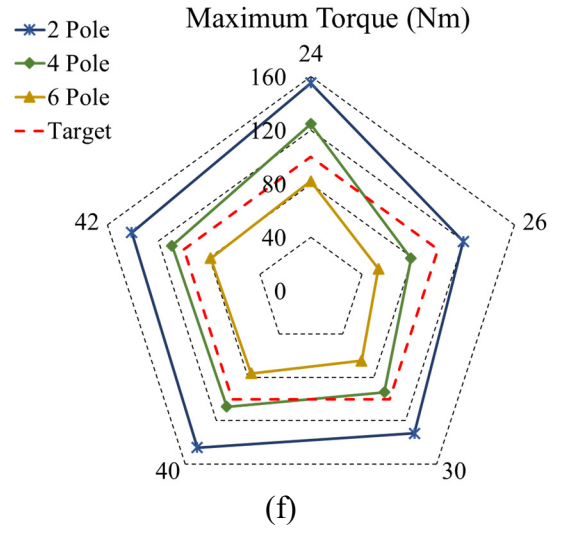
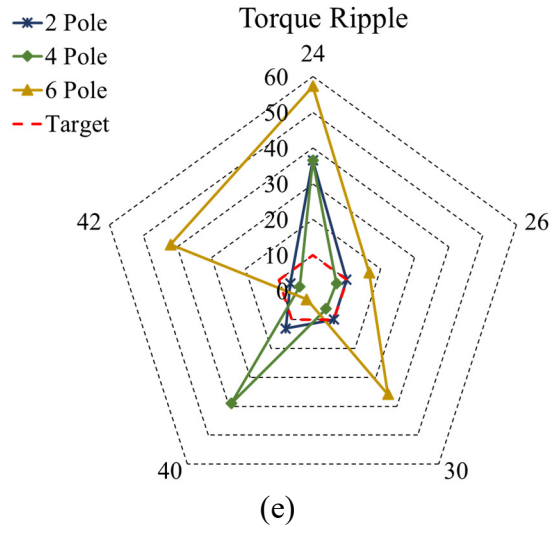
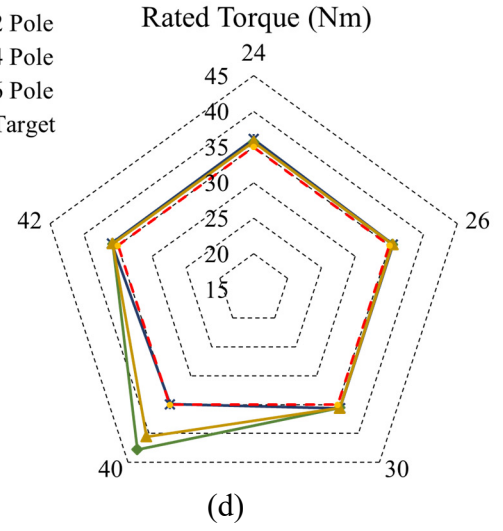
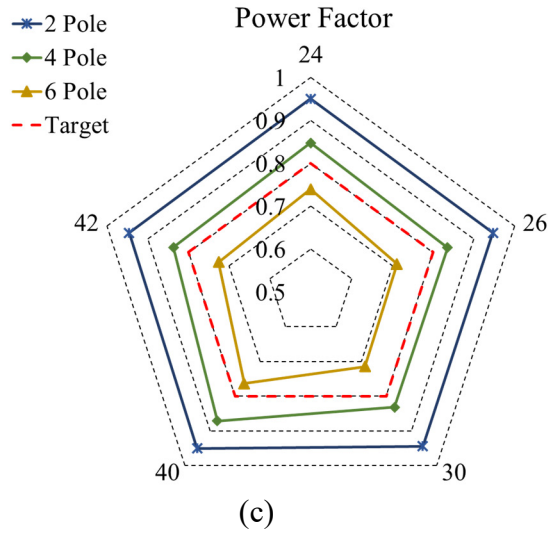


Figure. 2.4. Comparison of the selected designs obtained from automated parametric based optimization approach. (a) 36-24. (b) 36-26. (c) 36-30. (d) 36-40. (e) 36-42.

The impact of stator-rotor slot/pole combination on the electromagnetic performance is investigated using 2D FEA. With the intention of precise observation on the IM characterization, the same transient analysis has been conducted using the same FEA setup properties, including the design considerations given as follows:

1) The same winding layout with double-layer and full slot-pitch distributed windings has been utilized (the same fundamental winding factor); 2) All the IMs have trapezoidal 36 slots in the stators; 3) All the IMs are operated with 285 Vrms at 3,000 rpm; 4) Same stator and rotor core material have been used. Important stator-rotor slot/pole selection criteria for the three-phase IM is maximum fundamental MMF amplitude and minimum MMF harmonics while it provides peak rating as calculated targets. These parameters are related to the torque and power densities and excessive losses, the unbalanced magnetic pull, torque ripple, acoustic noise, and vibration issues. Even if the fundamental MMF for one turn and one ampere is almost the same for all IMs, the total harmonic distortion percentage is reduced as the stator slot, and pole number is increased. Therefore, it can be predicted that the parasitic effects will be lower if the stator slot and pole numbers are increased together. Due to the different magnitude of slotting and saturation harmonics for each case study lower number of poles in the IM has higher slip frequency, lower efficiency, and higher excessive losses because of significant saturation in the stator and rotor. However, it produces the same rated torque with higher overload capability compare to four and six pole IM. The high number of poles has overall good continuous output characteristics within a suitable flux density boundary. Though it produces lower peak torque and power, compare to the specified targets.





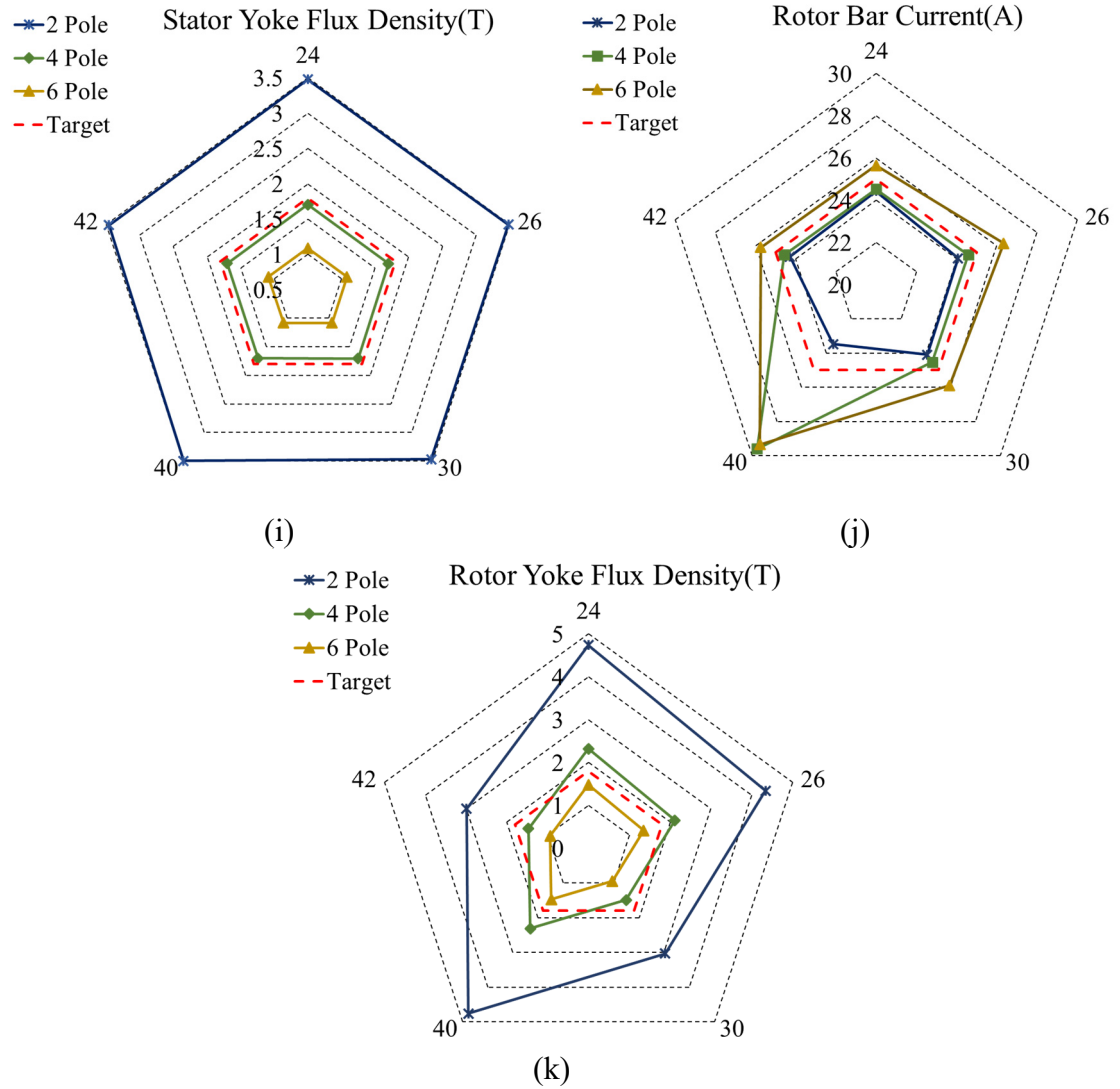


Figure. 2.5. Comparison of steady state output and magnetic characteristics for different stator-rotor slot-pole combinations. (a) Efficiency. (b) Rated speed. (c) Power factor. (d) Rated torque. (e) Torque ripple. (f) Maximum torque. (g) Inductance ratio. (h) Maximum torque. (i) Stator yoke flux density. (j) Rotor bar . (k) Stator yoke flux density at rated and peak operated conditions.

TABLE 2. 4.
PERMITTED FLUX DENSITIES OF THE MAGNETIC CIRCUIT FOR VARIOUS STANDARD ELECTRICAL MACHINES

| Structural Domain | Flux density B[T] |
|-------------------|-------------------|
| Stator yoke | 1.4 - 2 |
| Rotor yoke | 1 - 1.9 |

Based on the electromagnetic analysis results of the various structural designs, the suitable stator-rotor slot /pole combination is selected to satisfy the initial calculated targets in Table 2.2 is 36-42 pole combination. The proposed design has high efficiency and peak power rating with a lower torque ripple within reasonable magnetic flux density constraints in different structural domains of IM presented in Table 2.4. Figure 2.6 represents the schematic of the baseline IM.

2.4. Verification of Analytical Design Structural Sizing Through Electromagnetic Design

In this section, the four poles 36-42 stator-rotor slot combination IM is developed in FEA environment to investigate the higher harmonic content for the entire speed range. For this purpose, the constant torque and constant power region conditions are adopted as the different operating condition, and IM output characteristics are analyzed through 2D FEA for further optimization purposes. Figure 2.6 is representing the 2D cross section of the developed high speed IM with a double layer distributed winding. 11 AWG wire is chosen to form the stator winding. Twelve number of conductor per slot is fitted in each stator slot to keep the slot fill factor as high as 70 percent for the sake of higher power density. The rotor bar material is chosen as Aluminum with a relative permeability of 1.000021 and bulk conductivity of 38,000,000 Siemens/m, the thermal conductivity of 237.5 W/m.C, the mass density of 2,689 kg/m³ and specific heat coefficient of 951 J/k.C.

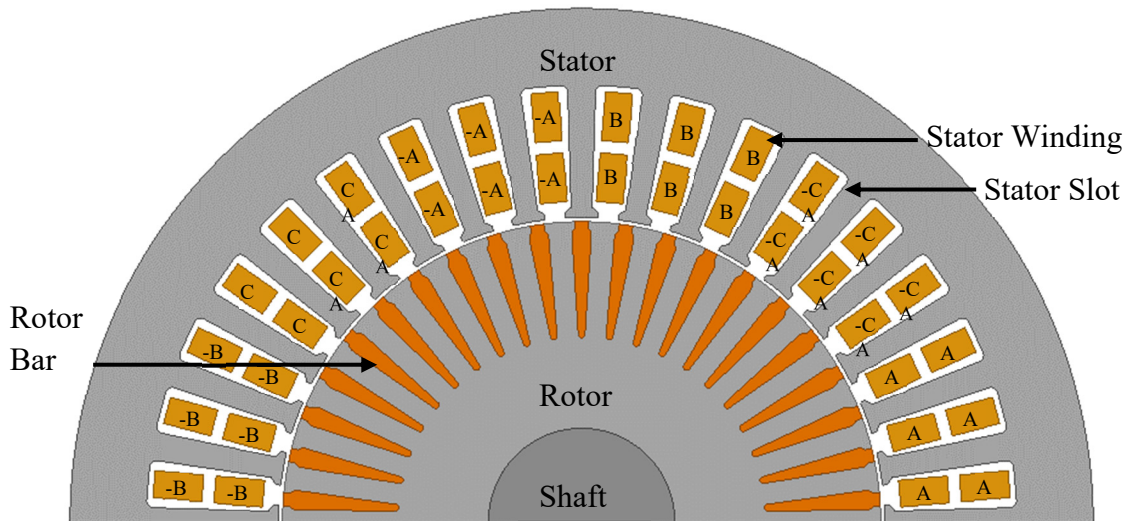


Figure. 2.6. A CAD drawing of developed high speed IM in FEA.

2.4.1. Comparative Analysis of Output Characteristics for Skewed and Non-Skewed Rotor Through 2D FEA.

The skewed rotors are employed extensively to reduce permeance harmonics, excessive losses [9] and [10], parasitic torque [11] and torque ripples in IMs because of slotting effect in both stator and rotor [12]. Rotor skewing increases the iron losses and decreases the level of iron saturation, acoustic noise, and average torque due to the axial variation of the air-gap flux [13]. Also, the leakage reactance becomes higher because of an additional component in leakage inductance, leading to reduction of efficiency [14]. Since skewing reduces the amplitude of rotor bar current, consequently the IM with skewed rotor bars starts in a shorter time than non-skewed IM [15]-[16]. Similarly, the axial variations of flux density in magnetic saturation in a skewed rotor might have a remarkable impact on the starting performance but have a relatively slight effect at full load operating condition. Since skewing has a considerable effect on the power losses including iron losses and rotor bar copper loss [17], therefore, the influence of skew angle on stator current, electromagnetic torque, torque ripple, torque-speed profile, and magnetic flux density is investigated through 2D-FEA. As known, there is a direct correlation between the stator current, bar current, and electromagnetic torque. More precisely, in an IM, the electromagnetic torque is produced as a consequence of the induction of the rotor bar current [18].

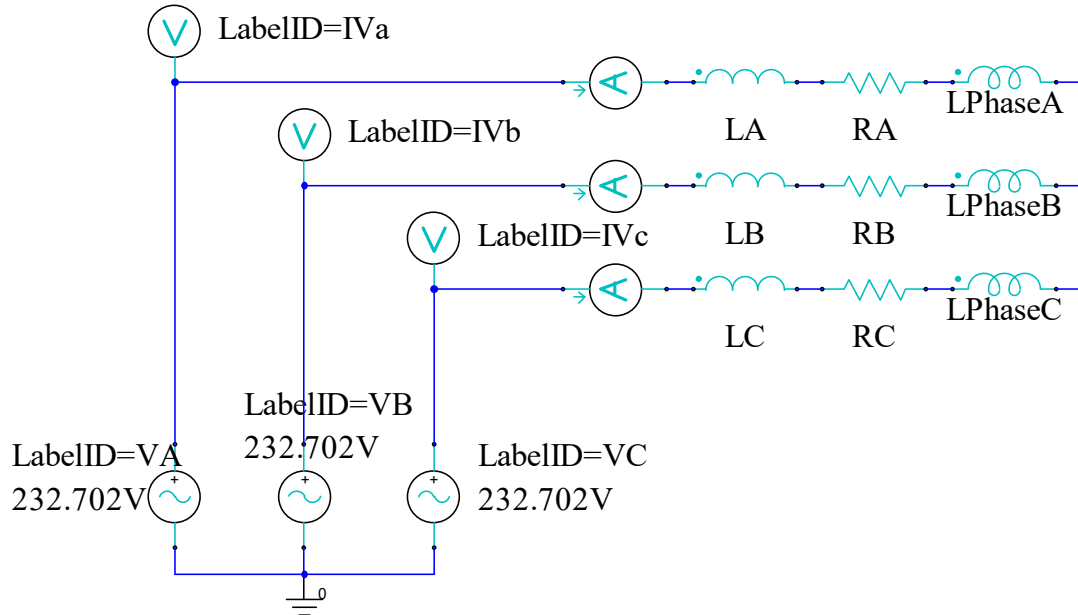


Figure. 2.7. Schematic of voltage fed external circuit excitation used in FE analysis.

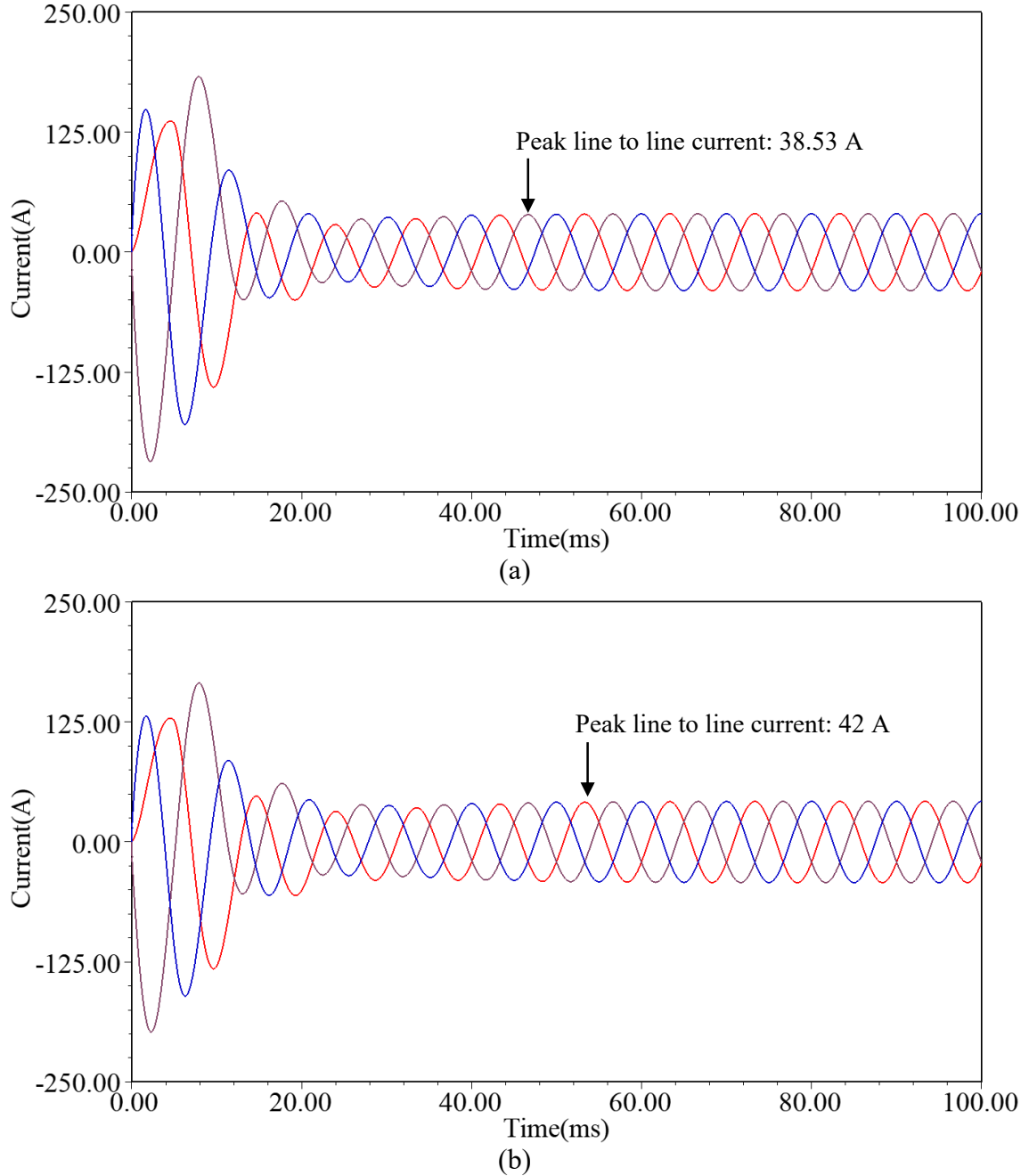


Figure. 2.8. The line to line peak current of developed high speed IM in 2D FEA at the rated operating condition with a sinusoidal supply voltage. (a) non-skewed rotor bars. (b) skewed rotor bars.

In this study, it has been shown that the rotor skew affects the performance characteristics, especially the torque-speed profile and individual electromagnetic torque for each individual operating condition. Figure 2.8 represents the line to line current of the developed IM with skewed and non-skewed rotor bars with the same voltage excitation circuit. Figure 2.9 is presenting the electromagnetic torque of developed design in FEA at

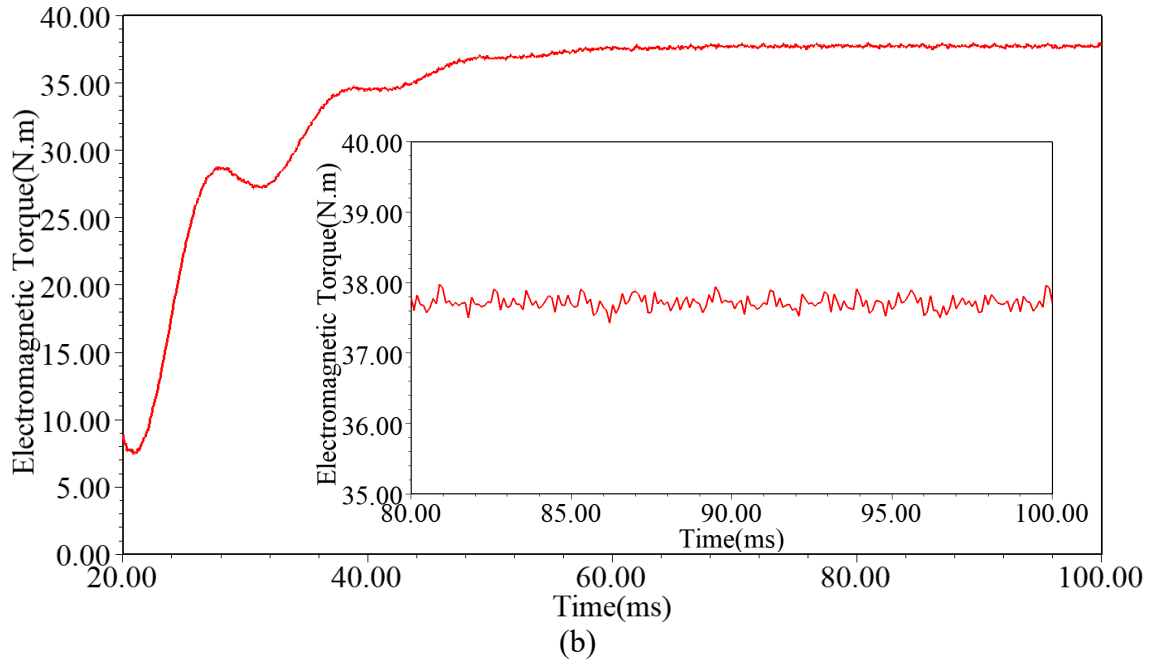
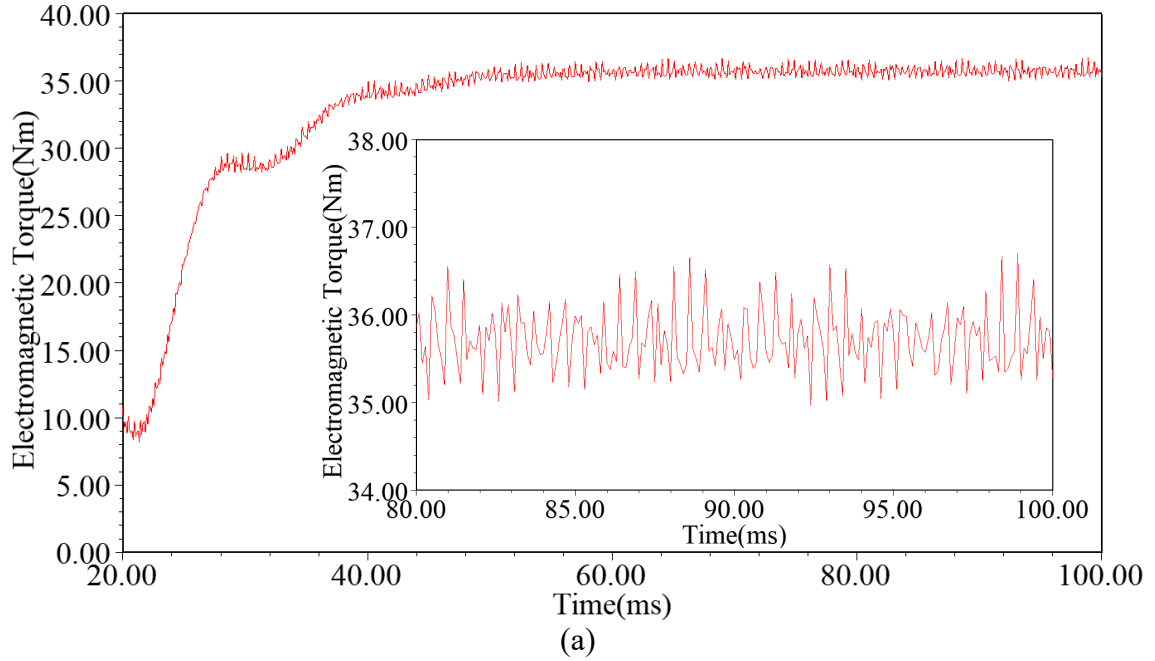


Figure. 2.9. Electromagnetic torque of developed high speed IM in 2D FEA at the rated operating condition with a sinusoidal supply voltage. (a) non-skewed rotor bars. (b) skewed rotor bars.

the rated operating condition, and it is proving that the torque ripple decreases significantly for the skewed IM from 7 percent to 2 percent. Figure 2.10 demonstrates the torque-speed profile and electromagnetic torque for each condition and compares the maximum torque and field weakening region for both skewed and non-skewed IMs. Level of saturation and

magnetic flux density is shown in figure 2.11 for skewed and non-skewed rotor bars and it establishes the lower flux density magnitude in case of skewed rotor bars because of improved performance of the IM.

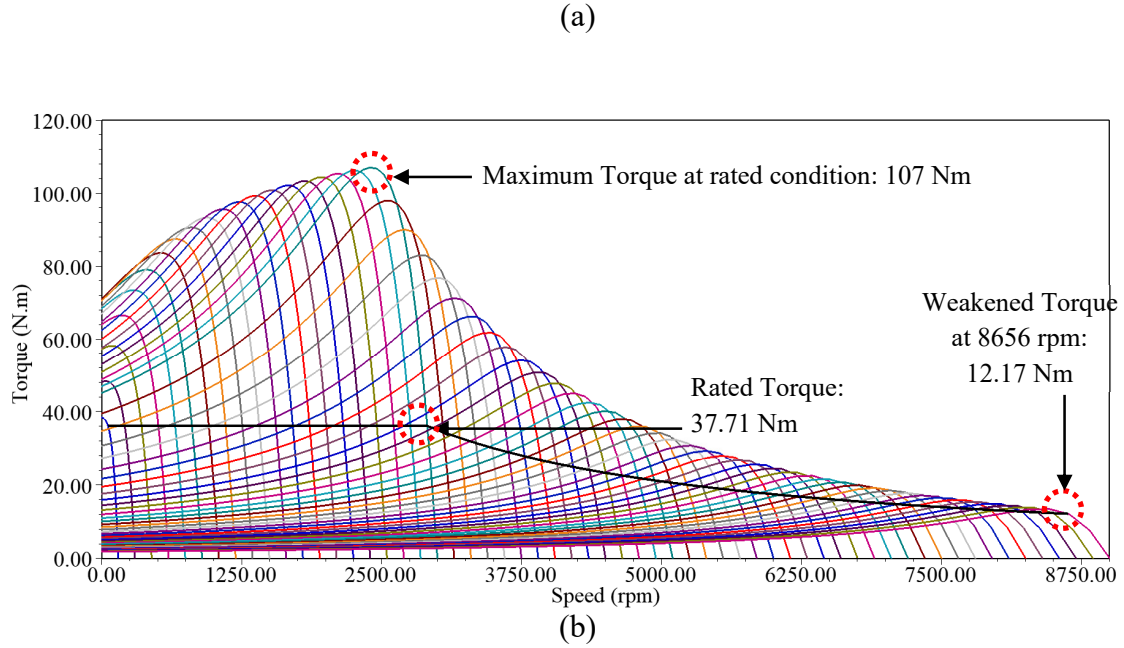
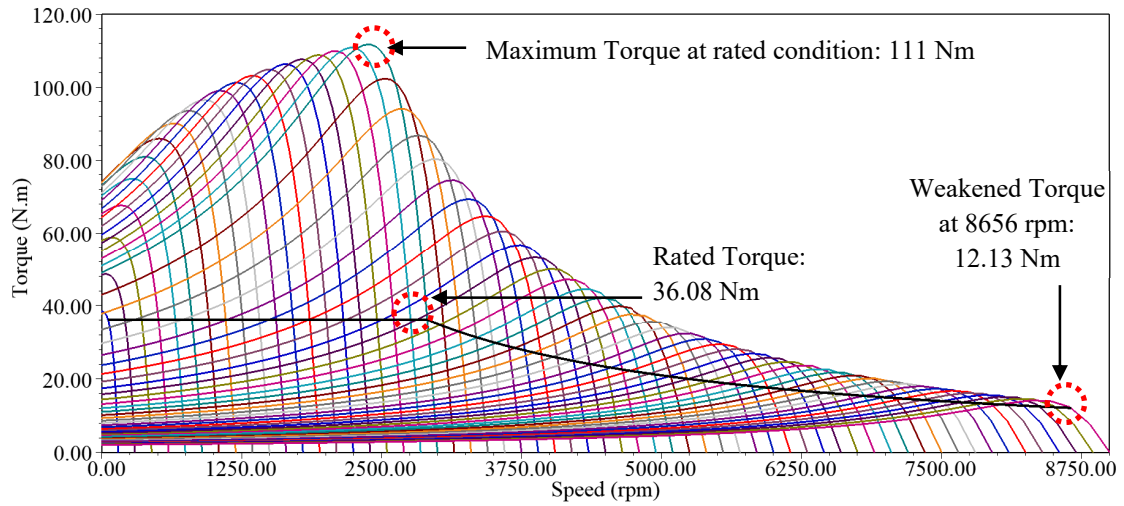
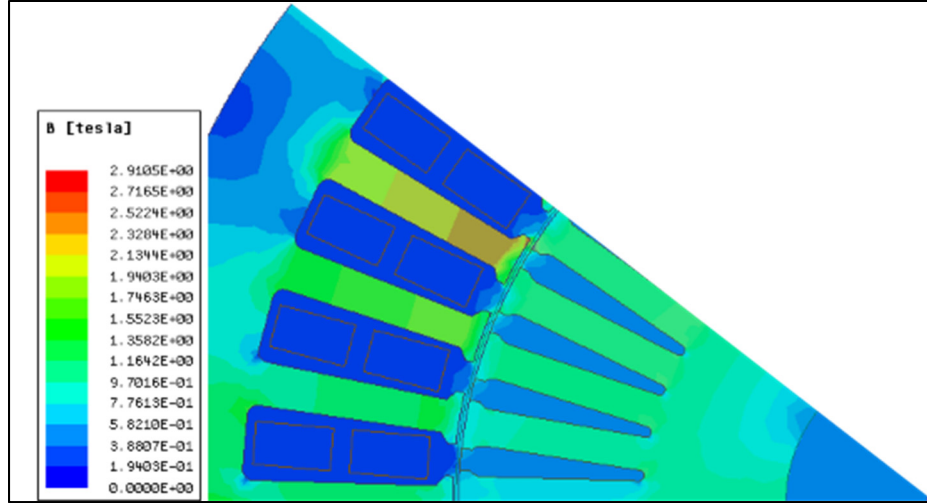
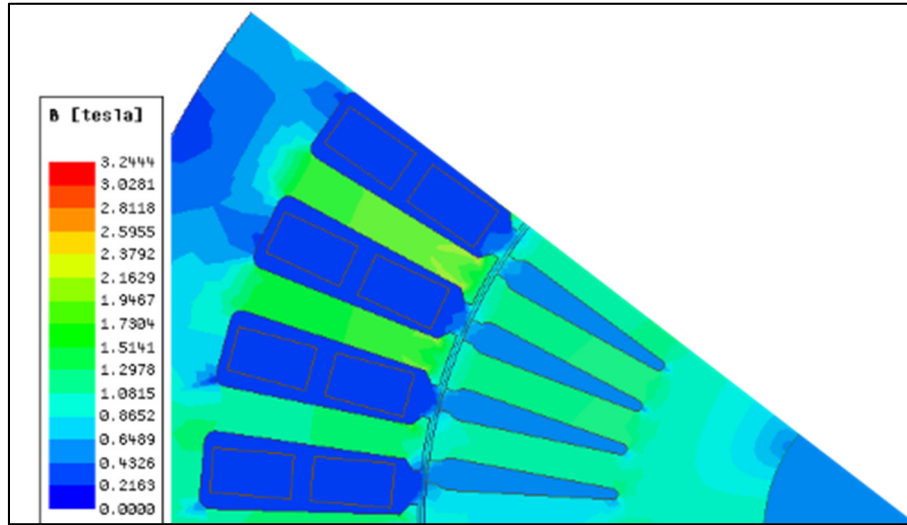


Figure. 2.10. Torque-Speed profile of developed high speed IM in 2D FEA. (a) non-skewed rotor bars. (b) skewed rotor bars.



(a)



(b)

Figure. 2.11. Cross section of developed high speed IM and magnetic flux density distribution at steady state condition and rated operating condition. (a) non-skewed rotor bars. (b) skewed rotor bars.

2.5. Conclusions

This chapter presents an automated design algorithm using analytical design equations to develop a high speed IM to meet variable speed requirement. For this purpose, a parametric based optimization in conjunction with 2D-FEA is employed to find the optimal number of stator-rotor/pole combination within a compact volume considering electromagnetic boundaries. Furthermore, it was found that to skewing rotor bars reduces the excessive permeance harmonics due to slotting effect and MMF interaction between stator and rotor slots and leads to a slight increase of constant power region. Therefore, the

precise investigation of the IM axial behavior magnetic flux density is vital for further optimization of developed IM.

2.6. References

- [1] 14 focus electric, online at: <https://www.ford.com/services/assets/Brochure?make=Ford&model=FocusElectric&year=2014>.
- [2] Basics of Vehicle Dynamics, online at: <http://mehanizacija.ftn.uns.ac.rs/wp-content/uploads/2017/07/Part-12.pdf>.
- [3] How to calculate wheel torque from engine torque online at: <https://x-engineer.org/automotive-engineering/chassis/longitudinal-dynamics/calculate-wheel-torque-engine>.
- [4] J. Pyrhönen T. Jokinen V. Hrabovcová, Design of Rotating Electrical Machines, 2nd edition, Wiley, 2014.
- [5] I. Boldea, Syed A. Nasar, The Induction Machines Design Handbook, Taylor & Francis, Dec. 9, 2009.
- [6] A. K. Sawhney, Electrical machine design, Dhanpat Rai & Co, 2013.
- [7] S. Mallampalli, Z. Q. Zhu, J. C. Mipo and S. Personnaz, "Influence of Rotor Slot Number on Flux Weakening Characteristics of Induction Machines," 2018 21st International Conference on Electrical Machines and Systems (ICEMS), pp. 549-554, 2018.
- [8] T.A. Lipo Introduction to AC machine design IEEE Press 2017.
- [9] Z. Haisen, W. Yilong, W. Yuhan, Z. Yang and X. Guorui, "Loss and Air-gap Force Analysis of Cage Induction Motors With Non-skewed Asymmetrical Rotor Bars Based on FEM," in *IEEE Transactions on Magnetics*, vol. 53, no. 6, pp. 1-4, 2017.
- [10] C.I. McClay S. Williamson "Influence of rotor skew on cage motor losses" *IEEE Elect. Power Appl.* vol. 145 no. 5 pp. 414-422 Sep. 1998.
- [11] S. L. Ho, W. N. Fu and H. C. Wong, "Estimation of stray losses of skewed rotor induction motors using coupled 2-D and 3-D time stepping finite element methods," in *IEEE Transactions on Magnetics*, vol. 34, no. 5, pp. 3102-3105, 1998.[10]
- [12] S.L. Nau "The influence of the skewed rotor slots on the magnetic noise of three-phase induction motors" *Int. Conf Elect. Mach. Drives (IEMDC'97)* pp. 396-399 1997.[12]
- [13] W. Xu, X. Bao, C. Di, L. Wang, and Y. Chen, "Optimal Angle Combination for Improving Electromagnetic Torque in Induction Motor with Double-Skewed Rotor," in *IEEE Transactions on Magnetics*, vol. 53, no. 11, pp. 1-5, Nov. 2017.
- [14] Byung-Il Kown, Byung-Taek Kim, Cha-Seung Jun, and Seung-Chan Park, "Analysis of axially non-uniform loss distribution in 3-phase induction motor considering skew effect," in *IEEE Transactions on Magnetics*, vol. 35, no. 3, pp. 1298-1301, 1999.
- [15] C. Wang X. Bao S. Xu Y. Zhou W. Xu Y. Chen "Analysis of vibration and noise for different skewed slot-type squirrel-cage induction motors" *IEEE Transactions on Magnetics*. vol. 53 no. 11 pp. 1-6 Nov. 2017.

- [16] S. Williamson C.I. McClay "The effect of axial variations in saturation due to skew on induction motor equivalent-circuit parameters" *IEEE Transactions on Industrial. Application.* vol. 35 no. 6 pp. 1323-1331 Nov. 1999
- [17] B. Heller, and A. L. Jokl, "Losses In Squirrel-Cage Motors Due To Rotor Skew," in *IEEE Transactions on Power Apparatus and Systems*, vol. PAS-90, no. 2, pp. 556-563, 1971.
- [18] Y. Kawase T. Yamaguchi Z. Tu N. Toida N. Minoshima K. Hashimoto "Effects of skew angle of rotor in squirrel-cage induction motor on torque and loss characteristics" *IEEE Transactions on Magnetics.* vol. 45 no. 3 pp. 1700-1703 Mar. 2009

CHAPTER 3

COMPARISON OF 2-D AND 3-D FINITE ELEMENT ANALYSIS BASED INDUCTION MACHINE DESIGN AND VALIDATION WITH MODIFIED EQUIVALENT CIRCUIT APPROACH

3.1. Introduction

Slotting effect is highly significant in induction machine (IM), because of the existence of slots in both, rotor and stator. As a result, acoustic noise and high frequency torque ripples are ominously high in IMs in variable speed applications. Additional iron losses and winding losses due to spatial harmonics, which is resultant of slots, can be reduced using proper slot/pole combination and chording of the stator winding in lower frequencies [1]-[6]. Additionally, the presence of skew in IM reduces slotting effect at higher frequencies by reduction of spatial harmonics, which is produced by slots [7]-[9]. However, owing to skewing, another problem that occurs is the axial air-gap magnetic flux variation. Results indicate that the axial variations due to skew and non-uniformity of flux distribution have a considerable impact on the starting performance of IM because of parameter changes along the machine axis [10].

Non-uniformity of flux distribution produces excessive losses, which results in a decrease in average torque production [11]- [13]. Background studies have investigated the influence of skew angle on rotor bar currents, electromagnetic torque, loss characteristics, and efficiency of IM [14]-[17]. Predominantly, most of the studies indicate that the nominal value for rotor bar skew angle ranges from 0 to 1.5 of the stator slot pitch. However, this is not necessarily the optimal value for the best possible performance [8]. Improvement of the air-gap flux density, which is distorted due to skewing in the axial direction, is more promising when the optimal skew angle is obtained as well as the reduction in axial harmonic of traveling magnetic flux waves is achieved to decrease unwanted losses [5].

2-D or 3-D finite element analysis (FEA) is used to analyze magnetic flux distribution in details and construct a high performance IM, depending on the geometrical aspects [18], [19]. In industrial development processes, 2-D analysis is preferred in case of machines

with no axial geometrical discontinuities because of shorter simulation time and faster data analysis. However, in the case of skewed machines, 3-D FEA is strongly desired due to axial magnetic flux and parameter variations for performance enhancement [20]-[22].

Considering spatial harmonic reduction in skewed IM and obtaining constant output torque with minimized ripples, this paper presents a hybrid analytical-3-D FEA algorithm to include the effect of axial field variation and hence develop an IM with enhanced performance. The necessity of using 3-D FEA instead of 2-D is given in section III. Modified equivalent parameters have been calculated to consider slotting harmonics and presented in detail in section IV. Subsequently, in section V, the calculated parameters are fed into an optimization process in order to enhance the overall performance by considering torque ripple minimization as the objective. The rotor bar geometry and skew angle are chosen as the design variables. Consequently, the improved IM has been compared with the initial IM in terms of spatial harmonics in the air-gap flux and other start-up performance aspects such as developed torque.

3.2. Comparative Analysis of Initial Design in 2-D FEA and 3-D FEA

In this section, the selection of an initial design for further analysis is explained. Additionally, the importance of considering axial flux variation in characteristics such as flux density, phase currents, and output torque has been proved through a comparative study in 2-D and 3-D FEA.

3.2.1 *Characteristics of Initial Design of IM*

A double cage squirrel cage IM is chosen as an initial model. The geometrical and electrical parameters of the three-phase IM with single layer concentric winding and one slot pitch skew angle as the initial model is given in Table 3.1. The cross section of the initial IM is given in Fig. 3.1(a). The experimental setup used to determine the equivalent circuit parameters (ECP) using IEEE 112 standards, which are shown in Fig. 3.1(b). Subsequently, the calculated ECP using Maxwell's equations, and the experimentally measured circuit parameters are compared and validated in Table 3.2 [23].

TABLE 3. 1.
RATED AND GEOMETRICAL PARAMETERS OF INITIAL IM FOR FEA MODELING

| Rated Parameters | | Geometrical parameters | |
|-------------------|-----------|------------------------|-------------|
| Output power | 7.5 hp | D_{so}/D_{si} | 220.137/134 |
| Phase voltage | 200 V | D_{ro}/D_{ri} | 133.4/42 |
| Phase current | 20.9 A | Stator slot number | 48 |
| Number of poles | 4 | Rotor slot number | 42 |
| Frequency | 60 Hz | Stack length | 136.02 mm |
| Synchronous speed | 1,800 rpm | Conductors/slot | 120 |

TABLE 3. 2.
CALCULATED AND MEASURED IM CIRCUIT PARAMETERS

| Equivalent Circuit Parameters | Measured | FEA Model |
|-------------------------------|----------|-----------|
| $R_s (\Omega)$ | 0.18 | 0.211 |
| $R_r (\Omega)$ | 0.59 | 0.51 |
| $X_{ls} (\Omega)$ | 0.57 | 0.620 |
| $X_{lr} (\Omega)$ | 0.86 | 0.91 |
| $X_m (\Omega)$ | 22.67 | 23.54 |

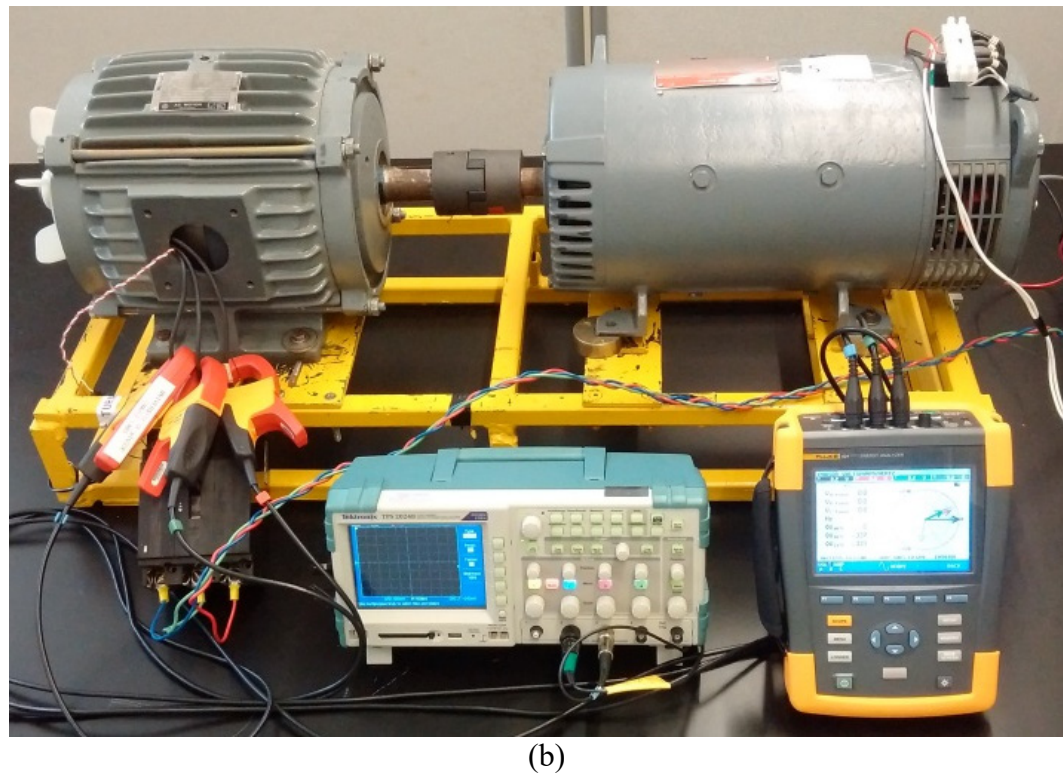
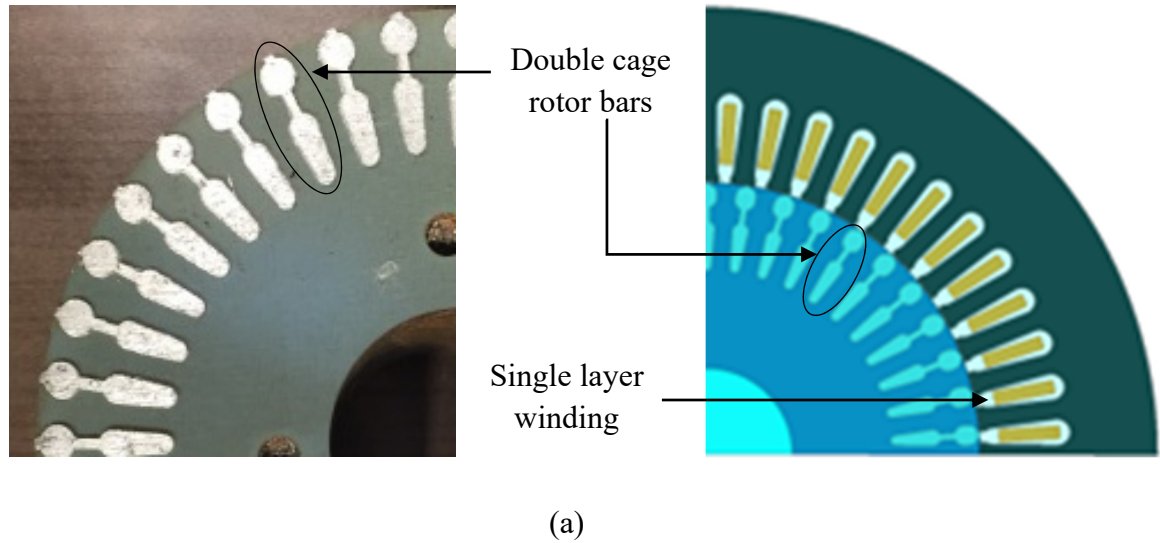


Figure. 3.1. Parameter determination of the 7.5 hp, 4-pole induction machine. (a) Schematic of 2-D FEA model and existing rotor. (b) Experimental setup.

3.2.2 Validation of 3-D FEA with Experimental Results

For further validation of the developed FEA model, an experimental set up is developed to measure magnetic flux density, as shown in Fig. 3.2. Search coils have been wound around entire stator tooth for accurate flux measurement. Faraday's law is used to calculate the magnetic flux density using the induced voltage in the air-gap region. The induced

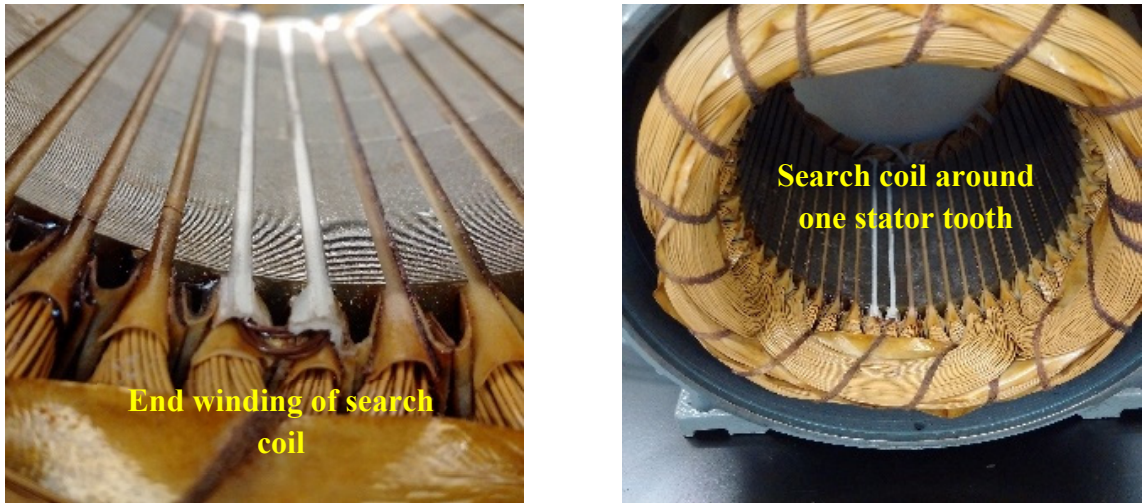


Figure. 3.2. Search coil in the stator slot opening. (a) End winding of the search coil. (b) Overview of a complete turn of the search coil around one stator slot.

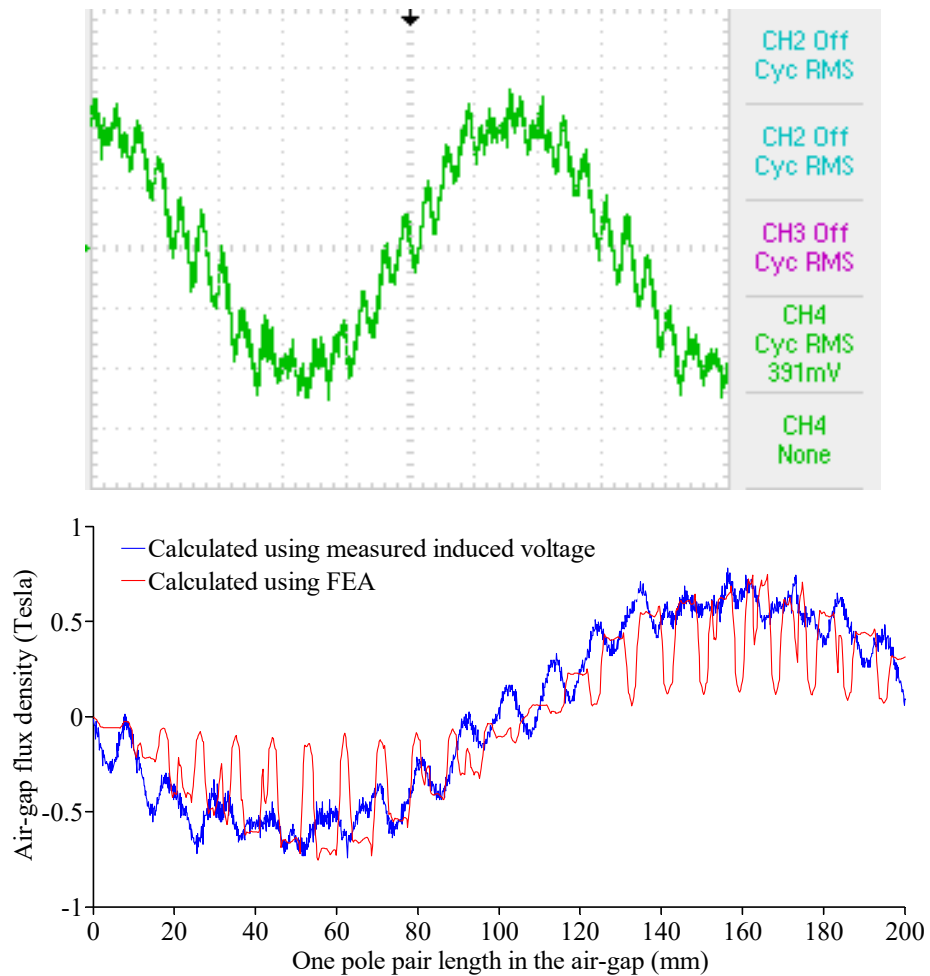
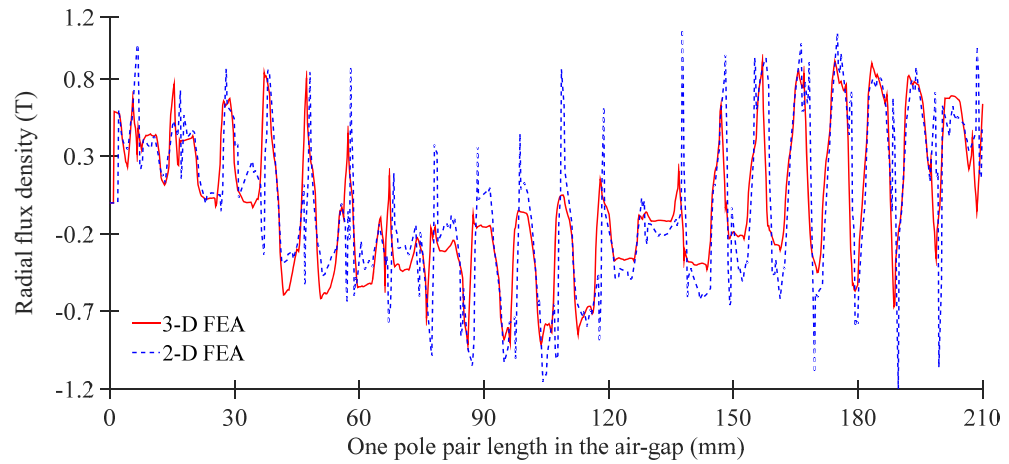


Figure. 3.3. Experimental measurement of flux. (a) Measured induced voltage from search coil at the no-load condition with a slip of 0.0061. (b) Comparison of the measured and calculated magnetic flux in the air-gap at the no-load condition with the slip of 0.0061.

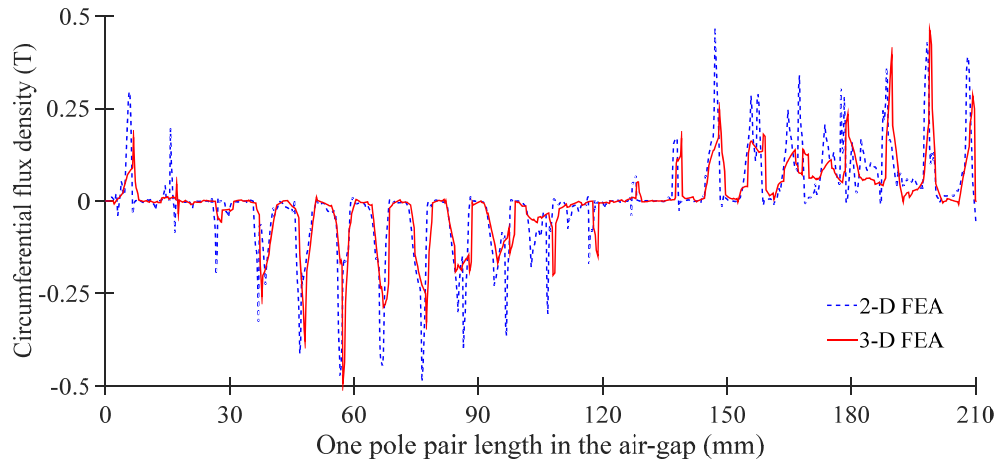
voltage is measured under no load condition. Search coils are designed using 22 AWG wire and six number of turns. The induced voltage at the no-load condition at a speed of 1,789 rpm is measured and represented in Fig. 3.3(a). In addition to the ECP validation, measured magnetic flux density is compared for both developed FEA model and actual IM, as shown in figure 3.3(b).

3.2.3 Performance Analysis of Initial Design in 2-D and 3-D FEA

The fundamental equations of the electromagnetic field analysis using finite element formulation adopt magnetic vector potential as an unknown parameter. A better understanding of the difference between 2-D and 3-D FEA is essential because of the



(a)



(b)

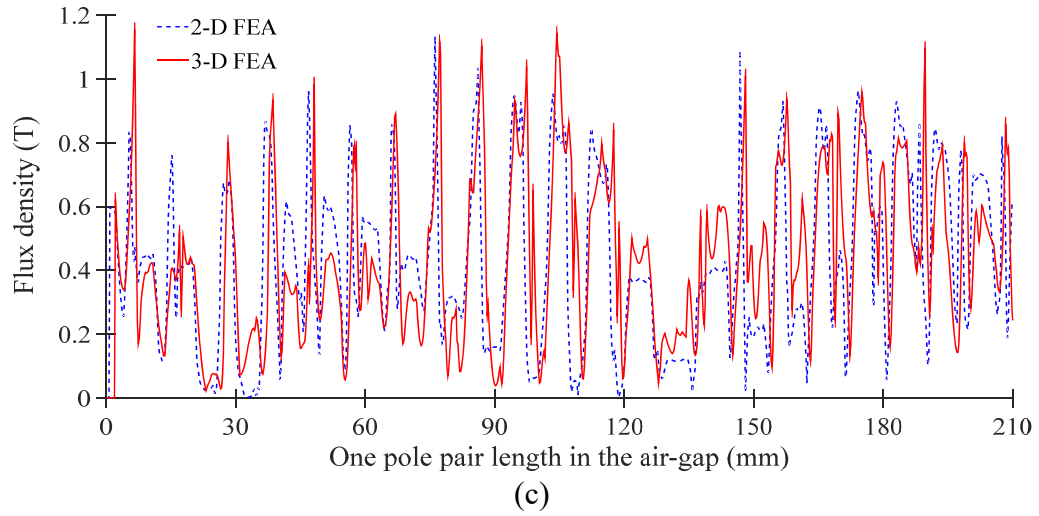
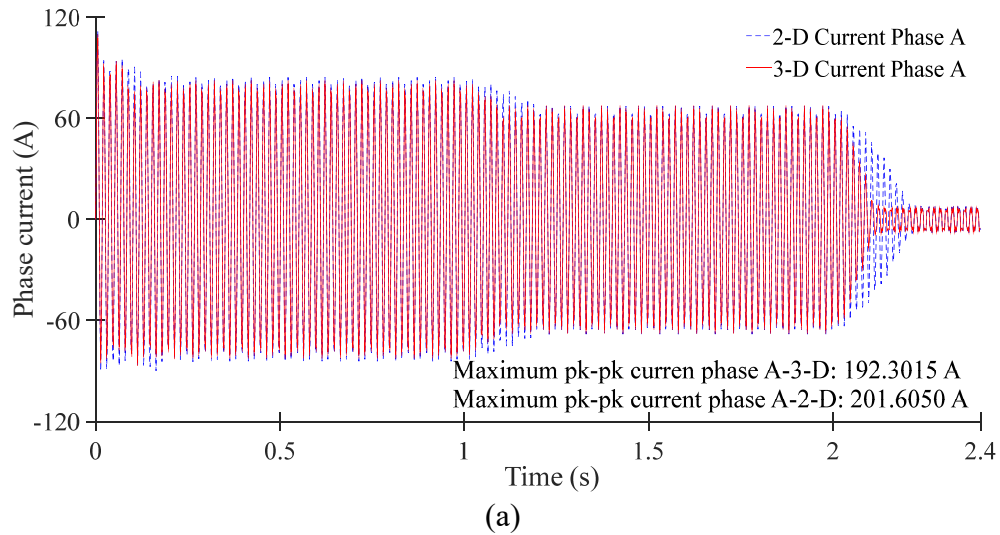


Figure. 3.4. Magnetic flux density distribution in the air-gap over one pole pair of 2-D and 3-D finite element model for variable speed under no-load condition. (a) Radial. (b) Circumferential. (c) Total flux.

physical nature of magnetic vector potential, which is a vector quantity. In this section, radial, circumferential, and total magnetic flux density is given in Figs. 3.5(a) – 3.5(b). The additional axial magnetic flux, which is due to skewing the rotor bars, is observed to cause a significant difference in the total magnetic flux density observed in 3-D, as seen in Figs. 3.5(c). The developed torque and phase A current are presented for initial model IM under variable speed condition in Figs. 3.6(a) and 3.6(b). It is observed that in 3-D analysis, the average torque and peak current are less due to additional axial spatial harmonics as a consequence of the difference in the ECP.



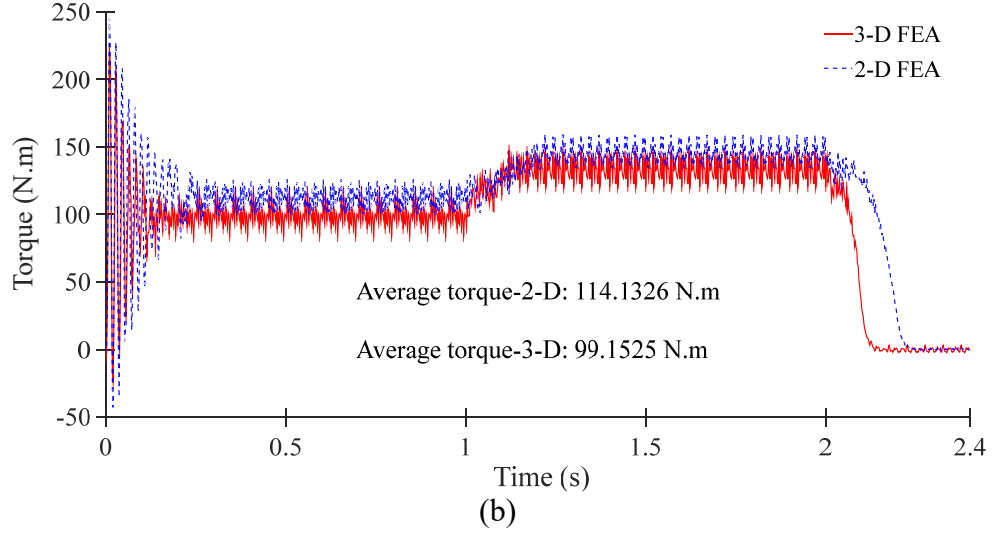


Figure. 3.5. Performance characteristics comparison of 2-D and 3-D finite element model for variable speed. (a) Current for phase A. (b) Developed torque for a variable speed range of 0-1,780 rpm.

3.3. Improvement in IM Design Process Considering Space Harmonics

In this section, a brief description of the proposed design process, including space harmonics due to the slotting effect in both stator and rotor is introduced and given in Fig. 3.7. First, the specification of the initial IM, which is investigated and given in Table I, is taken, including geometrical and electrical parameters as initial inputs to the proposed algorithm. Subsequently, analytical design model including skew effect and spatial harmonics and 3-D FEA are used to calculate the ECP. Modified circuit parameters from the novel proposed hybrid analytical-3-D FEA is used to calculate the output torque considering higher harmonics due to slotting and skew effect. The spatial harmonic reduction is achieved by minimizing torque ripples as an objective function and keeping average torque constant using improved particle swarm optimization (IPSO) algorithm incorporating the developed analytical design expressions. The improvement of the overall performance is achieved, and the characteristics of the improved model are provided in section VII.

3.4. Modified Equivalent Circuit Parameters Considering Axial Field Variation and Slot Harmonics

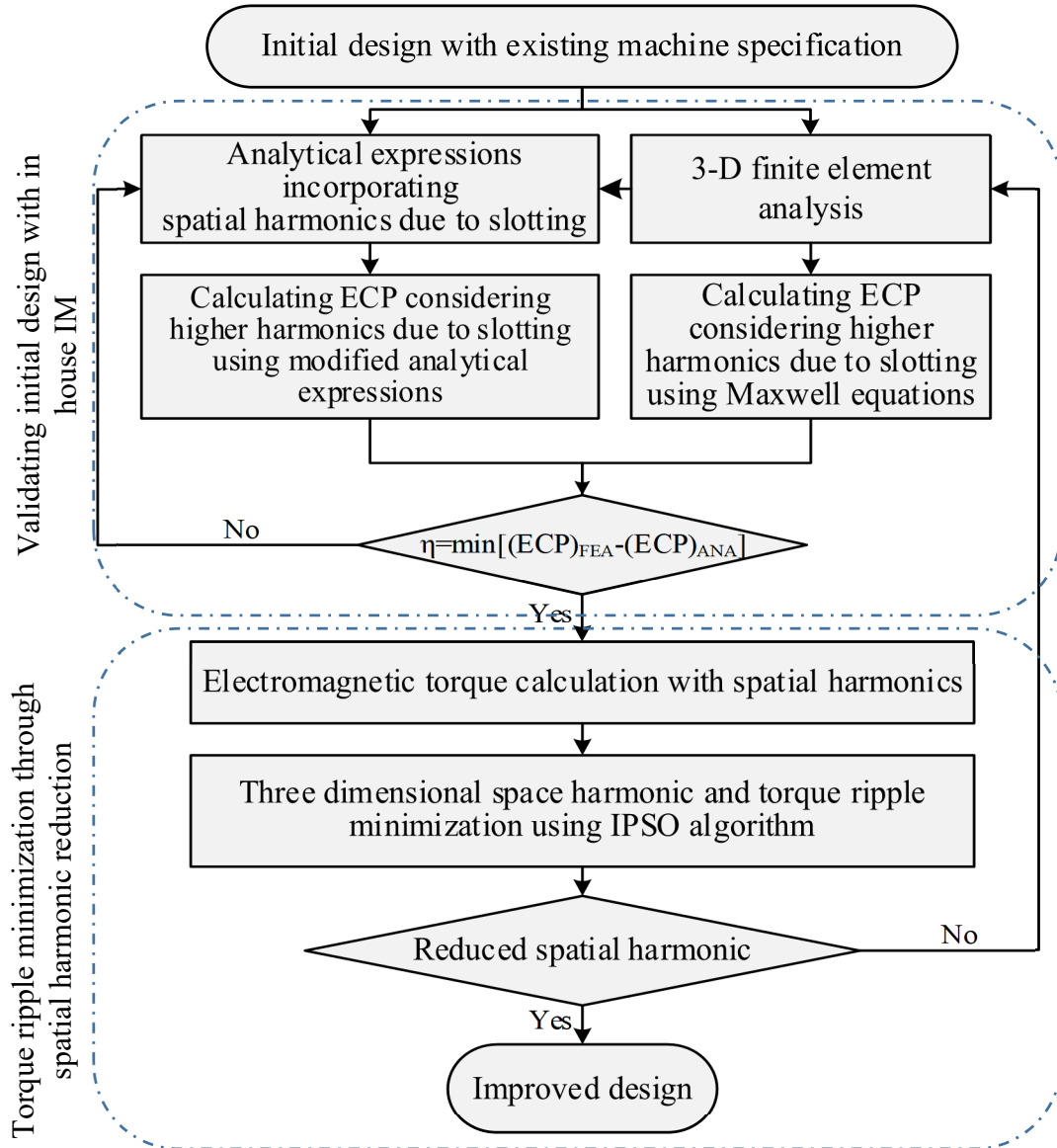


Figure 3.6. The design process of spatial harmonic reduction of IM.

The space harmonics due to stator and rotor slot sizing and rotor bar skewing are considered in this section To analyze vibrations and noises in the IM. Skewed rotor bars have two significant effects due to axial flux variation in IM analysis: first, the ability of the spatial harmonic reduction in the air-gap magnetic flux density to reduce the noises; and second the average torque reduction, which is a result of rotor induction weakening in the air-gap magnetic field. The phase shift of induced voltage because of skewing for the same winding turn causes a drop in induced voltage, which decreases the average torque production of IM. The effect of skewing factor and spatial harmonics are taken into account

in the circuit parameter calculation considering stator and rotor slot harmonics to study this phenomenon more accurately and is represented in Fig. 8, where R_s and R_{rv} are stator and rotor fundamental and slot harmonic resistances, L_{sov} , L_{rov} and L_{mv} are stator, rotor and air-gap leakage inductances for fundamental and slot using analytical design expressions, and consequently performance characteristics, such as torque production and phase current harmonics due to spatial harmonic reduction are investigated. The phase equivalent circuit of a three-phase IM harmonics, respectively. Stator winding resistance is predicted considering the end winding turn effect in (3.1) [24].

$$R_s = \rho \frac{Z_{ph} \left(L_{core} + K_{ew} \frac{\pi}{2p} (D_{is} + h_s) \right)}{A_{wire}} \quad (3.1)$$

Similarly, the per-phase equivalent rotor resistance referred to the stator side is calculated in (3.2) considering the skew effect. To simplify the equivalent circuit, the inter-bar currents, which are flowing between adjacent rotor bars due to lack of insulation between core and bars, are neglected. To maintain the magnetizing current. The length of the skewed rotor bar increases the rotor resistance due to the additional component in polar coordinate and considering higher space harmonics due to the slotting effect. In addition, the skin effect is included because of higher rotor frequency during the start-up performance.

$$R_{rv} = \frac{4m_s v}{Q_r} \left(\frac{Z_{ph}^k}{k_{sqv}} \right)^2 \left(\frac{K_b L_{core}}{A_b \cos^2 \gamma} + \frac{2\pi (D_{ir} + D_{or}) K_r}{t_r (D_{or} - D_{ir}) \sin^2 \left(\frac{v\pi p}{Q_r} \right)} \right) \quad (3.2)$$

where v is representing slot harmonic orders and t_r is the thickness of the end-ring in the axial direction. Magnetizing and leakage inductances are inductive parameters in the IM equivalent circuit. Since the inductances increase significantly in case of skewed rotor bars with respect to the stator, the exact calculation of individual inductances is compulsory.

Stator and rotor leakage inductances are classified based on traveling and non-traveling flux lines through the air-gap. Higher harmonics of the magnetizing inductance in the air-gap is the one crossing, and spatial distribution of the winding and skewing are its sources. The sources of non-traveling harmonics of the flux lines in the air-gap are the slotting, unevenness of the air-gap, end winding and skewing effects. In the proposed design algorithm, the same orders of slotting harmonics are considered as spatial harmonics in the leakage flux components leading to the derivation of modified circuit parameters. Individual leakage inductances for both stator and rotor are evaluated in (3.3), (3.4) and (3.5). The winding factor, k_{wv} including skewing factor in inductance calculation determines the presence of harmonics due to both slotting effect and skewing. Fundamental and harmonic electromagnetic torque from the modified circuit parameters is calculated in the next section.

$$L_m = \frac{m_s D \delta}{\pi p^2 \delta_{eff}} \mu_0 l' (k_{ws1} N_s)^2 \quad (3.3)$$

where the l' and δ_{eff} are the effective core length and air-gap length with stator and rotor slotting effect revised with Carter factor. Stator and rotor leakage inductance are broken down into individual components, namely, slot, tooth tip, air-gap, skewing and end winding leakage inductances. With considering skewing, and slotting harmonic effects, stator leakage inductance is calculated in (3.4).

$$L_{s\sigma} = \left(\sigma_{sqs} + \sigma_{\delta s} \right) L_m + 4m\mu_0 N_s^2 \left(L_{core} \left(\lambda_{us} + \lambda_{ds} \right) + q l_{ws} \lambda_{ws} \right) \quad (3.4)$$

where λ_{us} , λ_{ds} , and λ_{ws} are a slot, tooth tip, and end winding permeance factors in (3.5) and (3.6). The concept of magnetic stored energy is used to calculate these factors in the stator slot with specific stator slot shape represented in Fig. 3.1(a).

$$\lambda_{us} = \frac{h_4}{3b_4} + \frac{h_3}{b_4} + \frac{h_1}{b_1} + \frac{h_2}{b_4 - b_1} \ln \left(\frac{b_4}{b_1} \right) \quad (3.5)$$

$$\lambda_{ds} = k_2 5 \left(\frac{\delta}{b_1} \right) / 5 + 4 \left(\frac{\delta}{b_1} \right) \quad (3.6)$$

In (3.4), $l_{ws}\lambda_{ws} = 2l_{ew}\lambda_{lew} + W_{ew}\lambda_{weW}$ where l_{ew} is the average length of the end winding in the axial direction, W_{ew} is the corresponding stator winding coil span, and λ_{lew} , λ_{weW} is the constant coefficient following the winding structures. Furthermore, $\sigma_{sqS} = \frac{(1-k_{sq}^2)}{k_{sq}^2}$ and $\sigma_{\delta S} = \sum_{v=-\infty}^{\infty} \left(\frac{k_{wv}}{vk_{w1}} \right)$ are skewing, and the air-gap leakage factors. Also, k_2 is the coefficient, which is a function of the average value of the phase shift. The effect of skewed rotor bars on the leakage inductance is considered in terms of winding factor because the induced voltage by fundamental sine wave decreases because of phase shift, which is happening due to successive axial displacement of the rotor bars. Hence, the effect is seen in both rotor and stator leakage inductance: it is included as σ_{sqS} , and in the rotor side, referring skew leakage inductance is equal to the stator skew leakage inductance. Accordingly, rotor leakage inductance is formulated in (3.7).

$$L_{r\sigma} = \left(\sigma_{sqS} Q_r \left(k_{sqvr} \right)^2 / 4m \left(N_s k_{wvs} \right)^2 + \sigma_{\delta r} \right) L_m + \mu_0 L_{core} \lambda_{ur} + \mu_0 \frac{v\pi D_{ring} Q_r}{4p^3 m} \quad (3.7)$$

where λ_{ur} is the permeance factor in the rotor, and end-ring is the average diameter of the end ring. In (3.7), the first and second term is representing the skew and harmonic leakage inductances, the third term belongs to rotor slot leakage. Here, the slot opening effect is neglected in the slot leakage component. The last term is representing the end ring inductance. It can be seen from (3.2), (3.4) and (3.7), rotor resistance and leakage inductances are increasing as a result of skewing rotor bars and considering slot harmonics which is leading to major variation in performance characteristics. Magnetizing inductance is decreasing due to the skew effect, which is seen as a reduction in torque production due to the reduction in EMF of the rotor in the air-gap. To evaluate the torque profile, rotor leakage inductance needs to be referred to the stator side as well as rotor resistance by transformation ratio (K_{trans}) in (3.8).

$$K_{trans} = \frac{4m \left(N_s k_{wvs} \right)^2}{Q_r k_{sqvr}^2} \quad (3.8)$$

3.5. Optimal Design of IM Using Modified Equivalent Circuit Parameters for Spatial Harmonic Reduction

In this section, firstly, the output torque has been defined using the modified equivalent circuit parameters considering the effect of higher spatial harmonics in rotor bar resistance, and leakage and magnetizing inductances. Subsequently, IPSO has been used to optimize the rotor bar geometry and skew angle.

3.5.1 *Torque Considering Axial Field Variation and Slot Harmonics*

Output torque is derived with modified equivalent circuit parameters in section V using (3.1)-(3.7). And resultant torque is including fundamental and higher harmonic component considering slotting harmonics in both stator and rotor, as well as skew factor. The induced voltage is calculated using 3-D FEA and included in fundamental and higher harmonic torque calculation in (3.9) and (3.10) for no-load condition and loaded condition with corresponding slip value.

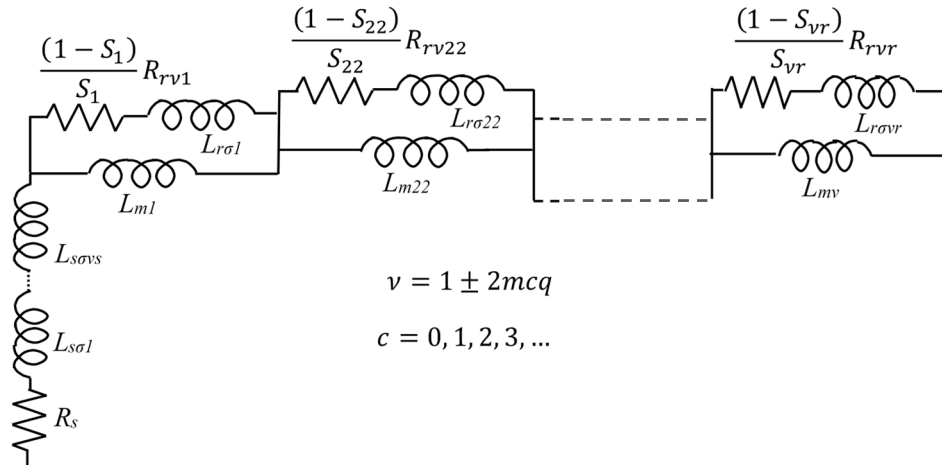


Figure. 3.7. Simplified equivalent circuit of IM considering stator and rotor slot harmonics.

$$T_{em, fun}(s) = \frac{pQ_r s R_r}{\omega_s R_r^2 + s^2 (\omega_s L_{rs})^2} V_{ind}^2 \quad (3.9)$$

$$T_{em, v}(s_v) = \frac{pQ_r^v s_v R_{rv}}{\omega_s R_{rv}^2 + (s_v \omega_s L_{rsv})^2} V_{ind}^2 \quad (3.10)$$

where s and $s_v=1-v(1-s)$ are the fundamental and harmonic slips, and V_{ind} is the root mean square (rms) value of the induced voltage in rotor bars.

3.5.2 Improved Particle Swarm Optimization towards Design Improvement

Torque ripple minimization approach using IPSO is applied to the modified equivalent circuit parameters including higher spatial harmonics to keep the torque production constant by reduction of spatial harmonics. IPSO as a popular heuristic optimization algorithm is selected owing to its easy implementation as well as high convergence when inertia and acceleration coefficients are selected accordingly [25], [26].

According to Fig. 3.8 the subscripts indicate the number of particles. r_p and r_g represent uniform random numbers between 0 and 1, which is generated repeatedly at each iteration. c_1 and c_2 normally are two positive constants, called the cognitive and social parameters, respectively, (in this IPSO model, time varying is considered as, c_1 start=1.5, c_1 end=2.5 and c_2 start=2.5, c_2 end=1.5). The inertia weight, w_i in IPSO algorithm should not be selected too large which might lead to premature convergence. It should not be too small because it can slow down the convergence excessively. The termination of the optimization is the number of generations chosen as 50. The selected IPSO converges to the optimal values of the fitness function over the defined iteration by updating the cognitive coefficients dynamically towards the best answers and subsequently, the pseudo velocity. Inputs to the optimization block are the initial rotor bar geometry, skew angle and the IPSO parameters. IPSO is applied at each time step to calculate the rotor bar geometry and skew angle as variables (X_1, \dots, X_{11}) in order to meet the constraints in an effort to minimize the torque ripples by keeping the volume and the average torque constant. Comparison of the

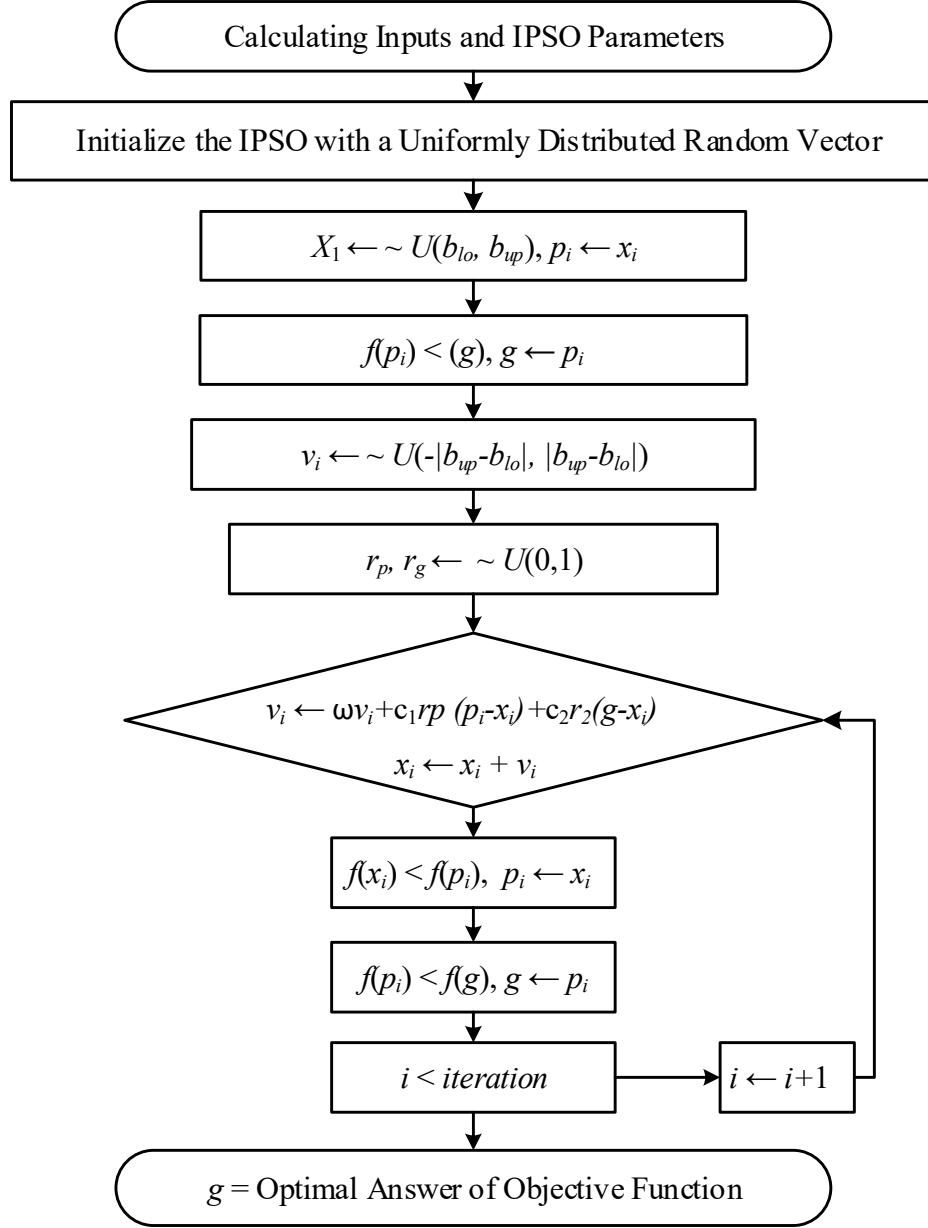


Figure. 3.8. IPSO algorithm to optimize the machine model.

best result among the entire swarm, the improved design variables are illustrated in Table 3 and Fig. 3.9. It is found that skewing rotor bars by 1.41 stator slot pitch skew angle is the best possible optimization output to improve the torque profile by the spatial harmonic reduction in the air-gap, and hence torque ripples drop. Furthermore, the same average torque is achieved with improved rotor bar geometry. Optimal rotor resistance and permeance factor have been calculated using rotor inductance formulation in the objective function. The initial and improved schematic rotor bar alongside matching skew angles is

shown in Fig. 3.9. Also, geometrical and rated parameters are compared for both designs in Table. 3.4. Calculated improved geometrical parameters through optimization are used to determine the improved characteristics in the air-gap represented in section 3.6.

TABLE 3. 3
IPSO PARAMETERS, BASE AND OPTIMAL VARIABLES

| IPSO Parameters | Values | Variables | Initial (mm) | Optimal(mm) |
|---------------------------|--------|-----------|--------------|-------------|
| Number of generations | 50 | X_1 | 1 | 1.41 |
| Number of populations | 30 | X_2 | 1 | 1 |
| Max inertia coefficient | 10 | X_3 | 0 | 0.001 |
| Min inertia coefficient | 0.001 | X_4 | 1 | 1 |
| Cognitive parameter start | 2.5 | X_5 | 5 | 4 |
| Cognitive parameter end | 1.5 | X_6 | 5 | 4 |
| Social parameter start | 1.5 | X_7 | 3.5 | 0.5 |
| Social parameter end | 2.5 | X_8 | 9 | 10 |
| Constriction factor | 0.7 | X_9 | 1.5 | 1.5 |
| Mutation | 0 | X_{10} | 4 | 5 |
| | | X_{11} | 2.5 | 1.5 |

TABLE 3. 4
COMPARISON OF ELECTRICAL PARAMETERS AND PERFORMANCE CHARACTERISTICS FOR
INITIAL AND IMPROVED DESIGN

| Parameters | Initial | Improved |
|-------------------|---------|----------|
| $R_s (\Omega)$ | 0.211 | 0.211 |
| $R_r (\Omega)$ | 0.510 | 0.551 |
| $X_{ls} (\Omega)$ | 0.620 | 0.643 |
| $X_{lr} (\Omega)$ | 0.914 | 0.760 |
| s | 0.025 | 0.011 |
| η | 87.23 | 88.38 |

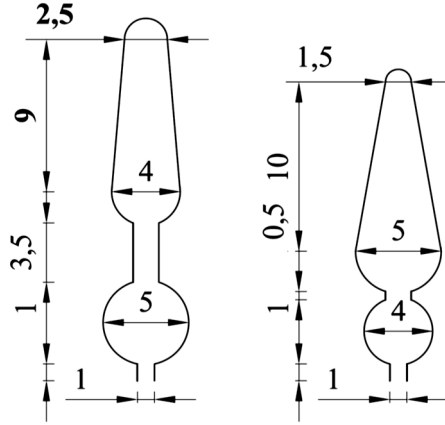


Figure. 3.9. Comparison Geometrical parameters for initial and improved design with respect to related skew angle.

3.6. Optimal Design of IM Using Modified Equivalent Circuit Parameters for Spatial Harmonic Reduction

The response of radial, circumferential and axial flux density in the middle of the air-gap under the no-load condition with a slip of 0.001 is provided for initial and improved designs in Figs. 3.10(a)-3.10(c). Subsequently, spectrum analysis of total air-gap flux density, which is vector quantity including radial, circumferential and axial components, is given in Fig. 3.11. Harmonic components of total flux are revealing the fundamental total magnetic flux density is improved under one per pole pair. Accordingly, average developed torque has been improved and higher frequency harmonic components are reduced especially the one belonging to the main rotor slot harmonic using $\nu = 1 \pm 2mcq$. Because of improved rotor slot size and skew angle, a major component of harmonic flux which is developing torque ripple is reduced and performance characteristics are enhanced.

Self-inductance, magnetizing inductance and developed torque for both designs are shown for the speed range of 0-1,789.2 rpm in Fig. 3.12. Accordingly, it can be seen that torque ripples are minimized as a result of space harmonic reduction in total magnetic flux density distribution in the air-gap for variable speed condition. It is worth mentioning that more reduction in the spatial harmonics is possible by defining different stator winding layout, which is the other major reason to produce space harmonics in IM. The continuation of this work by considering the winding layout and corresponding harmonics in the computational algorithm is set as one of the future works in the IM for further reduction in torque ripple and vibration.

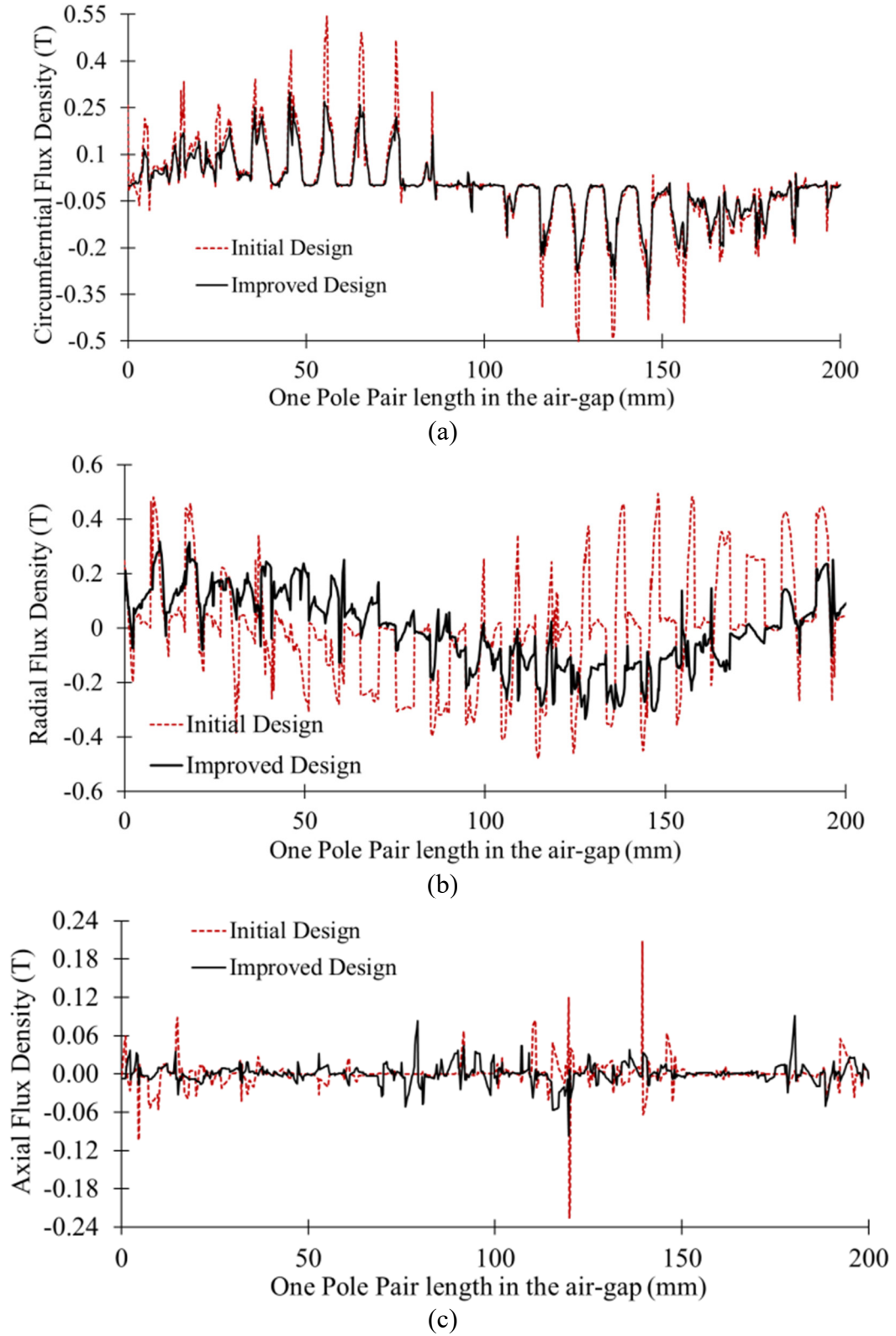


Figure. 3.10. Space distribution of magnetic flux density in the air-gap for the no-load operating condition for a single layer winding. (a) Radial. (b) Circumferential. (c) Axial in 3-D FEA.

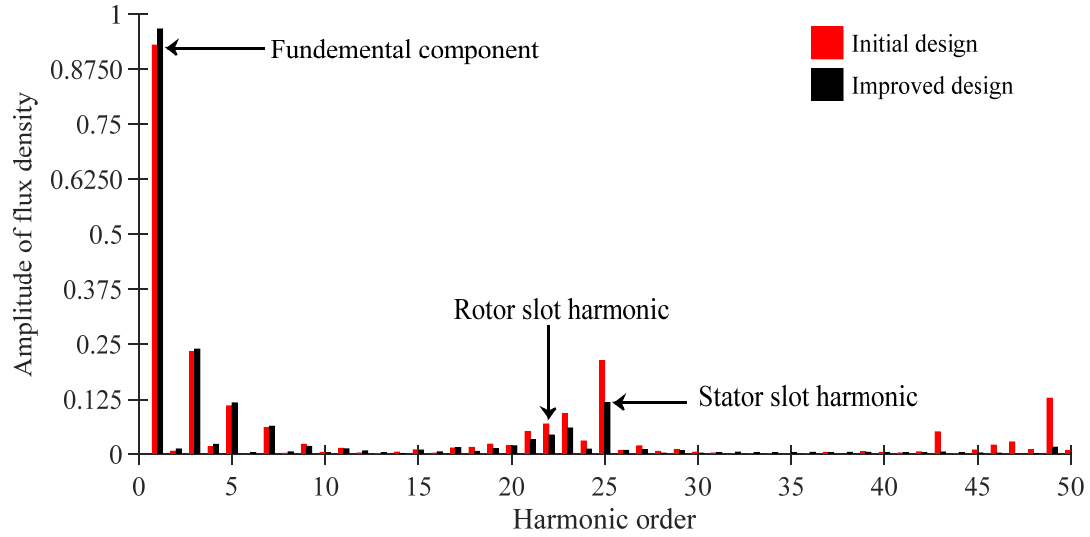


Figure. 3.11. Normalized harmonic components of total magnetic flux density in the air-gap for the no-load operating condition.

3.7. Conclusion

In this thesis, the necessity of 3-D FE analysis over 2-D FE analysis for skewed IM is highlighted by the inclusion of axial magnetic flux distribution in the air-gap. The significant difference in performance characteristics such as current and induced torque is presented. Equivalent circuit parameters are calculated using analytical design expressions including higher spatial harmonics due to slotting and skew effect in IM. A torque profile of a three-phase induction machine has been improved using the novel proposed hybrid analytical-3-D finite element algorithm incorporating IPSO. Comparison of improved design and initial designs in 3- D FEA shows a significant decrease in spatial harmonics due to optimal skewing and improved rotor bar geometry. Hence, the fundamental component of magnetic flux density is increased in the total air-gap flux density. As a result of the spatial harmonic reduction, and keeping the average torque constant in the optimization procedure, the torque production is enhanced in comparison to the conventional skewed rotor bar IMs.

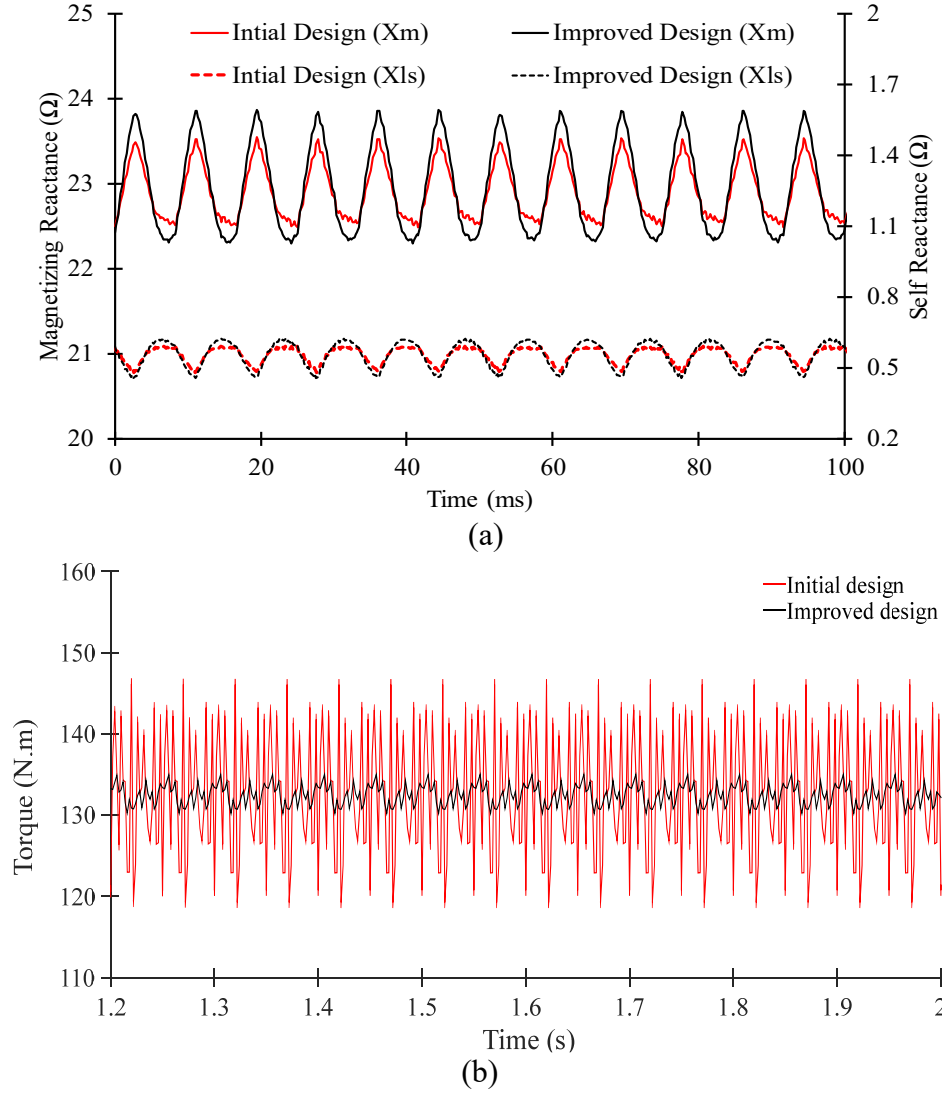


Figure. 3.12. Performance characteristics comparison of initial and improved designs of IM. (a) Self and magnetizing reactances under the no-load condition with a slip of 0.0061. (b) Electromagnetic torque production for 1,200 rpm.

3.8. References

- [1] E. K. Appiah, A. A. Jimoh, G. M Boungui, and J. L. Munda, "Effects of slot opening on the performance of a six- phase squirrel cage induction machine using finite element and field analysis," *AFRICON*, Pointe-Aux-Piments, pp. 1-5, 2013.
- [2] O. Keysan and H. B. Ertan, "Real-Time Speed and Position Estimation Using Rotor Slot Harmonics," *IEEE Trans. on Industrial Informatics*, vol. 9, no. 2, pp. 899-908, 2013.
- [3] K. Yamazaki, "Induction motor analysis considering both harmonics and end effects using combination of 2D and 3D finite element method," *IEEE Trans. on Energy Conversion*, vol. 14, no. 3, pp. 698-703, 1999.
- [4] M. Neto, J. R. Camacho, C. H. Salerno and B. P. Alvarenga, "Analysis of a three-phase induction machine including time and space harmonic effects: the a, b, c reference frame," *IEEE Trans. on Energy Conversion*, vol. 14, no. 1, pp. 80-85, 1999.

- [5] W. Lang, B. Xiaohua, D. Chong and L. Jiaqing, "Effects of Novel Skewed Rotor in Squirrel-Cage Induction Motor on Electromagnetic Force," *IEEE Transaction on Magnetism*, vol. 51, no. 11, pp. 1-4, 2015.
- [6] M. Ojaghi and S. Nasiri, "Modeling Eccentric Squirrel-Cage Induction Motors With Slotting Effect and Saturable Teeth Reluctances," *IEEE Transaction on Energy Conversion*, vol. 29, no. 3, pp. 619-627, 2014.
- [7] D.J. Kim, J.W. Jung, J.P. Hong, K.J. Kim, and C.J. Park, "A Study on the Design Process of Noise Reduction in Induction Motors," *IEEE Transaction on Magnetism*, vol. 48, no. 11, pp. 4638-4641, 2012.
- [8] Y. Kawase, T. Yamaguchi, Z. Tu, N. Toida, N. Minoshima, and K. Hashimoto, "Effects of Skew Angle of Rotor in Squirrel-Cage Induction Motor on Torque and Loss Characteristics," *IEEE Transaction on Magnetism*, vol. 45, no. 3, pp. 1700-1703, 2009.
- [9] L.D. Mori and T. Ishikawa, "Force and vibration analysis of induction motors," *IEEE Transaction on Magnetism*, vol. 41, no. 5, pp. 1948-1951, 2005.
- [10] M. Hadjami, A. Khezzar, M. E. K. Oumaamar, H. Razik, and A. Rezzoug, "Analytical model of cage induction machine dedicated to the study of axial non-uniformities," *IEEE Int. Symp. on Diagnostics for Electric Machines, Power Electronics & Drives*, Bologna, pp. 585-591, 2011.
- [11] S. L. Ho, W. N. Fu and H. C. Wong, "Estimation of stray losses of skewed rotor induction motors using coupled 2-D and 3-D time stepping finite element methods," *IEEE Transaction on Magnetism*, vol. 34, no. 5, pp. 3102-3105, 1998.
- [12] B. Heller and A. L. Jokl, "Losses in Squirrel-Cage Motors Due to Rotor Skew," *IEEE Transaction on Power Apparatus and Systems*, vol. PAS-90, no. 2, pp. 556-563, 1971.
- [13] K K. Boughrara, F. Dubas, and R. Ibtiouen, "2-D Analytical Prediction of Eddy Currents, Circuit Model Parameters, and Steady-State Performances in Solid Rotor Induction Motors," *IEEE Transaction on Magnetism*, vol. 50, no. 12, pp. 1-14, 2014.
- [14] D. Zhang, C. S. Park and C. S. Koh, "A New Optimal Design Method of Rotor Slot of Three-Phase Squirrel Cage Induction Motor for NEMA Class D Speed-Torque Characteristic Using Multi-Objective Optimization Algorithm," *IEEE Transaction on Magnetism*, vol. 48, no. 2, pp. 879-882, 2012.
- [15] Kyung-Won Jeon, Y. J. Kim, Seung-Ho Lee, Kwangdeok Kim, and S. Y. Jung, "Torque harmonic analysis of induction motor for electric vehicle propulsion," in *Proc. of IEEE Vehicle Power and Propulsion Conf. (VPPC)*, pp. 168-170, 2012.
- [16] X. Liang and Y. Luy, "Harmonic Analysis for Induction Motors," in *Proc. of IEEE Canadian Conf. on Elec. and Computer Engineering*, pp. 172-177, 2006.
- [17] J. L. Martinez, A. Belahcen and A. Arkkio, "3D permeance model of induction machines taking into account saturation effects and its connection with stator current and shaft speed spectra," *IET Electric Power Applications*, vol. 9, no. 1, pp. 20-29, 2015.
- [18] J. Bacher, F. Waldhart, and A. Muetze, "3-D FEM Calculation of Electromagnetic Properties of Single-Phase Induction Machines," *IEEE Transaction on Energy Conversion*, vol. 30, no. 1, pp. 142-149, 2015.
- [19] S. Williamson, T.J. Flack; and A.F. Volschenk, "Representation of Skew in Time-stepped Two-dimensional Finite-element Models of Electrical Machines," *IEEE Transaction on Industry Appl.*, vol. 31, pp. 1009-1015, 1995.

- [20] D. G. Dorrell, P. J. Holik and C. B. Rasmussen, "Analysis and Effects of Inter-Bar Current and Skew on a Long Skewed-Rotor Induction Motor for Pump Applications," *IEEE Transactions on Magnetics*, vol. 43, no. 6, pp. 2534-2536, 2007.
- [21] R. Carlson, C. A. da Silva, N. Sadowski, Y. Lefevre and M. Lajoie-Mazenc, "Analysis of the effect of inter-bar currents on the performance of polyphase cage-induction motors," *IEEE Transaction on Industry Applications*, vol. 39, no. 6, pp. 1674-1680, 2003.
- [22] A. Mollaeian, M. Mousavi, A. Balamurali, J. Tjong, and N. C. Kar, "Optimal Design of Skewed Rotor Induction Machine for Space Harmonic Reduction Considering z-Axis Magnetic Flux Density Variation," presented at the *IEEE Intermag Conference*, 2016.
- [23] K. Hafiz, G. Nanda and N. C. Kar, "Skin effect modeling of self-excited induction generator in wind power application," *Canadian Conference on Electrical and Computer Engineering*, Niagara Falls, ON, pp. 001587-001590, 2008.
- [24] A. Boglietti, A. Cavagnino, and M. Lazzari, "Computational Algorithms for Induction-Motor Equivalent Circuit Parameter Determination—Part I: Resistances and Leakage Reactances," *IEEE Transaction on Industrial Electronics*, vol. 58, no. 9, pp. 3723-3733, 2011.
- [25] Y. Del Valle, G. K. Venayagamoorthy, S. Mohagheghi, J.-C. Hernandez, and R. G. Harley, "Particle swarm optimization: Basic concepts, variants, and applications in power systems," *IEEE Transaction on Evolutionary Computation*, vol.12, pp. 171–195, 2008.
- [26] W. Yu and J.-S. Lai, "Ultra high efficiency bidirectional dc-dc converter with multi-frequency pulse width modulation," in *Proc. of IEEE Applied Power Electronics Conf. and Exposition*, 2008.

CHAPTER 4

3-D SUB-DOMAIN ANALYTICAL MODEL TO CALCULATE MAGNETIC FLUX DENSITY IN INDUCTION MACHINES WITH SEMI-CLOSED SLOTS UNDER NO-LOAD CONDITION

4.1. Introduction

In order to reduce loss and vibrations occurring due to axial magnetic flux variation in skewed electric machines, specially IMs, 3-D electromagnetic analysis is needed [1] and [2]. Numerical methods such as finite element analysis (FEA) is found to be an efficient option in machine design field due to its accuracy. However, 3-D FEA analysis is a time consuming and inefficient approach in design optimization process [3]. Hence, the necessity of an exact 3-D analytical solution is crucial in order to reduce research, time, and cost to obtain an optimal design for any industrial application.

The most favorite method by designers is the determination of Maxwell's equations using the analytical technique. It is fast and precise and is considered in optimization [3]-[4]. In [5], 2-D analytical solutions have been derived and proposed for non-skewed simple structures, solid and slotted rotor which mostly deals with eddy current calculation for rotor bars solving Maxwell's equations. However, the accuracy of electromagnetic performance analysis is compromised over the simplicity of developed differential equations, and axial asymmetrical effects are neglected. In this thesis, a novel method has been proposed to find a 3-D general solution for magnetic flux density considering z -axis variation unlike previous methods, and magnetic flux densities in the air-gap, stator, and rotor slots are calculated and compared to the ones with 3-D FEA.

4.2. 3-D Analytical Field Solution of IM

To solve Laplace and Poisson equations, the structure of three-phase IM with any combination of rotor and stator slots can be divided into five major subdomains shown in Fig. 1: stator slot, stator slot opening, air-gap, rotor slot, rotor slot opening. Rotor and stator subdomains include $2Q_r$ and $2Q_s$ number of sub-regions, where Q_s and Q_r represent stator

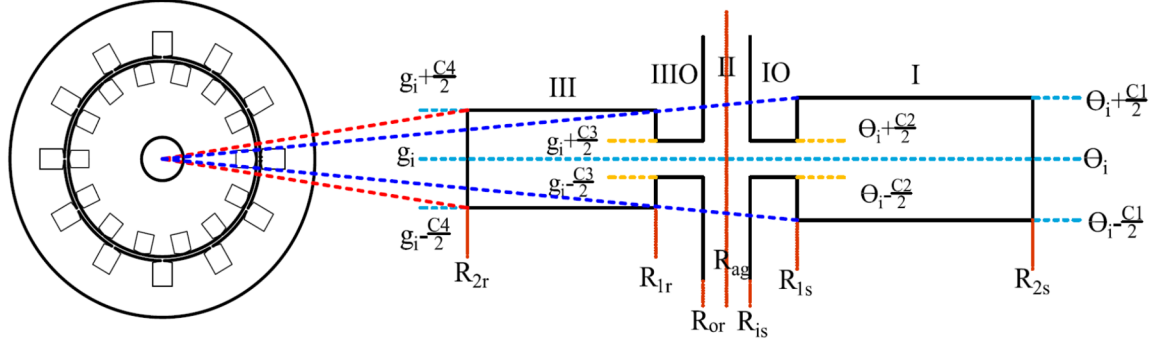


Figure. 4.1. Sketch of i^{th} stator semi-closed slot for a single layer concentric winding and i^{th} rotor cage bar with domain indexing bar for stator slot, stator slot opening, rotor slot and rotor slot opening and air-gap subdomains.

and rotor slot numbers. Therefore, in the case of a single layer windings the total number of sub-domains is $[2(Q_r + Q_s) + 1]$. The first step in solving Maxwell's equations is to make the following assumptions to simplify the analytical solution: a) supply is balanced sinusoidal currents; b) stator and rotor yokes are nonconductive and are infinite permeable materials; c) electric conductivity and magnetic permeability of rotor bars are constant; d) current density in stator slot is considered constant; and e) slots are considered rectangular in shape. Magnetic vector potential (MVP), defined as A , is used to calculate the magnetic flux density at no-load condition by considering the machine's geometrical configuration, as well as electrical and magnetic properties. As a consequence of axially uneven geometry, MVP has three components: A_ρ as radial, A_θ as circumferential and A_z as axial. Governing partial differential equations (PDEs) are expressed in each region as (4.1). Three terms in the right-hand side are expressed for the existence of the current source in air-gap, stator, and rotor slot openings, stator, and rotor slots accordingly.

$$\begin{aligned}
 (\nabla^2 A_m^i)_\rho &= \left(\frac{\partial^2 A_{m\rho}^i}{\partial \rho^2} + \frac{\partial^2 A_{m\rho}^i}{\rho^2 \partial \theta^2} + \frac{\partial^2 A_{m\rho}^i}{\partial z^2} + \frac{\partial A_{m\rho}^i}{\rho \partial \rho} - \frac{2 \partial A_{m\theta}^i}{\rho^2 \partial \theta} - \frac{A_{m\rho}^i}{\rho^2} \right) \hat{\rho} \\
 (\nabla^2 A_m^i)_\theta &= \left(\frac{\partial^2 A_{m\theta}^i}{\partial \rho^2} + \frac{\partial^2 A_{m\theta}^i}{\rho^2 \partial \theta^2} + \frac{\partial^2 A_{m\theta}^i}{\partial z^2} + \frac{\partial A_{m\theta}^i}{\rho \partial \rho} - \frac{2 \partial A_{m\rho}^i}{\rho^2 \partial \theta} - \frac{A_{m\theta}^i}{\rho^2} \right) \hat{\theta} = \begin{cases} 0 \\ -\mu_0 \vec{J}_s^i \\ -\mu_0 \mu_r \vec{J}_r^i \end{cases} \quad (4.1) \\
 (\nabla^2 A_m^i)_z &= \left(\frac{\partial^2 A_{mz}^i}{\partial \rho^2} + \frac{1}{\rho^2} \frac{\partial^2 A_{mz}^i}{\partial \theta^2} + \frac{\partial^2 A_{mz}^i}{\partial z^2} + \frac{1}{\rho} \frac{\partial A_{mz}^i}{\partial \rho} \right) \hat{z}
 \end{aligned}$$

where m is the index for sub-domains and i is the number of slots. Relationship between MVPs and magnetic flux densities in all directions in cylindrical coordinates is as (4.2):

$$\vec{B}_m^i = \left[\left(\frac{\partial A_{mz}^i}{\rho \partial \theta} - \frac{\partial A_{m\theta}^i}{\partial z} \right), \left(\frac{\partial A_{m\rho}^i}{\partial z} - \frac{\partial A_{mz}^i}{\partial \rho} \right), \frac{1}{\rho} \left(\frac{\partial \rho A_{m\theta}^i}{\partial \rho} - \frac{\partial A_{m\rho}^i}{\partial \theta} \right) \right] \quad (4.2)$$

Based on the above assumption and PDEs for each sub-domains two types of boundary and interface conditions are used for normal component of flux density (B_\perp) and the parallel component of the flux intensity (H_\parallel) of two adjacent materials.

$$(\vec{B}_m^i - \vec{B}_{m'}^i) \cdot \hat{n} = 0 \quad (4.3a)$$

$$\hat{n} \times (\vec{H}_m^i - \vec{H}_{m'}^i) = \vec{K}_m^i \quad (4.3b)$$

The current densities in stator and rotor slots under the no-load condition for single layer winding and skewed rotor bars are defined as in (4.4) and (4.5).

$$J_s^i = \left(\frac{N_s}{S_s} \right) W_l I_m \begin{bmatrix} 1 & e^{\frac{-2\pi i}{3}} & e^{\frac{2\pi i}{3}} \end{bmatrix} \quad (4.4)$$

where, N_s , S_s , W_l , and I_m are the number of conductors per phase, net area of wounded stator slot, winding layout and peak current in stator windings respectively. The current density in rotor bars follows the eddy current calculation and is derived for i^{th} slot using two polar components in tangential and axial directions due to the skew effect as shown in (4.5).

$$\vec{J}_r^i(\theta, z) = -i\omega_{rm} \mu_0 \mu_r \sigma \left(\left(A_{III,III}^i \right)_\theta \hat{\theta} + \left(A_{III,III}^i \right)_z \hat{k} \right) \quad (4.5)$$

where, ω_{rm} , μ_0 , μ_r , and σ are rotor speed, the permeability of the air gap and rotor bars and conductivity of rotor bars.

4.3. General 3-D Solution of Laplace's Equation

In II and IO regions which indicates air-gap and stator slot opening located between $R_{or} < \rho_{ag} < R_{is}$ and $R_{is} < \rho_{so} < R_{1s}$. The solution of radial, circumferential and axial components of MVPs without any external excitation is presented in (4.6)-(4.8) for a specific time instant.

$$(A_{II,IO})_{\rho} = \left[\sum_{m_1=1}^{\infty} \left(A_{1(II,IO)} \sinh(m_1 z) + B_{1(II,IO)} \cosh(m_1 z) \right) \left(C_{1(II,IO)} e^{\theta \sqrt{1-(m_1 \rho)^2}} + D_{2(II,IO)} e^{\theta \sqrt{1-(m_1 \rho)^2}} \right) \right] \quad (4.6)$$

$$(A_{II,IO})_{\theta} = \left[\sum_{m_2, k_2=1}^{\infty} \left(A_{2(II,IO)} \sinh(m_2 z) + B_{2(II,IO)} \cosh(m_2 z) \right) \left(\frac{\pi m_2^2 k_2^2 \rho Y_1(m_2 \rho)}{4} F_2 \left(\frac{1}{2}, \frac{3}{2}, 2; -\frac{m_2^2 \rho^2}{4} \right) - \frac{\pi m_2^2 J_1(m_2 \rho)}{4} G_{2,4}^{2,1} \left(\frac{m_2 \rho}{2}, \frac{1}{2} \middle| -\frac{1}{2}, \frac{1}{2}, -1, 0 \right) + C_{2(II,IO)} J_1(m_2 \rho) + D_{2(II,IO)} Y_1(m_2 \rho) \right) \right] \quad (4.7)$$

$$(A_{II,IO})_z = \left[\sum_{m_3=1}^{\infty} \left(A_{3(II,IO)} \sinh(m_3 \rho) + B_{3(II,IO)} \cosh(m_3 z) \right) \left(C_{3(II,IO)} \sin(m_3 \log(\rho)) + D_{3(II,IO)} \cos(m_3 \log(\rho)) \right) \right] \quad (4.8)$$

where, m_1 , m_2 , k_2 , and m_3 are positive orders of spatial harmonic in ρ , θ and z directions. $A_{1(II,IO)}$ - $A_{3(II,IO)}$, $B_{1(II,IO)}$ - $B_{3(II,IO)}$, $C_{1(II,IO)}$ - $C_{3(II,IO)}$ and $D_{1(II,IO)}$ - $D_{3(II,IO)}$ are integral coefficients. The number of integral constants is $[(m+k)Q_s]$ in case of stator slot opening. The air-gap region is treated as two layers and has $[(m+k)(Q_s+Q_r)]$ constants. J_1 and Y_1 are the first order of Bessel functions of first and second kinds. F_2 and $G_{2,4}^{2,1}$ are generalized hypergeometric and Meijer G -functions.

4.4. General 3-D Solution of Helmholtz's Equation

In III and IIIO regions which represent rotor slot and rotor slot opening with the magnetic property of $\mu_0\mu_r$, located between $R_{2r}<\rho_r<R_{1r}$ and $R_{1r}<\rho_{ro}<R_{or}$. The solution of radial, circumferential and axial components of MVPs with induced currents in rotor bars are derived in (4.9)- (4.11). Where, $A_{1(III, IIIO)}$ - $A_{3(III, IIIO)}$, $B_{1(III, IIIO)}$ - $B_{3(III, IIIO)}$, $C_{1(III, IIIO)}$ - $C_{3(III, IIIO)}$ and $D_{1(III, IIIO)}$ - $D_{3(III, IIIO)}$ are integral coefficients., J_i and Y_i are Bessel functions of first and second kinds and $\tan\gamma$ is the skew angle. No-load slip is considered in rotor speed calculation ω_{rm} as $(1-s) \omega_s$. The number of integral constants is $2mQ_r$ in the rotary region.

$$(A_{III, IIIO})_\rho = \left[\sum_{m_1=1}^{\infty} \left(A_{1(III, IIIO)} e^{\sqrt[3]{m_1^2 - i\omega_{rm}\mu_0\mu_r \tan(\gamma)}} + B_{1(III, IIIO)} e^{-\sqrt[3]{m_1^2 - i\omega_{rm}\mu_0\mu_r \tan(\gamma)}} \right) \left(\frac{C_{1(III, IIIO)} D_{\frac{m_1-i}{2m_1}}((i+1)\sqrt{m_1}\theta)}{2m_1} + D_{1(III, IIIO)} D_{\frac{m_1-i}{2m_1}}((i+1)\sqrt{m_1}\theta) \right) \right] \quad (4.9)$$

$$(A_{III, IIIO})_\theta = \left[\sum_{m_2, k_2=1}^{\infty} \left(A_{2(III, IIIO)} e^{\sqrt[3]{m_2^2 - i\omega_{rm}\mu_0\mu_r \tan(\gamma)}} + B_{2(III, IIIO)} e^{-\sqrt[3]{m_2^2 - i\omega_{rm}\mu_0\mu_r \tan(\gamma)}} \right) \left(\begin{aligned} &C_{2(III, IIIO)} \sin\left(\left(\sqrt{m_2^2 - 1}\right)\log(\rho)\right) \\ &+ D_{1(III, IIIO)} \cos\left(\left(\sqrt{m_2^2 - 1}\right)\log(\rho)\right) \\ &+ \frac{k_2^2}{m_2^2 - 1} \end{aligned} \right) \right] \quad (4.10)$$

$$(A_{III, IIIO})_z = \left[\sum_{m_3=1}^{\infty} \left(A_{3(III, IIIO)} J_{im_3} \left(-\sqrt[4]{-1} \sqrt{\omega_{rm}\mu_0\mu_r \tan(\gamma)\rho} \right) + B_{3(III, IIIO)} Y_{im_3} \left(-\sqrt[4]{-1} \sqrt{\omega_{rm}\mu_0\mu_r \tan(\gamma)\rho} \right) \right) \left(C_{3(III, IIIO)} e^{-m_3\theta} + D_{3(III, IIIO)} e^{-m_3\theta} \right) \right] \quad (4.11)$$

4.5. General 3-D Solution of Poisson's Equation

In region I which specifies stator slot region located between $R_{1s}<\rho_s<R_{2s}$, with a sinusoidal balanced current source, defined in (4.4), the solution of MVPs is presented in (4.12)- (4.14).

$$(A_I)_\rho = \left[\sum_{m_1=1}^{\infty} (A_{1(I)} \sinh(m_1 z) + B_{1(I)} \cosh(m_1 z)) \left(C_{1(I)} e^{\theta \sqrt{1-(m_1 \rho)^2}} + D_{1(I),IO} e^{\theta \sqrt{1-(m_1 \rho)^2}} \right) \right] \quad (4.12)$$

$$(A_I)_\theta = \left[\sum_{m_2, k_2=1}^{\infty} (A_{2(I)} \sinh(m_2 z) + B_{2(I)} \cosh(m_2 z)) \left(\frac{\pi m_2^2 k_2^2 \rho Y_1(m_2 \rho)}{4} F_2 \left(\frac{1}{2}, \frac{3}{2}, 2; -\frac{m_2^2 \rho^2}{4} \right) - \frac{\pi m_2^2 J_1(m_2 \rho)}{4} G_{2,4}^{2,1} \left(\frac{m_2 \rho}{2}, \frac{1}{2} \middle| \begin{matrix} 1, -1 \\ -\frac{1}{2}, \frac{1}{2}, -1, 0 \end{matrix} \right) + C_{2(I)} J_I(m_2 \rho) + D_{2(I)} Y_I(m_2 \rho) \right) \right] \quad (4.13)$$

$$(A_I)_z = \left[\mu_0 j_s^i R_{2s}^2 / 2 (\ln(\rho) - (\rho / \sqrt{2} R_{2s})^2) + \sum_{k_3=1}^{\infty} \left[A_{3(I)} \left(1 + (\rho / R_{2s})^{-2k_3 \pi / c_1} \right) \rho^{-k_3 \pi / c_1} \cos \left(k_3 \pi / c_1 \left(\theta - \theta_i + \frac{c_1}{2} \right) \right) + B_{3(I)} \right] \right] \hat{z} \quad (4.14)$$

where, θ_i , c_1 and j_s^i are the i^{th} slot position, slot opening, i^{th} slot current density. $A_{1(I)}$ - $A_{3(I)}$, $B_{1(I)}$ - $B_{3(I)}$, $C_{1(I)}$ - $C_{3(I)}$ and $D_{1(I)}$ - $D_{3(I)}$ are integral coefficients with $(m+k)Q_s$ elements.

4.6. Boundary and Interface Conditions

Integral coefficients of MVPs in given general solutions for all sub-domains are derived using boundary and interface conditions according to Figure. 4.1, considering axial component continuity of MVPs along the z -direction. Boundary conditions for stator slot and the interface between the stator slot opening and the air-gap are given in (4.15) - (4.18).

$$\left. \begin{aligned} \frac{\partial A_I^i}{\partial \theta} \bigg|_{\substack{\theta=\theta_i \pm C_1/2 \\ R_{1s} < \rho < R_{2s}}} &= 0 \\ \frac{\partial A_I^i}{\partial r} \bigg|_{\substack{\theta_i + C_4/2 < \theta < \theta_i - C_4/2 \\ \rho=R_{2s}}} &= 0 \end{aligned} \right\} \quad (4.15)$$

$$\left. \begin{aligned} \partial A_I^i / \partial r \Big|_{\substack{\theta_i - C_2/2 < \theta < \theta_i - C_1/2 \\ \rho = R_{1s}}} &= 0 \\ \partial A_I^i / \partial r \Big|_{\substack{\theta_i + C_1/2 < \theta < \theta_i + C_2/2 \\ \rho = R_{1s}}} &= 0 \end{aligned} \right\} \quad (4.16)$$

$$\left. \begin{aligned} \partial A_{IO}^i / \partial \theta \Big|_{\substack{\theta = \theta_i \pm C_2/2 \\ R_{is} < \rho < R_{1s}}} &= 0 \\ H_{IO}^i \Big|_{\substack{\theta > \theta_i - C_2/2 \\ \theta < \theta_i + C_2/2 \\ \rho = R_{1s}}} &= 0 \end{aligned} \right\} \quad (4.17)$$

$$\left. \begin{aligned} A_{IO}^i(R_{is}, \theta, z) &= A_{II}(R_{is}, \theta, z) \\ A_I^i(R_{is}, \theta, z) &= A_{IO}^i(R_{1s}, \theta, z) \\ H_{IO}^i(R_{is}, \theta, z) &= H_{II}(R_{is}, \theta, z) \\ H_I^i(R_{1s}, \theta, z) &= H_{IO}^i(R_{1s}, \theta, z) \end{aligned} \right\} \quad (4.18)$$

Fourier expansion similarly has been applied to the boundary and interface equations between rotor slot opening and air-gap, which are given in (4.19)-(4.22).

$$\left. \begin{aligned} \partial A_{III}^i / \partial \theta \Big|_{\substack{\theta = g_i \pm C_4/2 \\ R_{2r} < \rho < R_{1r}}} &= 0 \\ \partial A_{III}^i / \partial r \Big|_{\substack{g_i + C_4/2 < \theta < g_i - C_4/2 \\ \rho = R_{2s}}} &= 0 \end{aligned} \right\} \quad (4.19)$$

$$\left. \begin{aligned} \partial A_{III}^i / \partial r \Big|_{\substack{g_i + C_4/2 < \theta < g_i - C_4/2 \\ \rho = R_{1r}}} &= 0 \\ \partial A_{III}^i / \partial r \Big|_{\substack{g_i - C_3/2 < \theta < g_i - C_4/2 \\ \rho = R_{1r}}} &= 0 \end{aligned} \right\} \quad (4.20)$$

$$\left. \begin{aligned} \partial A_{III}^i / \partial \theta \Big|_{\substack{g_i = g_i \pm C_3/2 \\ R_{1r} \leq \rho \leq R_{or}}} &= 0 \\ H_{III}^i \Big|_{\substack{g_i > g_i - C_3/2 \\ g_i < g_i + C_3/2 \\ \rho = R_{or}}} &= 0 \end{aligned} \right\} \quad (4.21)$$

$$\left. \begin{aligned} A_{III O}^i(R_{lr}, \theta, z) &= A_{III}(R_{lr}, \theta, z) \\ A_{II}^i(R_{or}, \theta, z) &= A_{III O}^i(R_{or}, \theta, z) \\ H_{III O}^i(R_{lr}, \theta, z) &= H_{III}(R_{lr}, \theta, z) \\ H_{II}^i(R_{or}, \theta, z) &= H_{III O}^i(R_{or}, \theta, z) \end{aligned} \right\} \quad (4.22)$$

Magnetic flux density in the air gap, rotor, and stator slots are calculated using the proposed mathematical model for a single cage induction machine under the no-load condition with any pole-slot combinations. In addition to the flux variation, Maxwell stress tensor is applied to determine torque using the calculated magnetic flux density components in (4.23).

$$T = \left(\frac{L}{\mu_0} \right) \int_{\Gamma} \vec{r} \times \left((\vec{B} \cdot \hat{n}) \vec{B} ds - \frac{B^2 \vec{n}}{2} \right) d\Gamma \quad (4.23)$$

where L and B are the axial length of the machine and magnetic flux density in the air-gap, n is the normal unit vector, Γ is the integration path and r is the displacement vector from the rotor to the segment $d\Gamma$.

4.7. Validation of 3-D Sub-Domain Mathematical Model and 3-D Finite Element Analysis

1.

A case study is developed to validate the proposed 3-D sub-domain model with 3-D FEA using geometrical parameters of a 7.5 hp IM presented in the Table. 4.1. The stator has 128 conductors per phase and the wounded slot area is calculated by $c_1[(R_{2s})^2 - (R_{1s})^2]$. Angular rotor speed is calculated with a slip of 0.001 for no-load condition and the peak current is 20.9 A. According to the winding layout in (4.24) for three-phase under one pole, the current density is calculated using Fourier expansion for i^{th} stator slot.

$$W_l = \begin{bmatrix} 1 & 1 & 1 & 1 & 0 & 0 & 0 & 0 & 0 & 0 & 0 & 0 \\ 0 & 0 & 0 & 0 & 0 & 0 & 0 & 0 & 1 & 1 & 1 & 1 \\ 0 & 0 & 0 & 0 & -1 & -1 & -1 & -1 & 0 & 0 & 0 & 0 \end{bmatrix} \quad (4.24)$$

In order to increase the accuracy of magnetic flux density in five sub-domains, the transient analysis is performed using current source excitation. The total number of elements is chosen as 224,822 and time step size is 2×10^{-4} . The CPU time for 3-D FE model for an instant time is 70:21:41 and memory is 17 GB. CPU time in 3-D sub-domain model is 00:53:17 and memory used is 2.56 GB. In the calculation of the 3-D analytical solution, the number of spatial harmonic orders is chosen to be 40 for the slots and the air-gap domains.

For 3-D sub-domain model matrices and cells have been used to accelerate the computation time instead of loops. The main task in the model is to build the boundary condition matrix and the source vector using three-dimensional spatial harmonic orders. Comparing both approaches indeed depends on parameters such as the meshing density for the FEA and the programming capability as well as the number of harmonic orders for sub-domain model. However, the proposed analytical model is much faster compare to 3-D FEA.

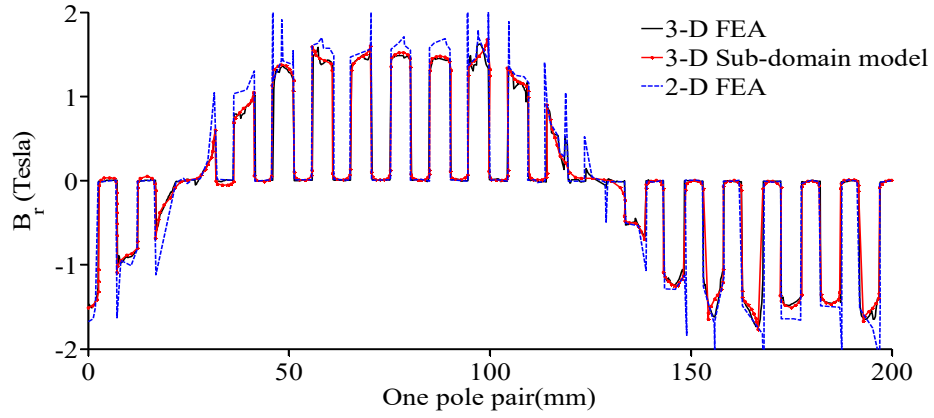
Figures 4.2a-4.2c shows the three-dimensional components of magnetic flux density in the middle of the air-gap on the cylindrical surface with the diameter of 133.7 mm and angular variation of 0 to 180°. It can be observed that the flux magnitudes calculated from two approaches are approximately close which validate the flux calculation using (4.6)-

TABLE 4. 1.
DESIGN DATA FOR FEA MODELING

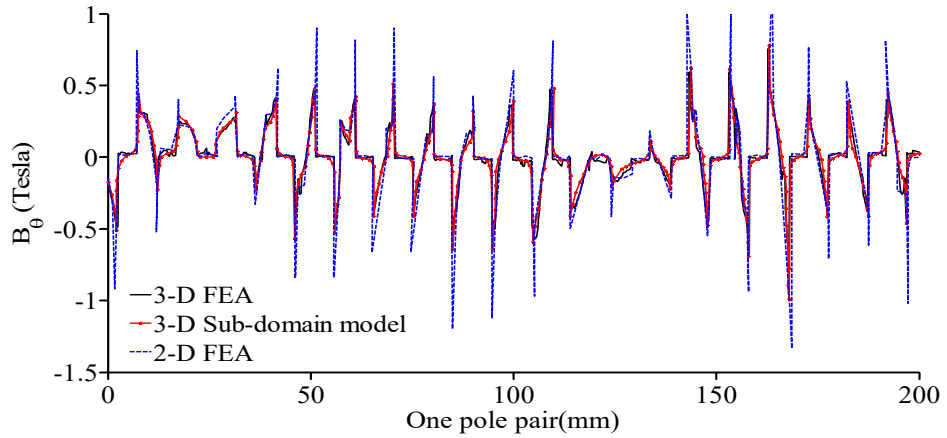
| Design Parameters for 3-D FEA and Proposed Model | | | | | |
|--|-------------|-------|---------------|------------|---------------|
| D_{so}/D_{si} | 220.137/134 | Q_s | 48 | L | 136.02 mm |
| D_{ro}/D_{ri} | 133.4/42 | Q_r | 42 | N_s | 120 |
| C_1 | 6.7 | C_2 | 3.8 | C_3 | 1.8 |
| C_4 | 2.8 | g_i | $i(2\pi)/Q_r$ | θ_i | $i(2\pi)/Q_s$ |

(4.8). Non-uniform distribution of flux density in the axial direction due to skewing and axial asymmetry is predicted using the novel 3-D proposed model as well as 3-D FEA.

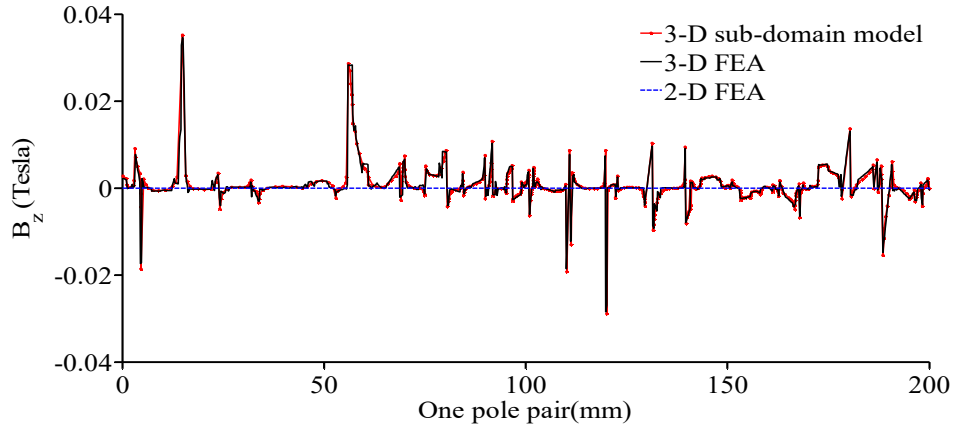
Figures 4.3(a)-4.3(f) shows the three-dimensional components of magnetic flux density in the stator and rotor slots. Magnetic flux components in rotor slot are solved using a cylindrical surface with a radius of 60.6 mm and angular variation of 0 to 2.8° for rotor slot opening, and cylindrical radius for stator slot is 75 mm and angular position varies from 0 to 6.7° . It can be observed that the flux magnitude calculated from 3-D sub-domain model follows 3-D FEA results, validating the flux calculation. Non-uniform distribution of flux density in the axial direction is as important as a circumferential component to be considered in the optimization process to reduce spatial harmonics.



(a)

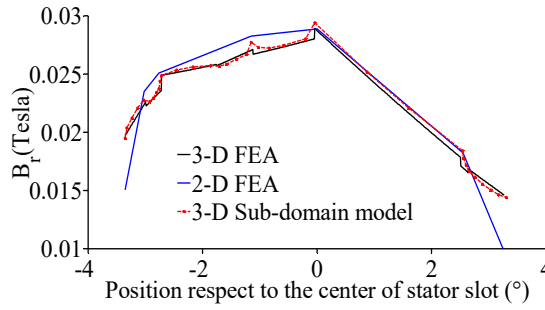


(b)

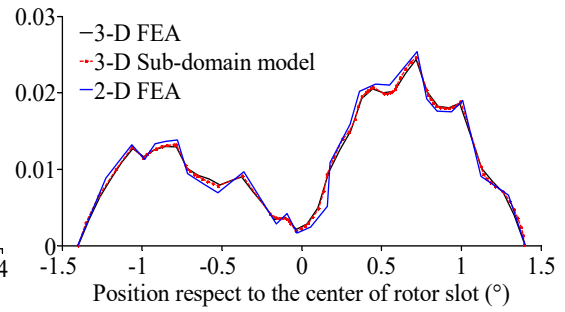


(c)

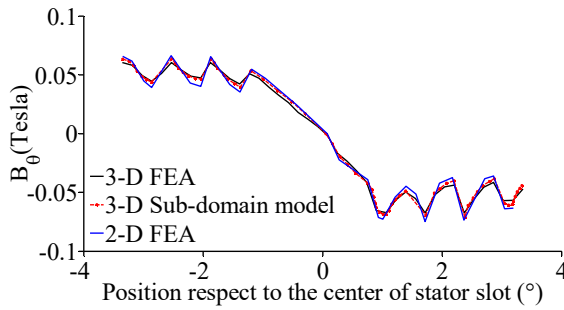
Figure. 4.2. 3-D FEA and analytical prediction of magnetic flux density with a slip of 0.001 in the middle of the air-gap. (a) Radial. (b) Circumferential. (c) Axial components.



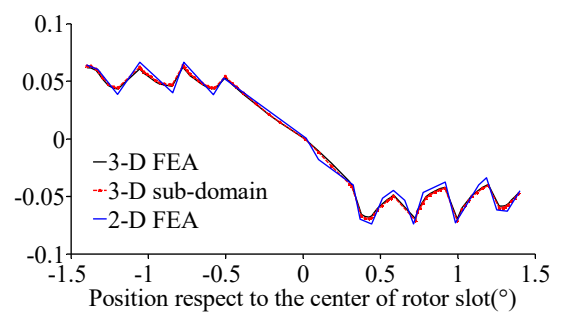
(a)



(b)



(c)



(d)

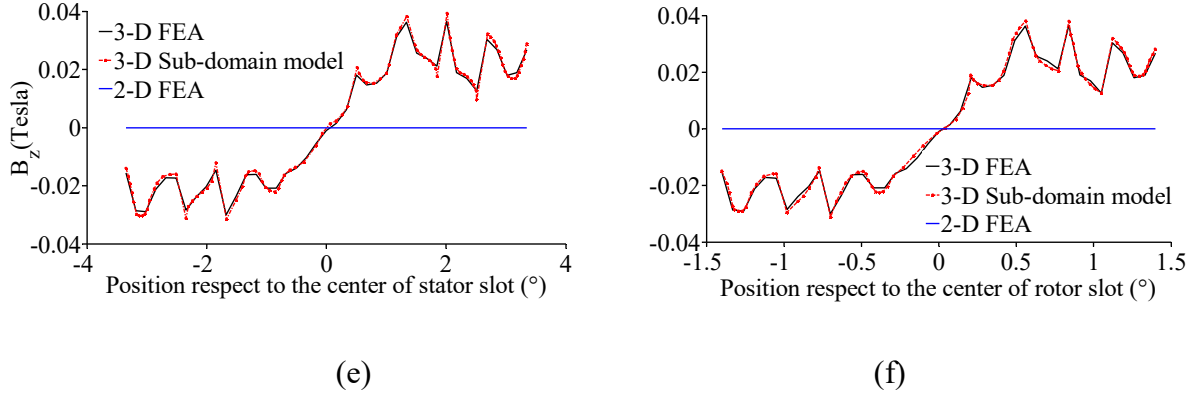


Figure. 4.3. 3-D FEA and analytical prediction of magnetic flux density with a slip of 0.001 in the rotor and stator slots. (a) Radial. (b) Circumferential. (c) axial components in the first stator slot. (d) Radial. (e) Circumferential. (f) Axial components in the first rotor slot.

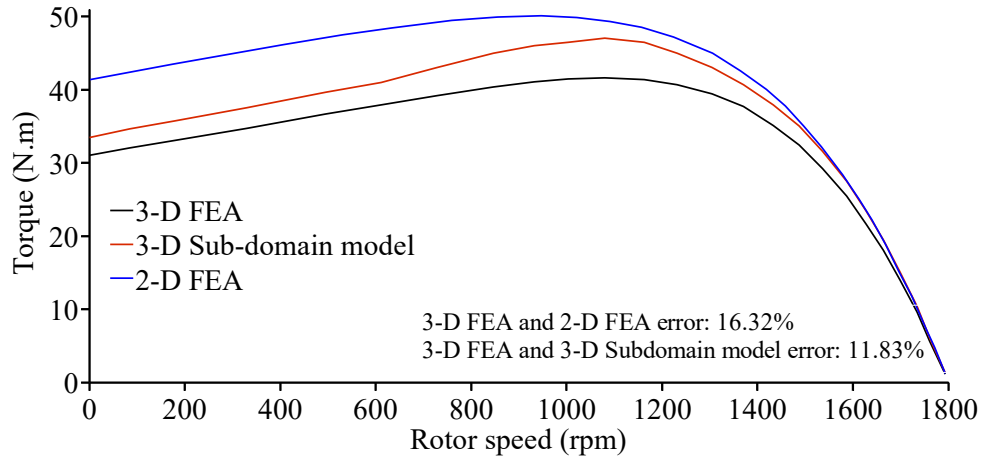


Figure. 4.4. Comparison of torque-speed characteristics with a slip of 0.05.

Figure 4.4. demonstrates the torque-speed characteristics of IM, which compares the results of 2-D FEA, 3-D FEA and proposed 3-D sub-domain model. Equivalent circuit parameters are calculated using (4.25) and (4.28). Comparison of error between 3-D FEA, sub-domain model and 2-D FEA demonstrates good agreement between both 3-D methods.

$$R_s = \frac{\rho N_s \left(L + K_{ew} \frac{\pi}{2p} (D_{is} + h_s) \right)}{A_{wire}} \quad (4.25)$$

$$R_r = \frac{4m_s}{Q_r} \left(\frac{N_s k_w}{k_{sq}} \right)^2 \left(\frac{LK_b}{A_b \cos^2 \gamma} + \frac{2\pi(D_A)K_r}{t_r(D_B) \sin^2(\pi p/Q_r)} \right) \quad (4.26)$$

$$[\Psi_a \quad \Psi_b \quad \Psi_c]^T = N_c W_l [\phi_1 \quad \phi_1 \quad \cdots \quad \phi_{Q_s}] \quad (4.27)$$

$$\phi_i = \frac{L}{S_s} \iiint_{\Omega} A_m^i r dr d\theta dz \quad (4.28)$$

where D_A and D_B are defined as $[D_{ir}+D_{or}]$ and $[D_{or}-D_{ir}]$. h_s , k_r , k_b , k_{ew} , k_w and k_{sq} slot height, end-ring and rotor bar resistance coefficients, end winding coefficient, winding and skewing factors. Ψ and ϕ represent phase flux and flux linkage which is used in inductance calculation.

4.8. Conclusion

In this thesis, 3-D sub-domain model has been proposed in cylindrical coordinates to predict magnetic flux density in the air-gap region, stator and rotor slots. The proposed mathematical model can be used for any slot- pole combination for a single cage induction machines. Slotting effect and tooth tips are considered for both stator and rotor domains. Computational speed and memory consumption are significantly less compared to the 3-D FEA analysis, which makes it more efficient for the optimization process in any industrial application. The proposed 3-D sub-domain model can be used in the optimization process in order to reduce spatial harmonics and decrease excessive losses and vibration due to axial asymmetry in induction machines.

4.9. References

- [1] G. Yanhui; T. Sanmaru, G. Urabe, H. Dozono; K. Muramatsu, K. Nagaki, Y. Kizaki, and T. Sakamoto, "Evaluation of stray load losses in cores and secondary conductors of induction motor using magnetic field analysis," *IEEE Transactions on Magnetics*, vol. 49, no. 5, pp.1965-1968, 2013.
- [2] A. Mollaeian, S. M. Sangdehi, A. Balamurali, G. Feng, J. Tjong, and N. C. Kar, "Reduction of space harmonics in induction machines incorporating rotor bar optimization through a coupled IPSO and 3-D FEA algorithm," *International Conference on Electrical Machines (ICEM)*, pp. 557-563, 2016.

- [3] S. Teymoori, A. Rahideh, H. Moayed-Jahromi, and M. Mardaneh, "2-D analytical magnetic field prediction for consequent-pole permanent magnet synchronous machines,"*IEEE Transactions on Magnetics*, vol. 52, 2016.
- [4] K. Boughrara, F. Dubas, and R. Ibtiouen, "2-D analytical prediction of eddy currents, circuit model parameters, and steady-state performances in solid rotor induction motors,"*IEEE Transactions on Magnetics*, 2014.
- [5] K. Boughrara, *et al.*, "Analytical analysis of cage rotor induction motors in healthy, defective, and broken bars conditions," *IEEE Transactions on Magnetics*, vol. 51, no. 2, pp. 1-17, 2015.

CHAPTER 5

SEMI-ANALYTICAL BASED MULTI-OBJECTIVE OPTIMIZATION OF ROTOR CONFIGURATION OF HIGH SPEED IM

5.1. Introduction

Induction machine is a promising candidate for electric vehicle (EV) application as compared with a permanent magnet synchronous machines (PMSMs) due to the absence of permanent magnets, mature control technology, and flux-weakening capability while keeping the required output performance characteristics for EVs [1-4]. Conventional design of IM focuses on the design at the rated frequency and operating condition. In addition, to calculate the rated electrical circuit parameters, the variation of the parameters needs to be evaluated from low to high speed to meet the propulsion system targets over a wide speed range. Starting performance requirement of IM for EV can be satisfied throughout wide speed range operation under variable load condition by adjusting necessary input current without the necessity for double cage bars [5] and [6]. Different rotor slot shape is investigated and optimized in the literature including short and wide shapes rotor and stator slots as well as narrow and long shapes depending on the trade-offs between efficiency, power factor, and maximum torque capability of IMs [7-9]. However, performance characterization did not take account of the variation of the IM parameters for various speed to study the full capability of the motor.

For EV application, the torque and power-speed profile is an important design criterion which is usually ignored due to consideration of the wide range of operating points making the design and optimization procedure computationally expensive [10-14]. PMSMs are naturally capable of satisfying suitable torque-speed characteristics for wide speed range in constant power region by adopting a proper design of the motor. However, wide speed operation of IM in the design process is a major drawback and challenge for EV application due to magnetizing and leakage inductances parameters which cannot guaranty the maximum power delivery at high speed range. Therefore, the maximum speed is limited compared to the PMSMs. Reduction of leakage inductances will extend the speed range, however, it will generate additional PWM losses leading to efficiency drop [15] and [16].

Therefore, structural optimization without sacrificing the maximum efficiency of the IM is a challenging task while extending the constant power speed ratio (CPSR) for EV applications.

The comparison of power-speed characteristics of IM and PMSM for EV application explains the need for design improvement of IM to enhance the performance beyond the base speed [17]. The speed range of IM is divided to three modes according to polar diagram and d- and q-axis currents and voltage limits for the rated frequency: (1) constant torque; (2) constant power; and (3) high speed range. Along with maximum torque per ampere capability in the low-speed region, a wide constant power region of 2-4 times of base speed is required for EV application [18-20].

The torque–speed characteristic of electrical machines depends on the control strategy and how the input current is being controlled, as well as motor design parameters. The desirable flux weakening region can be achieved using an optimal current control using vector control of IM [21], while the maximum torque control is usually implemented to obtain the maximum output torque of IM [22] and [23]. Besides improving the control methodology to obtain the maximum capability of the motor, speed range can be extended by increasing the air-gap length and slot opening as well as proper selection of stator-rotor slot combination [24-27]. However, selection of the optimal slot combination and structural parameters as a systematic procedure is still challenging due to non-linearity and complexity of relations between geometrical parameters and performance characteristics caused by equivalent circuit parameter variation under various frequencies from low to high. In [28] a six-phase pole-changing IM is proposed to extend the CPSR, and in [29] reconfigurable stator winding is proposed using decoupled controls for to obtained desired field weakening region. However, using a dual-inverter control strategy increases the system cost and complexity.

This chapter aims to minimize the leakage to magnetizing inductance ratio of IM in an effort to increase the maximum torque–speed capability of the motor through a novel semi-analytical and numerical procedure. The proposed novel design optimization procedure reduces the computational time for IM design development by: 1) Determining optimal pole and stator–/rotor–slot combination along with FEA considering local magnetic

saturation level; 2) Investigating IM torque-speed profile and circuit parameters determination considering saturation and supply frequency effect. Sensitivity analysis in conjunction with FEA is conducted to find the most effective variables affecting inductance ratio and capability of the motor. An objective function has been developed considering the inductance ratio to refine the IM rotor structure with genetic algorithm based optimization implemented in FEA. Finally, the experimentally determined inductance ratio and equivalent circuit parameters of the prototyped IM are compared and validated with the electromagnetic design from low to high speed.

5.2. Dimensioning of Inverter-fed Induction Motor Considering Magnetic Flux Level Boundaries

Design of IM for variable frequency applications is more complex than constant duty applications because of alternating load characteristics of the entire speed range. Also, the negative impact of the higher-order harmonics must be reflected at the design stage as it causes additional losses, overheating and increase of saturation level. A novel systematic design algorithm with a low computational cost is proposed including multi-physical steps: 1) Investigation of the most dominant structural parameters affecting the equivalent circuit parameters to minimize the inductance ratio with the proposed mathematical model. 2) Coarse optimization through the closed-loop analytical solution to reduce torque pulsation, and obtain target efficiency, maximum torque and speed along with FEA based parametric and sensitivity based approach. 3) Fine optimization of the design using a genetic algorithm in conjunction with FEA and proposed subdomain model for further minimization of inductance ratio without reduction of efficiency within a constant volume. The summary of the proposed systematic approach with a lower computational cost is demonstrated in Figure 5.1.

Design targets are scaled down because of the feasibility of the prototyping using continuous and overload rating of the laboratory traction motor, as presented in Table 5.1. Geometrical parameters of the baseline motor are calculated using the capability of the existing inverter and DC-link voltage in the lab, the optimal rms line-line voltage is found out to be 285 V. The rotor volume is calculated with the suitable tangential stress (σ_{Ftan}) in the air-gap to produce the desired torque (T).

$$T = 2\sigma_F \tan V_r \quad (5.1)$$

where the V_r is the rotor volume. The derived local current and flux density for the specified rotor volume is used to calculate the machine constant using (5.2).

$$C_{mec} = \frac{\pi^2}{2} K_{ws} \hat{A} \hat{B}_\delta \quad (5.2)$$

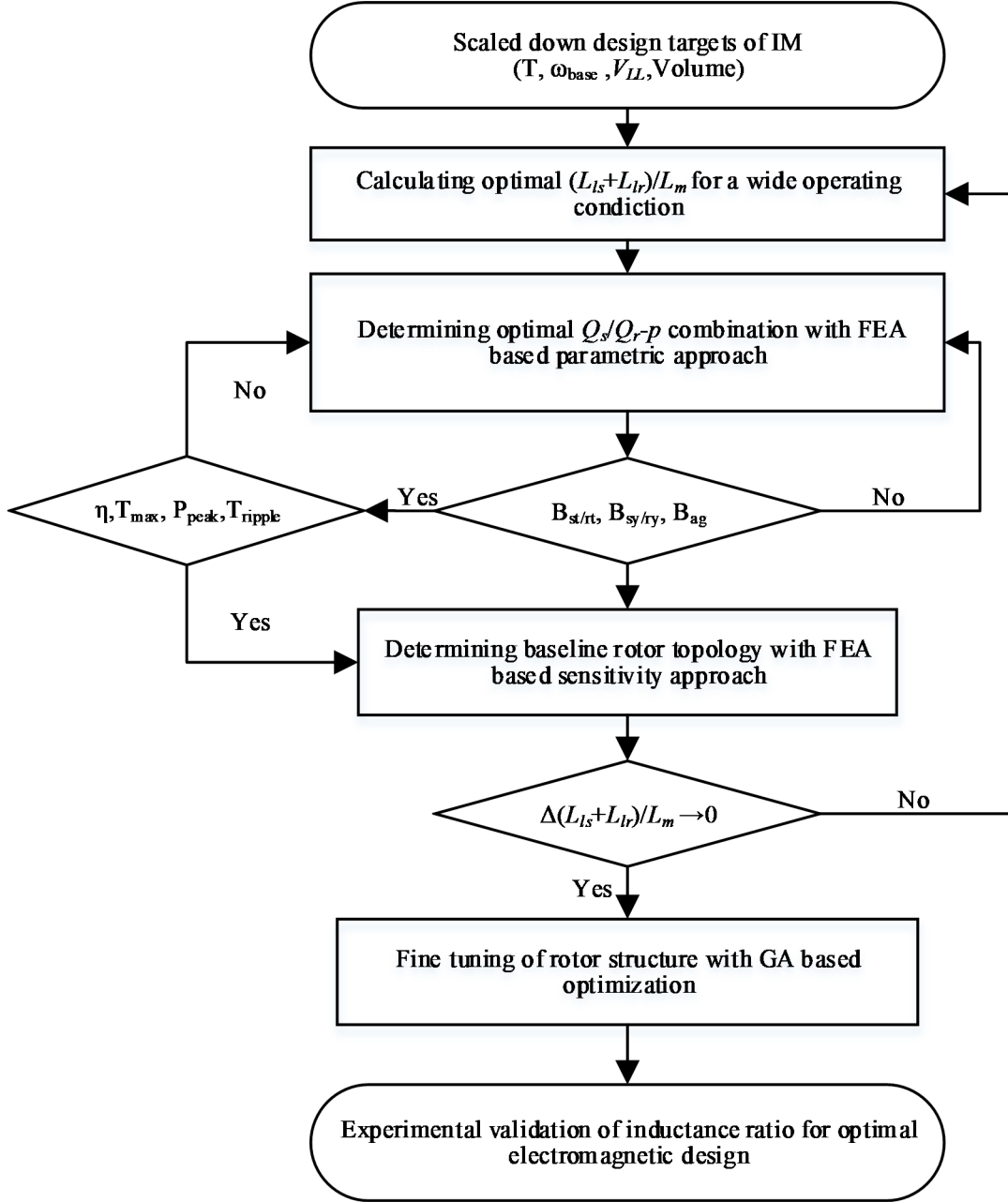


Figure. 5.1. Flowchart of the computationally efficient design procedure.

where K_w , A , and B_δ are the winding distribution factor, local current and flux densities. The power rating of the baseline IM calculated according to C_{mec} and presented in Table 5.2. For an in-depth analysis of the rotor structure and its influence on the performance characteristics, stator core is kept constant and prototyped in Figure 5.2. M230-35A is used to build the stator lamination with 36 trapezoidal and non-parallel slot and the thickness of 0.35 mm. Since base speed is chosen as 3,000 rpm, special attention is required while calculating the air-gap length to eliminate non-uniform magnetic pull [28].

$$L_{ag} = 0.001 + D_{or}/0.07 + v/400 \quad (5.3)$$

where L_{ag} is the air-gap length, D_{or} is outer rotor diameter and v is the peripheral speed of the rotor. Winding distribution factor is calculated for an integral winding. The number of turns per-phase is obtained with (5.4) using optimal phase voltage. To calculate the number of conductors per slot, the slot fill factor is limited to 70% to achieve higher power density.

$$Z_s = V_{ph} / \omega k_w l \tau_p \alpha_i B_{ag} \quad (5.4)$$

where ω , k_w , τ_p , α_i , and B_{ag} are rated frequency, winding factor, pole pitch, saturation factor, and the air-gap flux density. To calculate the rotor bar dimension, selection of the optimal number of stator and rotor slot combination is a crucial requirement to reduce parasitic

TABLE 5. 1.
POWER RATING AND GEOMETRICAL PARAMETERS OF THE BASELINE IM

| | |
|-----------------------------|-------|
| Peak Torque (N.m) | >94 |
| Continuous Torque (N.m) | 36 |
| Peak Power (kW) | 35 |
| Continuous Power (kW) | 11 |
| Base speed (rpm) | 3,000 |
| Weight of transmission (kg) | 37 |
| Motor weight (kg) | <22 |
| DC Link Voltage (V) | 400 |

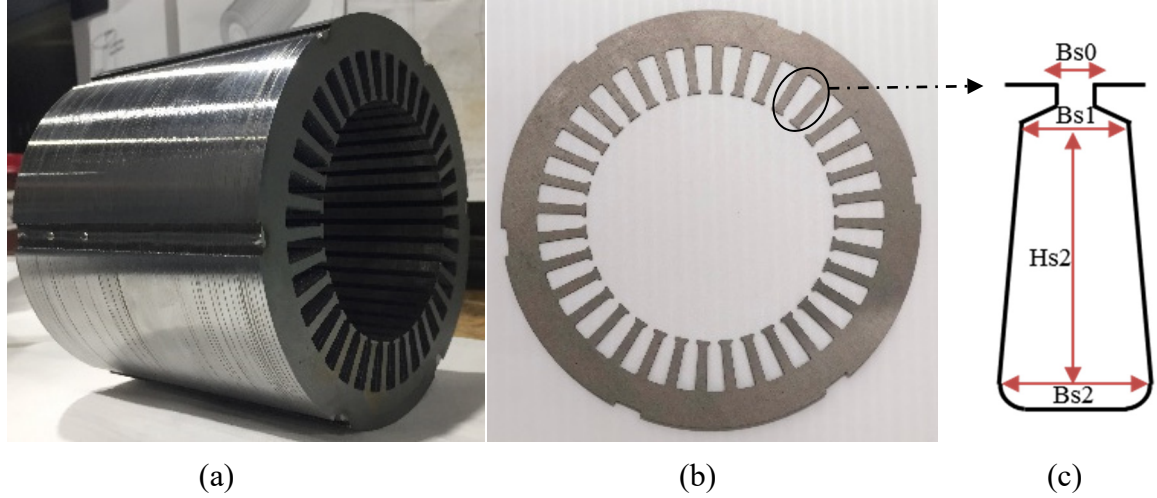


Figure. 5.2. Stator of developed high speed IM used for parametric based optimization. (a) Prototyped stator core with manufactured laminations. (b) Single lamination of the stator. (c) Schematic of the single slot.

torque, excessive losses, and radial electromagnetic forces. For this purpose, a parametric based optimization approach is followed to find the best combination within a specified design space. Figure 5.3 is presenting the sample results from the parametric approach combined with FEA used to search the optimal number of poles and stator-rotor slot combinations. Based on the parametric approach investigation, the optimal number of the stator-rotor slot/pole combination within a specified active volume is 36-42/4p, satisfying the constant torque and power region requirements of design targets.

TABLE 5. 2.
MAIN DIMENSION AND POWER RATING OF THE BASELINE IM USED IN PARAMETRIC
APPROACH BASED OPTIMIZATION

| | | | |
|-----------------|------------|------------------|-----------|
| D_{is}/D_{os} | 152/90.03 | V_{LL} | 285 V |
| D_{ir}/D_{or} | 89.3/28.57 | I_{LL} | 29 A |
| L_{core} | 131.5 mm | ω_{rated} | 3,000 rpm |

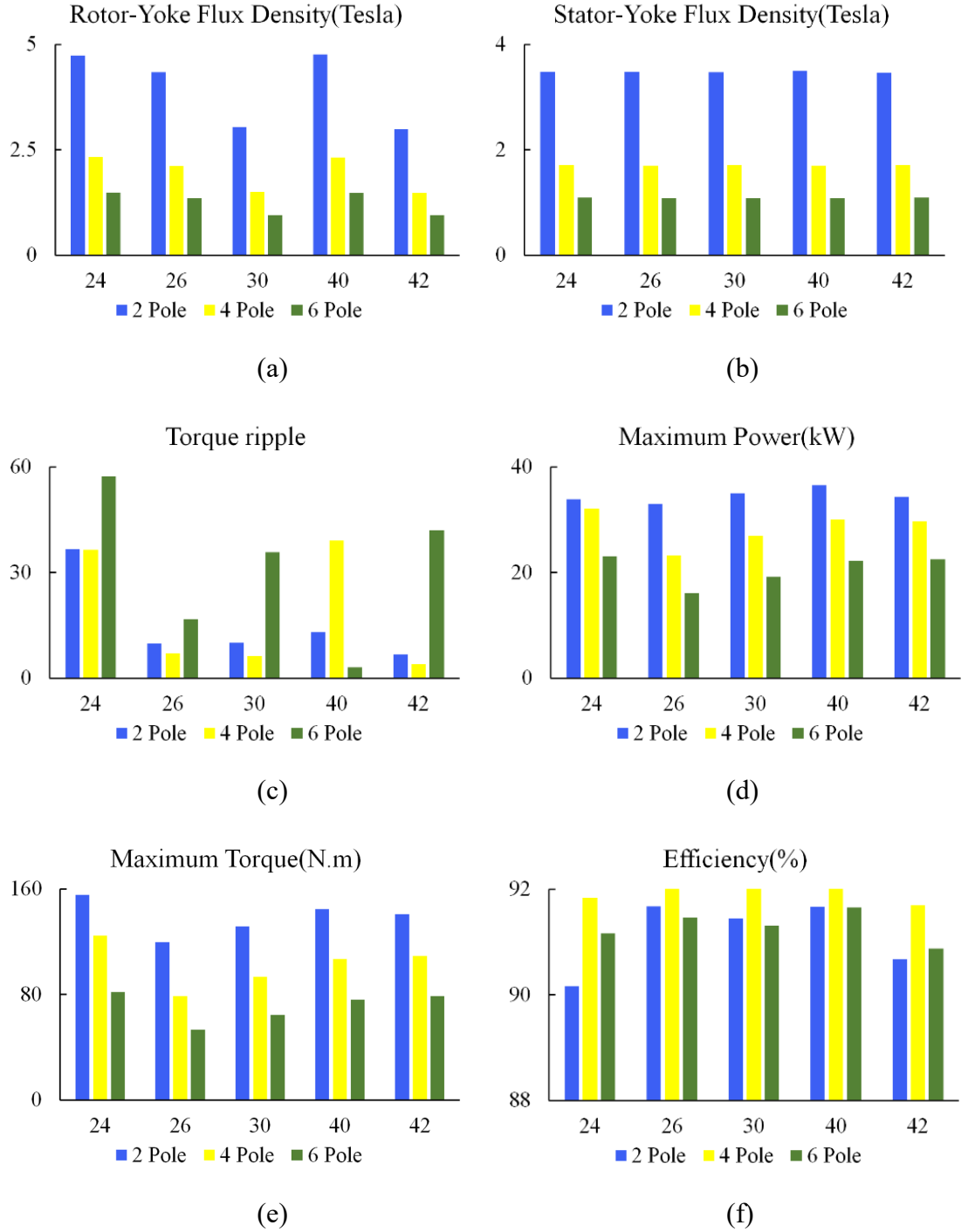


Figure. 5.3. Comparison of steady state output and magnetic characteristics at different stator-rotor slot-pole combinations. (a) Maximum torque. (b) Maximum power. (c) Efficiency. (d) Rotor yoke flux density. (e) Stator yoke flux density. (f) Torque ripple at the rated operating condition for corresponding full pitch double layer winding layout for each stator slot-rotor slot-pole combination.

5.3. Novel Mathematical Model of Inductance Ratio Incorporating Frequency and Core Saturation

The main reason for poor constant power region in IM is the absence of reluctance torque. Improving CPSR is possible if maximum torque capability increases which is directly affected by the circuit parameters of the motor. For this purpose, the inductance ratio is derived as a function of geometrical variables from the design perspective. Furthermore, maximum torque is derived as a function of the inductance ratio including frequency variations and the non-linearity of the parameters with voltage and current constraints.

5.1.1. *Inductance Ratio Expressing in Terms of Supply Frequency Variation and Core Saturation in Rotor Flux Oriented Control*

The flux distribution inside the machine varies by the supply frequency variation and iron saturation levels, which is reflected in the equivalent circuit parameters under different operating conditions. Determining the optimal inductance ratio within a current circle and voltage ellipse boundaries help to develop the optimal structural obtaining the wide operating range. The novel mathematical expression for inductance ratio is derived using field-oriented control assumptions to enhance the maximum capability of IM [25]. The steady state torque can be calculated using (5.5) considering iron saturation and current limit as (5.6).

$$T_{em} = \frac{3}{2} \frac{p}{2} \frac{L_m^2(i_{ds})}{L_r(i_{ds})} i_{ds} \sqrt{i_m^2 - i_{ds}^2} \quad (5.5)$$

$$i_{ds}^2 + i_{qs}^2 \leq i_m^2 \quad (5.6)$$

where i_m is the maximum current. Rewriting (5.5) the general factor depending on the inductances of the machine is obtained to maximize the torque using (5.7).

$$T_{em} = \frac{3}{2} \frac{p}{2} \frac{L_m(i_{ds})}{\left(1 + \frac{L_{lr}(i_{ds})}{L_m(i_{ds})}\right)} i_{ds} \sqrt{i_m^2 - i_{ds}^2} \quad (5.7)$$

Maximum torque occurs when $L_{lr}(i_{ds})/L_m(i_{ds})$ is minimum without considering stator leakage inductance which is usually considered in the previous studies and therefore the rotor configuration has not been selected precisely. For this purpose, a simplified methodology has been proposed for inverter-fed IM in the synchronous rotating frame, to obtain leakage and magnetizing inductances under variable flux with (5.8)-(5.13).

$$L_m(i_{ds}) = \frac{1}{i_{ds}^e} \left(\frac{(R_s i_{ds}^e - V_{ds}^e)^2}{(\omega_e V_{qs}^e - \sigma \omega_e^2 L_s(i_{ds}) i_{ds}^e)} + \frac{V_{qs}^e}{\omega_e} \right) - L_{ls}(i_{ds}) \quad (5.8)$$

where $\sigma L_s(i_{ds}) = L_{ls}(i_{ds}) + L_{lr}(i_{ds})$ and $L_{ls}(i_{ds}) = k L_{lr}(i_{ds})$. Equation (5.9) is used to eliminate $L_{ls}(i_{ds})$ in (5.7).

$$\sigma L_{ls}(i_{ds}) = (k+1) L_{lr}(i_{ds}) \quad (5.9)$$

$$\sigma = 1 - \left(\frac{L_m^2(i_{ds})}{L_s(i_{ds}) L_r(i_{ds})} \right) \quad (5.10)$$

where k is the positive factor which can be determined based on the class of the developed IM (class A or B). Rewriting and arranging (5.8) and replacing (5.9) and (5.10), a quadratic equation is obtained to calculate rotor leakage inductance which is a function of direct axis current and supply frequency in (5.13).

$$A_1 L_{lr}^2(i_{ds}) + A_2 L_{lr}(i_{ds}) + A_3 = 0 \quad (5.11)$$

where A_1 , A_2 , A_3 , and $\beta = L_{lr}/L_m$ are defined as follow:

$$A_1 = -\omega_e^2 i_{ds} \{1 + i_{ds} k \beta [k + (1/(1 + \beta))]\} \quad (5.12a)$$

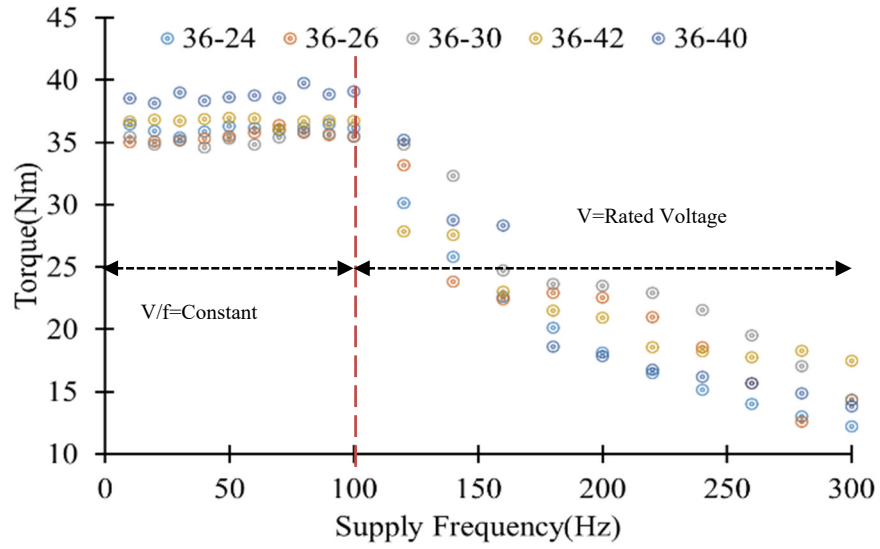
$$A_2 = 2 \omega_e i_{ds} v_{qs} [k + (1/(1 + \beta))] \quad (5.12b)$$

$$A_3 = -(R_s i_{ds} - v_{ds})^2 - v_{qs}^2 \quad (5.12c)$$

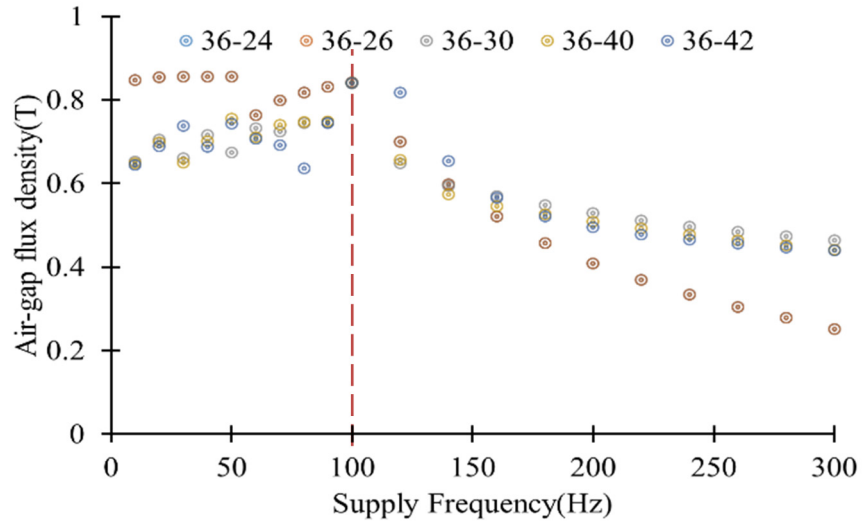
$$L_{lr}(i_{ds}) = \frac{-A_2 \pm \sqrt{A_2^2 - 4A_1 A_3}}{2A_1} \quad (5.13)$$

Figures 5.4 and 5.5 represents the behavior of IM parameter and their impact on the torque-speed profile for five selected case studies. These investigation results are used to find the optimal rotor bar dimensions and shaft diameter in order to meet the optimal value of the

inductance ratio obtained in this section. The defined inductance ratio has a significant impact on the IM performance. The slot combination of 36-42 meets the design targets with a satisfactory continuous and peak output characteristics compare to the other combinations [22-24].



(a)



(b)

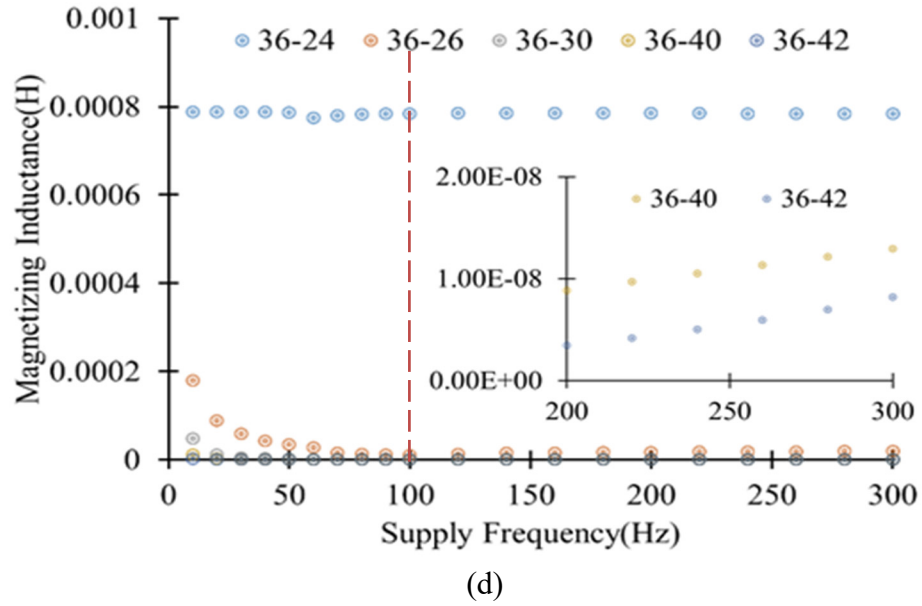
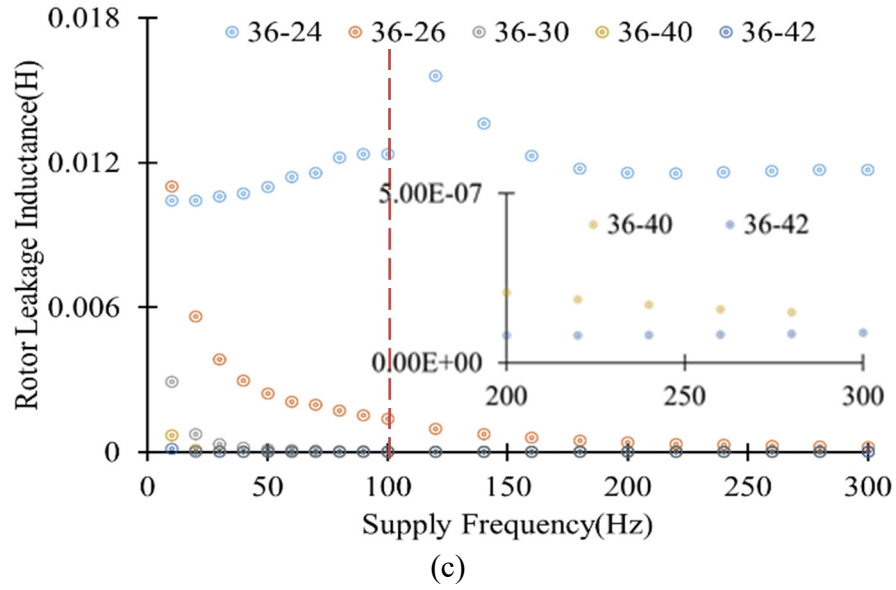


Figure. 5.4. Impact of IM parameters on the torque-speed profile considering saturation effect for a wide speed range. (a) Torque-speed profile. (b) air-gap flux density. (c) rotor leakage inductance. (d) magnetizing inductance variation for the various operating condition for the same voltage and frequency variations.

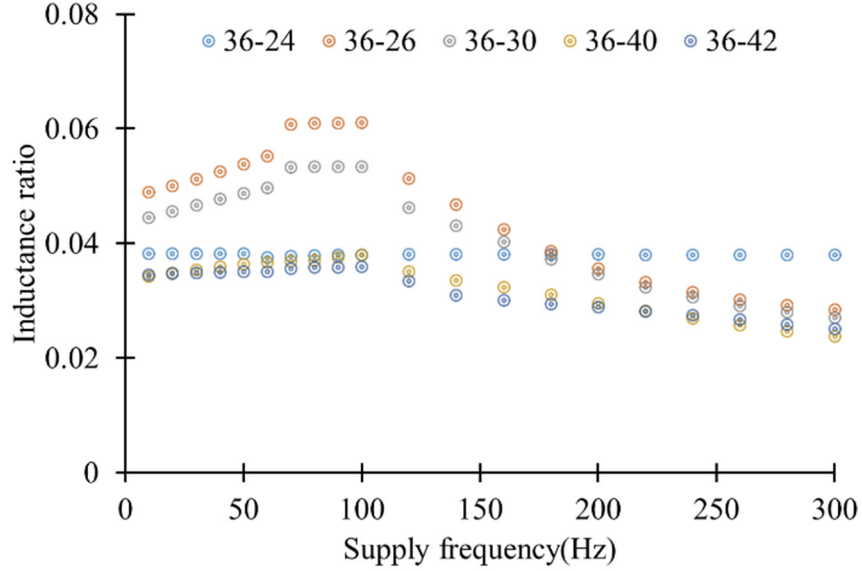


Figure. 5.5. Inductance ratio for different slot combination for a wide speed range considering saturation and supply frequency effect.

5.1.2. Inductance Ratio Expressing in Terms Of Supply Frequency and Core Saturation Using Structural Design Variables

The magnetizing inductance of IM for a three-phase winding can be determined using the peak value of the air-gap flux density over a one pole surface of the motor which leads to (5.14).

$$L_m = \alpha_i \frac{3D_{ag}}{2p^2 \delta_{ef}} \mu_0 l' (k_{wsf} N_s)^2 \quad (5.14)$$

where α_i is the saturation factor. D_{ag} , δ_{ef} , l' , $k_{wsf} N_s$ are air-gap diameter, length, stack length and the effective turns of winding. The magnetizing inductance depends on the voltage, torque, and iron saturation level. The stator and rotor leakage inductances are the sums of different components and they can be calculated from structural dimensions using (5.15a) and (5.15b).

$$L_{ls} = \left[\left(\left(1 - k_{sqsv}^2 \right) / k_{sqsv}^2 \right) + \Delta \left(\sum_{\substack{v=-\infty \\ v \neq 1}}^{v=\infty} (k_{wsv} / v k_{wsf})^2 \right) \right] L_m + \left(\frac{12}{Q_s} \right) \mu_0 l' N_s^2 \lambda_s + \frac{2 N_s^2 \mu_0 l_{ew} \lambda_{ew}}{p} \quad (5.15a)$$

$$L_{lr} = \left(\left(1 - k_{sqrv}^2 \right) / k_{sqrv}^2 \right) L_m + \left(\frac{(p\pi/Q_r)^2}{k_{sqrv}^2 \sin^2(p\pi/Q_r)} \right) + \mu_0 l' (\lambda_{or} + K_L \lambda_r) + \mu_0 \gamma \frac{\pi Q_r D'_r}{12 p^3} - 1 \quad (5.15b)$$

where k_{sqv} , k_{ws} , Q_s , Q_r , λ_s/r , λ_{ew} , λ_{or} , and γ are stator and rotor skew factor, slot numbers and slot, end-winding, slot opening permeance factors and correction factor. Δ is the damping factor for the cage winding. Aforementioned equations take into account higher order of harmonics as well as the iron saturation. The lower inductance ratio represents the enhanced performance characteristics of IM for a wide operating range. Therefore, the inductance ratio is derived using (5.14), (5.15a) and (5.15b) depending on the structural design variables.

$$\frac{L_\sigma}{L_m} = \left(\frac{k_{sqsv} - k_{sqrv}}{k_{sqsv} k_{sqrv}} \right)^2 + \Delta \sum_{\substack{v=-\infty \\ v \neq 1}}^{v=\infty} \left(\frac{k_{wsv}}{v k_{wsf}} \right)^2 + \frac{\delta_{ef} (A + B + C + D)}{\alpha_i l' D_{ag} (k_{wsf} N_s)^2} \quad (5.16)$$

where

$$\begin{cases} A = \frac{8 l' \lambda_s (N_s)^2 p^2}{Q_s} \\ B = \frac{2 p (p\pi/Q_r)^2}{3 \mu_0 k_{sqrv}^2 \sin^2(p\pi/Q_r)} \end{cases} \quad (5.17a)$$

$$C = \frac{2 l' p^2 (\lambda_{or} + K_L \lambda_r) + 4 l_{ew} \lambda_{ew} p}{3} \quad (5.17b)$$

$$D = \frac{\pi \mu_0 l' \gamma Q_r D'_r - 12 p^3}{18 p \mu_0 l'} \quad (5.17c)$$

Inductance ratio depends on the considerable number of dependent and non-dependent parameters which makes the computational procedure significantly expensive. This chapter aims to reduce the number of design variables to improve the efficiency of development. Hence, two individual approaches are followed incorporated in FEA: a) parametric which is implemented in the previous section, b) sensitivity approaches to determine the most effective parameters on the inductance ratio.

5.4. Structural Variable Reduction through Proposed Sensitivity Approach Coupled with FE Analysis

In this section, the tolerances of the rotor slot geometrical parameters as an inevitable factor in a mass production and optimization process are calculated and analyzed on maximum torque capability of the baseline IM proved by (5.5) and (5.17) using sensitivity approach. Furthermore, the effect of these parameters is presented on inductance ratio, maximum torque and efficiency on various sub-domain of IM as shown in Figure 5.7.

5.4.1. Sensitivity Analysis Formulation

The sensitivity of a variable Y with respect to β is the partial derivative of Y with respect to β as (5.18)

$$\delta_{Y,\beta} = \frac{\partial Y}{\partial \beta} \frac{\beta}{Y} \quad (5.18)$$

where Y can be electrical, magnetic or mechanical parameters. β and δ are geometrical parameters and normalized sensitivity of variable Y . The sensitivity factor of circuit parameters of the motor is calculated with respect to the structural parameter tolerances using (5.18)-(5.25). The sensitivity factor of T_{max} , with respect to different circuit parameters of the motor, is calculated using (5.5). The sensitivity factor of CPSR factor, with respect to different circuit parameters of the motor, is calculated using (5.8) and (5.13).

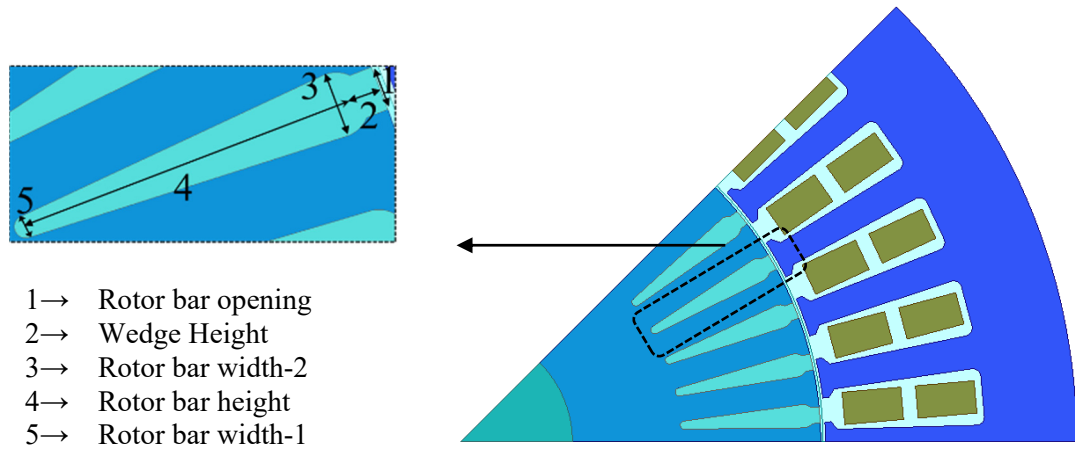


Figure. 5.6. Description of the investigated induction machine structural design variables for sensitivity analysis based optimization.

5.4.2. *Proposed Sensitivity Analysis Approach towards Investigation of Structural Parameter on the Operation of IM*

Rotor resistance is derived considering the nominal value of developed IM design and geometrical tolerances to investigate the effect on the maximum torque capability of machine, efficiency and inductance ratios. The final deviation of rotor resistance of a sample from the reference machine is an offset term as (5.25):

$$R_{r,dc}^{Bl} = (R_{bar} + R_{ring}) \frac{4m_s(Z_s k_p)^2}{N_r} \quad (5.19)$$

$$R_{r,dc}^{samp} = R_{r,dc}^{Bl} + \Delta R_{r,dc} \quad (5.20)$$

At high slip frequencies:

$$K_{R_r}^{Bl} = \frac{R_{r,ac}^{Bl}}{R_{r,dc}^{Bl}} = \zeta \frac{(\sinh 2\zeta + \sin 2\zeta)}{(\cosh 2\zeta - \cos 2\zeta)} \quad (5.21)$$

$$\zeta = \frac{h_r}{\delta_{Al}} = h_r \sqrt{\frac{\omega_{slip} \mu_0 \sigma h_r}{2b_r}} \quad (5.22)$$

$$K_{R_r}^{samp} = K_{R_r}^{Bl} + \Delta K_{R_r} \quad (5.23)$$

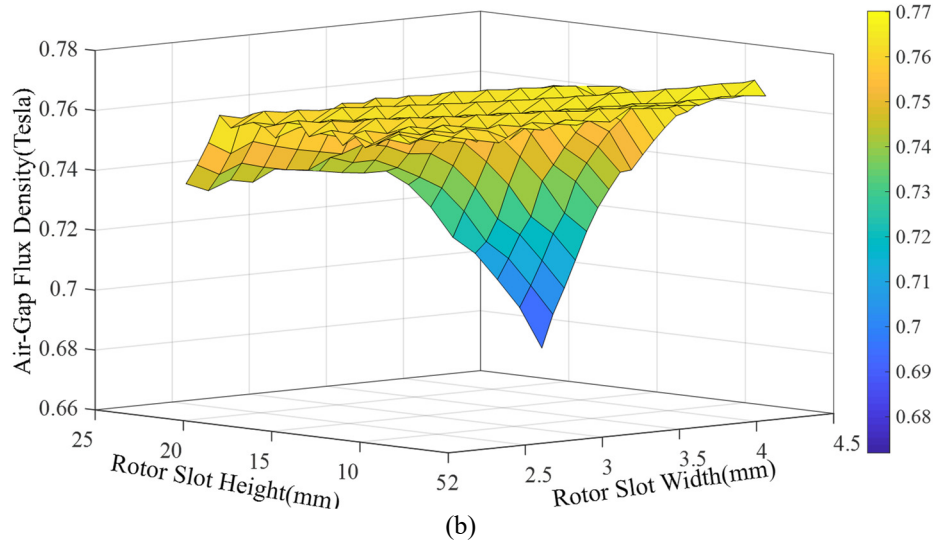
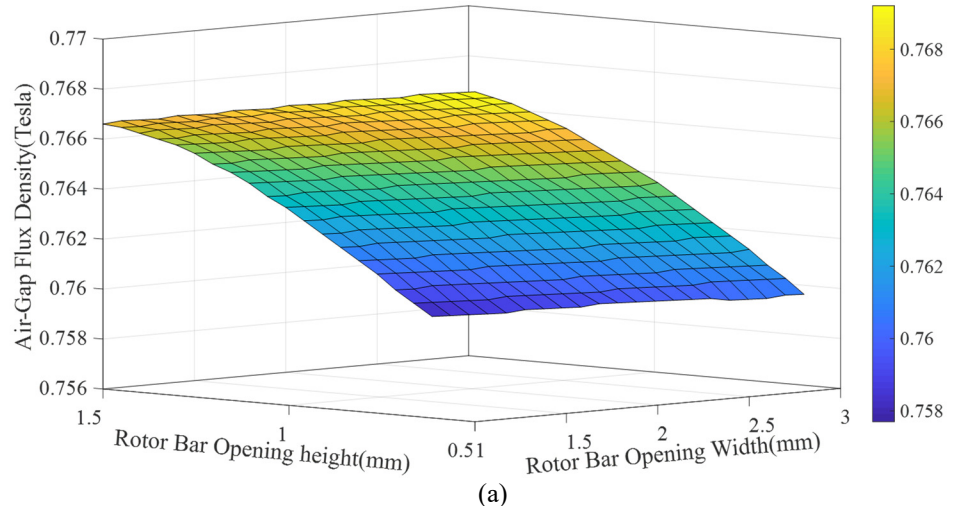
$$R_{r,dc}^{samp} = K_{R_r}^{samp} R_{r,dc}^{samp} \quad (5.24)$$

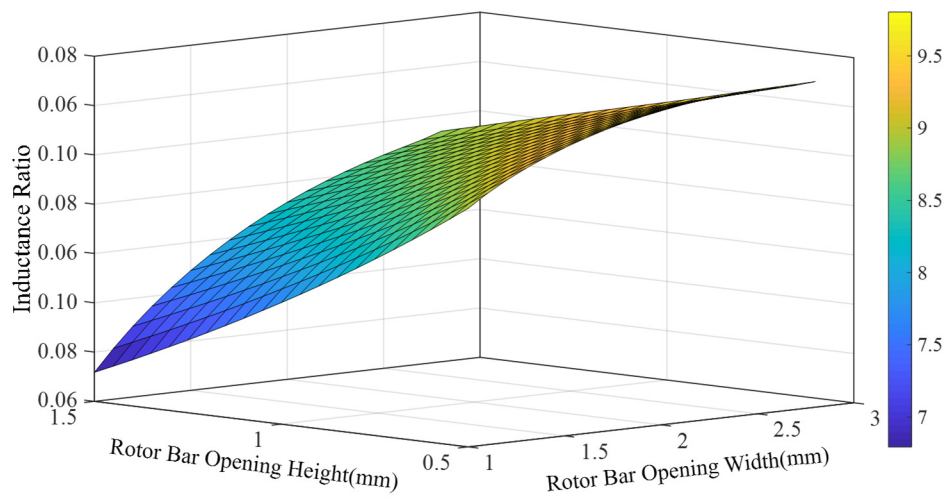
$$\left. \begin{aligned} R_{r,ac}^{samp} &= R_{r,ac}^{Bl} + \Delta R_r \\ R_{s,ac}^{samp} &= R_{s,ac}^{Bl} + \Delta R_s \end{aligned} \right\} \quad (5.25)$$

The dependency of leakage inductances for the rotor is derived for each sample design using calculated geometrical parameters through sensitivity analysis as (5.18). As mentioned in the previous section, the leakage ratio has a significant effect on the electrical machine performance beyond the rated speed. Therefore, finding critical parameters influencing leakage ratio will reduce the variables included in the optimization process. Deviation of the total leakage inductances is derived as (5.24).

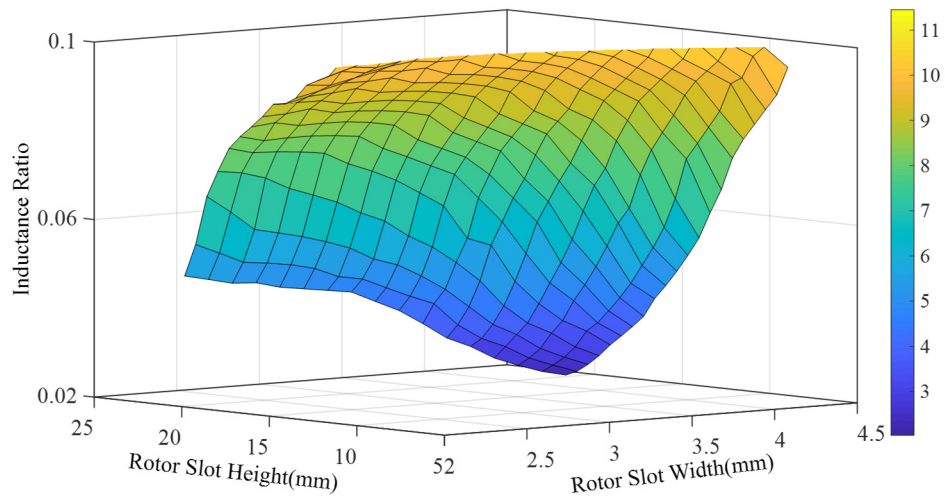
$$L_l^{smp} = L_l^{Bl} + \Delta L_l \quad (5.26)$$

The sensitivity of the rotor slot geometry is investigated through FE analysis to find out the effective slot geometrical parameters on the air-gap flux density, maximum torque, efficiency and inductance ratio. Comprehensive results are represented in Figure 5.6 for rotor slots corresponding to the geometries with a detail explanation of slot variables shown in Figures 5.5. Figure 5.7 represents the sensitivity approach incorporated in FE analysis for rotor bar geometrical parameters and their effect on the air-gap flux density, efficiency, inductance ratio, peak, and rated torque. Based on the investigation of rotor bar opening parameters and rotor bar height and width, the most complex parameters which are difficult to optimize are the rotor slot with and height compare to the rotor bar opening configuration. However, for most of the investigated parameters

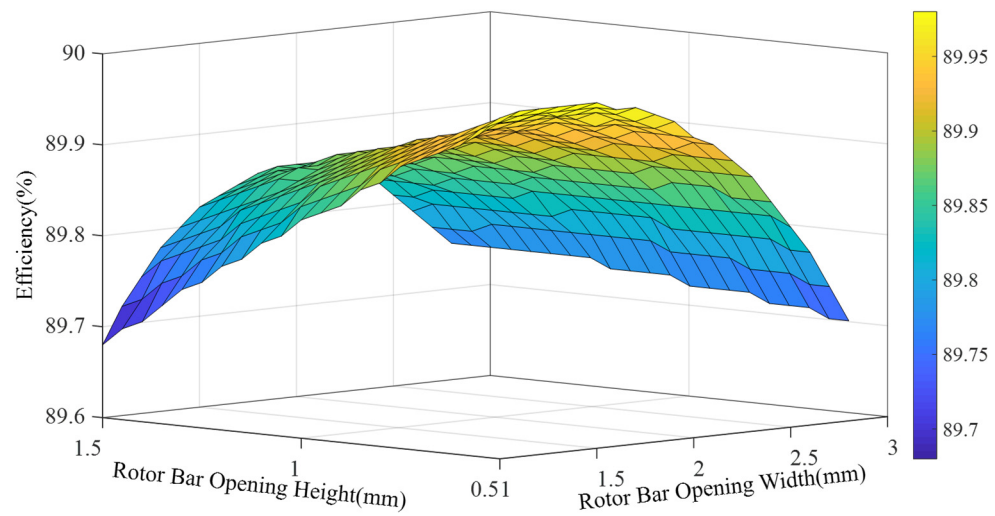




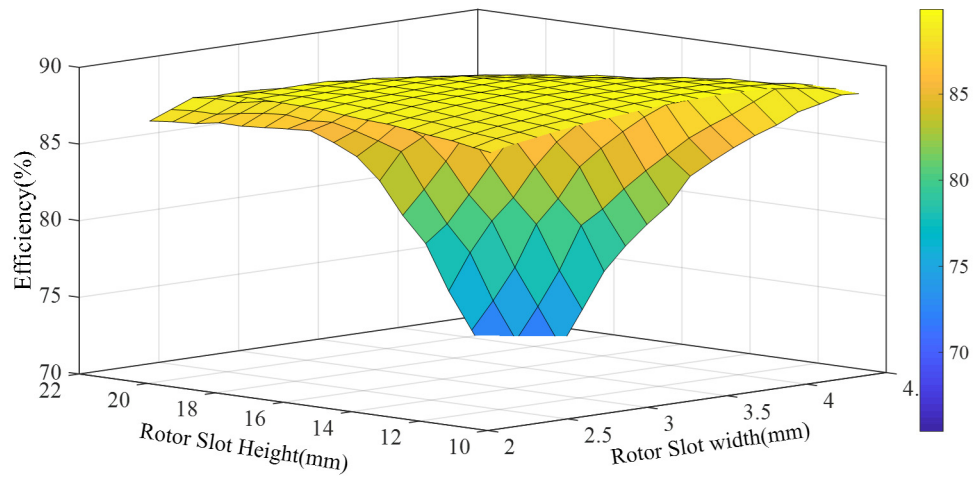
(c)



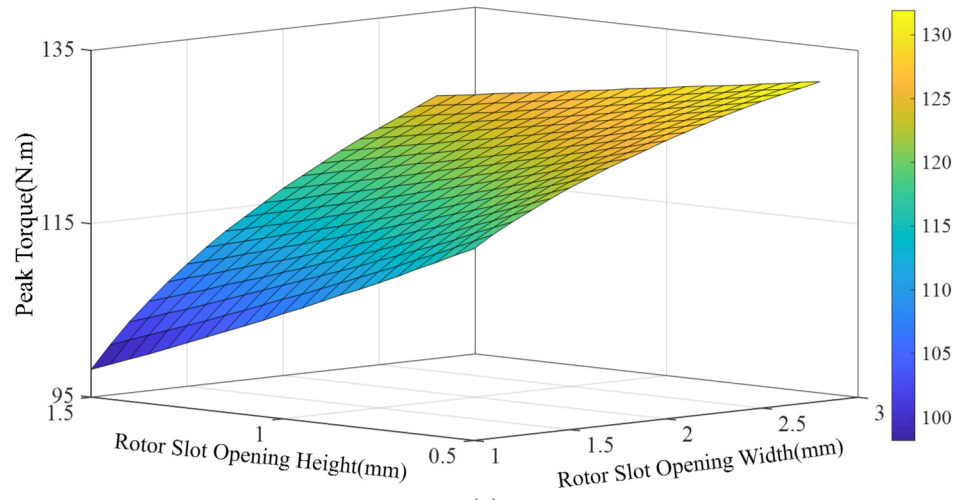
(d)



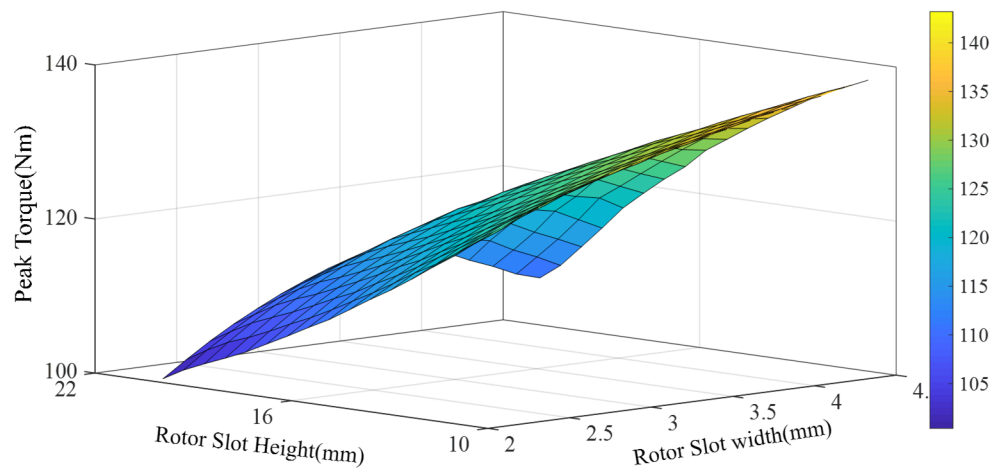
(e)



(f)



(g)



(h)

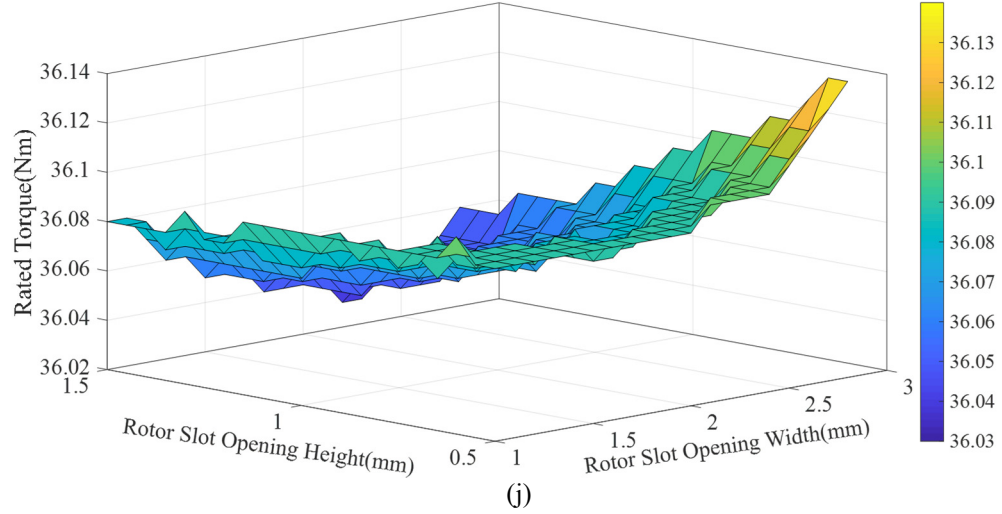


Figure. 5.7. Comparison of rotor bar geometrical parameter tolerances on output characteristics. (a) Sensitivity analysis of rotor bar opening height and width. (b) Sensitivity study of rotor bar height and width on inductance ratio, maximum torque, and efficiency.

5.5. Genetic Algorithm Based Structural Optimization Through FE and subdomain Analysis to Minimize Inductance Ratio to Enhance Capability of The IM

In this section, the genetic algorithm is employed in FEA and the proposed sub-domain model to maximize the peak torque capability of the baseline IM using (5.7) which is through reduction of the inductance ratio. Design variables in the rotor are defined as presented in the previous section based on the weighty of their effect on the torque development in the field weakening region and same variables are used when inductance ratio is going to be minimized.

5.5.1. Formulation of the Objective function to Optimize the Rotor Bar Geometry through Proposed Sub-Domain and FEA

In order to maximize the peak torque and increase the operating range of IM, this work proposes multi-objective function to minimize the inductance ratio by finding the optimal rotor configuration as it defines the operating range. By this objective function, the minimized inductance ratio is achieved for higher maximum torque and peak torque within a constant D^2L . The rotor bar is optimized for a fixed stator using (5.13). The proposed GA-based optimization approach is focused on the improvement of speed range with

minimized inductance ratio during steady state condition in both constant torque and power regions. The reason for using the proposed objective is that it can help to extend the constant power region without sacrificing overall efficiency of IM and constant torque region operation. The proposed objective function is defined by (5.27)–(5.29).

$$Obj_i = Minimize \left(\frac{X_l(i_{ds}, F_{syn})}{X_m(i_{ds}, F_{syn})} \right), i = a, b \quad (5.27)$$

Subject to:

$$(a) \begin{cases} 36Nm < T_{em}(i_{ds}, F_{syn}) < 37Nm \\ F_{syn} < 100Hz \\ i_{ds}^2 + i_{qs}^2 = i_m^2 \end{cases} \quad (5.28)$$

$$(b) \text{ Volume = Constant \& Efficiency} > 92\% \quad (5.29)$$

It should be noted, in an ideal scenario, if the Obj_a is close to zero, infinite constant power region, unity power factor, and 100% efficiency can be achieved. However, this is without considering resistance variation for higher frequencies and zero leakage inductances. The variation of conductor resistances can reduce the base speed since the maximum and rated torque will not change significantly. However, the maximum speed will be affected due to a decrease in rated speed even if the constant speed ratio is kept constant. Moreover, decreasing stator resistance will result in loss reduction and efficiency enhancement of IM. In order to minimize the losses, this paper seeks to maximize peak torque considering rotor resistance variation to enhance efficiency. In summary, the optimal design of IM involves two objectives, namely, optimizing Obj_a and Obj_b to improve the IM torque-speed profile.

The genetic algorithm is employed in FEA and the proposed sub-domain model to compare the convergence rate and number of iterations to obtain the optimal rotor bar structure. Since the developed IM is not skewed for simplifying the prototyping process, therefore 2-D sub-domain formulation is used in the optimization procedure. Figure 5. 8

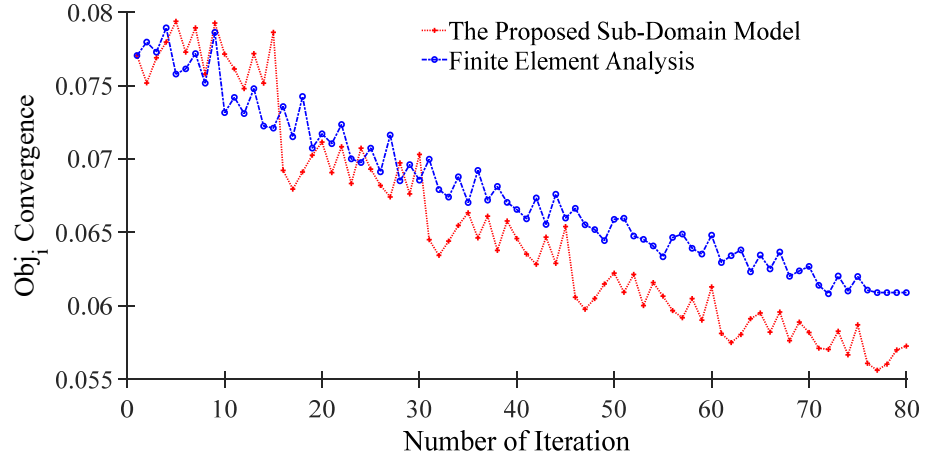


Figure. 5.8. Comparison of convergence rate using proposed sub-domain model and FEA to obtain the minimum inductance ratio to maximize the speed range.

presents the comparative analysis of the optimization procedure with the proposed sub-domain model presented in chapter 4 and the finite element analysis.

5.5.2. FEA Based Investigation and Comparison of the Baseline and Improved Designs Targets

The proposed mathematical model incorporated in section 5.3, is used to formulate Obj_i in conjunction with FE analysis. The method of obtaining torque/power–speed profile in FEA is carried out by defining slip variation and current characteristics of the vector–controlled IM for a wide frequency variation. In the field weakening region, the voltage limit is kept as the rated voltage by applying the specific frequency and slip ratios to satisfy the characteristics of the vector–controlled IM. Output torque is obtained for each step during steady state condition. Moreover, efficiency is calculated corresponding to each operating condition. Figure. 5.9 represents the convergence of the objective function derived for both constraints namely a and b. As shown in this figure, considering the most effective structural variables, rotor slot dimensions are optimized to improve and minimize the objective function for both constraints in (5.27) and (5.28). Therefore, the peak torque of the baseline is maximized with the efficiency as close as the target efficiency for the same volume. Figures 5.10 and 5.11 represent the 2D CAD drawing of the optimal IM and the magnetic flux density in the air–gap, respectively. Figures 5.12 and 5.13 presents improved maximum torque, inductance ratio for the optimal IM. Within a fixed volume

maximum torque capability is improved, however, there will be a small efficiency drop due to a decrease in the base speed which can be improved with increasing the outer diameter of the stator. Figure 5.14 presents the efficiency map of developed IM. table 5.3 shows the power rating of optimal design at rated and overload conditions. Calculated baseline structures are in a good agreement with the target design specification addressing the issues in the conventional design approach. Furthermore, the proposed objective function to improve the capability of IM in flux weakening region is addressed through proposed sensitivity approach by introducing the most significant rotor structural parameters to the inductance ratio, peak torque and efficiency of IM. The proposed objective function considers resistance effect in addition to leakage and magnetizing inductances on the field weakening operation and efficiency of the IM.

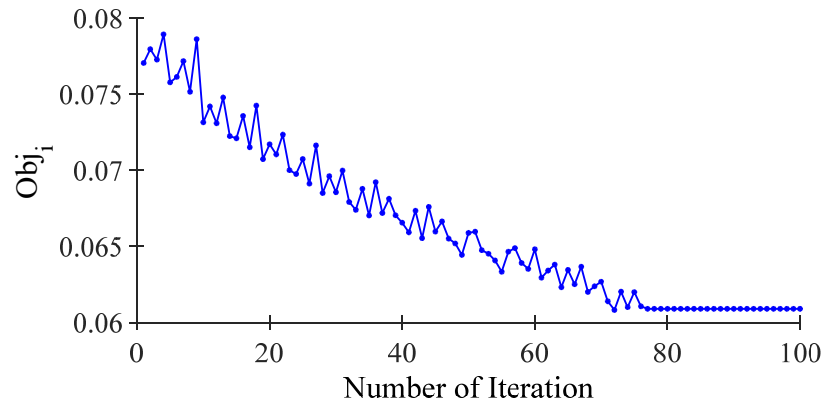


Figure. 5.9. Objective function evaluation for inductance ratio by optimizing rotor slot geometrical parameters using the main structural variables affecting the objective function a.

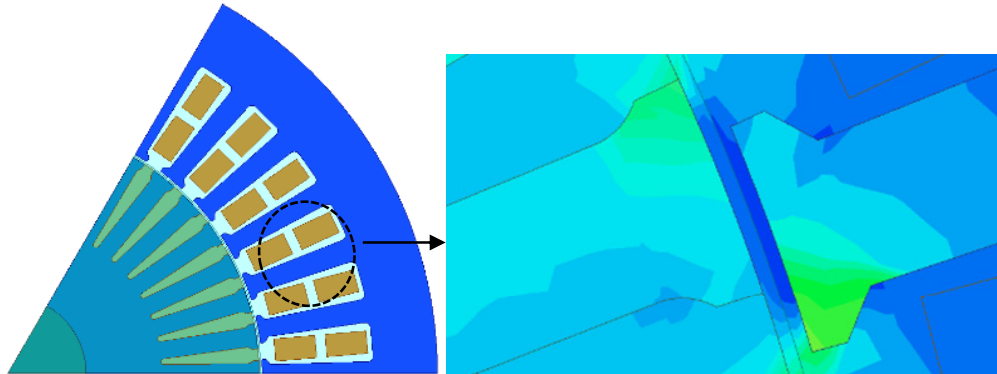


Figure. 5.10. Unsaturated magnetic field distribution of the optimal IM at 2,940 rpm and rated torque at rotor and stator slot edge.

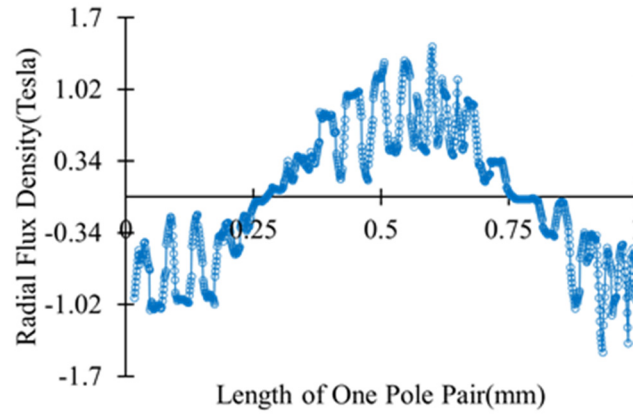


Figure. 5.11. Objective function convergence to maximize efficiency and peak torque by optimizing rotor slot geometrical parameters using the main structural variables affecting the objective function b.

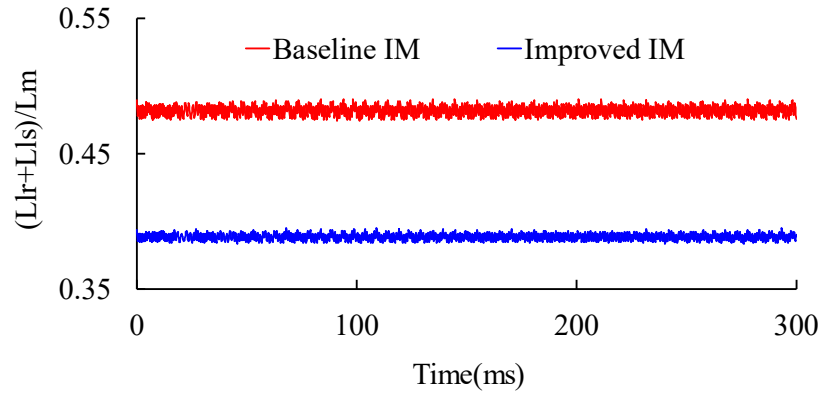


Figure. 5.12. Comparison of Inductance ratio of optimal IM and baseline design.

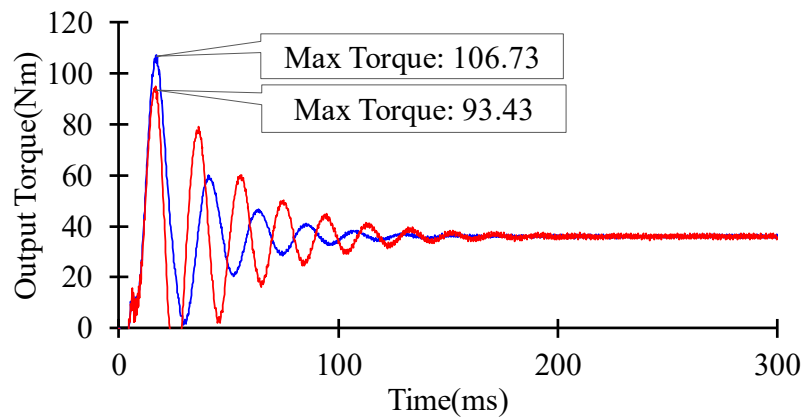


Figure. 5.13. Comparison of Maximum torque at the rated condition of optimal IM and baseline design.

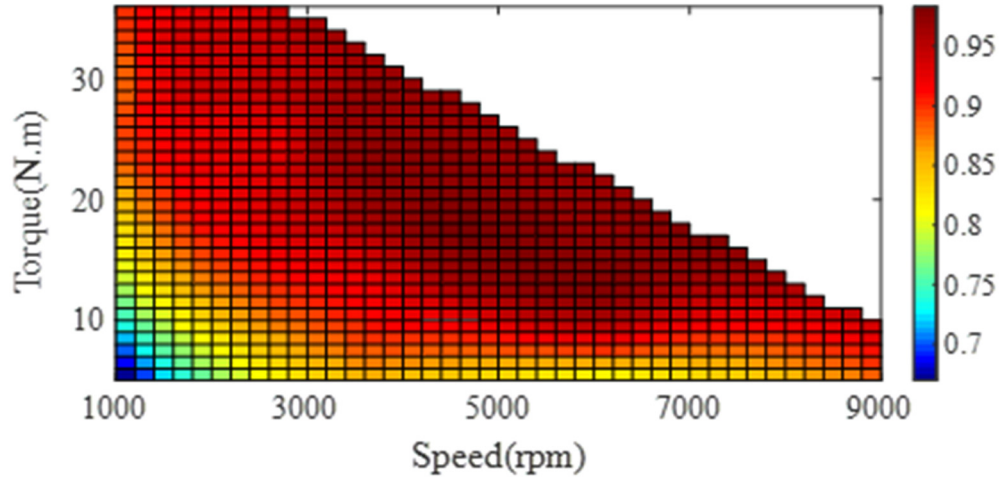


Figure. 5.14. Efficiency map of optimal IM.

TABLE 5. 3.
RATED AND PEAK PARAMETERS OF OPTIMAL IM

| | |
|------------------|-----------|
| Maximum Torque | 107 N.m |
| Maximum Power | 34 kW |
| Rated Efficiency | 91.59 |
| Power Factor | 0.83 |
| Rated Torque | 36 N.m |
| Rated Speed | 2,940 rpm |

5.6. Conclusion

In this thesis, a novel rotor configuration has been proposed and prototyped using the developed design procedure. This optimizes the IM for EV application with higher maximum torque capability. First, using parametric study based optimization approach, the optimal number of stator-rotor slot and pole combination was found out to be a 4 pole and 36–42 slot combination satisfying the initial requirements for the application. Minimum torque ripple, increased efficiency, and optimal inductance ratio were achieved for the baseline targets with a satisfactory constant power speed ratio close to the target value. Then the inductance ratio is minimized to enhance the peak torque capability of the developed IM design through optimal rotor slot dimension. Employing proposed design optimization procedure via reduced design space, the design and optimization process is

found to be more efficient and converges faster and can be implemented to any traction motor design for further improvement to meet the requirement for EV applications. The trend of experimentally obtained parameters is validated over a wide speed range and it demonstrates the prototyped IM capability beyond the base speed. The same methodology can be applied for the stator to enhance the efficiency and torque-speed profile of the IM.

5.7. References

- [1] M. Ehsani, Yimin Gao and S. Gay, "Characterization of electric motor drives for traction applications, in the proc of the" *Industrial Electronics Society*, 2003. *IECON'03*, vol.1, 2003.
- [2] G. Pellegrino, A. Vagati, B. Boazzo, and P. Guglielmi, "Comparison of Induction and PM Synchronous Motor Drives for EV Application Including Design Examples," in *IEEE Transactions on Industry Applications*, vol. 48, no. 6, 2012.
- [3] T. Finken, M. Felden, and K. Hameyer, "Comparison and design of different electrical machine types regarding their applicability in hybrid electrical vehicles, in the proc of the" *2008 18th International Conference on Electrical Machines*, 2008.
- [4] D. G. Dorrell, A. M. Knight, L. Evans and M. Popescu, "Analysis and Design Techniques Applied to Hybrid Vehicle Drive Machines—Assessment of Alternative IPM and Induction Motor Topologies," in *IEEE Transactions on Industrial Electronics*, vol. 59, no. 10, 2012.
- [5] Z. M. Zhao, S. Meng, C. C. Chan, and E. W. C. Lo, "A novel induction machine design suitable for inverter-driven variable speed systems," in *IEEE Transactions on Energy Conversion*, vol. 15, no. 4, 2000.
- [6] Z. Yang, F. Shang, I. P. Brown and M. Krishnamurthy, "Comparative Study of Interior Permanent Magnet, Induction, and Switched Reluctance Motor Drives for EV and HEV Applications," in *IEEE Transactions on Transportation Electrification*, vol. 1, no. 3, 2015.
- [7] C. Shumei, D. Ying and S. Liwei, "Rotor Slots Design of Induction Machine for Hybrid Electric Vehicle Drives, in the proc of the " *2006 IEEE Vehicle Power and Propulsion Conference*, 2006.
- [8] T. Wang, P. Zheng, Q. Zhang, and S. Cheng, "Design characteristics of the induction motor used for hybrid electric vehicle," in *IEEE Transactions on Magnetics*, vol. 41, no. 1, 2005.
- [9] S. Seo, G. J. Park, Y. J. Kim and S. Y. Jung, "Design method on induction motor of electric vehicle for maintaining torque performance at field weakening region, in the proc of the " *2017 20th International Conference on Electrical Machines and Systems (ICEMS)*, 2017.
- [10] A. Mollaeian, S. M. Sangdehi, A. Balamurali, G. Feng, J. Tjong, and N. C. Kar, "Reduction of space harmonics in induction machines incorporating rotor bar optimization through a coupled IPSO and 3-D FEA algorithm, in proc of the " *2016 XXII International Conference on Electrical Machines (ICEM)*, Lausanne, 2016.
- [11] F. Parasiliti, M. Villani, S. Lucidi, and F. Rinaldi, "Finite-Element-Based Multiobjective Design Optimization Procedure of Interior Permanent Magnet Synchronous Motors for Wide Constant-Power Region Operation," in *IEEE Transactions on Industrial Electronics*, vol. 59, no. 6, 2012.

- [12] D. Butterweck, M. Hombitzer, and K. Hameyer, "Multiphysical design methodology of a high-speed induction motor for a kinematic-electric powertrain, in the proc of the" 2017 *IEEE International Electric Machines and Drives Conference (IEMDC)*, 2017.
- [13] G. Bramerdorfer, A. C. Zăvoianu, S. Silber, E. Lughofer and W. Amrhein, "Possibilities for Speeding Up the FE-Based Optimization of Electrical Machines—A Case Study, " in *IEEE Transactions on Industry Applications*, vol. 52, no. 6, 2016.
- [14] D. Zarko, S. Stipetic, M. Martinovic, M. Kovacic, T. Jercic and Z. Hanic, "Reduction of Computational Efforts in Finite Element-Based Permanent Magnet Traction Motor Optimization," in *IEEE Transactions on Industrial Electronics*, vol. 65, no. 2, 2018.
- [15] Y. Liu, J. Zhao, R. Wang and C. Huang, "Performance Improvement of Induction Motor Current Controllers in Field-Weakening Region for Electric Vehicles," in *IEEE Transactions on Power Electronics*, vol. 28, no. 5, 2013.
- [16] H. Grotstollen and J. Wiesing, "Torque capability and control of a saturated induction motor over a wide range of flux weakening," in *IEEE Transactions on Industrial Electronics*, vol. 42, no. 4, 1995.
- [17] G. Pellegrino, A. Vagati, B. Boazzo, and P. Guglielmi, "Comparison of Induction and PM Synchronous Motor Drives for EV Application Including Design Examples," in *IEEE Transactions on Industry Applications*, vol. 48, no. 6, 2012.
- [18] M. S. Huang and C. M. Liaw, "Transient performance improvement control for IFO induction motor drive in field-weakening region, in proc of " *IEEE Electric Power Applications*, vol. 150, no. 5, 2003.
- [19] E. B. Agamloh, A. Cavagnino, and S. Vaschetto, "Impact of Number of Poles on the Steady-State Performance of Induction Motors," in *IEEE Transactions on Industry Applications*, vol. 52, no. 2, 2016.
- [20] E. B. Agamloh, A. Boglietti, and A. Cavagnino, "The Incremental Design Efficiency Improvement of Commercially Manufactured Induction Motors," in *IEEE Transactions on Industry Applications*, 2013.
- [21] Jul-Ki Seok and Seung-Ki Sul, "Optimal flux selection of an induction machine for maximum torque operation in flux-weakening region," in *IEEE Transactions on Power Electronics*, vol. 14, no. 4, 1999.
- [22] K. Wang, K. Lee, W. Ya, and F. Chen, "Maximum torque output for volts/Hz controlled induction machines in flux-weakening region, in proc of the " 2016 *IEEE Energy Conversion Congress and Exposition*, 2016.
- [23] H. Cai, L. Xu, and A. J. Pina, "Maximum torque control of induction machine in deep flux weakening region, in proc of the" 2015 *IEEE Energy Conversion Congress and Exposition (ECCE)*, 2015.
- [24] B. Gu and J. S. Lai, "Control of induction machine with extended range of maximum torque capability for traction drives, in proc of the" 2011 *IEEE Energy Conversion Congress and Exposition*, 2011.
- [25] T. Gundogdu, Z. Q. Zhu and J. C. Mipo, "Influence of stator slot and pole number combination on rotor bar current waveform and performance of induction machines, in proc of the" 2017 *20th International Conference on Electrical Machines and Systems (ICEMS)*, 2017.

- [26] I. P. Tsoumas, H. Tischmacher, and B. Eichinger, "Influence of the number of pole pairs on the audible noise of inverter-fed induction motors: Radial force waves and mechanical resonances, in proc of the " 2014 *International Conference on Electrical Machines (ICEM)*, 2014.
- [27] J. Le Besnerais, V. Lanfranchi, M. Hecquet and P. Brochet, "Optimal Slot Numbers for Magnetic Noise Reduction in Variable-Speed Induction Motors," in *IEEE Transactions on Magnetics*, vol. 45, 2009.
- [28] M. Mori, T. Mizuno, T. Ashikaga, and I. Matsuda, "A control method of an inverter-fed six-phase pole change induction motor for electric vehicles, in proc of the " *Power Conversion Conference*, 1997.
- [29] E. F. Fuchs, J. Schraud and F. S. Fuchs, "Analysis of Critical-Speed Increase of Induction Machines via Winding Reconfiguration With Solid-State Switches," in *IEEE Transactions on Energy Conversion*, vol. 23, no. 3, pp. 774-780, 2008.
- [30] S. J. Chapman, " Electric Machinery Fundamentals", McGraw-Hill College, USA, 2005.
- [31] E. Ghosh, A. Mollaeian, S. Kim, J. Tjong, and N. C. Kar, "Intelligent flux predictive control through online stator inter-turn fault detection for fault-tolerant control of induction motor, in proc of the" 2017 *IEEE International Conference on Industrial Technology (ICIT)*, Toronto, 2017.

CHAPTER 6

EXPERIMENTAL VALIDATION OF THE PROPOSED OPTIMIZED HIGH SPEED INDUCTION MACHINE

6.1. Introduction

The high speed induction motor designed in the previous chapters has been manufactured in house for verification of the proposed semi-analytical-numerical procedure. The detailed IM prototype development of structural components and mechanical supports are explained in detail. The experimental results are provided to support the concept of developed IM with the high power density and higher overload capability within a compact volume and fixed inverter output.

6.2. Prototyping High Speed Induction Motor

The exploded view of the proposed 11kw IM with the detailed mechanical structure is shown in Figure 6.1. All individual components are designed and built in house. The prototype includes: laminated stator core, laminated rotor core, the main body of the housing including cooling channels, cooling channel sealing cap, stator core retainer, ball bearings, end and front cap of the housing and shaft. Individual component development is explained in the next section. To start prototyping the stator and rotor cores firstly electrical steel which is satisfying the magnetic and electrical characteristics is chosen. The

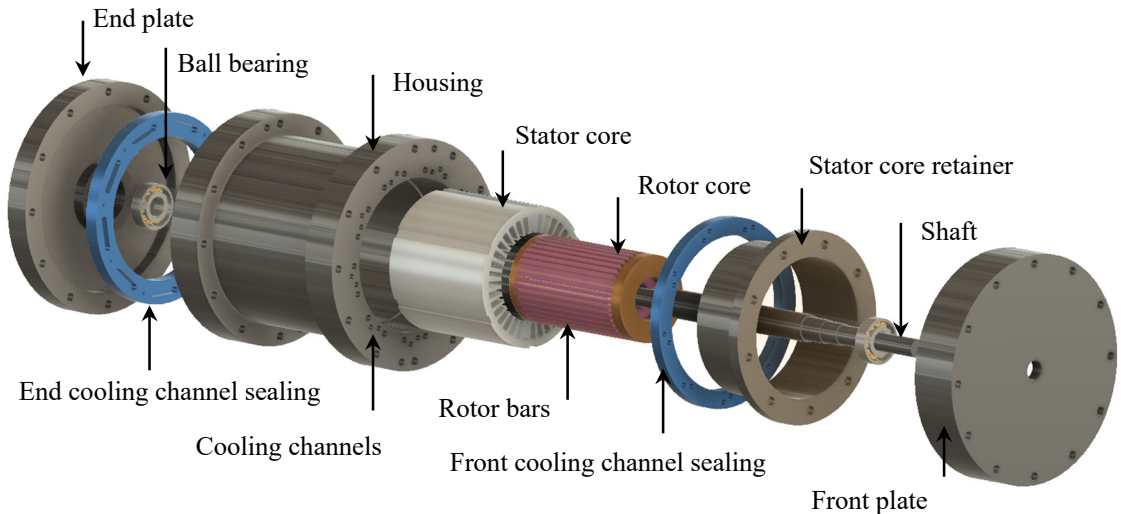


Figure. 6.1. The exploded view of the developed high speed induction machine.

TABLE 6. 1.
PROPERTIES OF THE STATOR AND ROTOR CORES

| Mass density | Electrical Resistivity | K_h | K_c | Bulk Conductivity |
|--------------------------|------------------------|---------|-------|------------------------|
| 7650(kg/m ³) | 56 (μ ohm/cm) | 173.312 | 0.343 | 1960000 (Siemens/m) |

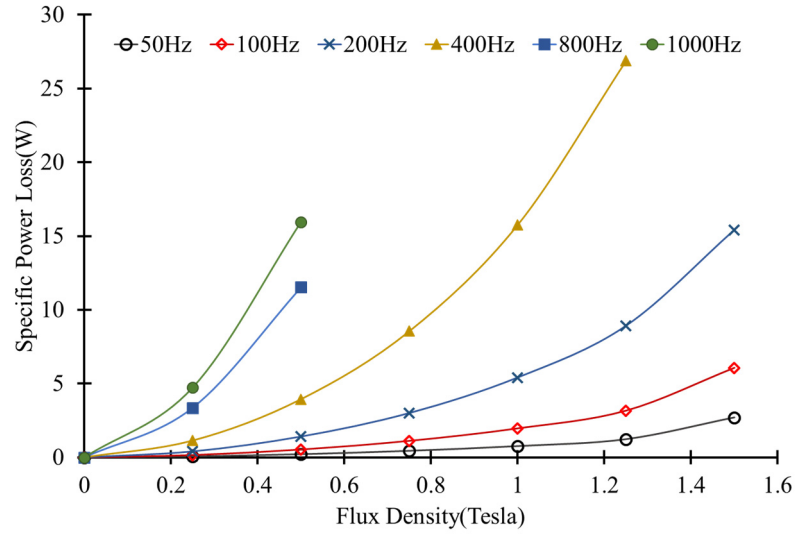
chosen electrical steel is M230-35A with the lamination thickness of 0.35 mm. The material properties are presented in Table 6.1. The measured specific power loss for different frequencies is demonstrated in Figure 6.1. These data have been used to calculate the core loss coefficients to calculate the stator and rotor core loss of the IM.

6.2.1. *Stator and Rotor Cores*

To build the stator and rotor cores, first, the electrical steel is selected based on availability in the market and the optimal flux requirement of the high power dense electric machine which was simulated previously in finite element environment and acceptable core losses under various frequencies. Since wire cutting has minimum thermal effect compare to laser cutting, the wire cutting machine is used to form the stator and rotor laminations [1-3]. However, it is a time consuming process compared to laser cutting and punching. The material properties and core loss characteristics have been modified in FE analysis based on the experimental measurement of M230-35A. The core loss coefficients have been calculated using the proposed Bertotti's core loss equation [4]. Figure 6.2 is presenting the electric steel sheets and measured specific core loss characteristics of

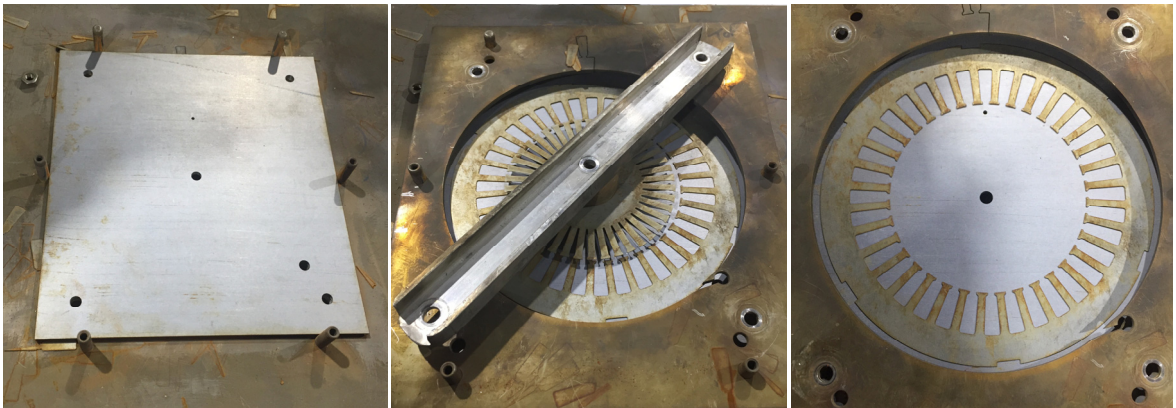


(a)



(b)

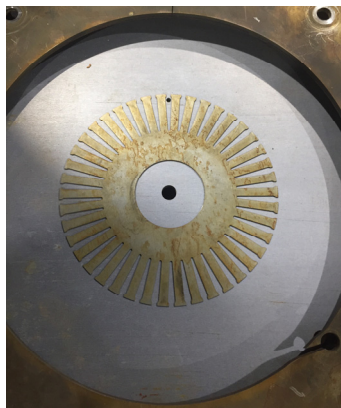
Figure. 6.2. Electrical steel used in prototyping high speed IM. (a) Material sheets with C5 coating. (b) The B-H characteristics of M230-35A under various frequencies.



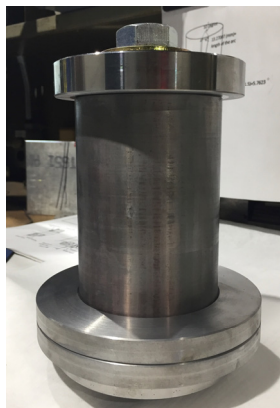
(a)

(b)

(c)



(d)



(e)



(f)

Figure. 6.3. Steps of forming stator and rotor cores. (a) Fixture used to cut the stator and rotor laminations. (b) Cutting process of laminations. (c) Stator lamination. (d) Rotor lamination. (e) Stator fixture. (f) Rotor fixture.

M230-35A. The stator and rotor laminations and the process of forming the laminations are presented in Figure 6.3. The stator and rotor fixture to assemble the laminations are designed and built which are presented in Figures 6.3(e) and 6.3(f). The final product of assembled stator and rotor cores is presented in Figure 6.4. The stator is hand-wound because of high slot fill factor and the stages of the forming the stator winding is presented in Figure 6.5. The rotor bars and end rings have been cut and formed using wire cutting machine as presented in Figure 6.6. Aluminum alloy 6061 has been used for rotor bars and end rings and they have been welded. Replacing aluminum bars with copper bars reduces rotor loss leading to enhancement of efficiency and rated torque, However increases the weight and cost of the prototype. Additionall peak torque of IM will not be affected with this replacement.

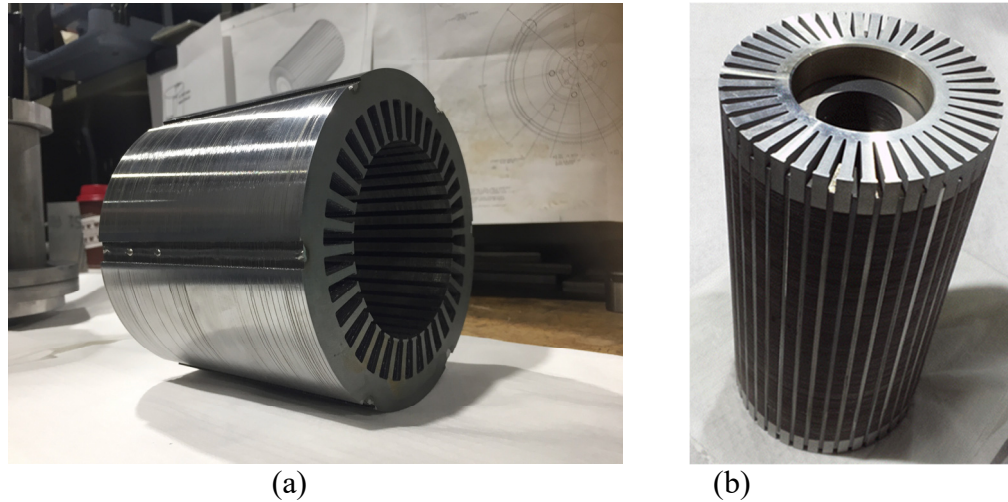


Figure. 6.4. High speed induction machine assembled cores. (a) 36 slot stator core. (b) 42 slot rotor core.

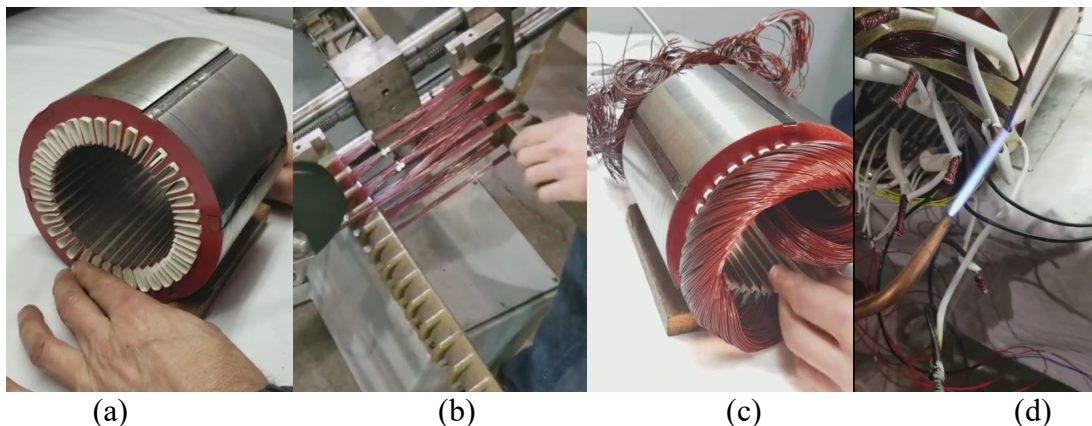


Figure. 6.5. Steps of winding the stator. (a) insertion of insulation paper. (b). coil forming, (c) insertion of coils in slots. (d) connecting the coil groups.



(a)

(b)

(c)

Figure. 6.6. Steps of rotor assembly. (a) Manufactured rotor end ring with aluminum alloy 6061. (b) wire cut rotor bar. (c) assembled and welded rotor.

Utilizing superconducting materials in both the stator and the rotor to maximize the power and torque density increases the efficiency as a result of higher air-gap magnetic flux density and also being capable of undertaking larger current in coils and reduction of AC losses. The challenge is to keep the motor cool while the high torque from the shaft is being transferred. Since, superconducting coils instead of the resistive ones dramatically reduce the energy needed to generate a magnetic field. Therefore, adoption of superconductor material can offer advantages of high reliability, high power density, and high efficiency compared with conventional conductors. However, it will bring some problems such as cooling, maintenance, mechanical speed and manufacture cost, etc., because of complex production technology.

6.2.2. *Housing*

In an electric machine, part of the supplied energy is always converted into losses and heat. Using adequate cooling with a proper flow rate is crucial to meet the motor performance and avoid damaging the motor at continuous and peak operating condition. Therefore, the housing of the developed high speed induction motor is designed and developed using Computational Fluid Dynamics (CFD) software to investigate the thermal distribution of the motor. Cooling channels are formed as holes in the housing for liquid cooling the motor because the designed IM is high voltage and high power density. Figure 6.7 is presenting the manufactured housing details.

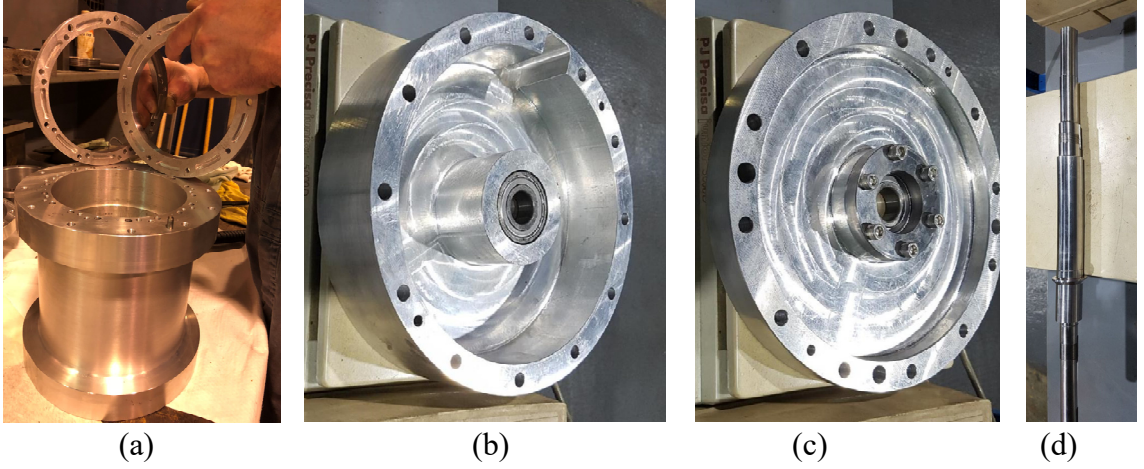


Figure. 6.7. Housing components of the developed high speed IM. (a) Main body of the housing and cooling channel sealing. (b) end cap. (c) front cap. (d) shaft.

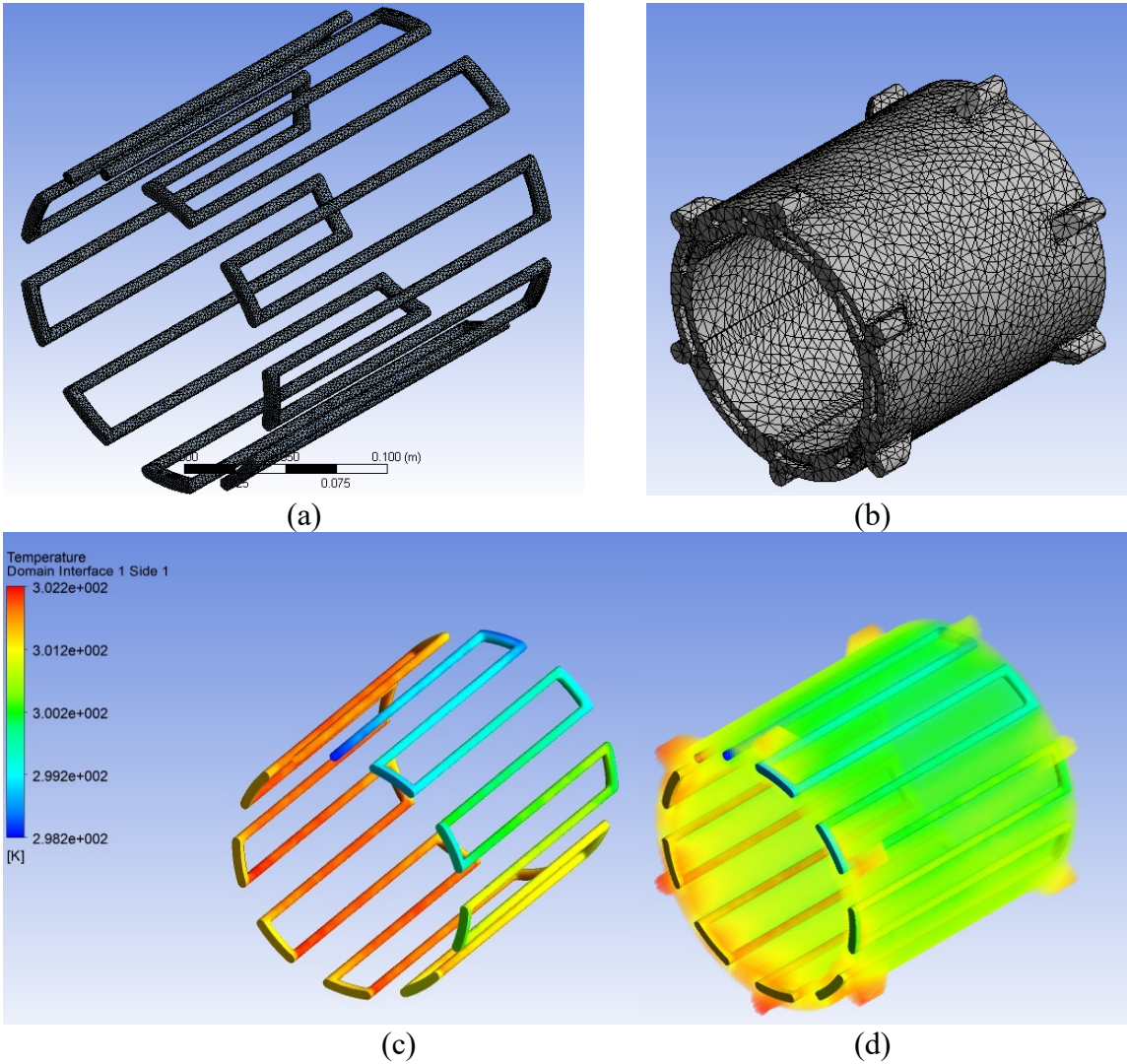


Figure. 6.8. Steady temperature rises of the high speed IM. (a) The 3D meshed model of cooling channels. (b) The 3D meshed model of the housing. (c) Thermal distribution of the

flowing liquid in cooling channels. (d) thermal distribution of the developed IM at the housing.

The required flow rate is calculated using (6.1)

$$P_{tot} = \rho C_p q \Theta \quad (6.1)$$

$$P_{tot} = P_{S-Cl} + P_{R-Cl} + P_{Iron} + P_{mec} + P_{additional} \quad (6.2)$$

where P_{S-Cl} , P_{R-Cl} , P_{Iron} , P_{mec} , and $P_{additional}$ are stator copper loss, rotor conductor loss, the sum of stator and rotor iron losses, mechanical (friction and windage) losses and excessive losses. ρ , C_p , q , and Θ are the density of the coolant, the capacity of the cooling fluid, volume of the flow rate of the coolant. To find the temperature rise, environment temperature is kept constant at room temperature and the flow rate is 8 liters per minute for 10.21 mm² cross section area for each cooling channel.

6.3. Investigation of Electromagnetic Torque Capability Reduction of Electric Machine Due to Magnetic Property Deterioration of Laminations

Electrical steel sheets of electric motors are formed as laminations by various mechanical procedure, such as punching, wire cutting, and laser cutting. Estimation of magnetic flux density is crucial for accurate determination of laminated core loss, torque and the maximum capability of an electric motor. Magnetic flux density tolerances are due to the air-gap length variation and the relative permeability of the stator and rotor cores. Magnetic flux distribution is adversely affected by the residual stress caused by the mechanical cutting procedure and reflected in relative permeability which is more influential close to the edges in a compact motor [5]. Hence, the deterioration of laminations needs to be quantified and modeled so that machine performance can be predicted accurately at the design stage.

As a result of permeability variation, the large discrepancy of the inductances and electrical parameters of the motor occurs and the IM performance such as losses and torque production varies consequently. It is well established that lamination deterioration increases core loss [6]-[8]. Comprehensive performance analysis on this issue was not

conducted over a wide speed range by taking magnetic property discrepancy into account in previous studies. Therefore, this paper proposes a systematic approach to include material degradation through electromagnetic analysis to investigate the effect of permeability drop on the output characteristics such as continuous and peak power and torque over a wide speed range. For this purpose, first, specific power losses are measured using Epstein frame test for the various frequency to model the permeability of the specimens of the electrical steel before cutting. This extensive measurement enables adequate material data to be utilized in 2-D FEM simulations of motor performances. A qualitative comparison is conducted to establish the core loss variation for M230-35A before and after cutting. Then, proposed relative permeability is implemented as a non-uniform characteristic to consider the degradation effect in the material. Extensive 2-D FEM analysis is conducted to compare the electrical parameters and performance characteristics of developed IM for both scenarios over a wide speed range.

6.3.1. Methodology: Derivation of Analytical Expression for Permeability Drop

In this section, the proposed procedure to include the permeability variation due to forming the laminations is presented. For this purpose, a parabolic permeability function is applied in the material properties through 2-D FEM to calculate the magnetic field distribution. Consequently, a qualitative comparative study has been done for M230-35A to evaluate the result of lamination manufacturing on the magnetic field through experiment and numerical solution.

6.3.2. Effective Relative Permeability

Stator and rotor teeth are the subject to the permeability variation in IM because of residual stress due to cutting. As a result, the magnetic saturation level increases in the teeth close to the cut edges with a lower cross section causing excessive harmonic losses which leads to a drastic change in hysteresis and excessive losses. Because of non-uniform distribution and rotation of the magnetic flux, the permeability of each tooth has time-varying characteristics. Therefore, the magnetic reluctance of the core increases because of higher tooth saturation degree which is usually ignored at the design stage. Hence, to

determine the increase of magnetic losses, the dependency of relative permeability on the tooth saturation needs to be considered in 2-D FEM analysis. Since permeability is a local dependent function and depends on three parameters: 1) the permeability of the material before cutting, 2) the maximum permeability drops at the cut surface, and 3) hyperbolic profile to describe local deterioration shape function [9], therefore permeability drop can be modeled using (6.3) and (6.4):

$$\mu_r(H, x) = \mu_r(H, 0) - \Delta\mu_{cut}(H) \cdot \eta(x) \quad (6.3)$$

$$\eta(x) = \begin{cases} 1 - \frac{x}{\delta} - a \cdot \frac{x}{\delta} \left(1 - \frac{x}{\delta} \right) & \text{for } 0 \leq x \leq \delta \\ 0 & \text{for } x > \delta \end{cases} \quad (6.4)$$

where $\mu_r(H, 0)$ is permeability of non-degraded material measured experimentally; a , δ and x are fitting parameter, the local boundary respect to cut edge and distance from the cutting edge to calculate the degraded material permeability at certain point respect to the cut edge. Based on the proposed solution in [9], the modified material curve is adopted into FEM as (6.3) using a hyperbolic function with dependency on the cut edge. This function for magnetic field intensity is adopted by defining a B - H profile for magnetic field intensity and relative permeability for M230-35A to consider the permeability drop. Considering the drop in magnetic permeability, non-homogenous characteristics of permeability is defined in the material property as shown in (6.5)

$$Y(H, x) = - \left(\frac{\mu_r(H, x)}{\mu_r(H, 0)} - 1 \right) \quad (6.5)$$

where Y is the relative drop. Using measured permeability characteristics of non-degraded material and along with the regression method, a generated look-up table has been implemented in material properties solving Maxwell's equations to investigate continuous and maximum performance characteristics for the developed IM. Furthermore, based on magnetic noise measurement method which is presented in next section, the core loss coefficients are computed using energy density and implemented in electromagnetic

analysis to investigate the magnetic flux distribution and output torque characteristics of IM using (6.6).

$$Energy = \sum_i \int V_i^2 dt \quad (6.6)$$

Due to permeability drop, saturation level and magnetic flux higher order of harmonics increases leading to higher core losses and lesser output torque. A comprehensive IM performance analysis for degraded and non-degraded laminations is adopted in the next sections by considering stator and rotor reactances.

6.3.3. Experiment Based Investigation of Core Loss Variation Due to Manufacturing

In this section, the standard strips of M230-35A are used to measure the Magnetic Barkhausen Noise (MBN). To compare the obtained data, a similar measurement has been done for the square specimen using the same mechanical cutting procedure used to form the laminations presented in figure 6.9. MBN measurement is implemented for the frequency range of 0.1-1,000 kHz and 20 MBN signal burst under the magnetizing frequency of 125 Hz and voltage 4 V for different local points. Magnetic Barkhausen Noise (MBN) test is conducted to measure the local magnetic noise on the different local points of the formed electrical steel to establish the core loss variation [10] and experimental results are presented in Table 6.2. Based on the aforementioned studies, there is a strong co-relationship between core loss and magnetic noise measurements [11]. The eddy current depends on the thickness of the lamination, therefore there will not be much of a variation in eddy current losses. However, hysteresis and excessive losses are influenced by the cutting process especially in the cut edge regions which are dominant in compact motors.

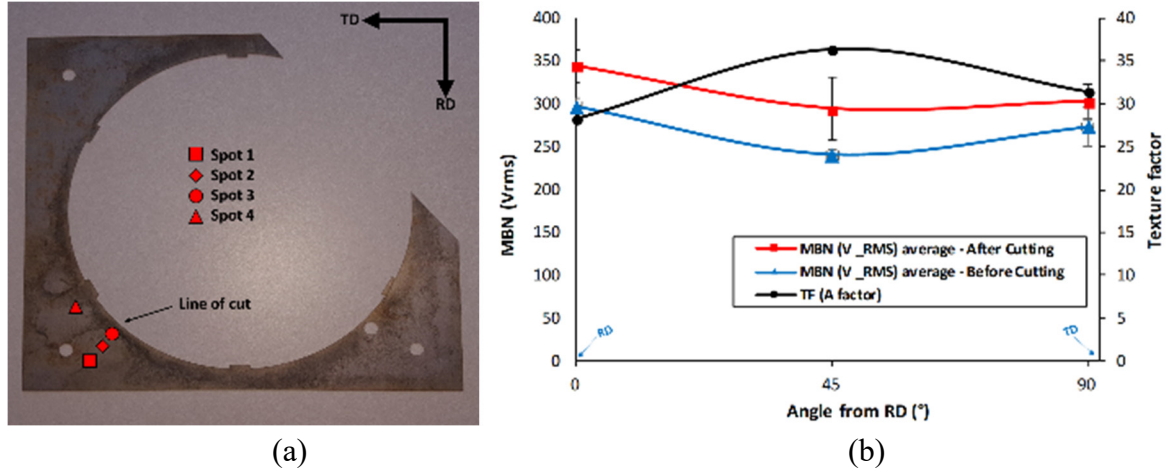


Figure. 6.9. The average MBN (V_{rms}) for the different spots at different magnetization directions before and after cutting compared with the texture factor arising from magnetocrystalline anisotropy.

TABLE 6. 2.
COMPARISON OF MBNM BEFORE AND AFTER CUTTING M230-35A

| Testing direction | MBN ($V_{average-rms}$) | | Percentage Increase |
|-------------------|---------------------------|---------------|---------------------|
| | Before cutting | after cutting | |
| 0° | 297 | 344 | 15.5% |
| 45° | 240 | 319 | 32.6% |
| 90° | 273 | 310 | 13.6% |

6.3.4. Implementation of the Material Curve in Fem

A well-established degradation profile presented in Figure 6.10 is adopted into 2-D FEM as a non-uniform material distribution to calculate the magnetic flux variation in the stator and rotor cores to include the effect of the local residual stress in the IM [5]. The magnetic field distribution within the stator and rotor laminations are studied for a given air-gap flux level for different degradation profiles and intensities provided as a B-H profile presented as Figure 6.10. The discrepancy of the IM parameters such as reluctances and magnetomotive forces results in a different stator and rotor inductances as well as core loss density and output power and torque characterization.

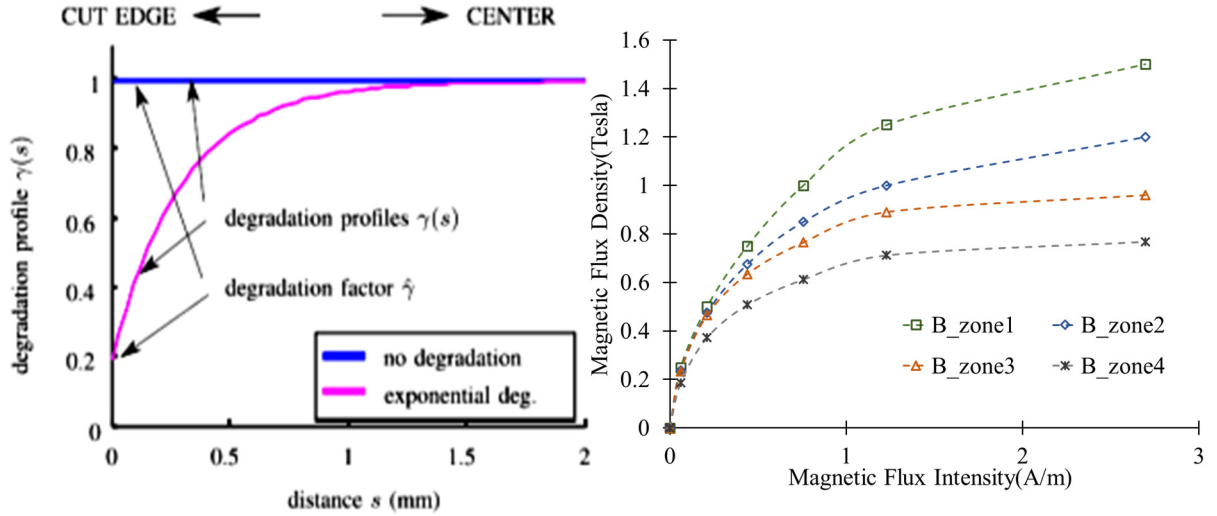


Figure. 6.10. Degradation profile [5] permeability drops for M230-35A.

6.4. Investigation of Cut Edge Degradation Effect on Torque Capability of IM

In this section, a squirrel cage aluminum bar induction motor is designed and modeled using 2-D FEM and output characteristics are compared for different permeability drops under different operating condition. Table 5.2 shows the electrical and geometrical parameters of the developed IM. To show how lamination is influenced by residual stress due to the cutting procedure, a mechanical 2-D FEM analysis is performed to present the most affected regions because of stress and strain production during the manufacturing which is presented in Figure 6.11. As it is shown in the Figures 6.11a and 6.11b the concentration of residual stress when the force is applied perpendicular to the surface along x and y -axes. Therefore, material property variation needs to be taken into account using (6.3) and (6.4), while cutting the electrical steel causes the concentration of stress on the regions close to the cut edge as well as regions perpendicular to the applied force. Figure 6.11c is demonstrating the interaction of both residual stresses which is the real case scenario and it is maximum on the cut edges which indicates non-uniformity of material property. Also, Figure 6.11d is presenting the maximum pressure applied to the laminations

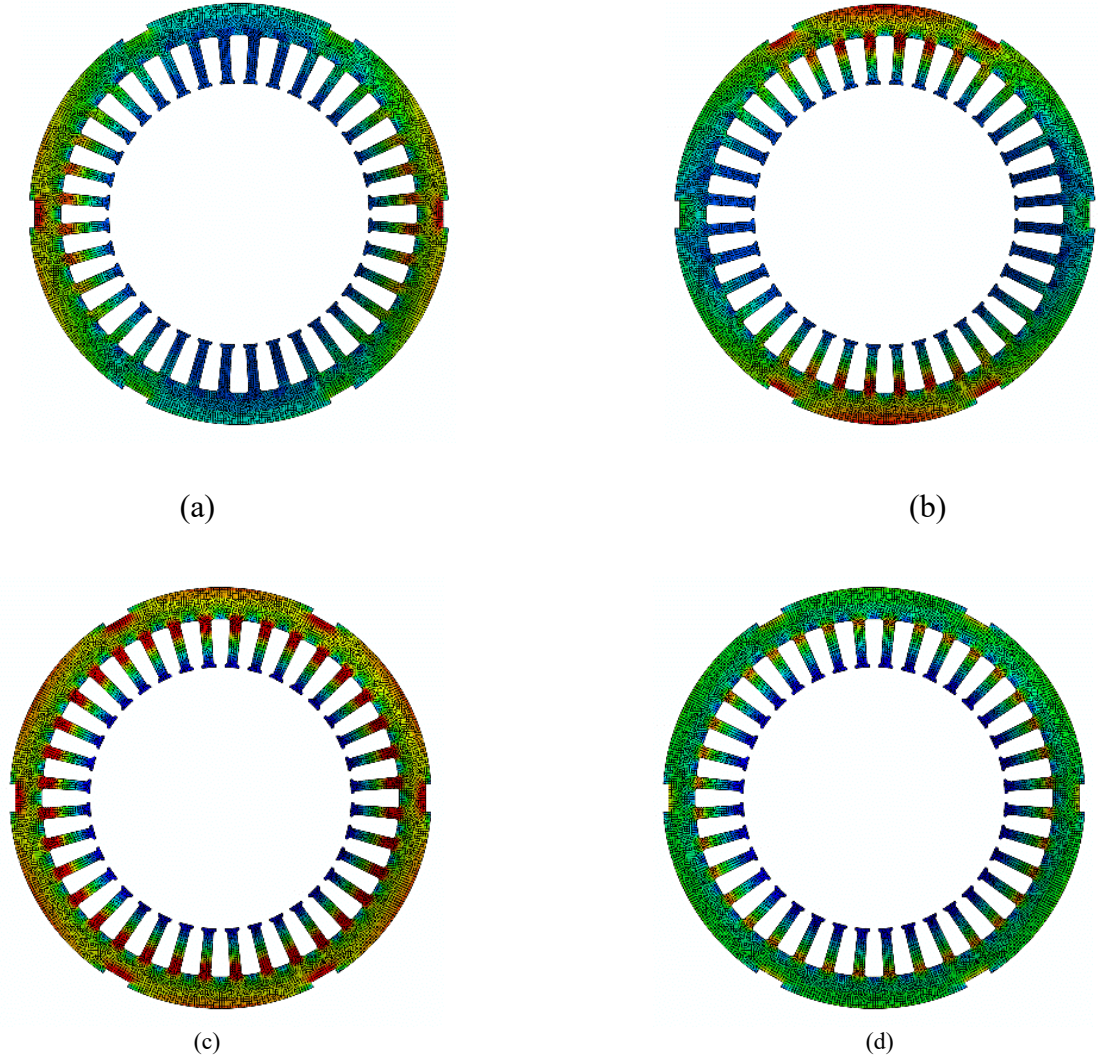


Figure. 6.11. The mechanical effect of cutting procedure on stator lamination. (a) stress in the x -axis. (b) stress in the y -axis. (c) mices. (d) maximum strain.

due to forming the lamination. Since it has been presented that edges are the crucial areas after cutting which are the teeth in the stator and rotor lamination. Hence, to predict the performance of IM in design stage precisely, stator and rotor teeth can be divided into different zones by splitting them in 2-D FEM in terms of stress and strain level produced by mechanical force due to cutting. The concept of having different material properties in teeth zone has been shown in the previous section through stress analysis. It is clear that the estimation of core losses by taking into account the aforementioned aspects lead to precise performance calculation. The dependency of iron loss to the magnetic flux density

and distance from the cut edge is presented using (6.6). Total iron loss density for the lamination is calculated by integrating over the lamination width (w) using (6.6) [12]:

$$p = \frac{2}{w} \int_0^{w/2} c \left(1 + e^{-dx}\right) B^2(H, x) dx \quad (6.6)$$

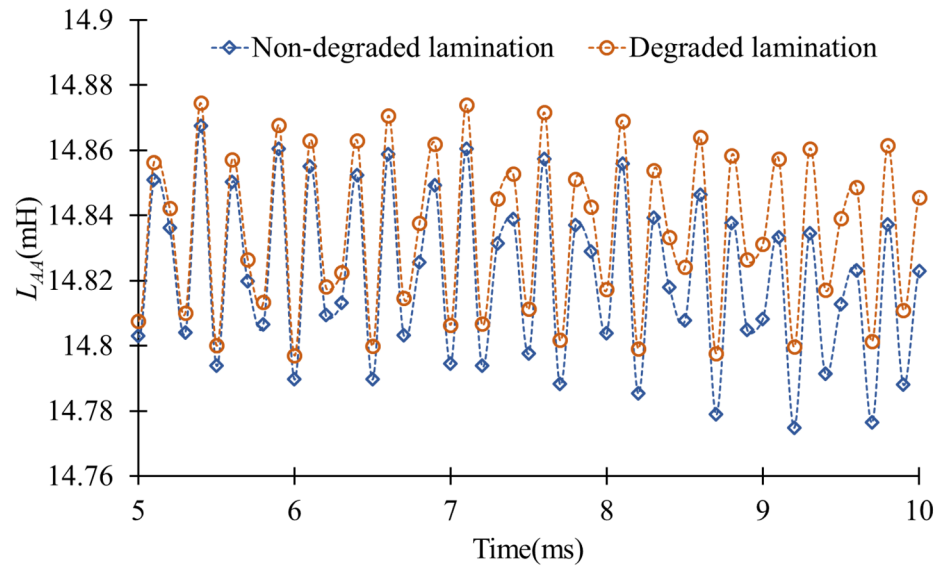
where $B(H, x)$ which is local magnetic flux density. c is found from defined lookup B-H profile as proposed polynomial function and x is the distance from the cut edge. Since loss rises because of residual stress, therefore parameters of the motor vary and output power decreases which result in lower torque production of IM as presented in Figures 6.12 and 6.13. Stator and rotor inductances represent the magnetic circuit property as stored magnetic energies which are generated as a result of variable magnetic flux because of the ac current excitation using (6.7):

$$L_{ij} = (\mu_r \mu_0)^{-1} \int_{\Omega} \vec{B}_i \cdot \vec{B}_j d\Omega \quad (6.7)$$

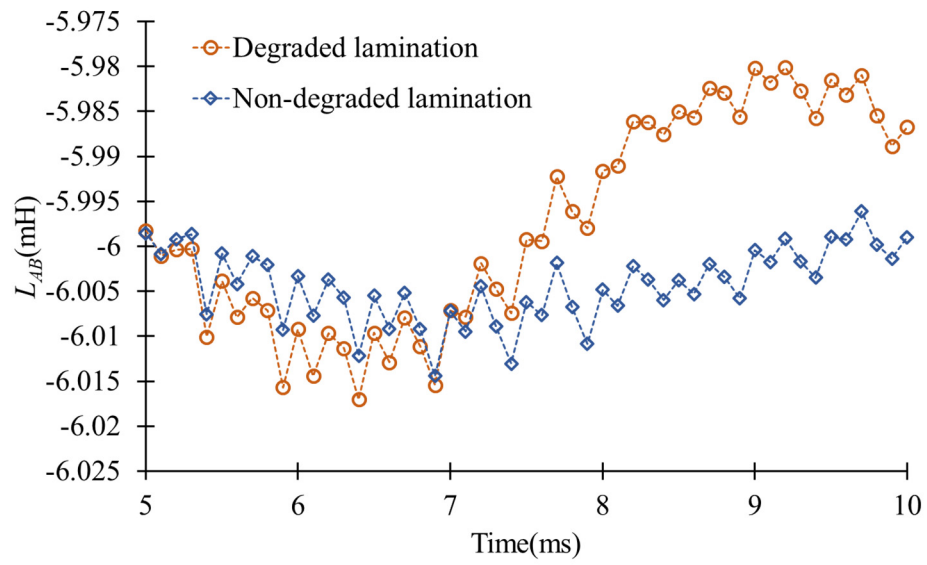
where i, j represents the conductors and Ω is the area that all current carrying conductor passes. Magnetic permeability varies by the saturation level in the tooth region. Since saturation degree is higher due to residual stress induced by a mechanical force applied close to the cut edge, therefore permeability drops. Lower permeability results in a higher reluctance which causes higher inductance for the same level of flux. Higher leakage inductance reduces the torque capability of IM using per unitized maximum torque formulation as (6.8).

$$(T_{\max})_{pu} = \frac{3(x_m/x_1 + x_m)}{2\omega_p \left(r_1(x_m/x_1 + x_m) + \sqrt{(r_1(x_m/x_1 + x_m))^2 + (x_1 + x_2)^2} \right)} \quad (6.8)$$

where r_1 , x_1 , x_m , ω_p and V_p are the stator resistance, leakage reactance, magnetizing reactance, synchronous speed and voltage in per unit system.



(a)



(b)

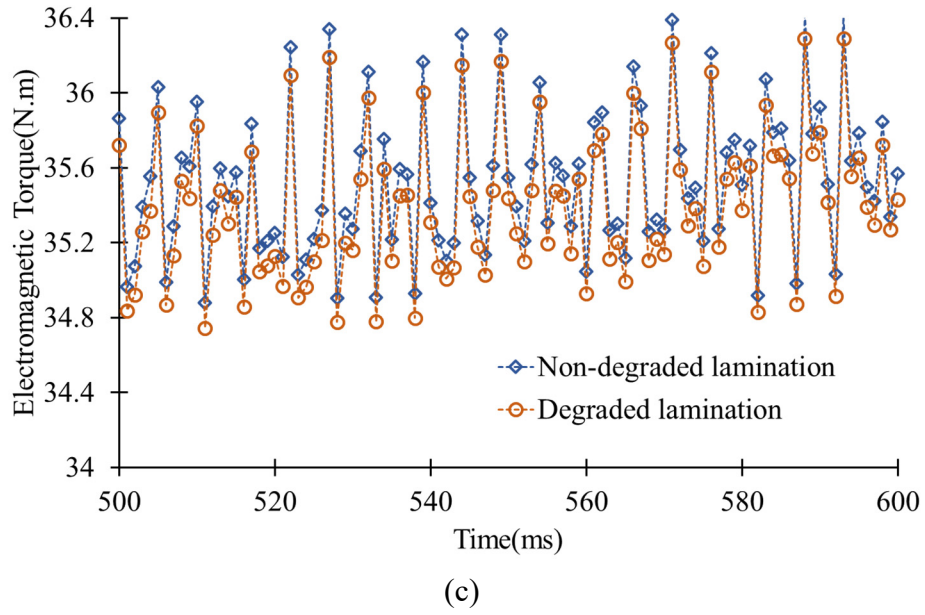
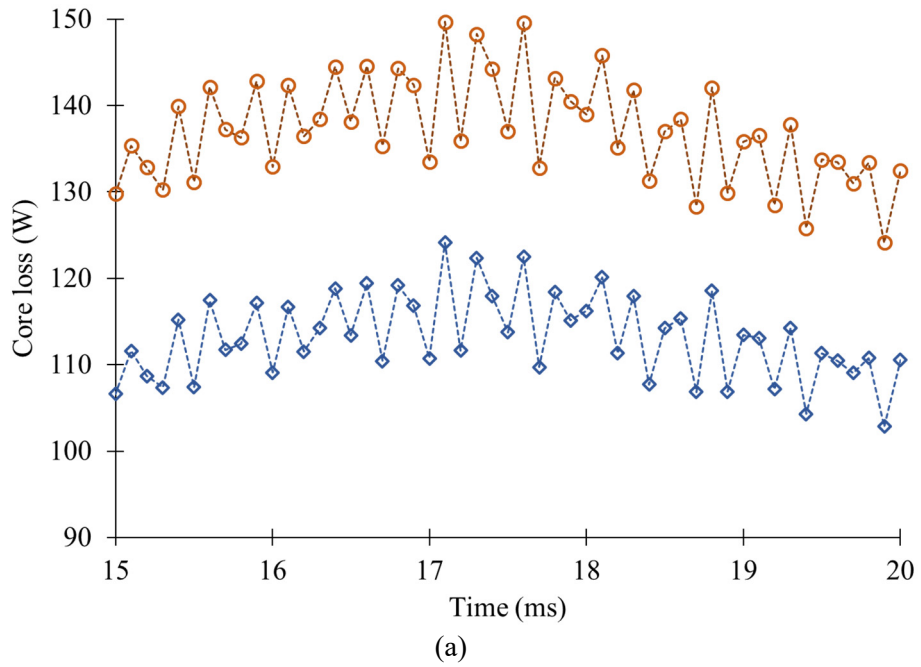


Figure. 6.12. A sample comparison of IM characterization for non-degraded and degraded steel. (a) self-inductance. (b) mutual inductance. (c) the rated electromagnetic torque at 2,915.74 rpm.



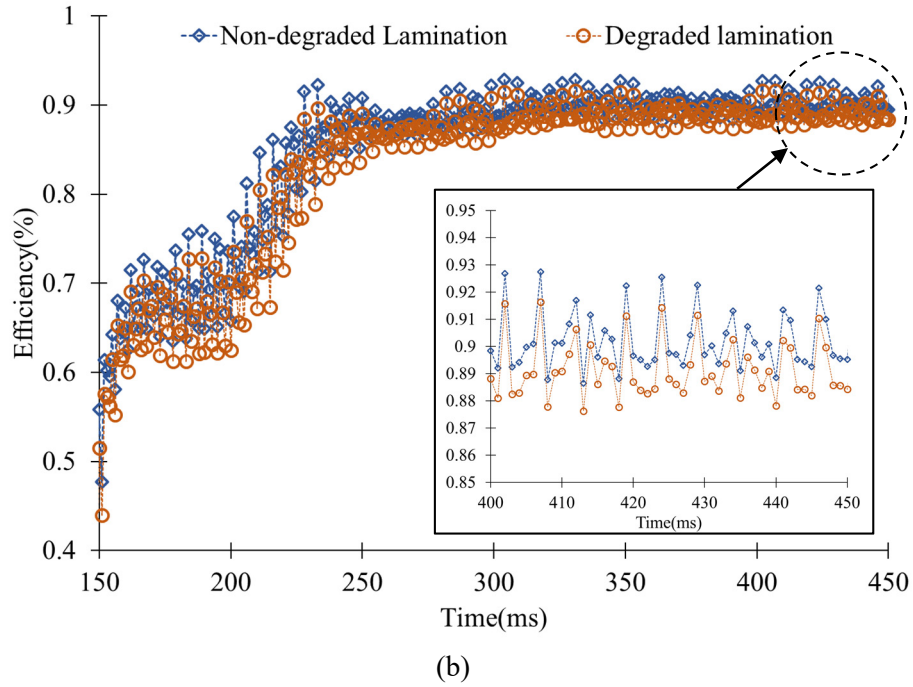


Figure. 6.13. A sample comparison of IM characterization for non-degraded and degraded steel: (a) Core loss, (b) Efficiency at 2,915.74 rpm.

6.5. Determination of Equivalent Parameter for a Wide-Speed Range through Experimental Investigation

Followed by the investigation of the electromagnetic analysis and proposed a semi-analytical approach, the proposed 11 kW high speed IM is prototyped and presented in the Figure. 6.14. A double layer distributed winding with a full coil span and slot fill factor of 70% is achieved. Formed M230-35A steel laminations with 36 slots. Resistance temperature detectors and flux sensors are embedded in all three phase windings to measure the temperature rise and flux density variation in the air-gap. 40/60 Water Glycol cooling is used for axial cooling to maintain the temperature during the experiment.

6.5.1. *Determination of Electrical Circuit Parameters at Rated Condition*

To validate the semi-analytical design optimization and modeling, different tests are performed such as DC-test, Locked-rotor test, No-load test, and load test to determine electrical circuit parameter at the rated operating condition and measured parameters are

compared with the one calculated through the proposed semi-analytical approach. Figure 6.14 is presenting the linear characterization of the stator winding resistance through DC test measurement. It was found out that experimentally measured stator winding resistance is higher because of temperature variation during the test and thermal effect needs to be included in the previously proposed sub-domain model to obtain higher accuracy.

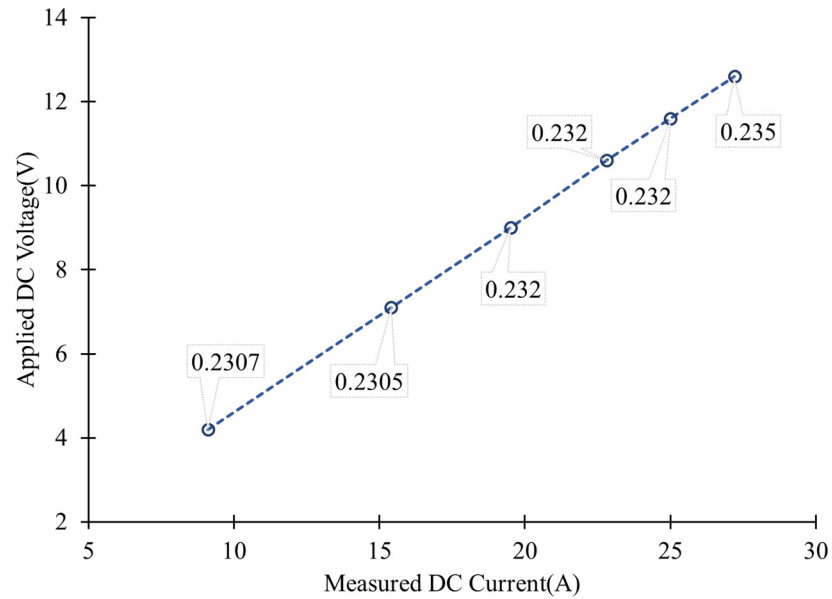
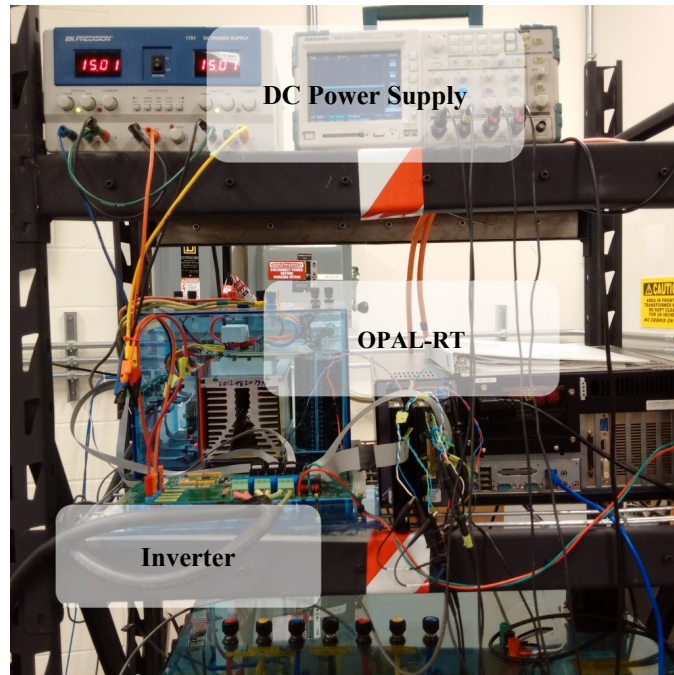
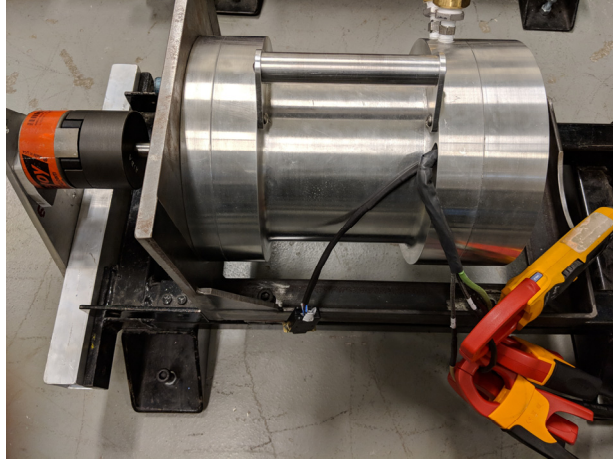


Figure. 6.14. measurement of DC current for various DC voltage excitation.



(a)



(b)



(c)

Figure. 6.15. Experimental set up with locked rotor fixture to determine leakage inductance and rotor resistance. (a) Drive unite set up to apply the voltage for locked rotor test. (b) Current measurement during the locked rotor test. (c) blocked rotor with the built fixture.

Figure 6.15 is presenting the locked rotor test set up. No-load test at rated condition has been performed without a prime mover. Table 6.3 is presenting the measured and FEA results at the rated operating condition for the proposed and prototyped design.

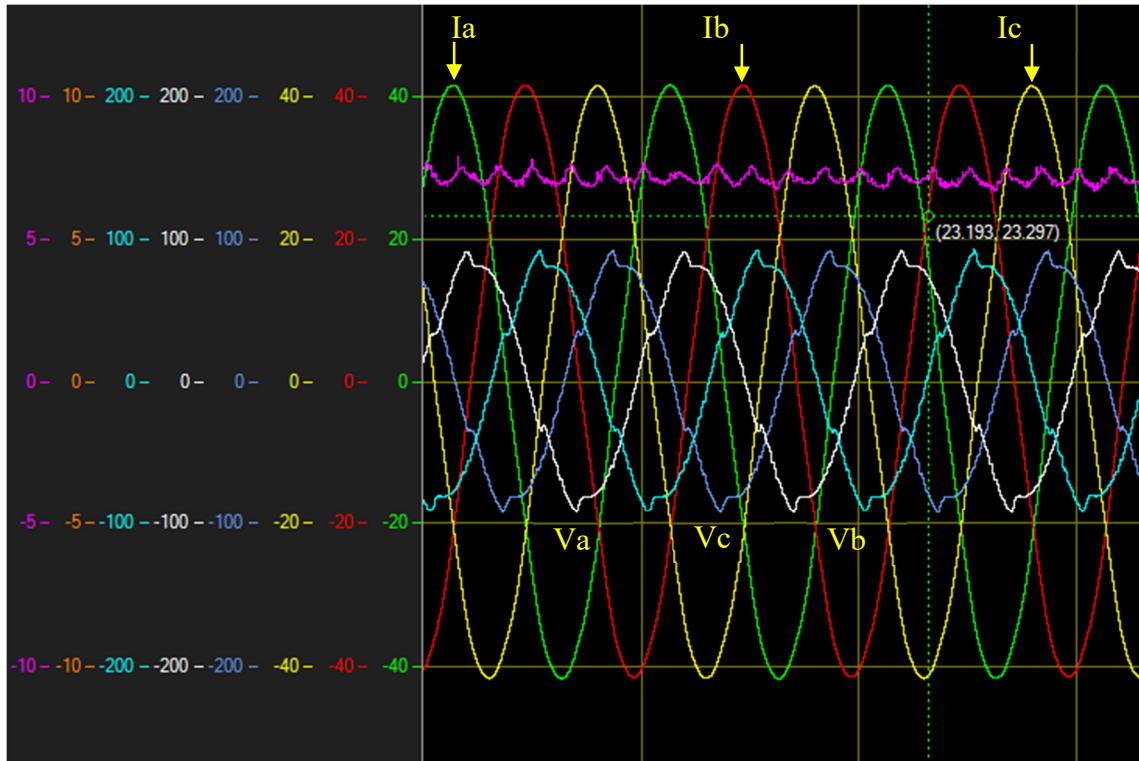
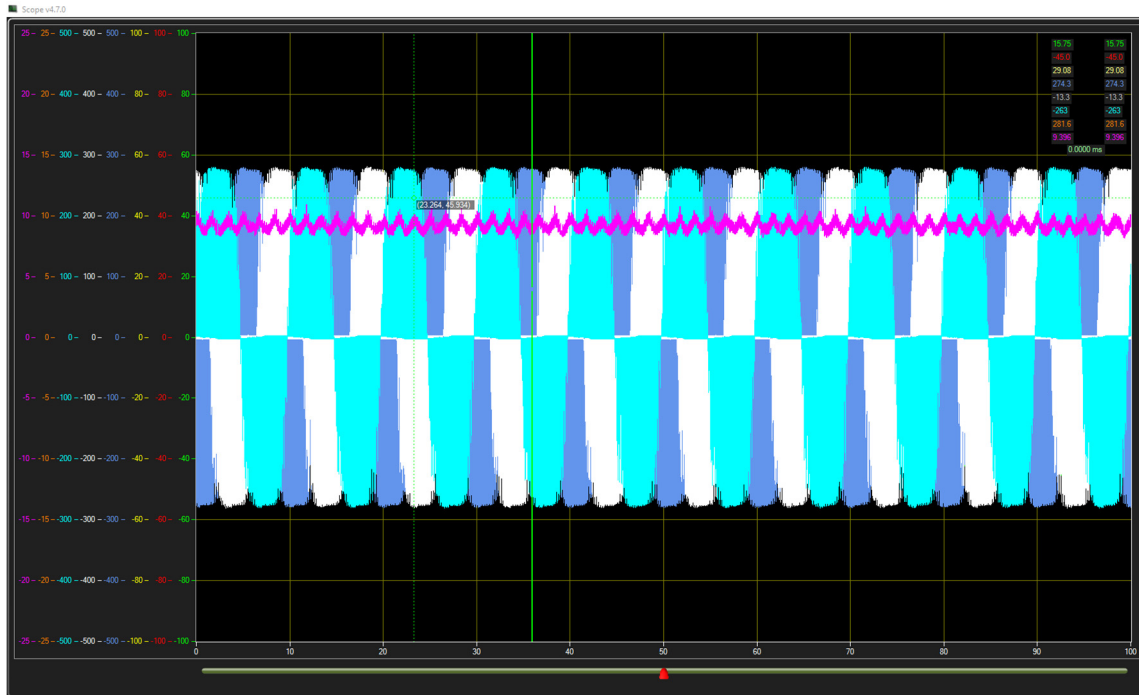
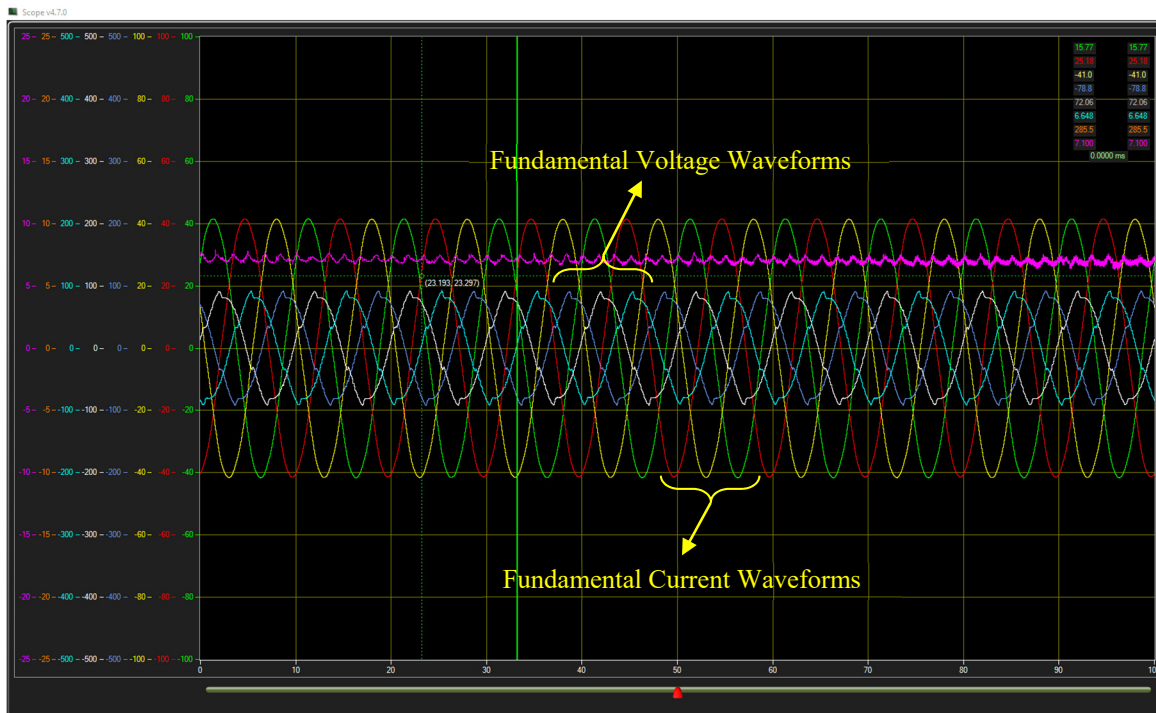


Figure. 6.16. Experimentally measured applied voltage and current waveforms at the no-load test and rated operating condition.



(a)



(b)

Figure. 6.17. Experimentally measured applied voltage and current waveforms at locked rotor test and rated operating condition, a) Applied PWM voltage signals, b) Fundamental voltage and current three-phase waveforms at 2,915.74 rpm.

TABLE 6. 3.
IMPROVED IM PARAMETERS VALIDATION AT RATED CONDITION

| Parameter | $R_s(\Omega)$ | $R_r(\Omega)$ | $X_s(\Omega)$ | $X_{lr}(\Omega)$ | $X_m(m\Omega)$ |
|------------|---------------|---------------|---------------|------------------|----------------|
| FEA | 0.2038 | 0.2414 | 0.725 | 0.689 | 0.0170 |
| Experiment | 0.2305 | 0.2110 | 0.6554 | 0.6554 | 0.0147 |
| Error% | 13% | 12% | 9% | 5% | 13% |

6.5.2.Determination Of the Electrical Circuit Parameters Variation Over Wide Speed Range

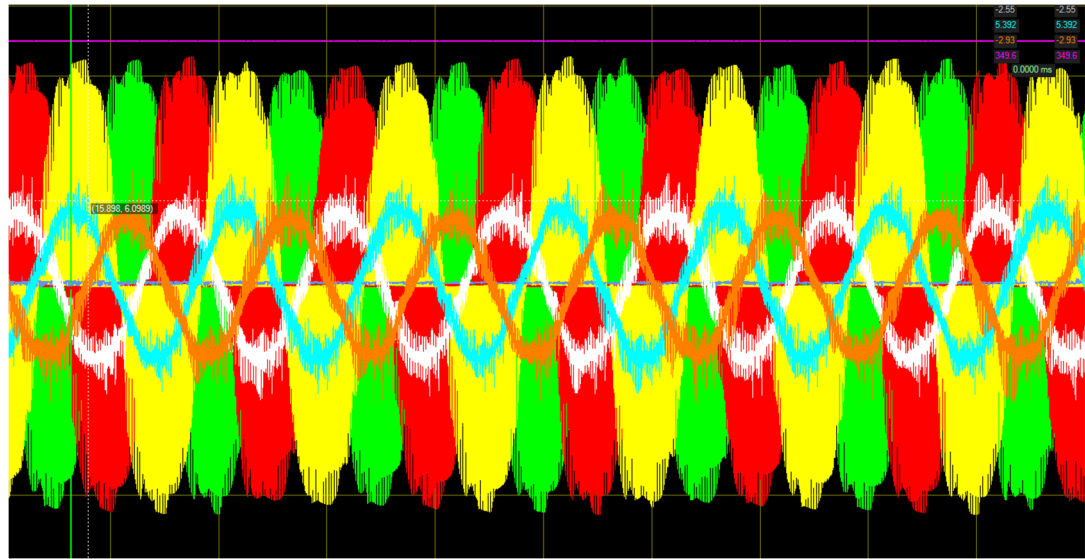
The saturation of the main flux path in the induction machine highly depends on the supply frequency variation [13]. Therefore, the importance of the dependency of IM parameter discrepancy over a wide speed range needs to be investigated. Since, motor performance beyond the rated operating condition depends on the control methodology as much as motor design, hence, it is essential to investigate the reduction of the flux linkage experimentally in order to incorporate the circuit parameters accurately in control algorithm so that the optimal performance can be achieved. Thus, IM parameters are measured and calculated for various operating conditions with the voltage source excitation using FEA and conducting the experiment. Since field-oriented induction motor operation at low speeds is usually achieved with constant flux, therefore, magnetizing inductance can be considered as its rated value for the constant torque region [14] and [15]. The experimental sample of measured applied voltage and current waveforms at the no-load condition for speeds below and beyond the rated operating condition are presented in Figure 6.18. Table 6.4 summarises the measured and calculated magnetizing branch electrical parameters at a different speed.

Optimal stator and rotor leakage inductances ensure operation up to the highest application speed with specified load demand using dynamometer, therefore experimentally measured stator and rotor leakage inductance variations are presented over a wide speed range. In Figures 6.19 and 6.20, some of the captured current and voltage

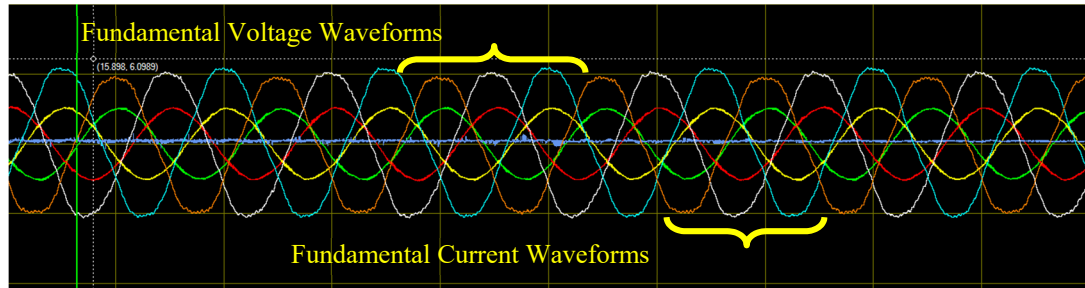
waveforms are presented under variable supply frequencies. These waveforms have been used to calculate the leakage inductances and rotor resistance variations for specified supply frequencies. measured and calculate rotor resistance and leakage inductances are compared with the one calculated numerically and presented in Figures 6.21 and 6.22. Variation of measured the stator leakage inductance and rotor resistance for different stator currents and synchronous speeds are presented in Figures 6.23 and 6.24. Decrease of the stator and rotor leakage inductance is the proof of flux weakening beyond the base speed.

Prototyped IM is tested at the no-load condition to measure the magnetizing inductance at various operating condition over a wide speed range to demonstrate the magnetizing inductance drop beyond the base speed. Measuring magnetizing inductances as a function of stator current estimates the nonlinearly of the magnetizing curve. Consequently, reduction of the magnetizing inductance is presented in Table 6.4 beyond the base speed which indicates the prototyped capability in FW region. The concept of magnetizing inductance reduction is presented in Figures 6.25 and table 6.4. In the constant power region, the rotor flux has to be reduced below the rated value to enable IM operation with constant power. Variation of the rotor flux reference in drive indicates variable saturation level, therefore magnetizing inductance of the machine varies accordingly.

Experimentally measured circuit parameters are in a good agreement with the one calculated using FEA. However, the discrepancy of the measured and calculated data is due to the manufacturing tolerances which has been explained and presented in the previous section.



(a)

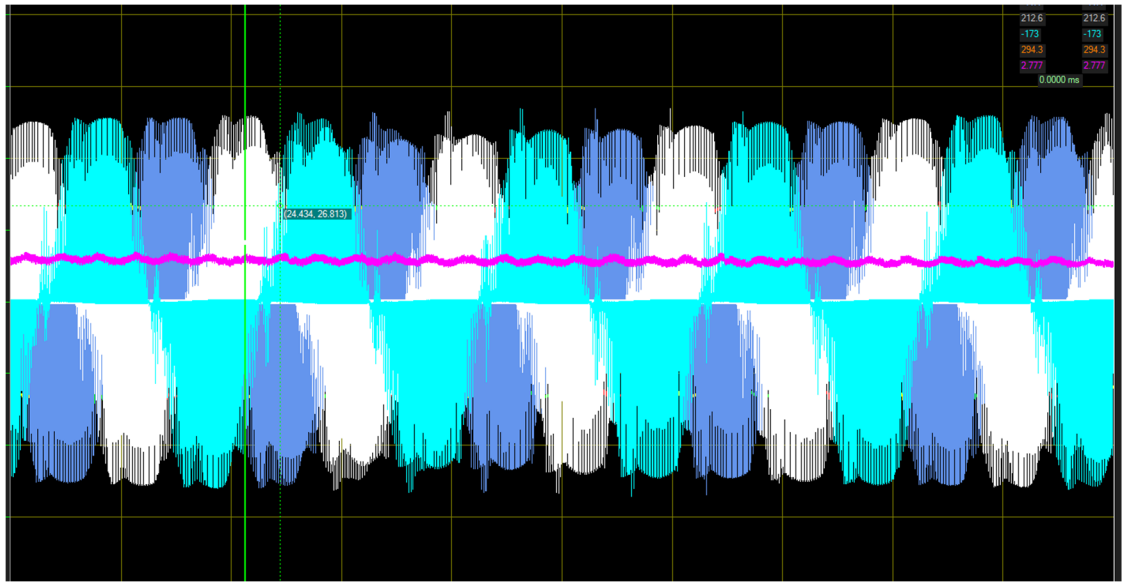


(b)

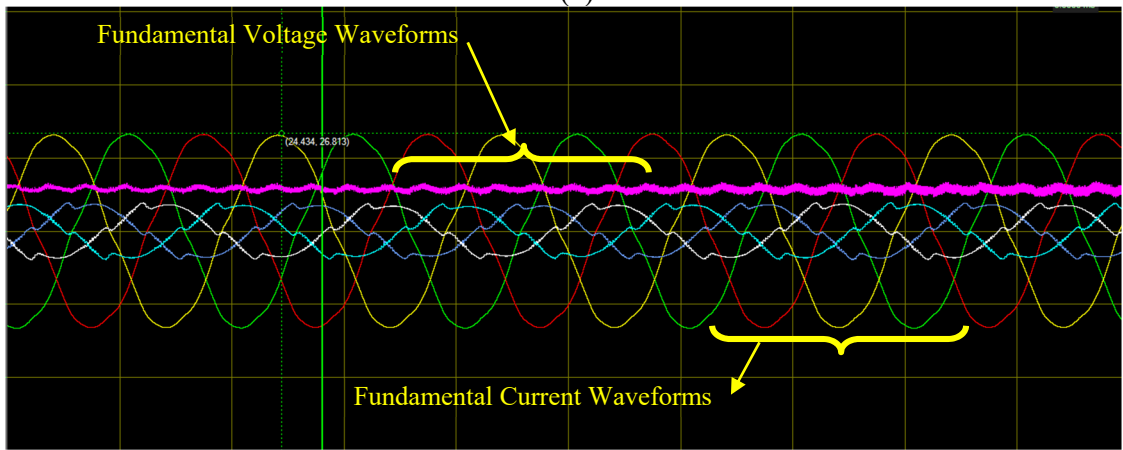
Figure. 6.18. Experimentally measured applied voltage and current waveforms at the no-load test from low to high speed operating conditions. (a) Applied PWM voltage signals. (b) Fundamental voltage and current three-phase waveforms at 1,500 rpm.

TABLE 6. 4.
EXPERIMENTAL VALIDATION OF MAGNETIZING FLUX WEAKENING BEYOND RATED SPEED

| Speed (rpm) | 1,000 | 2,000 | 3,000 | 4,000 |
|-------------|----------|----------|----------|----------|
| $V_{LL}(V)$ | 31.1127 | 57.27565 | 85.4185 | 141.5911 |
| $I_{LL}(A)$ | 3.959798 | 4.355778 | 4.548818 | 5.964446 |
| $I_m(A)$ | 3.764725 | 4.080274 | 4.339296 | 5.517032 |
| $L_m(H)$ | 0.011391 | 0.009674 | 0.009044 | 0.008843 |

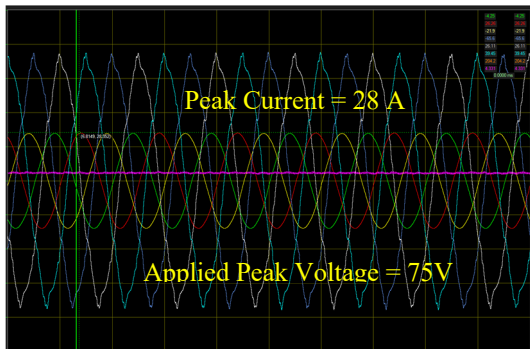


(a)

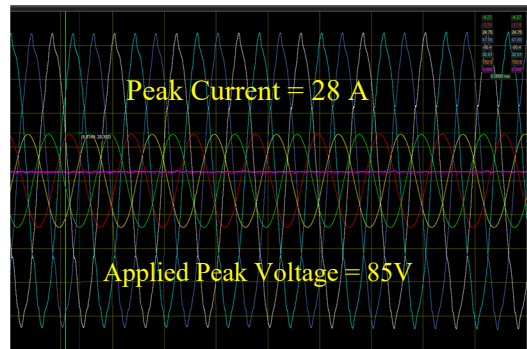


(b)

Figure. 6.19. Experimentally measured applied voltage and current waveforms at locked rotor test. (a) Applied PWM voltage signals. (b) Fundamental voltage and current three phase waveforms at 1,500 rpm.



(a)



(b)

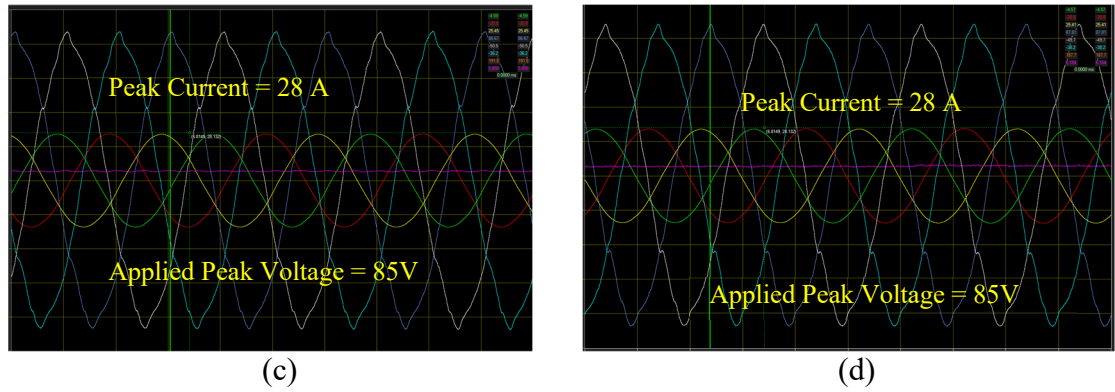


Figure. 6.20. Experimentally measured applied voltage and current waveforms at locked rotor test from low to high speed operating conditions applied voltage and current waveforms at locked rotor test. (a) at 4,000 rpm. (b) at 5,000 rpm. (c) at 6,000 rpm. (d) at 7,000 rpm.

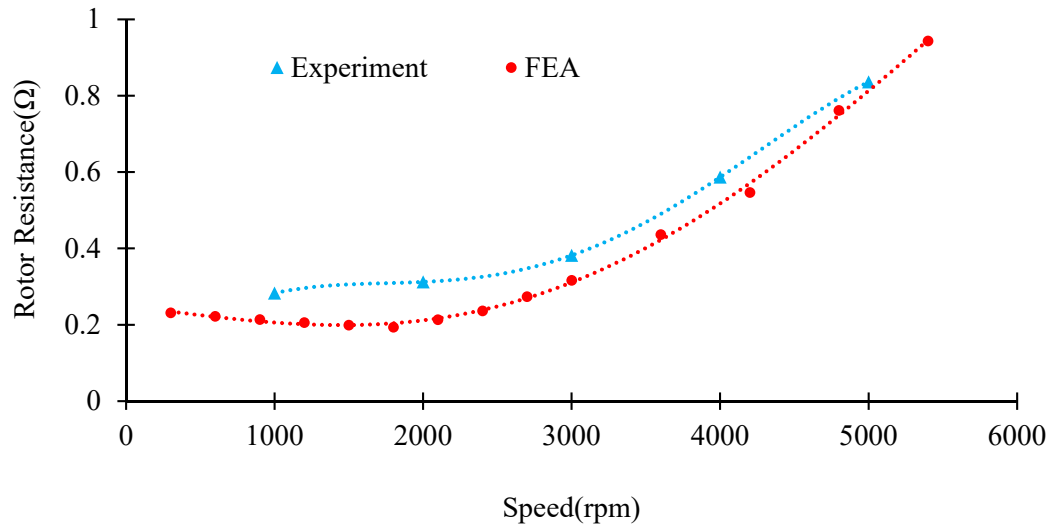


Figure. 6.21. Comparison of measured rotor resistances through experiment and finite element analysis with the similar operating condition for different supply frequencies.

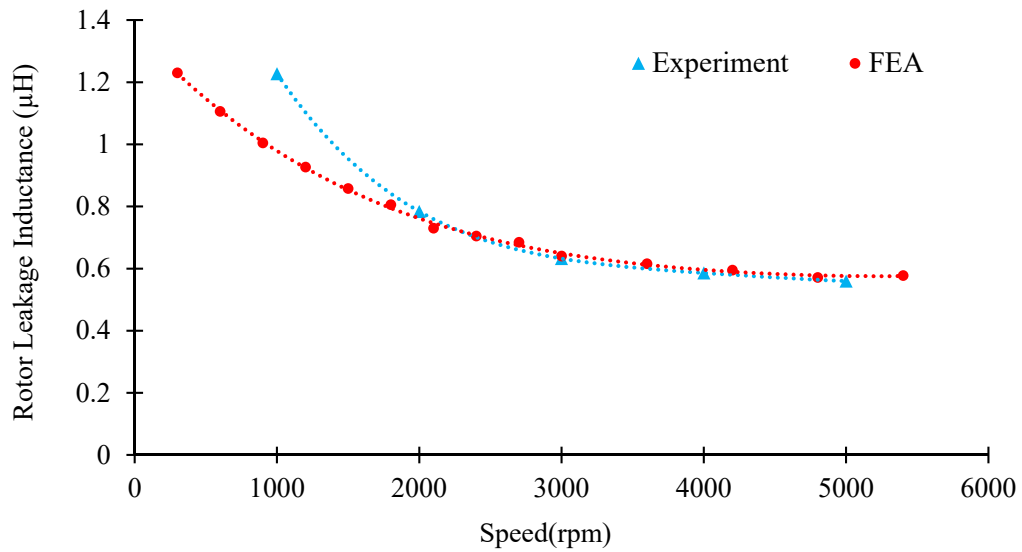


Figure. 6.22. Experimentally measured applied voltage and current waveforms at locked rotor test from low to high speed operating conditions applied voltage and current

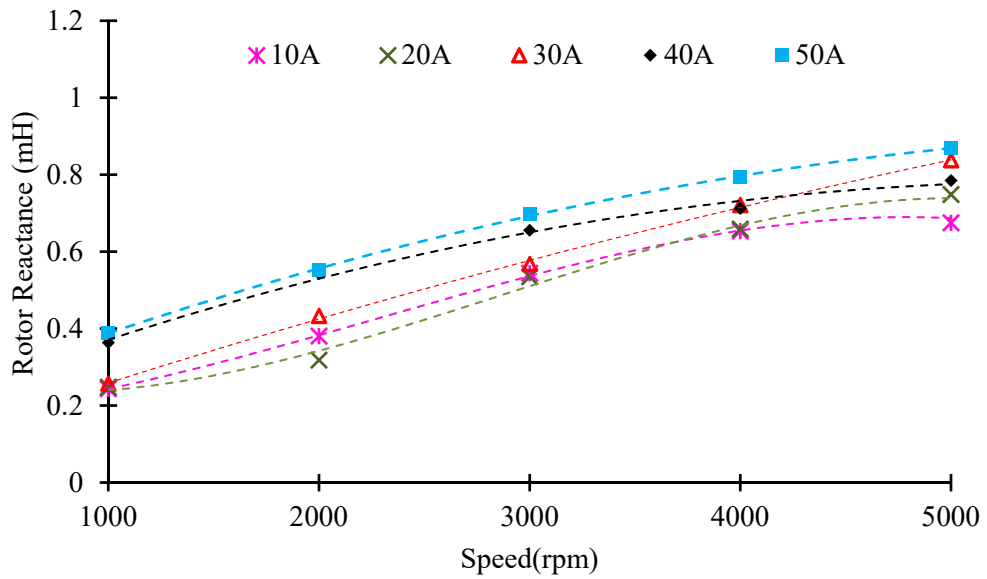


Figure. 6.23. Experimentally measured applied voltage and current waveforms at locked rotor test from low to high speed operating conditions applied voltage and current.

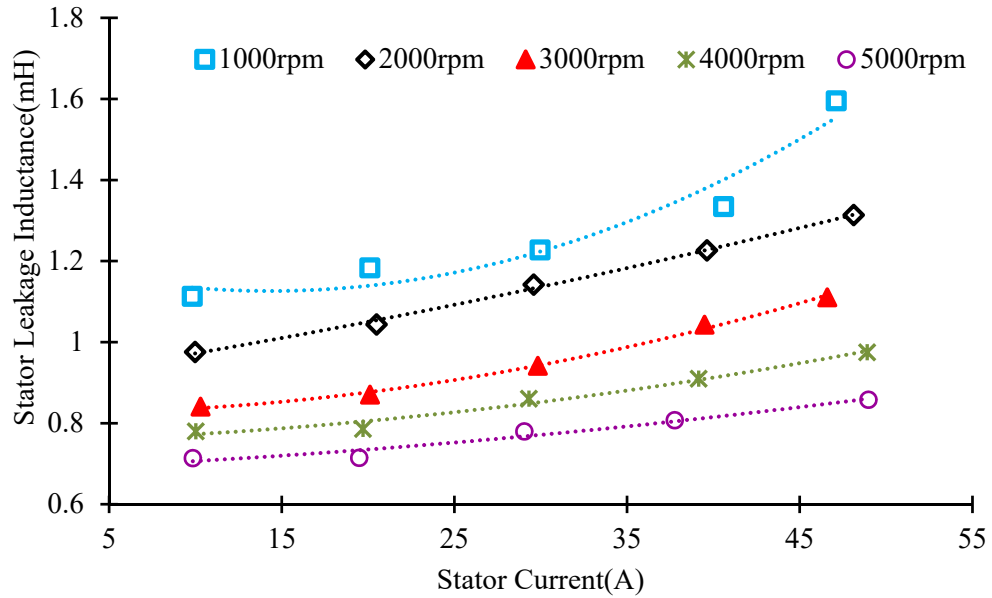


Figure. 6.24. Experimentally measured applied voltage and current waveforms at locked rotor test from low to high speed operating conditions applied voltage and current.

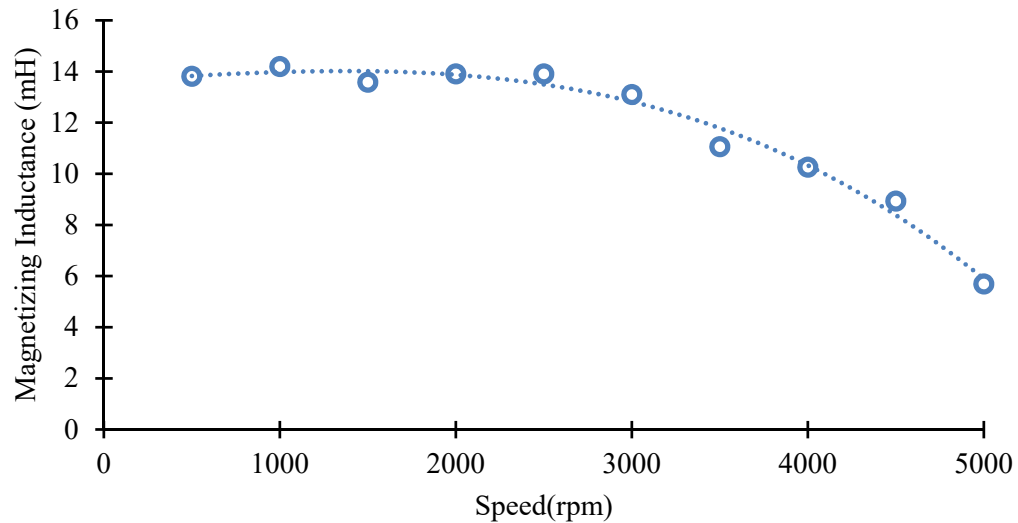
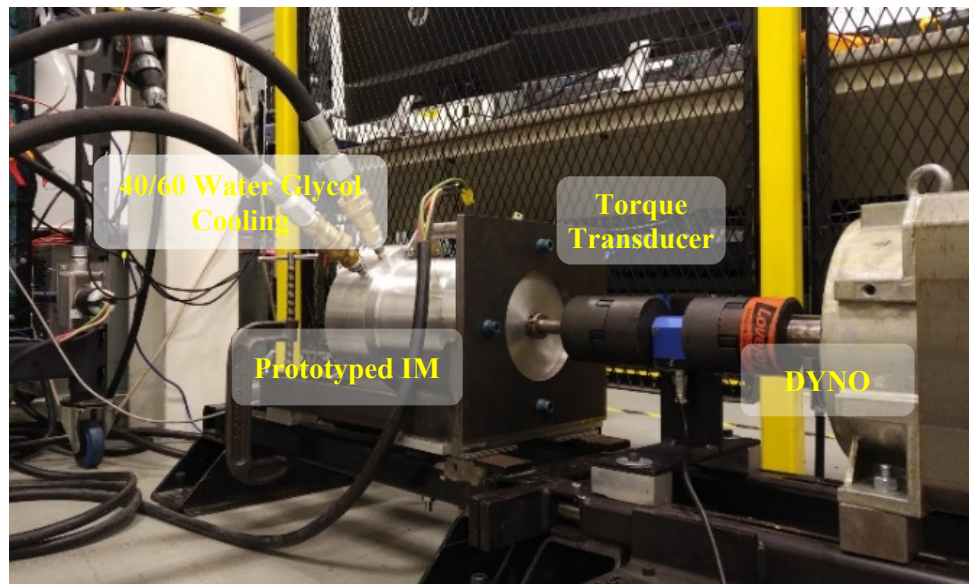


Figure. 6.25. Experimentally measured applied voltage and current waveforms at locked rotor test from low to high speed operating conditions applied voltage and current.

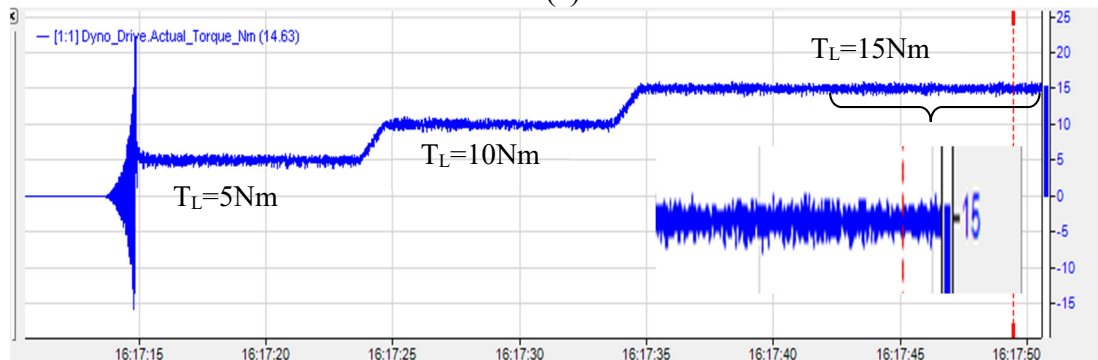
6.6. Load Test

The constant torque region is validated experimentally for the prototyped high speed IM for low speed. For this purpose, a dynamometer is coupled to the motor with the torque transducer to measure the output torque and the rotor speed is measured with the speed

sensor connected to the shaft of the motor. The demand for the torque is controlled through axially coupled dynamometer. Motor cooling is connected to the chiller and 40/60 water glycol cooling liquid has been used to maintain the temperature during the test. Figure 6.26(a) is presenting the experimentally coupled prototyped IM with the torque control dynamometer. Figure 6.26(b) demonstrates the sample measurement of the torque through a torque transducer for 5, 10, 15 Nm for 1,000 rpm. Figure 6.27 is presenting the measured output torque of the motor in constant torque region from 200 rpm to 1,500 rpm with the load torque variation of 5, 10, 15, 20, 25 Nm.



(a)



(b)

Figure. 6.26. Conducted load test for the prototyped high speed IM. (a) Load test experimental set up with cooling inlet and outlet connections. (b) Torque demand ramp at 1,000 rpm.

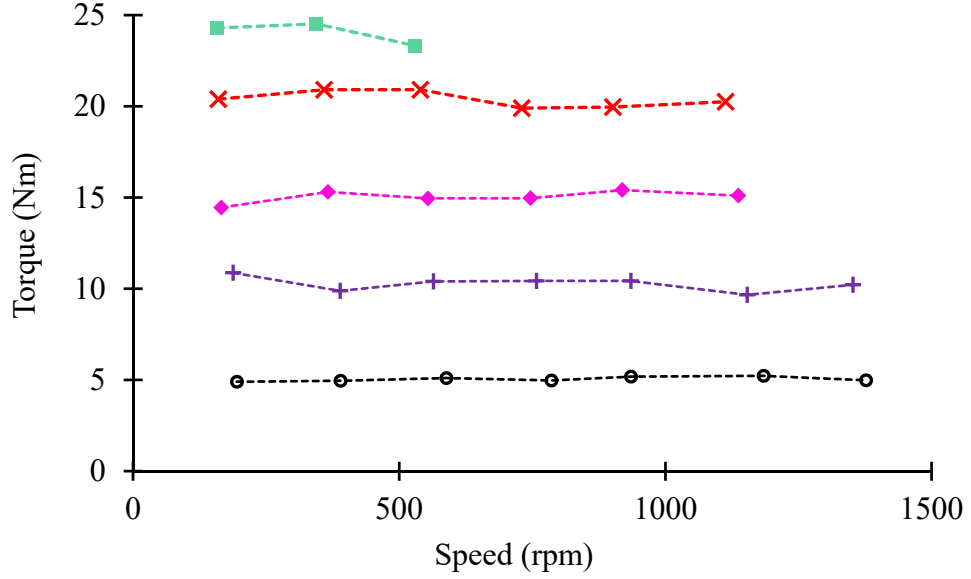


Figure. 6.27. Conducted load test for the prototyped high speed IM. (a) Load test experimental set up with cooling inlet and outlet connections. (b) Torque demand ramp at 1,000 rpm.

6.7. Conclusion

In this chapter, the proposed high speed IM is prototyped. The novel method is proposed to consider the degradation of steel during manufacturing due to cutting in the FEA model of IM. The degradation is characterized by the proposed B-H profile and has been applied to investigate the influence of this parameter on the magnetic characteristics of one example case IM. According to the evaluation of the cutting effect in the stator and rotor core, the calculation results of the iron loss is in a good agreement with experimental data from MBN measurement. Due to higher leakage inductance in degraded laminations, maximum torque capability of IM is reduced. Lower output torque results in a lower efficiency for degraded laminations. Furthermore, in this chapter, the prototyped high speed IM parameter variation which affects the output performance of the motor is experimentally measured through DC, no-load, locked rotor tests for variable supply frequencies and calculated to verify the obtained result with the one in FEA under similar operating condition. The load test conducted for low speeds for the prototyped IM with

40/60 Water Glycol cooling to maintain the temperature, measured torque through torque transducer is in a good agreement with the demand torque.

6.8. References

- [1] K. Yamazaki, K. Tanaka, and M. Ohto, "Impact of Core Material Grades on the Performance of Variable Speed Induction Motors Fed by Inverters," in *IEEE Transactions on Industry Applications*, vol. 54, no. 6, pp. 5833-5842, 2018.
- [2] K. Bourchas et al., "Quantifying Effects of Cutting and Welding on Magnetic Properties of Electrical Steels," in *IEEE Transactions on Industry Applications*, vol. 53, no. 5, pp. 4269-4278, 2017.
- [3] L. Vandenbossche, S. Jacobs, D. Van Hoecke and E. Attrazic, "Impact of mechanical stresses on the magnetic performance of non-oriented electrical steels and its relation to electric machine efficiency," 2015 *IEEE Transportation Electrification Conference and Expo (ITEC)*, Dearborn, MI, 2015
- [4] G. Bertotti, "General properties of power losses in soft ferromagnetic materials," in *IEEE Transactions on Magnetics*, vol. 24, no. 1, pp. 621-630, 1988.
- [5] M. Bali, H. De Gersem and A. Muetze, "Finite-Element Modeling of Magnetic Material Degradation Due to Punching," in *IEEE Transactions on Magnetics*, vol. 50, no. 2, pp. 745-748, 2014.
- [6] P. Rasilo, U. Aydin, T. P. Holopainen, and A. Arkkio, "Analysis of iron losses on the cutting edges of induction motor core laminations," 2016 *XXII International Conference on Electrical Machines (ICEM)*, 2016.
- [7] M. Bali, H. De Gersem and A. Muetze, "Determination of Original Nondegraded and Fully Degraded Magnetic Characteristics of Material Subjected to Laser Cutting," in *IEEE Transactions on Industry Applications*, vol. 53, no. 5, pp. 4242-4251, 2017.
- [8] M. Bali, H. D. Gersem and A. Muetze, "Determination of Original Nondegraded and Fully Degraded Magnetic Properties of Material Subjected to Mechanical Cutting," in *IEEE Transactions on Industry Applications*, vol. 52, no. 3, pp. 2297-2305, 2016.
- [9] S. Elfgen, S. Böhmer, S. Steentjes, D. Franck and K. Hameyer, "Continuous model of magnetic material degradation due to cutting effects in the numerical simulation of electro laminations, " in ETG-Fachbericht 146: IKMT, 2015.
- [10] He.Y, Mehdi. M, J. Hilinski. E, Edrisy. Afsaneh, "Through-process characterization of local anisotropy of Non-oriented electrical steel using magnetic Barkhausen noise", *Journal of Magnetism and Magnetic Materials*, Volume 453, 2018.
- [11] A. Samimi, W. Krause, L. Clapham, M. Gallagher, Y. Ding, P. Ghosh, R. Chromik, A. Knight, "Correlation Between AC Core Loss and Surface Magnetic Barkhausen Noise in Electric Motor Steel, *Journal of Nondestructive Evaluation*, Volume 33, pp 663–669, 2014.
- [12] R. Sundaria, A. Lehtikainen, A. Hannukainen, and A. Arkkio, "Higher-order finite element modeling of material degradation due to cutting," 2017 *IEEE International Electric Machines and Drives Conference (IEMDC)*, 2017.
- [13] R. R. Seebacher, K. Krischan, and G. Dannerer, "Investigating the dependency of an induction machine's main inductance on the supply frequency," 2008 18th *International Conference on Electrical Machines (ICEM)*, Vilamoura, 2008.

- [14] L. Monjo, F. Córcoles and J. Pedra, "Saturation Effects on Torque- and Current–Slip Curves of Squirrel-Cage Induction Motors," in *IEEE Transactions on Energy Conversion*, vol. 28, 2013.
- [15] A. G. Yepes et al., "Parameter Identification of Multiphase Induction Machines with Distributed Windings—Part 1: Sinusoidal Excitation Methods," in *IEEE Transactions on Energy Conversion*, vol. 27. 2012.

CHAPTER 7

CONCLUSION AND SUGGESTED FUTURE WORK

7.1. Conclusion

This chapter is the conclusions of the previous chapters which ultimately led to the development of a high speed induction motor using proposed semi-analytical approach and proposed design optimization procedure in an effort to reduce the computational cost which can be extended to design and optimize the other electric machine topologies. A brief conclusion is presented here.

- Optimal stator/rotor slot-pole combination is selected within a constant volume with reduced space harmonic due to slotting effect maintaining rated torque and enhancing efficiency of induction motor.
- Skewing rotor bars leads to reduction of the excessive permeance harmonics and increase of the constant power region.
- 3-D FEA is computationally expensive to optimize the structure of electric machines.
- Proposed 3-D sub-domain method considers material non- linearity, stator and rotor slotting, and axial asymmetry which is more efficient in optimization process in order to reduce spatial harmonics.
- The improved rotor configuration has wider constant power region without sacrificing constant torque region with low torque ripple, high power factor and high efficiency.
- Lamination degradation significantly effects IM parameters, which increases core loss, reduces torque production which creates a significant gap between simulation and prototyped performance characterization.

7.2. Future Work

- A. Extending 3-D sub-domain model to optimize permanent magnet synchronous machine.

- B. Reduction of rotor conductor loss by introducing new lightweight and superconductive materials to enhance the efficiency.
- C. Improving the cooling system to enable motor operation safely in the peak operating condition.

APPENDIX A: LIST OF PUBLICATIONS

Journals

- [1] **A. Mollaeian**, E. Ghosh, S. Kim, J. Tjong, and N. C. Kar, " Parametric and Sensitivity based Inductance Ratio Minimization of Induction Motor with Optimized Rotor Configuration for EV Application," submitted to *IEEE Transactions on Transportation Electrification*, 2019.
- [2] Y. He, M. Mehdi, E.J. Hilinski, A. Edrisy, S. Mukundan, **A. Mollaeian**, and N. C. Kar, "Evaluation of Local Anisotropy of Magnetic Response from Non-Oriented Electrical Steel by Magnetic Barkhausen Noise," *IEEE Transactions on Magnetics*, vol. 54, no. 11, pp. 1-5, 2018.
- [3] E. Ghosh, **A. Mollaeian**, S. Kim, J. Tjong, and N. C. Kar, "DNN-Based Predictive Magnetic Flux Reference for Harmonic Compensation Control in Magnetically Unbalanced Induction Motor," *IEEE Transactions on Magnetics*, vol. 53, no. 11, pp. 1-7, Nov. 2017.
- [4] **A. Mollaeian**, E. Ghosh, H. Dhulipati, J. Tjong, and N. C. Kar, "3-D Sub-Domain Analytical Model to Calculate Magnetic Flux Density in Induction Machines with Semiclosed Slots Under No-Load Condition," *IEEE Transactions on Magnetics*, vol. 53, no. 6, pp. 1-5, June 2017.
- [5] M. Mousavi, **A. Mollaeian**, N.C. Kar, and M. Timusk, "A Novel Parallel Modelling Wavelet Based Mechanical Fault Detection Using Stator Current Signature of Induction Machine under Variable Load Conditions, " *Journal of Electrical Engineering & Electronic Technology*, 2017.
- [6] E. Ghosh, **A. Mollaeian**, W. Hu and N. C. Kar, "A Novel Control Strategy for Online Harmonic Compensation in Parametrically Unbalanced Induction Motor," *IEEE Transactions on Magnetics*, vol. 52, no. 7, pp. 1-4, July 2016.
- [7] A. Balamurali, C. Lai, **A. Mollaeian**, V. Loukanov, and N.C. Kar, "Analytical Investigation of Magnet Eddy Current Losses in Interior Permanent Magnet Motor Using Modified Winding Function Theory Accounting for Pulse Width Modulation Harmonics, " *IEEE Transactions on Magnetics*, vol. 52, 2016.

- [8] **A. Mollaeian**, E. Ghosh, S. Kim, J. Tjong, and N. C. Kar, "Investigation of Iron Loss of Induction Machine due to Magnetic Property Deterioration of Laminations due to Manufacturing," will be submitted to IET Power systems and applications.

Conference

- [1] **A. Mollaeian**, M. Mehdi, E. Ghosh, A. Edrisy, S. Kim, J. Tjong, and N. C. Kar, "Investigation of Electromagnetic Torque Capability Reduction of Induction Machine due to Magnetic Property Deterioration of Laminations due to Manufacturing," accepted in the Proc. of *International Conference on Magnetism*, July, 2018.
- [2] Y. He, M. Mehdi, E.J. Hilinski, A. Edrisy, S. Mukundan, **A. Mollaeian**, and N. C. Kar, "Evaluation of Local Anisotropy of Magnetic Response from Non-Oriented Electrical Steel by Magnetic Barkhausen Noise," 2018 *IEEE International Magnetics Conference (INTERMAG)*, 2018.
- [3] E. Ghosh, **A. Mollaeian**, S. Kim and N. C. Kar, "DNN Predictive Magnetic Flux Control for Harmonics Compensation in Magnetically Unbalanced Induction Motor," in the Proc. of *IEEE International Magnetics Conference*, pp. 1-1 Dublin, 2017.
- [4] E. Ghosh, **A. Mollaeian**, S. Kim, J. Tjong, and N. C. Kar, "Intelligent Flux Predictive Control Through Online Stator Inter-Turn Fault Detection for Fault-Tolerant Control of Induction Motor," in the Proc. of *IEEE International Conference on Industrial Technology (ICIT)*, pp. 306-311, Toronto, ON, 2017.
- [5] E. Ghosh, **A. Mollaeian**, S. Kim, J. Tjong, and N. C. Kar, "Intelligent flux predictive control through online stator inter-turn fault detection for fault-tolerant control of induction motor," *IEEE International Conference on Industrial Technology (ICIT)*, Toronto, 2017.
- [6] **A. Mollaeian**, M. Mousavi, A. Balamurali, J. Tjong, and N. C. Kar, "Optimal Design of Skewed Rotor Induction Machine for Space Harmonic Reduction Considering z-Axis Magnetic Flux Density Variation," presented at the *IEEE Intermag Conference*, San Diego, USA, 2016.

- [7] **A. Mollaeian**, E. Ghosh, H. Dhulipati, J. Tjong and N. C. Kar, "3-D Sub-Domain Analytical Model to Calculate Magnetic Flux Density in Induction Machines with Semi-Closed Slots Under No-Load Condition," in the Proc. of *2016 IEEE Conference on Electromagnetic Field Computation (CEFC)*, pp. 1-1, Miami, FL, 2016.
- [8] E. Ghosh, F. Ahmed, **A. Mollaeian**, J. Tjong and N. C. Kar, "Online Parameter Estimation and Loss Calculation Using Duplex Neural — Lumped Parameter Thermal Network for Faulty Induction Motor," in the Proc. of *IEEE Conference on Electromagnetic Field Computation (CEFC)*, pp. 1-1, Miami, FL, 2016.
- [9] E. Ghosh, **A. Mollaeian**, W. Hu and N. C. Kar, "A Novel Control Strategy for Online Harmonic Compensation in Parametrically Unbalanced Induction Motor," in the Proc. of *2016 IEEE International Magnetism Conference*, pp. 1-1, San Diego, 2016.
- [10] **A. Mollaeian**, S. M. Sangdehi, A. Balamurali, G. Feng, J. Tjong, and N. C. Kar, "Reduction of space harmonics in induction machines incorporating rotor bar optimization through a coupled IPSO and 3-D FEA algorithm," *2016 XXII International Conference on Electrical Machines (ICEM)*, Lausanne, 2016.
- [11] A. Balamurali, **A. Mollaeian**, S. M. Sangdehi, and N. C. Kar, "Parameter identification of permanent magnet synchronous machine based on metaheuristic optimization," *2015 IEEE International Electric Machines & Drives Conference (IEMDC)*, 2015.

APPENDIX B: LIST OF INDUSTRIAL PROJECTS AND SCHOLARSHIPS

Projects Undertaken

1. *NSERC CRD project with Ford Motor Company Ltd. and D&V Electronics Ltd.*
 - Electric machine design and optimization for Next-generation Electric Vehicles
 - Motor prototype development for “Powertrain Components and Systems for Next-generation Electric Vehicles”
2. *ORF project with Ford Motor Company Ltd. and D&V Electronics Ltd.*
 - Attending technical workshops and courses related to project description
 - Motor prototype development for “Powertrain Components and Systems for Next-generation Electric Vehicles”
3. Collaborative *Research* Project with BorgWarner PDS
 - Induction Machine Characterization and Performance Testing
4. *NSERC Engage project entitled with IGB Automotive Ltd.*
 - Investigation of noise reduction schemes for bldc motors in comfort seat ventilation module. Performance mapping of BLDC motors in a car seat under various operating conditions.

Scholarships Received

1. Research Scholarship received from Canada Research Chair Program in Electrified Transportation Systems, Centre for Hybrid Automotive Research and Green Energy, 2013 – 2019.
2. University of Windsor Graduate Teaching Assistance, 2013 – 2017.
3. Outstanding Graduate Student Scholarship honored by Graduate Student Society, University of Windsor, March 2017.
4. Outstanding Graduate Student Scholarship honored by the Frederick Atkins Award, April 2015.

APPENDIX C: PERMISSION FOR USING IEEE PUBLICATIONS

5/23/2019

Rightslink® by Copyright Clearance Center



RightsLink®

Home

Create Account

Help



Title: 3-D Sub-Domain Analytical Model to Calculate Magnetic Flux Density in Induction Machines With Semiclosed Slots Under No-Load Condition

Author: Aida Mollaeian

Publication: Magnetics, IEEE Transactions on

Publisher: IEEE

Date: June 2017

Copyright © 2017, IEEE

LOGIN

If you're a **copyright.com** user, you can login to RightsLink using your copyright.com credentials.

Already a **RightsLink** user or want to [learn more?](#)

Thesis / Dissertation Reuse

The IEEE does not require individuals working on a thesis to obtain a formal reuse license, however, you may print out this statement to be used as a permission grant:

Requirements to be followed when using any portion (e.g., figure, graph, table, or textual material) of an IEEE copyrighted paper in a thesis:

- 1) In the case of textual material (e.g., using short quotes or referring to the work within these papers) users must give full credit to the original source (author, paper, publication) followed by the IEEE copyright line © 2011 IEEE.
- 2) In the case of illustrations or tabular material, we require that the copyright line © [Year of original publication] IEEE appear prominently with each reprinted figure and/or table.
- 3) If a substantial portion of the original paper is to be used, and if you are not the senior author, also obtain the senior author's approval.

Requirements to be followed when using an entire IEEE copyrighted paper in a thesis:

- 1) The following IEEE copyright/ credit notice should be placed prominently in the references: © [year of original publication] IEEE. Reprinted, with permission, from [author names, paper title, IEEE publication title, and month/year of publication]
- 2) Only the accepted version of an IEEE copyrighted paper can be used when posting the paper or your thesis online.
- 3) In placing the thesis on the author's university website, please display the following message in a prominent place on the website: In reference to IEEE copyrighted material which is used with permission in this thesis, the IEEE does not endorse any of [university/educational entity's name goes here]'s products or services. Internal or personal use of this material is permitted. If interested in reprinting/republishing IEEE copyrighted material for advertising or promotional purposes or for creating new collective works for resale or redistribution, please go to http://www.ieee.org/publications_standards/publications/rights/rights_link.html to learn how to obtain a License from RightsLink.

If applicable, University Microfilms and/or ProQuest Library, or the Archives of Canada may supply single copies of the dissertation.

BACK

CLOSE WINDOW

Copyright © 2019 [Copyright Clearance Center, Inc.](#) All Rights Reserved. [Privacy statement.](#) [Terms and Conditions.](#)
Comments? We would like to hear from you. E-mail us at customercare@copyright.com



RightsLink®

[Home](#)
[Create Account](#)
[Help](#)


Title: 3-D sub-domain analytical model to calculate magnetic flux density in induction machines with semi-closed slots under no-load condition

Conference Proceedings: 2016 IEEE Conference on Electromagnetic Field Computation (CEFC)

Author: Aida Mollaeian

Publisher: IEEE

Date: Nov. 2016

Copyright © 2016, IEEE

LOGIN

If you're a **copyright.com user**, you can login to RightsLink using your copyright.com credentials. Already a **RightsLink user** or want to [learn more?](#)

Thesis / Dissertation Reuse

The IEEE does not require individuals working on a thesis to obtain a formal reuse license, however, you may print out this statement to be used as a permission grant:

Requirements to be followed when using any portion (e.g., figure, graph, table, or textual material) of an IEEE copyrighted paper in a thesis:

- 1) In the case of textual material (e.g., using short quotes or referring to the work within these papers) users must give full credit to the original source (author, paper, publication) followed by the IEEE copyright line © 2011 IEEE.
- 2) In the case of illustrations or tabular material, we require that the copyright line © [Year of original publication] IEEE appear prominently with each reprinted figure and/or table.
- 3) If a substantial portion of the original paper is to be used, and if you are not the senior author, also obtain the senior author's approval.

Requirements to be followed when using an entire IEEE copyrighted paper in a thesis:

- 1) The following IEEE copyright/ credit notice should be placed prominently in the references: © [year of original publication] IEEE. Reprinted, with permission, from [author names, paper title, IEEE publication title, and month/year of publication]
- 2) Only the accepted version of an IEEE copyrighted paper can be used when posting the paper or your thesis online.
- 3) In placing the thesis on the author's university website, please display the following message in a prominent place on the website: In reference to IEEE copyrighted material which is used with permission in this thesis, the IEEE does not endorse any of [university/educational entity's name goes here]'s products or services. Internal or personal use of this material is permitted. If interested in reprinting/republishing IEEE copyrighted material for advertising or promotional purposes or for creating new collective works for resale or redistribution, please go to http://www.ieee.org/publications_standards/publications/rights/rights_link.html to learn how to obtain a License from RightsLink.

If applicable, University Microfilms and/or ProQuest Library, or the Archives of Canada may supply single copies of the dissertation.

[BACK](#)
[CLOSE WINDOW](#)

Copyright © 2019 [Copyright Clearance Center, Inc.](#) All Rights Reserved. [Privacy statement](#). [Terms and Conditions](#). Comments? We would like to hear from you. E-mail us at customercare@copyright.com



RightsLink®

[Home](#)
[Create Account](#)
[Help](#)


Title: Reduction of space harmonics in induction machines incorporating rotor bar optimization through a coupled IPSO and 3-D FEA algorithm

Conference Proceedings: 2016 XXII International Conference on Electrical Machines (ICEM)

Author: Aida Mollaeian

Publisher: IEEE

Date: Sept. 2016

Copyright © 2016, IEEE

LOGIN

If you're a **copyright.com user**, you can login to RightsLink using your copyright.com credentials. Already a **RightsLink user** or want to [learn more?](#)

Thesis / Dissertation Reuse

The IEEE does not require individuals working on a thesis to obtain a formal reuse license, however, you may print out this statement to be used as a permission grant:

Requirements to be followed when using any portion (e.g., figure, graph, table, or textual material) of an IEEE copyrighted paper in a thesis:

- 1) In the case of textual material (e.g., using short quotes or referring to the work within these papers) users must give full credit to the original source (author, paper, publication) followed by the IEEE copyright line © 2011 IEEE.
- 2) In the case of illustrations or tabular material, we require that the copyright line © [Year of original publication] IEEE appear prominently with each reprinted figure and/or table.
- 3) If a substantial portion of the original paper is to be used, and if you are not the senior author, also obtain the senior author's approval.

Requirements to be followed when using an entire IEEE copyrighted paper in a thesis:

- 1) The following IEEE copyright/ credit notice should be placed prominently in the references: © [year of original publication] IEEE. Reprinted, with permission, from [author names, paper title, IEEE publication title, and month/year of publication]
- 2) Only the accepted version of an IEEE copyrighted paper can be used when posting the paper or your thesis online.
- 3) In placing the thesis on the author's university website, please display the following message in a prominent place on the website: In reference to IEEE copyrighted material which is used with permission in this thesis, the IEEE does not endorse any of [university/educational entity's name goes here]'s products or services. Internal or personal use of this material is permitted. If interested in reprinting/republishing IEEE copyrighted material for advertising or promotional purposes or for creating new collective works for resale or redistribution, please go to http://www.ieee.org/publications_standards/publications/rights/rights_link.html to learn how to obtain a License from RightsLink.

If applicable, University Microfilms and/or ProQuest Library, or the Archives of Canada may supply single copies of the dissertation.

[BACK](#)
[CLOSE WINDOW](#)

Copyright © 2019 [Copyright Clearance Center, Inc.](#) All Rights Reserved. [Privacy statement](#). [Terms and Conditions](#). Comments? We would like to hear from you. E-mail us at customer@copyright.com



RightsLink®

[Home](#)
[Create Account](#)
[Help](#)


Title: DNN-Based Predictive Magnetic Flux Reference for Harmonic Compensation Control in Magnetically Unbalanced Induction Motor

Author: Eshaan Ghosh

Publication: Magnetics, IEEE Transactions on

Publisher: IEEE

Date: Nov. 2017

Copyright © 2017, IEEE

LOGIN

If you're a **copyright.com user**, you can login to RightsLink using your copyright.com credentials. Already a **RightsLink user** or want to [learn more?](#)

Thesis / Dissertation Reuse

The IEEE does not require individuals working on a thesis to obtain a formal reuse license, however, you may print out this statement to be used as a permission grant:

Requirements to be followed when using any portion (e.g., figure, graph, table, or textual material) of an IEEE copyrighted paper in a thesis:

- 1) In the case of textual material (e.g., using short quotes or referring to the work within these papers) users must give full credit to the original source (author, paper, publication) followed by the IEEE copyright line © 2011 IEEE.
- 2) In the case of illustrations or tabular material, we require that the copyright line © [Year of original publication] IEEE appear prominently with each reprinted figure and/or table.
- 3) If a substantial portion of the original paper is to be used, and if you are not the senior author, also obtain the senior author's approval.

Requirements to be followed when using an entire IEEE copyrighted paper in a thesis:

- 1) The following IEEE copyright/ credit notice should be placed prominently in the references: © [year of original publication] IEEE. Reprinted, with permission, from [author names, paper title, IEEE publication title, and month/year of publication]
- 2) Only the accepted version of an IEEE copyrighted paper can be used when posting the paper or your thesis online.
- 3) In placing the thesis on the author's university website, please display the following message in a prominent place on the website: In reference to IEEE copyrighted material which is used with permission in this thesis, the IEEE does not endorse any of [university/educational entity's name goes here]'s products or services. Internal or personal use of this material is permitted. If interested in reprinting/republishing IEEE copyrighted material for advertising or promotional purposes or for creating new collective works for resale or redistribution, please go to http://www.ieee.org/publications_standards/publications/rights/rights_link.html to learn how to obtain a License from RightsLink.

If applicable, University Microfilms and/or ProQuest Library, or the Archives of Canada may supply single copies of the dissertation.

[BACK](#)
[CLOSE WINDOW](#)

Copyright © 2019 [Copyright Clearance Center, Inc.](#) All Rights Reserved. [Privacy statement.](#) [Terms and Conditions.](#) Comments? We would like to hear from you. E-mail us at customercare@copyright.com



RightsLink®

[Home](#)
[Create Account](#)
[Help](#)


Title: DNN predictive magnetic flux control for harmonics compensation in magnetically unbalanced induction motor

Conference Proceedings: 2017 IEEE International Magnetics Conference (INTERMAG)

Author: E. Ghosh

Publisher: IEEE

Date: April 2017

Copyright © 2017, IEEE

LOGIN

If you're a **copyright.com** user, you can login to RightsLink using your copyright.com credentials. Already a **RightsLink** user or want to [learn more?](#)

Thesis / Dissertation Reuse

The IEEE does not require individuals working on a thesis to obtain a formal reuse license, however, you may print out this statement to be used as a permission grant:

Requirements to be followed when using any portion (e.g., figure, graph, table, or textual material) of an IEEE copyrighted paper in a thesis:

- 1) In the case of textual material (e.g., using short quotes or referring to the work within these papers) users must give full credit to the original source (author, paper, publication) followed by the IEEE copyright line © 2011 IEEE.
- 2) In the case of illustrations or tabular material, we require that the copyright line © [Year of original publication] IEEE appear prominently with each reprinted figure and/or table.
- 3) If a substantial portion of the original paper is to be used, and if you are not the senior author, also obtain the senior author's approval.

Requirements to be followed when using an entire IEEE copyrighted paper in a thesis:

- 1) The following IEEE copyright/ credit notice should be placed prominently in the references: © [year of original publication] IEEE. Reprinted, with permission, from [author names, paper title, IEEE publication title, and month/year of publication]
- 2) Only the accepted version of an IEEE copyrighted paper can be used when posting the paper or your thesis online.
- 3) In placing the thesis on the author's university website, please display the following message in a prominent place on the website: In reference to IEEE copyrighted material which is used with permission in this thesis, the IEEE does not endorse any of [university/educational entity's name goes here]'s products or services. Internal or personal use of this material is permitted. If interested in reprinting/republishing IEEE copyrighted material for advertising or promotional purposes or for creating new collective works for resale or redistribution, please go to http://www.ieee.org/publications_standards/publications/rights/rights_link.html to learn how to obtain a License from RightsLink.

If applicable, University Microfilms and/or ProQuest Library, or the Archives of Canada may supply single copies of the dissertation.

[BACK](#)
[CLOSE WINDOW](#)

Copyright © 2019 [Copyright Clearance Center, Inc.](#) All Rights Reserved. [Privacy statement.](#) [Terms and Conditions.](#)
Comments? We would like to hear from you. E-mail us at customercare@copyright.com

VITA AUCTORIS

| | |
|-----------------|--|
| NAME: | Aida Mollaeian |
| PLACE OF BIRTH: | Tabriz, Iran |
| YEAR OF BIRTH: | 1981 |
| EDUCATION: | Tehran Islamic Azad University, Iran 2001 – 2006, B.Sc. in Physics-Solid states Tehran Islamic Azad University, Iran 2008 – 2012, M.Sc. in Physics-Solid states |